Proceedings of the 2nd symposium on threshold meson production in pp and pd interaction

Extended COSY-11 Collaboration Meeting, 1 – 3 June 2004
Collegium Maius, Jagellonian University, Cracow

Edited by Paweł Moskal

Technical Editors:

Rafał Czyżykiewicz
Michał Janusz
Paweł Klaja
Joanna Przerwa

Local organizing committee:

Michał Janusz
Lucjan Jarczyk
Paweł Moskal
Cezary Piskor-Ignatowicz
Joanna Przerwa

Financed by:
Forschungszentrum Jülich,
The Faculty of Physics, Astronomy and Applied Computer Science, Jagellonian University,
University of Silesia,
Department of Nuclear Physics, Institute of Physics, Jagellonian University,
Nuclear Physics Institute in Cracow

Schriften des Forschungszentrum Jülich:
Matter and Material 21 (2004)
ISBN 3-89336-366-1

Contents

List of Attendees **5**

Conference photo **6**

Acknowledgements **8**

Foreword **9**
Richard Wagner

Welcome of the Prorector of the Jagellonian University **11**
Karol Musioł

Welcome of the Consul General of the German Consulate in Cracow **12**
Maren Klingler

PAPERS

Dynamics of strangeness production in the near threshold nucleon-nucleon collisions **15**
Radhey Shyam

Study of the ground and excited states of Λ and Σ hyperon production at COSY **30**
Dieter Grzonka

Towards the excitation function of the $pp \to ppK^+K^-$ reaction at COSY-11 **45**
Peter Winter

Drift chamber with a U-shaped frame **52**
Jerzy Smyrski

Production of Σ^+ at COSY-11 **63**
Tomasz Rożek, Dieter Grzonka

Molecule formation in the $K\bar{K}$- and DK-channels **75**
Felix P. Sassen

The $\Theta^+(1540)$ resonance and its influence on the reactions K^+N and K^+d **81**
Johann Haidenbauer

On the possibility of studying properties of the exotic Θ^+ baryon using WASA at COSY **94**
Józef Złomańczuk

The puzzle of apparent narrowing of widths of meson resonances produced at or near maximum momentum transfer **102**
Bogdan C. Maglić

Polarized proton and deuteron beams at COSY **106**
Hans Stockhorst

COSY-11 as a polarimeter **122**
Rafał Czyżykiewicz

Spin-observables in meson production in nucleon-nucleon collisions **138**
Pachattu Deepak, Gowravaram Ramachandran, Christoph Hanhart

η' meson production in gamma-nucleon and nucleon-nucleon collisions **150**
Kanzo Nakayama

Recent results on η and η' photoproduction on the proton **177**
Barry G. Ritchie

Total and differential cross sections for the $pp \to pp\eta'$ reaction near threshold **193**
Alfons Khoukaz

Production of η meson in NN collisions **199**
Vadim Baru et al.

Three-pair final-state interaction in the $pp \to pp\eta$ reaction close to threshold **206**
Andrzej Deloff

Quasi-free production of the η and η' mesons in nucleon-nucleon collisions **224**
Joanna Stepaniak, Hans Calén

Bremsstrahlung radiation in the deuteron – proton collision **231**
Joanna Przerwa

Measurement of the η meson production via the quasi-free $pn \to pn\eta$ reaction **238**
Michał Janusz, Paweł Moskal

How to disentangle contributions from a single meson and multi-pion production in the missing mass spectra of the quasi-free $pn \to pnX$ reactions **249**
Paweł Moskal

Precise scan of the $dp \to {}^3\mathrm{H}\pi^+/{}^3\mathrm{He}\pi^0$ cross section ratio at the η production threshold **260**
Jerzy Smyrski

New results on the pd$\to{}^3$He η production near threshold **266**
Heinz-Hermann Adam et al.

Study of the $d-\eta$ interaction in the $dp \to dp\eta$ reaction **272**
Cezary Piskor-Ignatowicz, Paweł Moskal, Jerzy Smyrski

The gluon content of η and η' mesons **280**
Nicos Stefanis, Shahin S. Agaev

Tests of Chiral Perturbation Theory in η decays **298**
Andrzej Kupść

Hadronic decays of η and η' **307**
Niklas Beisert, Bugra Borasoy

Measurements of η' decays using WASA@COSY **314**
Magnus Wolke

List of Attendees

Heinz-Hermann Adam	adamh@uni-muenster.de
Andrzej Bałanda	balanda@if.uj.edu.pl
Vadim Baru	v.baru@fz-juelich.de
Bugra Borasoy	borasoy@physik.tu-muenchen.de
Andrzej Budzanowski	andrzej.budzanowski@ifj.edu.pl
Rafał Czyżykiewicz	r.czyzykiewicz@fz-juelich.de
Pachattu N. Deepak	d.pachattu@fz-juelich.de
Andrzej Deloff	deloff@fuw.edu.pl
Dieter Grzonka	d.grzonka@fz-juelich.de
Johann Haidenbauer	j.haidenbauer@fz-juelich.de
Michał Janusz	m.janusz@fz-juelich.de
Lucjan Jarczyk	jarczyk@if.uj.edu.pl
Alfons Khoukaz	khoukaz@uni-muenster.de
Maren Klingler	dt.gk-krakau@gmx.net
Reinhard Kulessa	kulessa@jetta.if.uj.edu.pl
Andrzej Kupść	kupsc@tsl.uu.se
Bogdan C. Maglić	maglich@hienergyinc.com
Tomasz N. Matulewicz	tomasz.matulewicz@fuw.edu.pl
Paweł Moskal	ufmoskal@if.uj.edu.pl
Karol Musioł	ufmusiol@cyf-kr.edu.pl
Kanzo Nakayama	nakayama@arches.uga.edu
Walter Oelert	w.oelert@fz-juelich.de
Cezary Piskor-Ignatowicz	c.piskor-ignatowicz@fz-juelich.de
Joanna Przerwa	j.przerwa@fz-juelich.de
Barry G. Ritchie	barry.ritchie@asu.edu
Felix P. Sassen	f.p.sassen@fz-juelich.de
Thomas Sefzick	t.sefzick@fz-juelich.de
Radhey Shyam	shyam@theory.saha.ernet.in
Marek Siemaszko	siemaszk@us.edu.pl
Jerzy Smyrski	smyrski@if.uj.edu.pl
Nikos G. Stefanis	stefanis@tp2.ruhr-uni-bochum.de
Joanna Stepaniak	joanna.stepaniak@fuw.edu.pl
Hans Stockhorst	h.stockhorst@fz-juelich.de
Adam Strzałkowski	ufstrzal@cyf-kr.edu.pl
Alexander Täschner	taschna@uni-muenster.de
Władysław Waluś	walus@jetta.if.uj.edu.pl
Peter Winter	p.winter@fz-juelich.de
Magnus Wolke	m.wolke@fz-juelich.de
Peter Wüstner	p.wuestner@fz-juelich.de
Wiktor Zipper	zipper@us.edu.pl
Józef Złomańczuk	jozef.zlomanczuk@tsl.uu.se

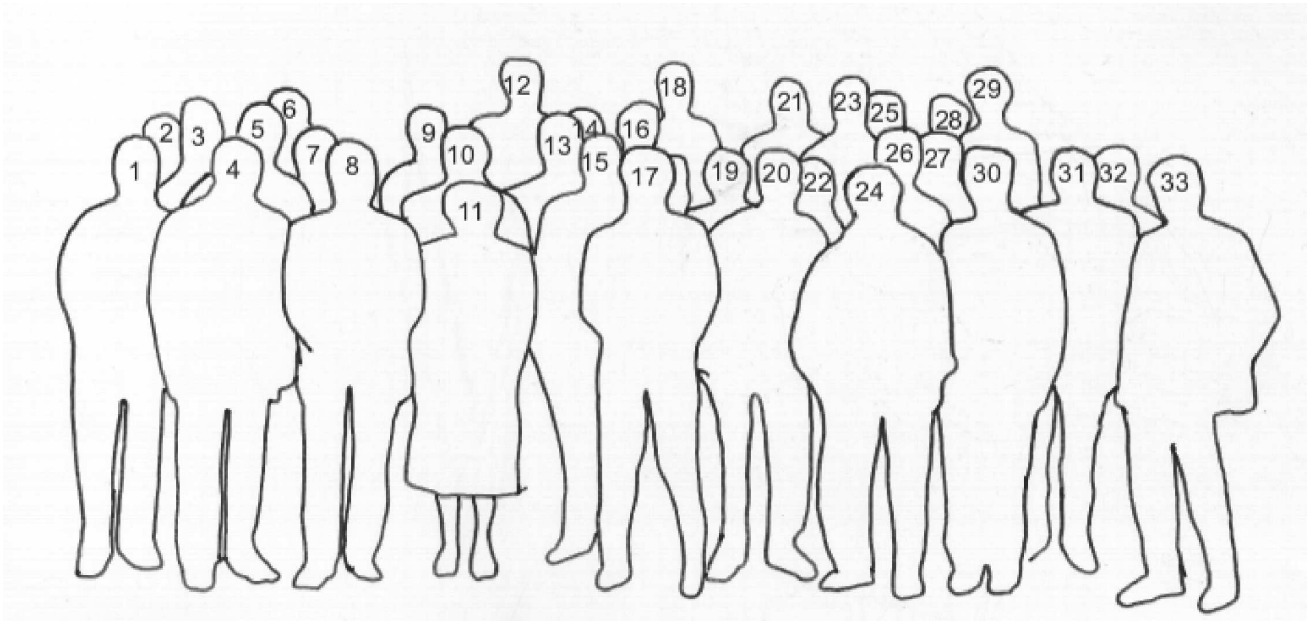

1 Marek Siemaszko
2 Tomasz N. Matulewicz
3 Alexander Täschner
4 Wiktor Zipper
5 Heinz-Hermann Adam
6 Bugra Borasoy
7 Thomas Sefzick
8 Władysław Waluś
9 Peter Winter
10 Dieter Grzonka
11 Krystyna Szałkowska
12 Reinhard Kulessa
13 Barry G. Ritchie
14 Andrzej Kupść
15 Michał Janusz
16 Joanna Stepaniak
17 Józef Złomańczuk
18 Magnus Wolke
19 Nikos G. Stefanis
20 Vadim Baru
21 Rafał Czyżykiewicz
22 Radhey Shyam
23 Cezary Piskor-Ignatowicz
24 Kanzo Nakayama
25 Felix P. Sassen
26 Johann Haidenbauer
27 Walter Oelert
28 Lucjan Jarczyk
29 Joanna Przerwa
30 Pachattu N. Deepak
31 Andrzej Deloff
32 Hans Stockhorst
33 Paweł Moskal

Acknowledgements

Results of the investigations carried out by the COSY-11 collaboration reported in this proceedings wouldn't be possible without the financial support which we received from the Forschungszentrum Jülich directorates, the European Community - Access to Research Infrastructure action of the Improving Human Potential Programme, the DAAD Exchange Programme (PPP-Polen), from the Polish State Committe for Scientific Research (grants No. 2P03B07123 and PB1060/P03/2004/26), and the FFE grants (41266606 and 41266654) from the Forschungszentrum Jülich.

Foreword

The Cooler Synchrotron COSY was built at the Research Centre Jülich for studies in the field of hadron physics. This accelerator is dedicated to be used by international collaborations to work at the frontiers of modern science. It is devoted to address the fundamental questions related to particle and nuclear physics. The Research Centre Jülich takes all effort to run this facility at a high level and thus gives the opportunity of performing basic and topical research both to well established scientists and to young students being trained in this exciting field.

The COSY-11 collaboration – consisting essentially of Polish and German scientists and technicians – which has been working at COSY for quite some time very successfully, met to "The second symposium on threshold meson production in pp and pd interactions" in Cracow from 1^{st} to 3^{rd} of June, 2004 at the Michał Bobrzyński Conference Hall in Collegium Maius, the oldest building of the Jagellonian University.

Achievements of the COSY–11 collaboration should be summarized as:

- Neutral hyperon productions in the fundamental proton-proton scattering, comparison of excitation functions and determination of spin averaged $\Lambda - p$ scattering parameters from a Dalitz plot distribution of the $pp \to pK^+\Lambda$ reaction.
- K^+K^- open strangeness two meson production cross sections in the 1 GeV mass range. Total cross sections and rough determination of the upper limit for the close to threshold production cross section of the overlapping $a_0(980)$ and $f_0(980)$ resonances.
- Excitation functions of near threshold meson production, especially of the η and η' mesons. Background free determination of invariant mass distributions of the two particle subsystems in the $pp\eta$ channel.

Plans for the near future activities at COSY–11 are:

- Systematic studies of isospin dependence of the hyperon and pseudoscalar mesons production in the nucleon-nucleon collision.
- High statistics η' meson production for invariant mass analysis of the two particle subsystems of the $pp\eta'$ final state.
- Analysing power A(y) in meson production in the threshold range.

- Excitation function of K^+K^- meson pair production in the 1 GeV mass range.
- Study of the η and η' meson production in three nucleon systems: determination of excitation functions of the $\eta(\eta')^3He$ and $dp\eta(\eta')$ final states.
- Study of bremsstrahlung radiation in free and quasi-free nucleon-nucleon collisions.
- Precise scan of the $dp \rightarrow {}^3H\pi^+/{}^3He\pi^0$ cross section ratio at the threshold for the η meson production.

All these items were discussed at the meeting in close connection to international experts in the field.
I would like to wish the COSY-11 collaboration and their members a fruitful future and a successfull research with exciting results, satisfactory work and lots of fun doing what they have to do.

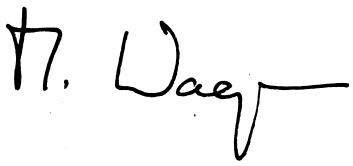

Richard Wagner
Forschungszentrum Jülich
Jülich, August 20^{th}, 2004

Welcome of the Prorector of the Jagellonian University

Mister Chairman,
Missis Consul General of Germany,
Ladies and Gentlemen,

It is a great pleasure and honour for me to welcome, on behalf of the Rector and Senate of the Jagiellonian University, all participants of the symposium in Collegium Maius.

This is a very special building for our University: it was bought by King Władysław Jagiełło in 1400 and has been in use since then. It is symbolic that your symposium takes place on the second floor of this building: on the first floor Copernicus participated in various lectures and discussions at the end of the fifteenth century. You are presenting and discussing the latest achievements of the contemporary nuclear physics in historical surroundings. It somehow shows you the philosophy of our University: to respect and learn from the history as well as to work hard on our contribution to the contemporary science.

One of the very important aspects of scientific research is international cooperation: your meeting is a good example. We all have always benefited from well developed cooperation: we have not only got important scientific results, but also have made new friends ready to help us both in laboratories and in our everyday life. It is a pleasure for me to see many of them in this conference room.

On May 1^{st} 2004 Poland entered the European Union. It was a very moving moment for us: we witnessed a historical event which we have never expected to happen during our life! I am sure that your long time collaboration and friendship have contributed to this day as well. I would like to thank you all for it.

We invite our very important guests and friends to Collegium Maius. We can show you a few pages of our history here: you will discover our Universities traditions in Germany and Poland are quite similar. So I strongly recommend you to have coffee in our café located in a sixteenth century cave and consider what we all may do for further development of our collaboration and friendship.

I wish you great professional and personal satisfaction from this symposium in this historical building.

Prof. Dr. Karol Musioł
Prorector of the Jagellonian University

Welcome of the Consul General of the German Consulate in Cracow

Sehr geehrte Damen und Herren Professoren,
verehrte Konferenzteilnehmer,

die Zusammenarbeit der Physiker der Jagiellonen Universität und des Kernforschungszentrums Jülich hat eine lange Tradition. Sie reicht zurück in die Zeit, in der Deutschland und Polen noch durch den Eisernen Vorhang getrennt waren. Wie wunderbar, dass Sie sich heute in einer grundlegend neuen politischen Situation treffen können: seit dem 1. Mai diesen Jahres ist Polen wieder da angelangt, wohin es immer schon gehörte, in Europa, ja sogar in seiner Mitte.

Und dass Sie eben sich hier in Krakau treffen, der alten Königsstadt mit ihrer ehrwürdigen Jagiellonen Universität, gibt ihrer Konferenz eine besondere Prägung. Das feste Fundament der Tradition und der mutige Blick in die Zukunft waren für Krakau immer schon typisch.

Wissenschaftliche Zusammenarbeit, fachlicher Austausch über die nationalen Grenzen hinweg und — im Verbund damit — das gegenseitiges Kennenlernen sind der Nährboden für Partnerschaft und Freundschaft. Sie sind damit auch die Basis, auf der sich über die Jahre hinweg das so wichtige Netzwerk individueller Beziehungen und persönlichen Vertrauens entwickeln kann.

Gerade jetzt, im Anfangsstadium der neuen europäischen Orientierung, nach dem beide Seiten — die alten Mitgliedsländer der Europäischen Union und die neuen Beitrittsländer — den mutigen Schritt zu einer neuen Zusammengehörigkeit getan haben, brauchen wir menschliche Begegnungen, die — wissenschaftlich geprägt — die Eliten zusammenführen. Noch das letzte Jahr — ich nenne nur die Diskussionen über die Errichtung eines Zentrums für die Opfer der Vertreibung in Berlin oder auch die Verhandlungen in Brüssel über eine europäische Verfassung — hat deutlich gezeigt, wie dünn das europäische Eis noch ist, das uns gemeinsam in eine friedlichere europäische Zukunft tragen soll.

Ich heiße Sie alle, vor allem diejenigen unter Ihnen, die von Jülich hierher gekommen sind, sehr herzlich willkommen. Fühlen Sie sich sozusagen hier in Krakau "zu Hause", zu Hause im europäischen Haus und lassen Sie sich nicht abschrecken davon, dass das Polnische und das Deutsche recht

schwierige und unterschiedliche Sprachen sind. Latein, die "lingua franca" der Humanisten ist zwar heute längst von English als der modernen Weltsprache abgelöst worden. Man mag es bedauern, dass sich die sprachlichen Rahmenbedingungen heute verändert haben. Über die Jahrhunderte unverändert geblieben hingegen ist das gegenseitige Interesse von deutschen und polnischen Wissenschaftlern, sich über den jeweiligen Gegenstand ihrer Forschung auszutauschen und ihn gemeinsam voranzubringen. Beweis hierfür ist z.B. Ihr heutiger Kongress.

Ihnen allen wünsche ich — in Anlehnung an die Ihnen sicher bekannte deutsche Fernseh–Talkmasterin — eine erfolgreiche Tagung und vor allem viel Freude beim Vermehren der dabei gewonnenen Einsichten.

Dr. Maren Klingler
Generalkonsulin der Bundesrepublik Deutschland
in Krakau

Dynamics of strangeness production in the near threshold nucleon-nucleon collisions

Radhey Shyam
Saha Institute of Nuclear Physics, Calcutta, India and
Department of Radiation Sciences, Uppsala University, Uppsala, Sweden

Abstract: We investigate the associated strangeness production reactions $pp \to p\Lambda K^+$ and $pp \to p\Sigma^0 K^+$ within an effective Lagrangian model. The initial interaction between the two nucleons is modeled by the exchange of π, ρ, ω and σ mesons and the strangeness production proceeds via the excitation of the $N^*(1650)$, $N^*(1710)$, and $N^*(1720)$ baryonic resonances. The parameters of the model at the nucleon-nucleon-meson vertices are determined by fitting the elastic nucleon-nucleon scattering with an effective interaction based on the exchange of these four mesons, while those at the resonance vertices are calculated from the known decay widths of the resonances as well as the vector meson dominance model. Experimental data taken recently by the COSY-11 collaboration are described well by this approach. The one-pion-exchange diagram dominates the production process at both higher and lower beam energies. The excitation of the $N^*(1650)$ resonances dominate both the production channels at near threshold energies. Our model with final state interaction effects among the outgoing particles included within the Watson-Migdal approximation, is able to explain the observed beam energy dependence of the ratio of the total cross sections of these two reactions.

1 Introduction

In recent years, there has been a considerable amount of interest in the study of the associated strangeness production reactions in proton-proton (pp) collisions. This is expected to provide information on the manifestation of quantum chromodynamics (QCD) in the non-perturbative regime of energies larger than those of the low energy pion physics where the low energy theorem and partial conservation of axial current (PCAC) constraints provide a useful insight into the relevant physics [1]. The strangeness quantum number introduced by this reaction leads to new degrees of freedom into this domain which are expected to probe the admixture of $\bar{s}s$ quark pairs in the

nucleon wave function [2] and also the hyperon-nucleon and hyperon-strange meson interactions [3, 4].

The elementary nucleon-nucleon-strange meson production cross sections are the most important ingredients in the transport model studies of the K^+-meson production in the nucleus-nucleus collisions, which provide information on not only the initial collision dynamics but also the nuclear equation of state at high density [5, 6, 7, 8, 9, 10, 11, 12]. Furthermore, the enhancement in the strangeness production has been proposed as a signature for the formation of the quark-gluon plasma in high energy nucleus-nucleus collisions [13, 14].

The measurements performed in late 1960s and 1970s provided the data on the total cross sections for the associated hyperon (Y)-kaon production at beam momenta larger than 2.80 GeV/c (these cross sections are listed in Ref. [15]). With the advent of the high-duty proton-synchrotron (COSY) at the Forschungszentrum, Jülich, it has become possible to perform systematic studies of the associated strangeness production at beam momenta very close to the reaction threshold (see, e.g.,Ref. [16] for a comprehensive review). At the near threshold beam energies, the final state interaction (FSI) effects among the outgoing particles are significant. Therefore, the new set of data are expected to probe also the hyperon-nucleon and hyperon-strange meson interactions.

A very interesting result of the studies performed by the COSY-11 collaboration is that the ratio (R) of the total cross sections for the $pp \to p\Lambda K^+$ and $pp \to p\Sigma^0 K^+$ reactions (to be referred as ΛK^+ and $\Sigma^0 K^+$ reactions, respectively) at the same excess energy (defined as $\epsilon = \sqrt{s} - m_p - m_Y - m_K$, with m_p, m_Y, and m_K being the masses of proton, hyperon, and kaon respectively and s the invariant mass of the collision), is about 28^{+6}_{-9} for $\epsilon <$ 13 MeV [17]. This result is very intriguing because at higher beam energies ($\epsilon \approx 1000$ MeV) this ratio is only around 2.5.

Several calculations have been reported [18, 19, 20] to explain this result. Assuming that the π- and K- exchange processes are the only mechanism leading to the strangeness production, the authors of Ref. [18] show within a (non-relativistic) distorted wave Born approximation (DWBA) model that while the ΛK^+ reaction is dominated by the K-exchange only, both K- and π-exchange processes play an important role in the case of $\Sigma^0 K^+$ reaction.Therefore, if the amplitudes corresponding to the two exchanges in the latter case interfere destructively, the production of Σ^0 is suppressed as compared to that of Λ. It should however, be noted that in Ref. [19], K- and π- exchange amplitudes are reported to be of similar magnitudes for both ΛK^+ and $\Sigma^0 K^+$ reactions.

Nevertheless, a conclusive evidence in support of the relative signs of π- and K- exchange amplitudes being opposite to each other is still lacking. Furthermore, other mechanisms like excitation, propagation, and decay of intermediate baryonic resonances which play (see, e.g., [21, 22, 23]) an important role in the strangeness production, have not been considered by these authors. In the calculations reported in Ref. [20] also the relative sign of $K-$ and $\pi-$ exchange terms is chosen solely by the criteria of reproducing the experimental data, although in this work the theory has been applied to describe a wider range of data (which includes the polarization transfer results of the DISTO experiment [24] and the missing mass distribution obtained in the inclusive K^+ production measurements performed at SATURNE [25] apart from the ratio R).

We have investigated the ΛK^+ and $\Sigma^0 K^+$ reactions at near threshold as well as higher beam energies in the framework of an effective Lagrangian approach (ELA) [21, 22, 28, 29]. In this theory, the initial interaction between two incoming nucleons is modeled by an effective Lagrangian which is based on the exchange of the π-, ρ-, ω-, and σ- mesons. The coupling constants at the nucleon-nucleon-meson vertices are determined by directly fitting the T-matrices of the nucleon-nucleon (NN) scattering in the relevant energy region. The ELA uses the pseudovector (PV) coupling for the nucleon-nucleon-pion vertex which is consistent with the chiral symmetry requirement of the quantum chromodynamics [31]. In contrast to some earlier calculations [26], both (ΛK^+ and $\Sigma^0 K^+$) reactions proceed via excitation of the $N^*(1650)$, $N^*(1710)$, and $N^*(1720)$ intermediate baryonic resonance states. The interference terms between the amplitudes of various resonances are retained. To describe the near threshold data, the FSI effects in the final channel are included within the framework of the Watson-Migdal theory [27, 29]. ELA has been used to describe rather successfully the $pp \to pp\pi^0$, $pp \to pn\pi^+$ [29, 28], $pp \to pK^+Y$ [21, 22] as well as $pp \to ppe^+e^-$ [30] reactions.

2 Description of the Model

We consider the tree-level structure (Fig. 1) of the amplitudes for the associated K^+Y production in proton-proton collisions, which proceeds via the excitation of the $N^*(1650)(\frac{1}{2}^-)$, $N^*(1710)(\frac{1}{2}^+)$, and $N^*(1720)(\frac{3}{2}^+)$ intermediate resonances. To evaluate these amplitudes within the effective Lagrangian approach, one needs to know the effective Lagrangians (and the coupling constants appearing therein) at (a) the nucleon-nucleon-meson, (b)

the resonance-nucleon-meson, and (c) the resonance-K^+-hyperon vertices.

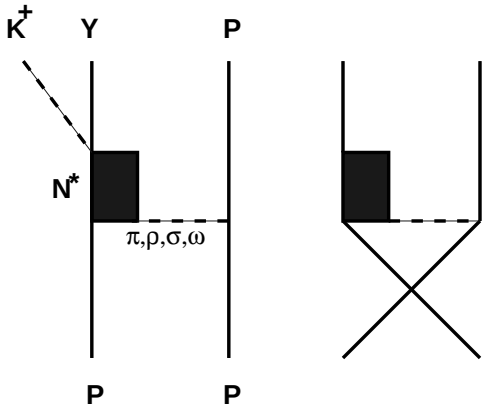

Figure 1: Feynman diagrams for K^+Y production in pp collisions. The diagram on the left shows the direct process while that on the right the exchange one.

The parameters for NN vertices are determined by fitting the NN elastic scattering T matrix with an effective NN interaction based on the π, ρ, ω and σ meson exchanges. The effective meson-NN Lagrangians are

$$\mathcal{L}_{NN\pi} = -\frac{g_{NN\pi}}{2m_N}\bar{\Psi}_N\gamma_5\gamma_\mu\boldsymbol{\tau}\cdot(\partial^\mu\boldsymbol{\Phi}_\pi)\Psi_N. \quad (1)$$

$$\mathcal{L}_{NN\rho} = -g_{NN\rho}\bar{\Psi}_N\left(\gamma_\mu + \frac{k_\rho}{2m_N}\sigma_{\mu\nu}\partial^\nu\right)\boldsymbol{\tau}\cdot\boldsymbol{\rho}^\mu\Psi_N. \quad (2)$$

$$\mathcal{L}_{NN\omega} = -g_{NN\omega}\bar{\Psi}_N\left(\gamma_\mu + \frac{k_\omega}{2m_N}\sigma_{\mu\nu}\partial^\nu\right)\omega^\mu\Psi_N. \quad (3)$$

$$\mathcal{L}_{NN\sigma} = g_{NN\sigma}\bar{\Psi}_N\sigma\Psi_N. \quad (4)$$

We have used the notations and conventions of Bjorken and Drell [32]. In Eq. (1) m_N denotes the nucleon mass. Note that we have used a PV coupling for the $NN\pi$ vertex. Since we use these Lagrangians to directly model the T-matrix, we have also included a nucleon-nucleon-axial-vector-isovector vertex, with the effective Lagrangian given by

$$\mathcal{L}_{NNA} = g_{NNA}\bar{\Psi}\gamma_5\gamma_\mu\boldsymbol{\tau}\Psi\cdot\mathbf{A}^\mu, \quad (5)$$

where A represents the axial-vector meson field. This term is introduced because in the limit of large axial meson mass (m_A) it cures the unphysical behavior in the angular distribution of NN scattering caused by the contact term in the one-pion exchange amplitude [33], if g_{NNA} is chosen to be

$$g_{NNA} = \frac{1}{\sqrt{3}}m_A\left(\frac{f_\pi}{m_\pi}\right), \quad (6)$$

with very large ($\gg m_N$) m_A. f_π appearing in Eq. (6) is related to $g_{NN\pi}$ as $f_\pi = (\frac{g_{NN\pi}}{2m_N})m_\pi$.

We introduce, at each interaction vertex, the form factor

$$F_i^{NN} = \left(\frac{\lambda_i^2 - m_i^2}{\lambda_i^2 - q_i^2}\right), i = \pi, \rho, \sigma, \omega, \quad (7)$$

where q_i and m_i are the four momentum and mass of the ith exchanged meson, respectively. The form factors suppress the contributions of high momenta and the parameter λ_i, which governs the range of suppression, can be related to the hadron size. Since NN elastic scattering cross sections decrease gradually with the beam energy (beyond certain value), we take energy dependent meson-nucleon coupling constants of the following form

$$g(\sqrt{s}) = g_0 exp(-\ell\sqrt{s}), \quad (8)$$

in order to reproduce these data in the entire range of beam energies. The parameters, g_0, λ and ℓ were determined by fitting to the elastic proton-proton and proton-neutron scattering data at the beam energies in the range of 400 MeV to 4.0 GeV [33, 28]. It may be noted that this procedure fixes also the signs of the effective Lagrangians [Eqs. (1)-(5)]. The values of various parameters are given in Table 1 of Ref. [21]. The same parameters for these vertices were also used in calculations of the pion and the dilepton production in pp collisions. Thus we ensure that the NN elastic scattering channel remains the same in the description of various inelastic channels within this approach, as it should be.

Below 2 GeV center of mass (c.m.) energy, only three resonances, $N^*(1650)$, $N^*(1710)$, and $N^*(1720)$, have significant decay branching ratios into KY channels. Therefore, we have considered only these three resonances in our calculations. The $N^*(1700)$ resonance having very small (and uncertain) branching ratio for the decay to these channels, has been excluded. Since all the three resonances can couple to the meson-nucleon channel considered in the previous section, we require the effective Lagrangians for all the four resonance-nucleon-meson vertices corresponding to all the included resonances. Since the mass of the strange quark is much higher than that of the $u-$ or $d-$ quark, one does not expect the pion like strict chiral constraints for the case of other pseudoscalar mesons like η and K (to be called ζ in the following). Thus, one has a choice of psuedoscalar (PS) or PV couplings for the $NN\zeta$ and $N^*_{1/2}N\zeta$ vertices (forms of the corresponding effective Lagrangians are given in Ref. [21]). The same holds also for the $N^*_{1/2}YK$ vertices.

In principle, one can select a linear combination of both and fit the PS/PV ratio to the data. However, to minimize the number of parameters we choose either PS or PV coupling at a time. In the results shown below, we have used PS couplings for both $N^*N\pi$ and $N^*\Lambda K^+$ vertices involving spin-1/2 resonances of even and odd parities. Calculations have also been performed with the corresponding PV couplings. The cross sections calculated with this option for the $N^*_{1/2}YK$ vertex deviate very little from those obtained with the corresponding PS couplings. However, data shows a clear preference for the PS coupling at the $N^*_{1/2}N\pi$ vertices.

The couplings constants for the vertices involving resonances are determined from the experimentally observed quantities such as branching ratios for their decays to corresponding channels. It may however, be noted that such a procedure can not be used to determine the coupling constant for the $N^*(1650)\Sigma K$ vertices, as the on-shell decays of this resonance to ΣK channel are inhibited. Therefore, we have tried to determine this coupling constant by fitting the available data on the $\pi^+p \to \Sigma^+K^+$, $\pi^-p \to \Sigma^0K^0$, and $\pi^-p \to \Sigma^-K^+$ reactions in an effective Lagrangian coupled channels approach [34, 35], where all the available data for the transitions from πN to five meson-baryon final states, πN, $\pi\pi N$, ηN, $K\Lambda$, and $K\Sigma$ are simultaneously analyzed for center of mass energies ranging from threshold to 2 GeV. In this analysis all the baryonic resonances with spin $\leq \frac{3}{2}$ up to excitation energies of 2 GeV are included as intermediate states. Since the resonances considered in this study have no known branching ratios for the decay into the $N\omega$ channel, we determine the coupling constants for the $N^*N\omega$ vertices by the strict vector meson dominance (VMD) hypothesis [36], which is based essentially on the assumption that the coupling of photons on hadrons takes place through a vector meson.

It should be stressed that the branching ratios determine only the square of the corresponding coupling constants; thus their signs remain uncertain in this method. Predictions from independent calculations (*e.g* the quark model) can, however, be used to constrain these signs. The magnitude as well as signs of the coupling constants for the $N^*N\pi$, $N^*\Lambda K$, $N^*N\rho$, and $N^*N(\pi\pi)_{s-wave}$ vertices were determined by Feuster and Mosel [34] and Manley and Saleski [37] in their analysis of the pion-nucleon data involving the final states πN, $\pi\pi N$, ηN, and $K\Lambda$. Predictions for some of these quantities are also given in the constituent quark model calculations of Capstick and Roberts [38]. Guided by the results of these studies, we have chosen the positive sign for the coupling constants for these vertices. Unfortunately, the quark model calculations for the $N^*N\omega$ vertices are still sparse and an unambiguous prediction for the signs of the corresponding coupling con-

stants may not be possible at this stage [39]. Nevertheless, we have chosen a positive sign for the coupling constants for these vertices as well.

The resonance properties used in the calculations of the decay widths are given in Table 1, where the resulting coupling constants and the adopted values of the cut-off parameters ($\lambda_i^{NN^*}$) are also shown. It may be noted that we have fixed the latter to one value in order to minimize the number of free parameters.

Table 1: Coupling constants and cut-off parameters for the N^*N-meson and N^*-hyperon-meson vertices used in the calculations

Resonance	Decay channel	Branching ratio (GeV)	$g^2/4\pi$	cut-off (GeV)
$N^*(1710)$	$N\pi$	0.150	0.0863	850.0
	$N\rho$	0.150	1.3653	850.0
	$N\omega$		0.1189	850.0
	$N\sigma$	0.170	0.0361	850.0
	ΛK	0.150	2.9761	
	ΣK		4.4044	
$N^*(1720)$	$N\pi$	0.100	0.0023	850.0
	$N\rho$	0.700	90.637	850.0
	$N\omega$		22.810	850.0
	$N\sigma$	0.120	0.1926	850.0
	ΛK	0.080	0.0817	
	ΣK		0.2204	
$N^*(1650)$	$N\pi$	0.700	0.0521	850.0
	$N\rho$	0.08	0.5447	850.0
	$N\omega$		0.2582	850.0
	$N\sigma$	0.025	0.2882	850.0
	ΛK	0.070	0.0485	
	ΣK		0.0165	

After having established the effective Lagrangians, coupling constants and form of the propagators (which are given in Ref. [21]), it is straight forward to write down the amplitudes for various diagrams associated with the $pp \to pYK$ reactions which can be calculated numerically by following *e.g.* the techniques discussed in [28]. The isospin part is treated separately. This gives rise to a constant factor for each graph, which is unity for the

reaction under study. It should be noted that the signs of various amplitudes are fixed by those of the effective Lagrangian densities, coupling constants and propagators as described above. These signs are not allowed to change anywhere in the calculations.

In the present form of our effective Lagrangian theory, the energy dependence of the cross section due to FSI is separated from that of the primary production amplitude and the total amplitude is written as,

$$A_{fi} \quad = \quad M_{fi}(pp \to pYK^+) \cdot T_{ff}, \tag{9}$$

where $M_{fi}(pp \to pYK^+)$ is the primary associated YK production amplitude, while T_{ff} describes the re-scattering among the final particles which goes to unity in the limit of no FSI. The latter is taken to be the coherent sum of the two-body on-mass-shell elastic scattering amplitudes t_i (with i going from 1 to 3), of the interacting particle pairs $j-k$ in the final channel. This type of approach has been used earlier to describe the pion [29, 40, 41], η-meson [42, 43, 44], ΛK^+ [21] and ϕ-meson [45] production in pp collisions.

An assumption inherent in Eq. (9) is that the reaction takes place over a small region of space (which is fulfilled rather well in near threshold reactions involving heavy mesons). Under this condition the amplitudes t_i can be expressed in terms of the inverse of the Jost function [27, 29] which has been calculated by using a Coulomb modified effective range expansion of the phase-shift [46]. The required effective range and scattering length parameters are given in Refs. [21, 22].

3 Results and Discussions

The total cross sections for the ΛK^+ and $\Sigma^0 K^+$ reactions as a function of the excess energy are shown in Fig. 2. The calculations are the coherent sum of all resonance excitation and meson exchange processes as described earlier. In both cases a good agreement is obtained between theory and the data available from the COSY-11 collaboration. Keeping in mind the fact that all parameters of the model, except for those of N^*Yp vertices and the FSI, were the same in the two calculations and that no parameter was freely varied, this agreement is quite satisfactory. It should be noted that we do not require to introduce arbitrary normalization constants to get the agreement between calculations and the data. We also show in this figure the results obtained without including the FSI effects (dashed line). It can be seen that the FSI effects are vital for a proper description of the experimental data in both the cases.

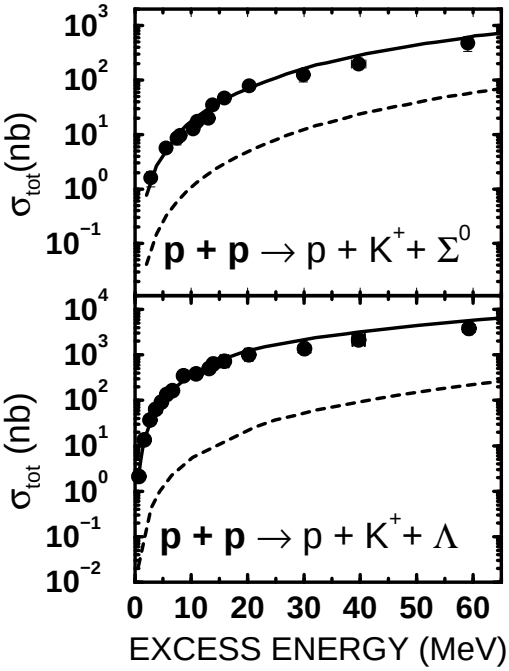

Figure 2: Comparison of the calculated and the experimental total cross sections for the $pp \to p\Lambda K^+$ and $pp \to p\Sigma^0 K^+$ reactions as a function of the excess energy. Results obtained with no FSI effects are shown by dashed lines. The experimental data are from Refs. [17] .

In Fig. 3, we have investigated the role of various meson exchange processes in describing the total cross sections. The dashed, long-dashed, dashed-dotted, and solid with black square curves represent the contributions of π, ρ, ω and σ meson exchanges, respectively. The contribution of the heavy axial meson exchange is not shown in this figure as it is negligibly small. The coherent sum of all the meson-exchange processes is shown by the solid line. It is clear that the pion exchange graphs dominate the production process for both the reactions in the entire range of beam energies. Contributions of ρ and ω meson exchanges are almost insignificant. On the other hand, the σ meson exchange, which models the correlated $s-$wave two-pion exchange process and provides about 2/3 of this exchange in the low energy NN interaction, plays a relatively more important role. This observation has also been made in case of the $NN \to NN\pi$ reaction [47, 48, 49, 28].

The individual contributions of various nucleon resonances to the total cross sections of the two reactions are shown in Fig. 4. We note that in both the cases, the cross section is dominated by the $N^*(1650)$ resonance excitation for $\epsilon < 30$ MeV. Since $N^*(1650)$ is the lowest energy baryonic resonance having branching ratios for the decay to YK^+ channels, its dominance in these reactions at beam energies very close the kaon production threshold is to be expected. In the near threshold region the relative dominance of

various resonances is determined by the dynamics of the reaction where the difference of about 60 MeV in excitation energies of $N^*(1650)$ and $N^*(1710)$ resonances plays a crucial role.

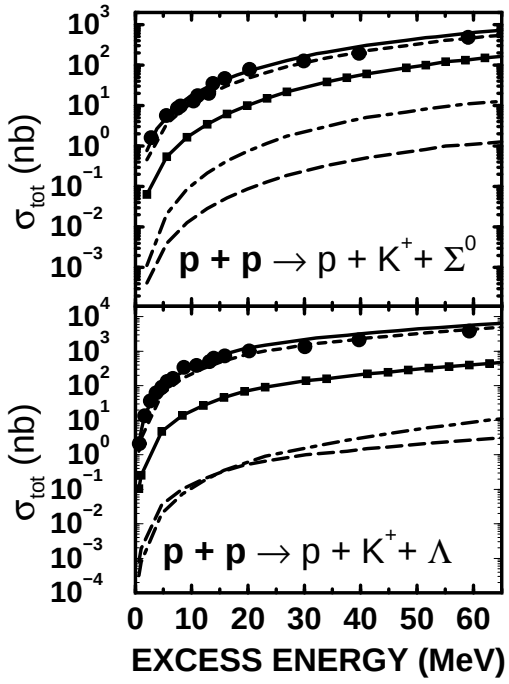

Figure 3: Contributions of various meson exchange processes to the total cross section for the $pp \to pK^+\Lambda$ and $pp \to pK^+\Sigma^0$ reactions. The dashed, long-dashed, dashed-dotted and solid with black squares curves represent the contributions of π, ρ, ω and σ meson exchanges, respectively. Their coherent sums are shown by the solid lines .

However, for ϵ values between 30 - 60 MeV, while the $pp \to pK^+\Lambda$ reaction continues to be dominated by $N^*(1650)$ excitation, the $pp \to pK^+\Sigma^0$ reaction gets significant contributions also from $N^*(1710)$ and $N^*(1720)$ resonances. This difference in the role of the three resonances in the two cases can be understood in the following way. For a resonances to contribute significantly, we should have $m_Y + m_K + \epsilon \geq m_R + \Gamma_R/2$, where m_R and Γ_R are the mass and width of the resonance, respectively. Therefore, in the region of excess energies $\geq Q[= (m_R + \Gamma_R/2) - (m_Y + m_K)]$, the particular resonance R should contribute significantly. The values of Q for the $pp \to pK^+\Lambda$ reaction, are 115 MeV, 150 MeV, and 185 MeV, for the $N^*(1650)$, $N^*(1710)$, and $N^*(1720)$ resonances, respectively. On the other hand, for the $pp \to pK^+\Sigma^0$ case, they are 36 MeV, 72 MeV and 105 MeV, respectively for these three resonances. Therefore, contributions of the $N^*(1710)$ and $N^*(1720)$ resonance excitations are negligibly small for the $K^+\Lambda$ production in the entire energy range of the COSY-11 data (i.e., for $\epsilon \leq 60.$ MeV) while they are significant for the $K^+\Sigma^0$ case for $\epsilon > 30$

MeV. It would be helpful to have data on the invariant mass spectrum at these excess energies in order to confirm these theoretical observations.

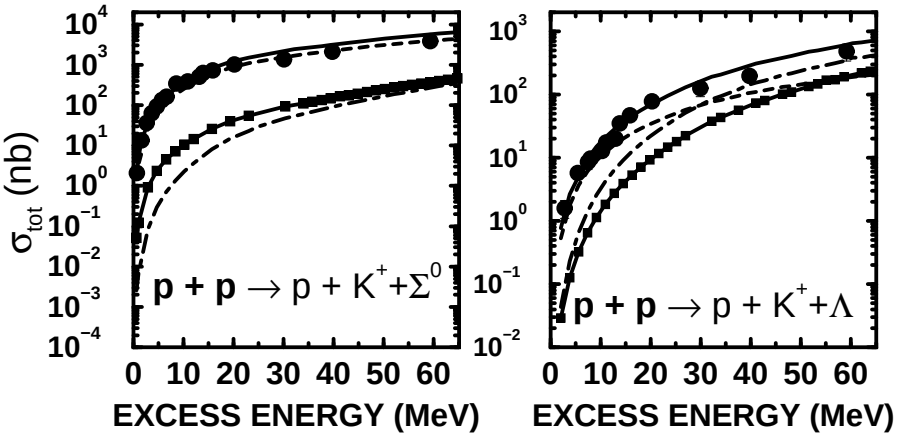

Figure 4: Contributions of N*(1650) (dashed line), N*(1710) (full line with black squares) and N*(1720) (dashed-dotted line) baryonic resonances to the total cross section for the two reactions studied in Fig. 2. Their coherent sum is shown by the solid line.

In Fig. 5, we compare our calculations with the data for the ratio R as a function of ϵ. We have shown here the results for excess energies up to 60 MeV, where the COSY-11 data are available. It is clear that our calculations are able to describe well the trend of the fall-off of R as a function of the excess energy. It should be noted that FSI effects account for about $60\% - 80\%$ of the observed ratio for $\epsilon < 30$ MeV and about 50% of it beyond this energy. Therefore, not all of the observed value of R at these beam energies can be accounted for by the FSI effects, which is in agreement with the observation made in [18]. It should again be emphasized that without considering the contributions of the $N^*(1650)$ resonance for the $\Sigma^0 K^+$ reactions, the calculated ratio would be at least an order of magnitude larger. Therefore, these data are indeed sensitive to the details of the reaction mechanism. At higher beam energies ($\epsilon > 300$ MeV), values of R obtained with and without FSI effects are almost identical. In this region the reaction mechanism is different; here all the three resonances contribute in one way or the other, their interference terms are significant [21], and FSI related effects are unimportant.

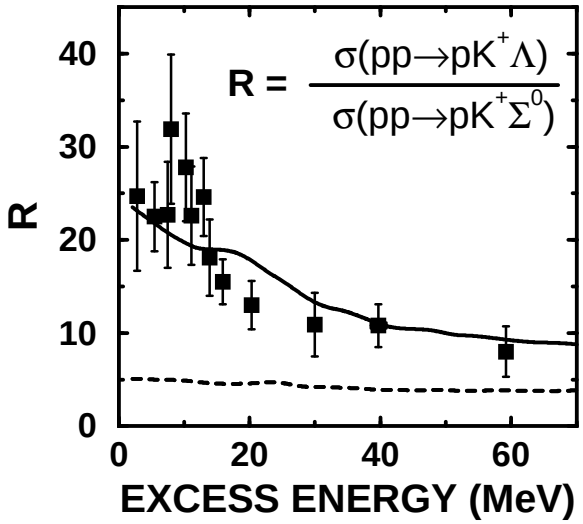

Figure 5: Ratio of the total cross sections for $pp \to p\Lambda K^+$ and $pp \to p\Sigma^0 K^+$ reaction as a function of the excess energy. The solid and dashed lines show the results of our calculations with and without FSI effects, respectively. The data are from [17].

4 Summary and conclusions

In summary, we have studied the $pp \to p\Lambda K^+$ and $pp \to p\Sigma^0 K^+$ reactions within an effective Lagrangian model. Most of the parameters of the model are fixed by fitting to the elastic NN T-matrix which restricts the freedom of varying them freely in order to fit the data. The reactions proceed via excitation of the $N^*(1650)$, $N^*(1710)$, and $N^*(1720)$ intermediate baryonic resonant states. An important result of our study is that the $N^*(1650)$ resonant state contributes predominantly to both these reactions at near threshold beam energies. Therefore, these reactions in this energy regime, provide an ideal means of investigating the properties of this S_{11} baryonic resonance. To the extent that the final state interaction effects in the exit channel can be accounted for by the Watson-Migdal theory, our model is

able to explain the experimentally observed large ratio of the total cross sections of the two reactions in the near threshold region.

This work is supported by the Wenner-Gren Center Foundation, Stockholm. The author wishes to express his sincere thanks to Anders Ingemarsson and Bo Höistad for their very kind hospitality in the Department of Radiation Science of the Uppsala University. He also wishes to acknowledge useful discussions with Bo Höistad, Göran Fäldt, Ulrich Mosel, and Walter Oelert.

References

[1] T.E.O Ericson and W. Weise, *Pions and Nuclei*, Clarendon, Oxford, 1988.

[2] M. Alberg, Prog. Part. Nucl. Phys. **36** (1996) 217.

[3] A. Deloff, Nucl. Phys. **A 505** (1989) 583.

[4] R.A. Adelseck and B. Saghai, Phys. Rev. **C 42** (1990) 108.

[5] U. Mosel, Annu. Rev. Nucl. Part. Sci. **41** (1991) 29 and references therein.

[6] G.E. Brown, C.M. Ko, Z.G. Wu and L.H. Xia, Phys. Rev. **C 43** (1991) 1881.

[7] T. Maruyama, W. Cassing, U.Mosel, S. Teis and K. Weber, Nucl. Phys. **A 573** (1994) 653.

[8] D. Miskowiec et al., Phys. Rev. Lett. **72** (1994) 3650.

[9] C. Hartnack, J. Jaenicke, L. Sehn, H. Ströcker and J. Aichelin, Nucl. Phys. **A 580** (1994) 643.

[10] X.S. Fang, C.M. Ko, G.Q. Li, Y.M. Zheng, Nucl. Phys. **A 575** (1994) 766.

[11] G.Q. Li and C.M. Ko, Phys. Lett. **B 349** (1995) 405.

[12] G.Q. Li, C.M. Ko and W.S. Chung, Phys. Rev. **C 57** (1998) 434.

[13] J. Rafelski and B. Müller, Phys. Rev. Lett. **48** (1982) 1066.

[14] H.W. Barz, B.L. Friman, J. Knoll and H. Schulz, Nucl. Phys. **A 485** (1988) 685.

[15] Landolt-Börnstein, New Series, Ed. H. Schopper, I/12 (1988).

[16] P. Moskal, M. Wolke, A. Khoukaz, and W. Oelert, Prog. Part. Nucl. Phys. **49** (2002) 1.

[17] S. Sewerin et al., Phys. Rev. Lett. **83** (1999) 682; P. Kowina et. al., nucl-ex/0402008.

[18] A.M. Gasparian, J. Haidenbauer, C. Hanhart, L. Kondratyuk, and J. Speth, Phys. Lett. **B 480** (2000) 273.

[19] A. Sibirtsev, K. Tsushima, W. Cassing, and A.W. Thomas, LANL preprint, nucl-th/0004022.

[20] J. M. Laget, Nucl. Phys. **A 691** (2001) 11c.; *ibid.*, Phys. Lett. **B 359** (1991) 24.

[21] R. Shyam, Phys. Rev. **C 60** (1999) 055213.

[22] R. Shyam, G. Penner, and U. Mosel, Phys. Rev. **C 63** (2001) 022202(R).

[23] G. Fäldt and C. Wilkin, Z. Phys. **A 357** (1997) 241.

[24] F. Balestra et al., Phys. Rev. Lett. **83** (1999) 1534.

[25] R. Siebert et al., Nucl. Phys. **A 567** (1994) 819.

[26] A. Sibirtsev, K. Tsushima, and A.W. Thomas, Phys. Lett. **B 421** (1998) 59; A. Sibirtsev, K. Tsushima, W. Cassing, and A.W. Thomas, Nucl. Phys. **A 646** (1999) 427.

[27] M.L. Goldberger and K.M. Watson, *Collision Theory*, Wiley, New York, 1969, pp 549.

[28] A. Engel, R. Shyam, U. Mosel and A.K. Dutt-Majumdaer, Nucl. Phys. **A 603** (1996) 387.

[29] R. Shyam and U. Mosel, Phys. Lett. **B 425** (1998) 1.

[30] R. Shyam and U. Mosel, Phys. Rev. **C 67** (2003) 065202.

[31] S. Weinberg, Phys. Rev. **166** (1996) 1568.

[32] J.D. Bjorken and S.D. Drell, *Relativistic Quantum Mechanics*, McGraw-Hill, New York, 1964.

[33] M. Schäfer, H.C. Dönges, A. Engel and U. Mosel, Nucl. Phys. **A 575** (1994) 429.

[34] T. Feuster and U. Mosel, Phys. Rev. **C 58** (1998) 457; *ibid.* **59** (1999) 460.

[35] G. Penner and U. Mosel, Phys. Rev. **C 66** (2002) 055211; **66** (2002) 055212.

[36] J.J. Sakurai, *Currents and Mesons*, Univ. of Chicago Press, Chicago, 1969; Ann. Phys. **11** (1960) 1.

[37] D.M. Manley and E.M. Saleski, Phys. Rev. **D 45** (1992) 4002.

[38] S. Capstick and W. Roberts, Phys. Rev. **D 49** (1994) 4570.

[39] Fl. Stancu and P. Stassart, Phys. Rev. **D 46** (1993) 2140.

[40] J. Dubach, W.M. Kloet, and R.R. Silbar, Phys. Rev. **C 33** (1986) 373.

[41] V. Bernard, N. Kaiser, and Ulf-G. Meissner, Eur. Phys. J. **A 4** (1999) 259.

[42] A. Moalem, E. Gedalin, L. Razdolskaja, and Z. Shorer, Nucl. Phys. **A 600** (1996) 445.

[43] B.L. Druzhinin, A.E. Kudryavtsev, and V.E. Tarasev, Z. Phys. **A 359** (1997) 205.

[44] A. Deloff, Phys. Rev. **C 69** (2004) 035206.

[45] A.I. Titov, B. Kämpfer, and B.L. Reznik, Eur. Phys. J. **A 7** (2000) 543.

[46] H.P. Noyes, Annu. Rev. Nucl. Sci. **22** (1972) 465.

[47] V. Dmitriev, O. Sushkov and C. Gaarde, Nucl. Phys. **A 459** (1986) 503.

[48] T.S.H. Lee and D.O. Riska, Phys. Rev. Lett, **70** (1993) 1137.

[49] C.J. Horowitz, H.O. Meyer and D.K. Griger, Phys. Rev. **C 49** (1994) 1337.

Study of the ground and excited states of Λ and Σ hyperon production at COSY

D. Grzonka

Institut für Kernphysik, Forschungszentrum Jülich, Germany

Abstract: COSY with a maximum beam momentum of $\sim$ 3.65 GeV/c allows the production of ground state (Λ and Σ) and excited hyperons ($\Lambda(1405)$, $\Sigma(1385)$ and $\Lambda(1520)$) in elementary NN interactions. The existing data base in this field is rather poor. A systematic study of the hyperon production at COSY will result in an improvement of our understanding concerning topics like hyperon–nucleon interaction, kaon–nucleon interaction, nucleon resonances, strangeness production mechanism and structure of the $\Lambda(1405)$. Precise data on Λ and Σ production have been produced at the COSY-11 and TOF installation. With the WASA detector at COSY these studies can be continued and extended to channels including photons in the final state.

1 Introduction

The cooler synchrotron COSY with a maximum beam momentum of $\sim$ 3.65 GeV/c allows the production of Λ and Σ hyperons in elementary NN-interactions via the associated strangeness production $NN \rightarrow NYK$. Ground state (Λ, Σ^-, Σ^0, Σ^+) as well as the excited hyperon states $\Lambda(1405)$, $\Sigma(1385)$ and $\Lambda(1520)$ are accessible.

The physics motivation for the production of ground state hyperons is very different from the motivation to study their excited states. The ground state hyperons are well defined (qqq) states of the $J^P = 1/2^+$ baryon octet with S=-1 and its properties like mass and decay modes are very well known. Production studies of the ground state hyperon aims at information on the production mechanism and on the interaction with hadrons. Concerning the excited hyperons especially the $\Lambda(1405)$ the main focus is on the resonance shape and its structure. It is under discussion if or how much of the $\Lambda(1405)$ can be attributed to a 3-quark state or a meson-baryon molecule.

From the experimental point of view the studies of ground and excited hyperons are comparable. In both cases delayed decays are involved which

state	$I(J^P)$	M [MeV]	$c\tau$	decay modes
Λ	$0(\frac{1}{2}^+)$	1115.683±0.006	7.89 cm	$p\pi^-(64\%)$, $n\pi^0(36\%)$
Σ^+	$1(\frac{1}{2}^+)$	1189.37 ± 0.07	2.404 cm	$p\pi^0(52\%)$, $n\pi^+(48\%)$
Σ^0	$1(\frac{1}{2}^+)$	1192.642±0.024	2.22 10^{-11} cm	$\Lambda\gamma(\sim 100\%)$
Σ^-	$1(\frac{1}{2}^+)$	1197.449±0.03	4.434 cm	$n\pi^-$ ($\sim$100%)

Table 1: Properties of Λ and Σ ground state hyperons [1].

state	$I(J^P)$	M [MeV]	Γ [MeV]	decay
$\Lambda(1405)$	$0(\frac{1}{2}^-)$	1406± 4	50.0±2.0	$\Sigma\pi(100\%)$
$\Lambda(1520)$	$0(\frac{3}{2}^-)$	1519.5±1.0	15.6±1.0	$N\bar{K}(45\%)$,$\Sigma\pi(42\%)$ $\Lambda\pi\pi(10\%)$
$\Sigma^+(1385)$	$1(\frac{3}{2}^+)$	1382.8±0.4	35.8±0.8	
$\Sigma^0(1385)$	$1(\frac{3}{2}^+)$	1383.7±1.0	36±5	$\Lambda\pi(88\%)$,$\Sigma\pi(12\%)$
$\Sigma^-(1385)$	$1(\frac{3}{2}^+)$	1387.2±0.5	39.4± 2.1	

Table 2: Properties of excited hyperon states relevant for experimental studies at COSY [1] .

allows very efficient trigger generation and event identification. The multiplicity and particle configuration to be detected in the final states is the same.

In table 1 and 2 some properties of the hyperon states relevant for the experimental studies at COSY are summarized [1].

2 Ground state hyperons

A systematic study of the ground state hyperon production will result in an extended data base for the hyperon-nucleon interaction which is an important ingredient in different physics questions. The dynamics of few body systems containing strangeness is not well known. Models describing hyperon–nucleon scattering [2, 3, 4, 5, 6] rely on flavour SU(3) symmetry to fix the baryon–meson couplings and the remaining parameters are fitted to the data. The existing data on hyperon–nucleon scattering are insufficient to prove the validity of this procedure. A better understanding of the hyperon–nucleon interaction has an impact on various topics like the

formation of hyper-nuclei [7] or the structure of neutron stars [8].

Data on Λ and Σ ground state hyperon production related to hyperon–nucleon interaction studies mainly result from hyperon– nucleon scattering extracted from bubble chamber experiments. The hyperon production was induced by a K^- beam via $K^- + p \rightarrow Y\pi$ where Y is a Λ or a Σ hyperon. These Λ and Σ hyperons then may scatter elastically on another proton of the hydrogen bubble chamber. Experiments have been performed at CERN [9, 10, 11, 12, 13] or at SLAC [14]. Scattering data for higher Λ momentum (1-17 GeV/c) have been produced at BNL by using a proton beam [15]. The available data on low energy elastic hyperon scattering are shown in figure 1.

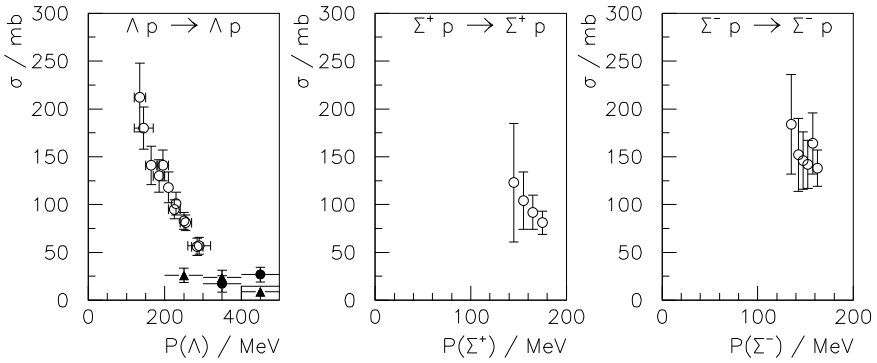

Figure 1: Available data on low energy elastic hyperon scattering $Yp \rightarrow Yp$ for Λ (open circle [9], filled circle [14], triangle [13]) , Σ^+ ([10]) and Σ^- ([10]) hyperons.

Most of the data are available for the Λ-p system but also here the experimentally extracted low energy parameters of s-wave scattering, the scattering length and the effective range, have large error bars. A detailed analysis of the world data set for elastic Λp scattering result in $a_s = -1.8 + (+2.3 - 4.2)$ fm and $a_t = -1.6 + (+1.1 - 0.8)$ fm [9] for the spin singlet and spin triplet scattering lengths, respectively, where the errors are strongly correlated. Furthermore a clear separation of the spin singlet and triplet channel is not possible from the data. An analysis within an effective range

approximation has been performed also for the Σ^+ elastic scattering data [10] but due to the poor data base only a wide region for the scattering lengths could be extracted by applying some model based relations for the scattering lengths with $-6fm < a_s < +2.5fm$ and $-2fm < a_t < 1.3fm$ in which singlet and triplet scattering lengths are correlated. These secondary scattering experiments are limited at the low momentum end due to the hyperon decay and the necessity to have a detectable track of the scattered proton. Therefore the data have to be extrapolated to the threshold resulting in a large error width.

The data on elastic hyperon scattering will be extended by measurements at KEK where first results on differential observables are published [16, 17]. The hyperons are produced via the $(\pi^+/\pi^-, K^+)$ reactions and the detection system consists of a scintillating fiber arrangement [16, 18, 17] or a "Scintillating track image camera" [19] where the tracks of charged particles in a scintillator are viewed by ccd cameras.

An alternative way to study the nucleon–hyperon interaction are production reactions with a nucleon and a hyperon in a multi particle exit channel. First data in this field were extracted from the reaction $K^-d \to \pi^- p\Lambda$ [20], leading to a scattering length of -2 ± 0.5 fm via fitting the invariant mass distribution to an effective range expansion. The author argued that this value is to be interpreted as the spin triplet scattering length but it is difficult to estimate the theoretical uncertainty, the error given includes the experimental uncertainty only.

Also at COSY a first attempt to determine the low energy parameters of the ΛN interaction via the reaction $pp \to K^+ p\Lambda$ has been performed [21]. We extracted an average value of -2 ± 0.2 fm for the ΛN scattering length in a Dalitz plot analysis that utilizes the effective range expansion. The effective range parameters a and r are strongly correlated and for their determination the ΛN elastic cross sections data had to be included in the analysis to determine the parameters. Furthermore the spin singlet and triplet Y-N states contributes to the data i.e. only a spin averaged value was extracted.

In Ref. [22] it was suggested to use the reaction $K^-d \to n\Lambda\gamma$, where the initial state is in an atomic bound state, to determine the ΛN scattering lengths. From the experimental side so far, a feasibility study was performed which demonstrated that a separation of background and signal is possible [23]. The reaction $K^-d \to n\Lambda\gamma$ was studied theoretically in more detail in [24, 25, 26]. The main results especially of the last work are that it is indeed possible to use the radiative K^- capture to extract the ΛN scattering lengths and that polarization observables could be used to disentangle the

different spin states.

In a 3 particle exit channel like $pp \to pK^+\Lambda$ the relative momentum in each individual 2 particle subsystem ranges from the maximum momentum given by the kinematics down to 0. Therefore event samples can be selected with very low relative hyperon–nucleon momentum down to the threshold which is not accessible by conventional elastic scattering. In figure 2 [27] the situation is illustrated in a comparison of the Λp scattering data with a data set of inclusive K^+ production via $pp \to K^+X$ measured at SATURNE [28]. Below the Σ^0 production threshold the dominant reaction channel is $pp \to pK^+\Lambda$. Neglecting other reaction channels like $pp \to pK^+\Lambda\gamma$ the kinetic energy of the K^+ is directly related to $m_{\Lambda p}$. In figure 2 it is clearly shown that the $m_{\Lambda p}$ distribution is covered by data points up to the threshold. The extraction of the scattering length by fitting the data with theoretical curves is much more precise than the extrapolation of the scattering data. The different curves fitted to the scattering data cover the present error range for the scattering length. The highest sensitivity is at smallest $m_{\Lambda p}$ values where no data are available. These inclusive K^+ data are not really useful to improve the knowledge of the Λp scattering length because singlet and triplet state are not separated. This example should only demonstrate the advantages of the $pp \to pK^+\Lambda$ reaction for such studies. Another important feature of the $pp \to pK^+\Lambda$ reaction is the high momentum transfer in the reaction. High momentum transfer is correlated with a production process of short-range nature [29] which is insensitive to details of the production mechanism resulting in reliable error estimates in the theoretical treatment.

The curves in figure 2 result from a new method to determine the Λp scattering lengths proposed in Ref. [29]. It allows the extraction of the YN scattering lengths from the production data directly. In particular, an integral representation for the ΛN scattering lengths in terms of a differential cross section of reactions with large momentum transfer such as $pp \to K^+p\Lambda$ or $\gamma d \to K^+n\Lambda$ was derived. This formula should enable the determination of the scattering lengths to a theoretical uncertainty of at most 0.3 fm. Experimentally production data of sufficient accuracy can be achieved as is seen by the SATURNE data [28] introducing an experimental uncertainty in the extraction of the scattering length of 0.2 fm.

In Ref. [29] it was also shown that already a measurement of a single spin asymmetry in $\vec{p}p \to YNK$ enables to isolate the spin triplet contribution from the final YN state, since the Pauli Principle strongly limits the number of structures allowed for the initial state. It was especially shown that

$$\frac{d^2\sigma(\uparrow)}{dm'^2 dt} - \frac{d^2\sigma(\downarrow)}{dm'^2 dt}$$

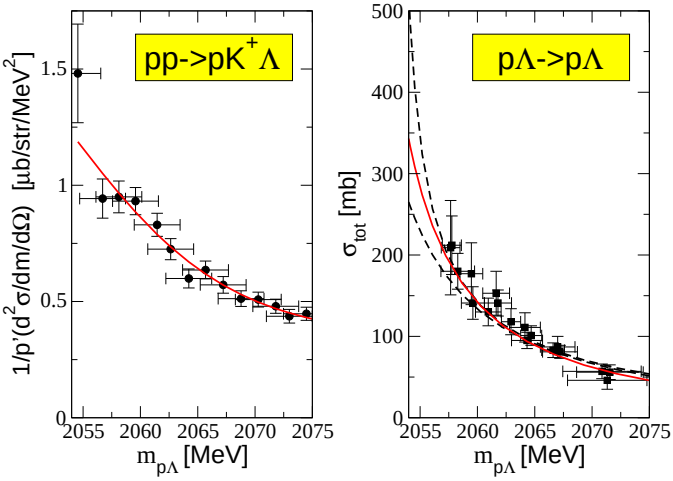

Figure 2: Left panel: $pp \to K^+X$ inclusive missing mass spectrum at $T_p = 2.3$ Gev corrected by the two body phase space. Right panel: world data set on total cross sections for ΛN elastic scattering. In both panels the solid curve represents a best fit to the data. In the right panel two more fits still consistent with the data were added to show the uncertainty in the extrapolation.

gets contributions from the spin triplet final state only, as long as the kaon in the final state is emitted at 90^o in the cm system and the outgoing YN is in an S–wave. The arrows in the above expression denote the polarization of either the beam or the target that is to be chosen perpendicular to the beam axis.

The method in Ref. [29] was derived under the assumption that there is no inelastic channel available for the hyperon–nucleon system. This condition only holds for the ΛN, $\Sigma^+ p$ as well as the $\Sigma^- n$ channel (where for an analysis of the second channel the Coulomb interaction needs to be included in the formalism—work on this straight forward extension of the formalism is in progress). These ΣN channels are purely isospin 3/2 states and thus do not couple to the ΛN channel. The other ΣN channels, however, are inelastic. As a consequence their scattering lengths aquire imaginary parts and the dispersion analysis in Ref. [29] can no longer be applied.

The future studies of the hyperon production at COSY induced by NN interactions via $NN \to NKY$ will significantly extend and improve the data base on the hyperon–nucleon interaction.

But apart from the hyperon–nucleon interaction there is much more physics which can be extracted from these data. First of all the produc-

tion mechanism can be studied. Dalitz plot analysis of $pp \to pK^+\Lambda$ data taken at COSY by the TOF collaboration showed that the lowest nucleon resonances which couple to the KY channel are a dominant strongly energy dependent contribution to the hyperon production [30]. At a beam momentum of 2.85 GeV/c (Q = 171 MeV) only the N*(1650) is relevant, at 2.95 GeV/c (Q = 204 MeV) also the N*(1710) gives a significant contribution and at 3.2 GeV/c (Q = 284 MeV) both, N*(1650) and N*(1710), contribute with comparable strength. Close to threshold data have been supplied by the COSY-11 collaboration [31, 32, 33] resulting in information on the hyperon-nucleon interaction [21] as discussed above but especially the comparison of threshold production of different hyperon channels like the Λ/Σ^0 comparison [33, 34]. will help to disentangle the production mechanisms close to threshold. Spin transfer coefficients by using a polarized proton beam and measuring the Λ polarization $\vec{p}p \to pK^+\vec{\Lambda}$ have been produced by the DISTO collaboration at a beam momentum of 3.67 GeV/c (Q = 430 MeV) [35]. The model dependent interpretation of the data indicates a production mechanism dominated by kaon exchange.

With the hyperon production data available up to now first indications of the relevant production mechanisms are available but much more informations are still needed.

The kinematically complete measurement of the 3 particle NKY exit channel allows a detailed investigation of all individual 2-body subsystems. Besides the YN system also the NK as well as the KY system can be studied. The KY system is mainly important for the investigation of nucleon resonances, especially the $N^*(1650)$, $N^*(1710)$ and $N^*(1720)$ which have large branching ratios into the ΛK channel. In the NK subsystem the interaction between nucleons and K mesons can be observed. Of special interest here is the Θ^+ resonance which was observed by many experiments and is interpreted as a penta-quark system [36] proposed by Diakonov et al. [37]. A clear signal of the Θ^+ has also been detected in the K^0p system by the COSY TOF collaboration [38]. Further measurements at TOF with improved statistics are on the way and a double polarization experiment to determine the parity of the Θ^+ [39] is in preparation.

3 Excited hyperons

The most interesting topic in the excited hyperon sector is the shape and the structure of the $\Lambda(1405)$ resonance. Its a long standing discussion if the $\Lambda(1405)$ is a 3-quark state or a $\bar{K}N$ / $\pi\Sigma$ bound state, see [40] and references

cited therein.

In a recent study of the poles in the meson-baryon scattering matrix in a chiral unitary approach some resonances are dynamically generated close to the $\Lambda(1405)$ mass [41]. It is argued that the $\Lambda(1405)$ is not only one but a superposition of two close resonances which could be experimentally separated due to the different couplings to the $\pi\Sigma$ and $\bar{K}N$ states. Whereas the resonance at lower mass couples stronger to the $\pi\Sigma$ state the resonance at higher mass couples mostly to the $\bar{K}N$ state. Similar results have been obtained in other studies, see [40, 41] and the references cited therein. But a definite conclusion about the structure of the $\Lambda(1405)$ can not be drawn from the existing data.

The data in the excited hyperon sector mostly result from production studies in bubble chambers via $\pi^- p$ or $K^- p$ interactions [42, 43, 44, 45, 46, 36]. Recently the photoproduction of the $\Lambda(1405)$ has been studied at SPring-8/LEPS via $p(\gamma, K^+)Y^*$ [47]. In the missing mass distribution the $\Lambda(1405)$ is overlapping with the $\Sigma(1385)$. A separation is achieved in the $(\pi\Sigma)$ invariant mass distribution because the $\Lambda(1405)$ decays with 100% into the $\pi\Sigma$ channel but the $\Sigma(1385)$ has a branching of only 12% into this channel. The comparison of the $\pi^+\Sigma^-$ and the $\pi^-\Sigma^+$ invariant mass distributions shows different line shapes which could be an indication that the $\Lambda(1405)$ is a meson-baryon bound state.

At COSY the production of overlapping $\Lambda^*(1405)$ and $\Sigma^*(1385)$ hyperons have been observed in pp interactions [48, 49]. But for a detailed study first of all a separation of these resonances by measuring their decay products is necessary.

4 Experimental study of hyperons at COSY

The experimental details to study the ground and excited hyperons are very similar. Up to now the hyperon production at COSY has been investigated at the COSY-11 and at the TOF installation.

COSY-11 [52] is an internal experiment operating with a beam of hydrogen clusters as target in front of a COSY machine dipole used as a magnetic spectrometer for the charged reaction products. The tracks and velocity of positively charged reaction products are measured resulting in the determination of its 4-momentum vectors. This system is limited in acceptance but achieves a high momentum resolution of the measured particles. Hyperon production is studied via $pp \to NK^+Y$ where the hyperons are identified via the missing mass method. Due to the high missing mass resolution the

hyperons can be clearly identified on a rather low background level. Excitation functions from about 1 - 60 MeV excess energy have been measured for $pp \to pK^+\Lambda$ and $pp \to pK^+\Sigma^0$ and data of the $pp \to nK^+\Sigma^+$ channel are under analysis. For the $pp \to pK^+\Lambda$ reaction also a Dalitz plot analysis has been performed resulting in the determination of a spin averaged Λp scattering length. These studies will be continued by a measurement with polarized beam. In the analysis the method of Gasparian et al. [29] will be used to isolate the spin triplet scattering length which requires the measurement of kaons emitted in 90^o in the cm system. Although COSY-11 is a magnetic spectrometer device the special configuration of a C-type magnet, open to the detector side with a thin exit window for the reaction products, allows to measure the full scattering angle distribution for a thin slice in the beam plane. Therefore kaons emitted around 90^o cms can be detected. The proposal for this experiment has been accepted and the measurement is planned for spring 2005 [53].

The TOF spectrometer [54] is a large acceptance external experiment. A small liquid hydrogen cell (a few tens mm^3 volume) is used as a target surrounded by a first layer of scintillators followed by a second layer in a distance of a few m dependent on the actual setup. A special decay spectrometer is installed close to the target with several layers of Si-μstrip and scintillating fiber detectors. This decay spectrometer allows to trigger on delayed decays and measures the tracks of charged decay products. The event identification is mainly done by geometry which is sufficient if a precise definition of target vertex and hit positions is realized as it is the case at TOF. Data have been produced for $pp \to pK^+\Lambda$ for Q values between 55 MeV and 284 MeV resulting in Dalitz plots with a full coverage of the phase space [30]. Due to the decay asymmetry of the weak Λ decay also the Λ polarization could be determined by measuring the tracks of the charged decay particles. Furthermore the reactions $pp \to pK^+\Sigma^0$, $pp \to pK^0\Sigma^+$ and $pp \to nK^+\Sigma^+$ have been studied.

In table 4 all ground state hyperon production channels accessible in elementary NN interactions at COSY are listed.

For a systematic detailed study of the hyperon production the full information of the measured events including the 4-momentum vectors of the decay particles is needed. This will allow to extract nearly background free event samples required for Dalitz plot analysis. Some reaction channels in table 4 could be studied at TOF as is shown by the produced data but at TOF no photon detector is installed. In most channels one or more γ's are included in the exit channel. Therefore the WASA detector [50, 51] which will move to COSY in the near future seems to be well suited for

primary reaction	final state	br.
$pp \to pK^+\Lambda$	$pK^+p\pi^-$	0.64
	$pK^+n\pi^0 \to pK^+n\gamma\gamma$	0.36
$pp \to pK^+\Sigma^0$	$pK^+\Lambda\gamma \to pK^+p\pi^-\gamma$	0.64
	$pK^+\Lambda\gamma \to pK^+n\pi^0\gamma \to pK^+n\gamma\gamma\gamma$	0.36
$pp \to pK^0\Sigma^+$	$p\pi^0\pi^0p\pi^0 \to p\gamma\gamma\,\gamma\gamma p\gamma\gamma$	0.08
	$p\pi^+\pi^-p\pi^0 \to p\pi^+\pi^-p\gamma\gamma$	0.18
	$p\pi^0\pi^0n\pi^+ \to p\gamma\gamma\,\gamma\gamma n\pi^+$	0.08
	$p\pi^+\pi^-n\pi^+$	0.16
$pp \to nK^+\Sigma^+$	$nK^+p\pi^0 \to nK^+p\gamma\gamma$	0.52
	$nK^+n\pi^+$	0.48
$pn \to nK^+\Lambda$	$nK^+p\pi^-$	0.64
	$nK^+n\pi^0 \to nK^+n\gamma\gamma$	0.36
$pn \to nK^+\Sigma^0$	$nK^+\Lambda\gamma \to nK^+p\pi^-\gamma$	0.64
	$nK^+\Lambda\gamma \to nK^+n\pi^0\gamma \to nK^+n\gamma\gamma\gamma$	0.36
$pn \to nK^0\Sigma^+$	$n\pi^0\pi^0p\pi^0 \to n\gamma\gamma\,\gamma\gamma p\gamma\gamma$	0.08
	$n\pi^+\pi^-p\pi^0 \to n\pi^+\pi^-p\gamma\gamma$	0.18
	$n\pi^0\pi^0n\pi^+ \to n\gamma\gamma\,\gamma\gamma n\pi^+$	0.08
	$n\pi^+\pi^-n\pi^+$	0.16
$pn \to pK^0\Lambda$	$p\pi^0\pi^0p\pi^- \to p\gamma\gamma\,\gamma\gamma p\pi^-$	0.1
	$p\pi^+\pi^-p\pi^-$	0.22
	$p\pi^0\pi^0n\pi^0 \to p\gamma\gamma\,\gamma\gamma n\gamma\gamma$	0.06
	$p\pi^+\pi^-n\pi^0 \to p\pi^+\pi^-n\gamma\gamma$	0.12
$pn \to pK^0\Sigma^0$	$p\pi^0\pi^0\Lambda\gamma \to p\gamma\gamma\,\gamma\gamma p\pi^-\gamma$	0.1
	$p\pi^+\pi^-\Lambda\gamma \to p\pi^+\pi^-p\pi^-\gamma$	0.22
	$p\pi^0\pi^0\Lambda\gamma \to p\gamma\gamma\,\gamma\gamma n\gamma\gamma\gamma$	0.06
	$p\pi^+\pi^-\Lambda\gamma \to p\pi^+\pi^-n\pi^0\gamma \to p\pi^+\pi^-n\gamma\gamma\,\gamma$	0.12
$pn \to pK^+\Sigma^-$	$pK^+n\pi^-$	1.0

these hyperon production studies. WASA includes a detection system for charged particles as well as an electromagnetic calorimeter for the detection of photons.

With the possible production channels of the excited hyperons: $pp \to \Lambda^* pK^+$ / $\Sigma^{*+} pK^0$ / $\Sigma^{*0} pK^+$ and $pn \to \Lambda^* pK^0$ / $\Sigma^{*0} pK^0$ / $\Sigma^{*-} pK^+$ a corresponding table for the exit particle configuration can be prepared with the dominant Y^* decays given in table 2. The final states are similar to the ground state hyperons with a particle multiplicity of about 6 including charged particles and photons. As an example in fig. 3 the momentum distribution of the final state particles in the reaction channel $pp \to \Lambda(1405) pK^+ \to p\pi^- \gamma\gamma\gamma pK^+$ is shown for a Monte Carlo generated event sample. The straight lines in the plots indicate the acceptance of the WASA calorimeter for photon detection. The charged particles are mainly emitted in forward direction which requires a high resolution tracking system in this area. How well the existing WASA detection system will be suitable for these hyperon production studies and which modifications would be necessary has to be studied via Monte Carlo event samples. A close to target tracking system, not existing in the present WASA setup, to identify the delayed decay vertices is for sure indispensable to select clean event samples. This point is discussed in letters of intend for possible experiments with WASA at COSY [55].

5 Summary

A systematic study of hyperon production at COSY in the 3-body final state $NN \to NKY^*$ will result in detailed information on various topics. By measuring all final state particles including the decay products nearly background free event samples of the various reaction channels can be selected which is important for efficient Dalitz plot analysis. With the use of a polarized beam (and target) and the measurement of the hyperon polarization (at least for Λ and Σ^+ with their high decay asymmetry) very selective studies will be possible.

By selecting appropriate kinematic regions – difficult or even impossible to access by conventional scattering experiments – the interactions of the individual subsystems (NY), (NK) and (KY) can be analyzed. Precise data will result on the hyperon–nucleon interaction, requested for a better understanding of the dynamics in baryon systems with strangeness, the kaon–nucleon system, of special interest in view of the recent observations of the Θ^+ resonance and the kaon–hyperon system, important for the investi-

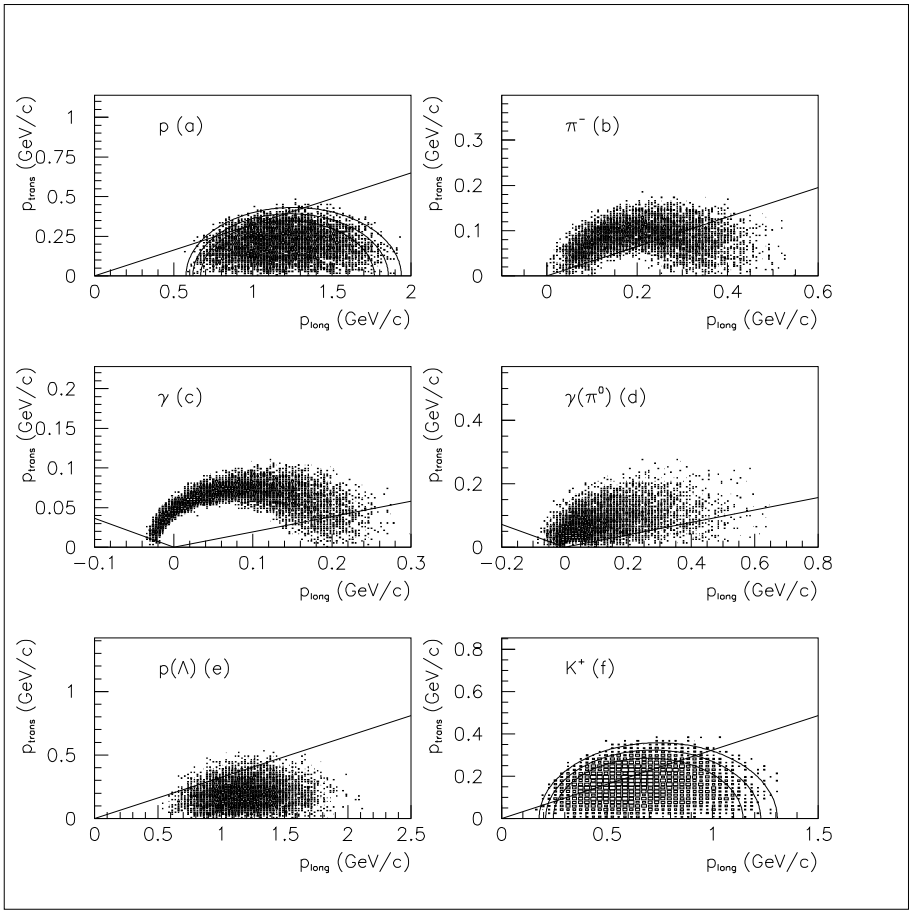

Figure 3: Momentum distribution of the final state particles for the reaction channel :$pp \to \Lambda(1405)pK^+ \to p^{(a)}\pi^{-(b)}\gamma^{(c)}\gamma\gamma^{(d)}p^{(e)}K^{+(f)}$. The ellipses show the kinematic limits for a $\Lambda(1405)$ production with PDG mass $\pm$ 25 MeV. The straight lines indicate the acceptance region covered by the em calorimeter of the WASA detector.

gation of nucleon resonances. In case of the excited hyperons the knowledge about the structure of these resonances will be much improved. Furthermore with these detailed studies the mechanisms of hyperon production can be clarified.

By their results on hyperon production the running experiments have proven that high precision data in this field are possible at COSY. Valuable results have been obtained but much more information is necessary in order to fully understand the strangeness sector.

Acknowledgments

The work has been supported by the European Community - Access to Research Infrastructure action of the Improving Human Potential Programme and by the DAAD Exchange Programme (PPP-Polen).

References

[1] S. Eidelmann et al. (Particle Data Group) Phys. Lett. **B 592** (2004) 1.

[2] P. M. M. Maessen, Th. A. Rijken, J. J. de Swart, Phys. Rev. **C 40** (1989) 2226.

[3] B. Holzenkamp, K. Holinde, J. Speth, Nucl. Phys. **A 500** (1989) 485.

[4] A. Reuber, K. Holinde, J. Speth, Nucl. Phys. **A 570** (1994) 543.

[5] Th. A. Rijken, V. G. Stoks, Y. Yamamoto, Phys. Rev. **C 59** (1999) 21.

[6] J. Haidenbauer, W. Melnitchouk, and J. Speth, AIP Conf. Proc. **603** (2001) 421, `nucl-th/0108062`.

[7] A. Nogga, H. Kamada, and W. Glöckle, Phys. Rev. Lett. **88** (2002) 172501.

[8] J. A. Pons et al., Astrophys. J. **513** (1999) 780.

[9] G. Alexander, U. Karshon, A. Shapira, G. Yekutieli, Phys. Rev. **173** (1968) 1452.

[10] Eisele et al., Phys. Lett. **37 B** (1971) 204.

[11] B. Sechi-Zorn et al., Phys. Rev. **175** (1968) 1735.

[12] R. Engelmann et al., Phys. Lett. **21** (1966) 587.

[13] J.A.Kadyk, G.Alexander, J.H.Chan, P.Gaposchkin, G.H.Trilling, Nuc. Phys. **B 27** (1971) 13.

[14] J.M. Hauptmann, J.A. Kadyk and G.H. Trilling, Nuc. Phys. **B 125** (1977) 29.

[15] K.J. Anderson, N.M. Gelfand, J.Keren, and T.H. Tan, Phys. Rev. **D 11** (1975) 473.

[16] J.K. Ahn et al., Nucl. Phys. **A 648** (1999) 263.

[17] Y. Kondo et al., Nucl. Phys. **A 676** (2000) 371.

[18] M. Ieiri et al., Nucl. Phys. **A 691** (2001) 354.

[19] J. Asai Nucl. Phys. **A 721** (2003) 1091c.

[20] H.H. Tan, Phys. Rev. Lett. **23** (1969) 395.

[21] J. T. Balewski et al., Eur. Phys. J. **A 2** (1998) 99.

[22] B.F. Gibson et al., BNL Report No. **18335** (1973).

[23] K.P. Gall et al., Phys. Rev. **C 42** (1990) R475.

[24] A.I. Akhiezer, G.I. Gakh, A.P. Rekalo, and M.P. Rekalo, Sov. J. Nucl. Phys. **27** (1978) 115.

[25] R.L. Workman and H.W. Fearing, Phys. Rev. **C 41** (1990) 1688.

[26] W.R. Gibbs et al., Phys. Rev. **C 61** (2000) 064003.

[27] C. Hanhart Phys. Rep. **397** (2004) 155.

[28] R. Siebert et al., Nucl. Phys. **A 567** (1994) 819.

[29] A. Gasparyan, J. Haidenbauer, C. Hanhart and J. Speth, Phys. Rev. **C 69** (2004) 034006.

[30] W. Eyrich, Prog. Part. Nucl. Phys. **50** (2003) 547.

[31] J. T. Balewski et al., Phys. Lett. **B 420** (1998) 211.

[32] S. Sewerin et al., Phys. Rev. Lett. **83** (1999) 682.

[33] P. Kowina et al., Eur. Phys. J. A, in print, nucl-ex/0402008.

[34] T. Rozek et al., e-Print Archive: nucl-ex/0407024;
Int. J. Mod. Phys. **A**. in print, and contribution to this proceedings.

[35] F. Ballestra et al., Phys. Rev. Lett. **83** (1999) 1534.

[36] References in: S. Eidelmann et al. (Particle Data Group) Phys. Lett. **B 592** (2004) 1.

[37] D. Diakonov, V. Petrov and M. Polyakov, Z. Phys. **A 359** (1997) 305.

[38] M. Abdel-Bary et al., Phys. Lett. **B 595** (2004) 127.

[39] C. Hanhart et al., Phys. Lett. **B 590** (2004) 39.

[40] M. Kimura et al., Phys. Rev. **C 62** (2004) 015206.

[41] D. Jido et al., Nucl. Phys. **A 725** (2003) 181.

[42] R. J. Hemingway, Nucl. Phys. **B 253** (1985) 742.

[43] D. W. Thomas et al.,Nucl. Phys. **B 56** (1973) 15.

[44] M. Baubillier et al., Z. Phys. **C 23** (1984) 213.

[45] M. Aguilar-Benitez et al., Ana. Fis. **A 77** (1981) 144.

[46] S. J. M. Barlag et al., Nucl. Phys. **B 149** (1979) 220.

[47] J. K. Ahn Nucl. Phys. **A 721** (1979) 715c.

[48] C. Quentmeier et al., Phys. Lett. **B 515** (2001). 276.

[49] M. Buescher et al. (editors), Proc. ANKE workshop on Strangeness Production on Nucleons and Nuclei (2003), to be published.

[50] H. Calen et al., PiN Newslett. **16** (2002) 238.

[51] J. Zabierowski et al., Phys. Scripta **T 99** (2002) 159.

[52] S. Brauksiepe et al., Nucl. Inst. Meth. **A 376** (1996) 397.

[53] D. Grzonka and T. Rozek, COSY Proposal **143** (2004).

[54] TOF collaboration, www.fz-juelich.de/ikp/COSY-TOF.

[55] A. Gillitzer, D. Grzonka et al., LoI for WASA at COSY (2004), http://www.fz-juelich.de/ikp/wasa/loi.shtml

Towards the excitation function of the $pp \to ppK^+K^-$ reaction at COSY-11

P. Winter

Institut für Kernphysik, Forschungszentrum Jülich, Germany

Abstract: The ongoing discussion concerning the nature of the scalar resonances $f_0(980)$ and $a_0(980)$ implicated to extend the studies of the $pp \to ppK^+K^-$ reaction near the production threshold. Furthermore, such elementary production processes allow to study the interaction of the outgoing particles due to their low relative momenta. Therefore, final state interactions in the pK or $K\bar{K}$ system can be perfectly studied in such experiments.
The acquired data at the excess energies $Q = 10$ and 28 MeV have been taken at COSY-11 and the status of the ongoing analysis will be presented.

1 Introduction

The experimental facility used for the studies described below is the internal COSY-11 detection setup [1] at the COoler SYnchrotron COSY [2]. Its schematical assembly with the relevant detector parts is shown in figure 1.

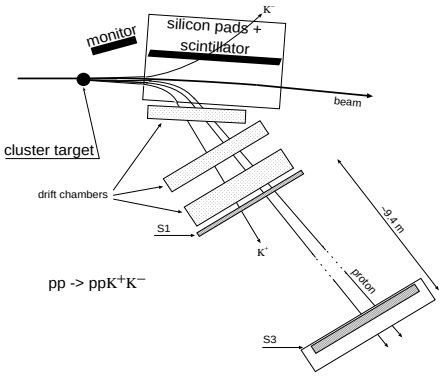

Figure 1: Schematic top view of the COSY-11 detection setup with only the relevant parts for the measurement of the reaction $pp \to ppK^+K^-$. The different components are described in the text.

The hydrogen cluster target is mounted in front of one of the COSY bending dipole magnets which acts like a magnetic spectrometer for the

outgoing interacting particles. The positively charged particles are bend towards the interior of the ring and are then detected by a set of 3 drift chambers allowing for a momentum reconstruction. The following time of flight (TOF) measurement – with two scintillator hodoscopes S1 and S3 – in combination with the momentum reconstruction gives access to the particles' four momenta. The remaining negative kaon in the reaction $pp \to ppK^+K^-$ is registered in a detector mounted in the inner part of the dipole gap consisting of a scintillator and granulated silicon pads. Since the four momentum of the K^- cannot be directly deduced, it is identified by means of the missing mass method.
In order to calculate an absolute cross section from the extracted number of events one needs a normalisation in form of the luminosity. Therefore, in this proton proton collision, a trigger was set up to record in parallel the elastic scattered protons. While one proton is registered in the main detector part, the second has to pass the so called monitor detector, a combination of a scintillator and a silicon pad detector.

2 Motivation

Elementary meson production in nucleon nucleon collisions near the production threshold enables to study besides the production mechanism also the interactions among the outgoing particles. Especially for short living particles, these studies are only possible in such production reactions. Therefore, the studies of the excitation function of the reaction $pp \to ppK^+K^-$ will help to understand the $K\bar{K}$ interaction as well as possible final state effects in the pK system.
Calculations of the $\pi^+\pi^- \to K\bar{K}$ [3] based on the Jülich model [4] show a strong difference in the total cross section when switching on and off the $K\bar{K}$ interaction (see figure 2). The strong rise with inclusion of the $K\bar{K}$ interaction (solid lines) leads to the interpretation of the scalar meson $f_0(980)$ as a $K\bar{K}$ molecule.

Up to now, various scenarios have been proposed to describe the still unknown structure of the $f_0(980)$ meson, namely – besides the mentioned $K\bar{K}$ molecule [5, 6] – a usual $q\bar{q}$ state [7] or a $qq\bar{q}\bar{q}$ configuration [8]. Furthermore, other scenarios forsee a hybrid $q\bar{q}$/meson-meson sytem due to the strong coupling to S-wave two-meson channels [9] or even quarkless gluonic hadrons [10]. Since the analysis of the reaction $pp \to ppK^+K^-$ gives a quite model independent way to learn about the $K\bar{K}$ interaction strength this might shed light on the open question concerning the $f_0(980)$ meson.

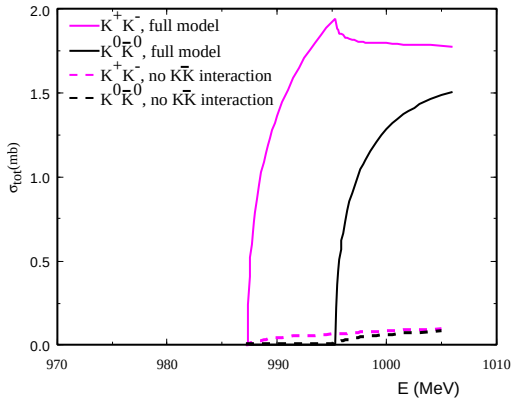

Figure 2: Excitation function of the $\pi^+\pi^- \rightarrow K\bar{K}$ [3] calculated in a one boson exchange model. Inclusion of the $K\bar{K}$ interaction (solid lines) strongly rises the slope of the total cross section for both the charged and uncharged channel.

Another issue linked with the near threshold meson production is the fact that the outgoing particles have low relative momenta and hence, possible final state interaction (FSI) effects are pronounced. A prominent example is the *pp*-FSI which shows up for example in $pp \rightarrow pp\eta'$ at excess energies below $\sim 40\,\mathrm{MeV}$ (compare figure 3), where the cross section no longer follows a pure phase space distribution or the calculations without the *pp*-FSI (compare the pure Q^2 phase space dependenece (dashed line) and a calculation without FSI [11]). Only the dotted line reproduces the set of data at low energies well since it accounts for the proton-proton FSI.

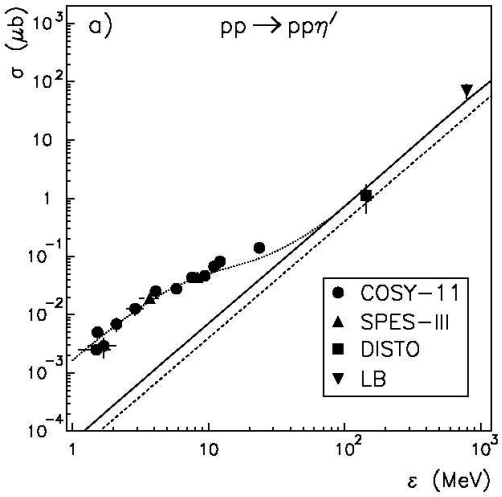

Figure 3: Cross section data for the reaction $pp \rightarrow pp\eta'$ [12, 13, 14, 15, 16]. The dashed line represents an arbitrarily normalized phase space integral and the solid a calculation in a meson exchange model without inclusion of the FSI [11]. The dotted line incorporates the *pp*-FSI by including the on-shell *pp* amplitude in order to reproduce the phase space population.

This example shows that such final state effects are pronounced at low

excess energies. Therefore, further data of the reaction $pp \to ppK^+K^-$ will help to investigate the strength of the interaction in the pK system.

3 Results

The COSY-11 collaboration has extended its previous measurement at an excess energy of $Q = 17\,\mathrm{MeV}$ [17] at two new energies, namely $Q = 10$ and $28\,\mathrm{MeV}$, both lying below the ϕ threshold. The analysis is based on the identification of two protons in the exit channel via their mass. They are registered in the drift chambers and by tracing back the trajectory through the known magnetic field, their momentum is deduced. The subsequent TOF measurement between the two scintillators S1 and S3 over a distance of about 9.4 m then gives in combination with the momentum the invariant mass, i.e. the four momentum. Due to their decay, the number of kaons registered in the S3 scintillator is rather low. Therfore, the S1 scintillator is used as the stop counter for the TOF measurement. The start time is the time of the interaction itself which is calculable via the momentum of the identified protons [18]. The remaining negative kaon is then identified via the missing mass of the ppK^+ system, shown in figure 4(a) for the data set at $Q = 10\,\mathrm{MeV}$. Besides the physical background mainly stemming from the reactions $pp \to pK^+\Lambda(1405)/\Sigma(1385)$ and from misidentified pions [17] a signal at the K^- mass is visible. The additional demand for a hit in the scintillator mounted in the dipole gap reduces much more the background than the signal (see figure 4(b)). Similar spectra were also obtained for the higher energy at Q=28 MeV where the K^- peak is apparent.

For the final cross sections, a further step is the determination of the luminosity via the reaction $pp \to pp$ recorded in parallel. While it is required that one proton is registered in the drift chambers and in the S1 scintillator, the other one has to pass the monitor detector which is installed towards the outer part of the accelerator in front of the dipole magnet. Due to the two body kinematics, there is a fixed correlation between the position of the first proton in the S1 detector and the position of the other proton passing the monitor detector. Figure 5 shows the x-position of the track in the S1 detector versus the pad number corresponding to the spatial crossing position of the particle for events with one reconstructed track and a hit in the monitor scintillator. The clear correlation band expected from Monte Carlo simulation (see fig. 5(a)) is clearly visible in the data as well (compare fig. 5(b)) with only a low background outside of the correlation area mainly from the reaction $pp \to pn\pi^+$.

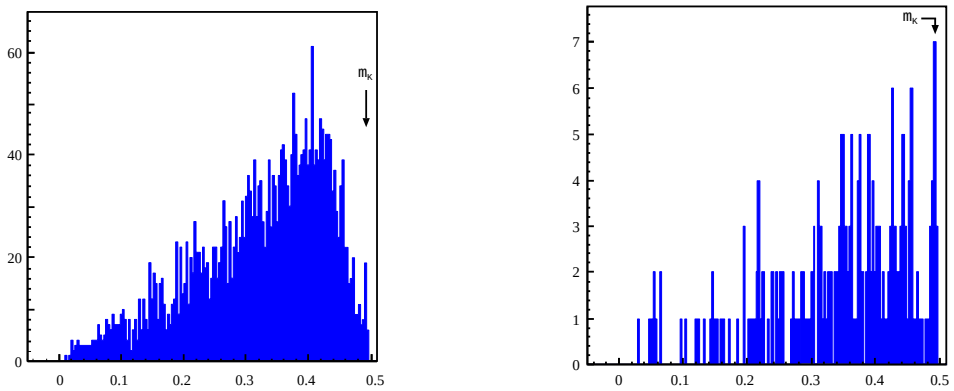

(a) (b)

Figure 4: Missing mass for the identified system ppK^+ for a) all events and b) with an additional request for a hit in the scintillator mounted in the dipole gap.

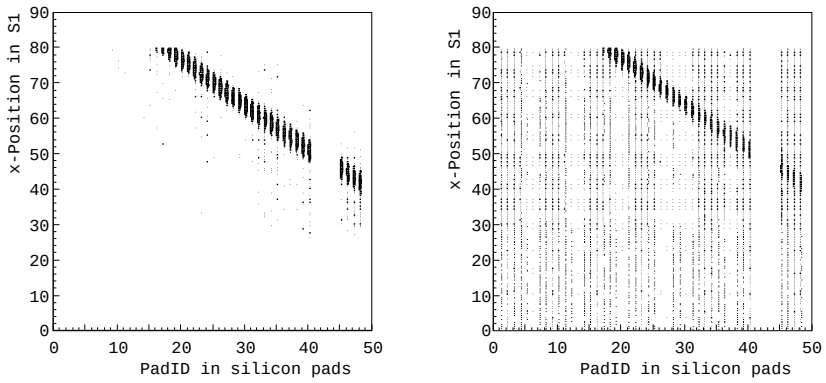

(a) (b)

Figure 5: x-Position of the first particle in the S1 detector versus the pad number in the silicon pads behind the monitor scintillator for a) Monte Carlo simulations and b) for real data. Taken into account are events with one reconstructed track and a simultaneous hit in the monitor scintillator. The pads with number 41 to 44 were excluded from the analysis due to the fact, that they were not working properly during the experiment.

By cutting out the correlation region, an extraction of the elastically scattered events is possible. Details of the whole standard procedure can

be found elsewhere [18, 19] and for this specific analysis soon in ref. [20]. The analysis includes several different steps using Monte Carlo studies for the efficiency determination in case of the elastic reaction $pp \to pp$. Up to now, the total integrated luminosity $\mathcal{L}$ for both energies were extracted to be:

Q [MeV]	$\boldsymbol{\mathcal{L}}$ **[cm^{-2}]**
10 MeV	$2.71 \cdot 10^{36}$
28 MeV	$2.31 \cdot 10^{36}$

The statistical and systematical errors were not yet deduced from the data but will be available soon.

4 Outlook

The new data the COSY-11 collaboration acquired in $pp \to ppK^+K^-$ are still under analysis. The total integrated luminosity has been determined whereas systematic error studies are still in progress. Missing mass spectra of the ppK^+ system show a clear signal at the K^- mass. Prior to the determination of the absolute cross sections, there will be a further cut performed in order to get the spectrum nearly background free. Since the four momentum of the K^- is calculable, the measured position of the hit in the dipole scintillator can be compared with the expected position in this detector by tracking the K^- momentum through the magnetic field. From the former analysis [17], it is known that this crucial last step eliminates the background and therefore will be applied for the new data, too. In combination with efficiency studies via Monte Carlo simulations, the number of registered events will give the absolute cross sections at $Q = 10$ and 28 MeV.

Acknowledgments

The work has been supported by the European Community - Access to Research Infrastructure action of the Improving Human Potential Programme and by the DAAD Exchange Programme (PPP-Polen).

References

[1] S. Brauksiepe et al., Nucl. Instr. & Meth. **A 376** (1996) 397.

[2] R. Maier, Nucl. Instr. & Meth. **A 390** (1997) 1.

[3] O. Krehl, R. Rapp and J. Speth, Phys. Lett. **B 390** (1997) 23, [nucl-th/9609013].

[4] G. Janssen, B. C. Pearce, K. Holinde and J. Speth, Phys. Rev. **D 52** (1995) 2690, [nucl-th/9411021].

[5] J. D. Weinstein and N. Isgur, Phys. Rev. **D 41** (1990) 2236.

[6] D. Lohse, J. W. Durso, K. Holinde and J. Speth, Nucl. Phys. **A 516** (1990) 513.

[7] D. Morgan and M. R. Pennington, Phys. Rev. **D 48** (1993) 1185.

[8] R. L. Jaffe, Phys. Rev. **D 15** (1977) 267.

[9] E. Van Beveren et al., Z. Phys. **C 30** (1986) 615.

[10] R. L. Jaffe and K. Johnson, Phys. Lett. **B 60** (1976) 201.

[11] A. A. Sibirtsev, W. Cassing and C. M. Ko, Z. Phys. **A 358** (1997) 101, [nucl-th/9612040].

[12] F. Hibou et al., Phys. Lett. **B 438** (1998) 41.

[13] P. Moskal et al., Phys. Rev. Lett. **80** (1998) 3202, [nucl-ex/9803002].

[14] P. Moskal et al., Phys. Lett. **B 482** (2000) 356, [nucl-ex/0001001].

[15] F. Balestra et al., Phys. Lett. **B 491** (2000) 29, [nucl-ex/0008017].

[16] A. Khoukaz et al., Eur. Phys. J. **A 20** (2004) 345, [nucl-ex/0401011].

[17] C. Quentmeier et al., Phys. Lett. **B 515** (2001) 276, [nucl-ex/0103001].

[18] M. Wolke, *Schwellennahe assoziierte Strangeness-Erzeugung in der Reaktion* $pp \to ppK^+K^-$ *am Experiment COSY-11*, Dissertation, Westfälische Wilhelms-Universität Münster, 1997, IKP Jül-3532.

[19] P. Moskal, η' *meson production in the* $pp \to pp\eta'$ *reaction near threshold*, Dissertation, Jagellonische Universität Krakau, 1998, IKP Jül-3685.

[20] P. Winter, Dissertation in preperation.

Drift chamber with a U-shaped frame

J. Smyrski

Institute of Physics, Jagellonian University, Cracow, Poland

Abstract: We present the construction of a planar drift chamber with wires stretched between two arms of a U-shaped aluminium frame. The special shape of the frame allows to extend the momentum acceptance of the COSY-11 detection system towards lower momenta without suppressing the high momentum particles. For a three-dimensional track reconstruction a computer code was developed using a simple algorithm of hit preselection.

1 Introduction

The drift chamber which is described in this report was built for the COSY-11 experimental facility at the Cooler Synchrotron COSY-Jülich [1]. The COSY-11 described in details in Ref. [2] is a magnetic spectrometer for measurements at small angles and is dedicated to studies of near–threshold meson production in proton–proton and proton–deuteron collisions (see e.g. Refs. [3, 4, 5]). It uses one of the regular COSY dipole magnets for momentum analysis of charged reaction products originating from interaction of the internal COSY beam with the target of a cluster type [6]. Trajectories of positively–charged particles which are deflected in the dipole magnet towards the center of the COSY–ring are registered with a set of two planar drift chambers D1 and D2. The chambers cover only the upper range of momenta of the outgoing particles which is sufficient to measure e.g. two outgoing protons in the $pp \to pp\eta'$ [5] or $p-p-K^+$ tracks in the $pp \to ppK^+K^-$ reaction close to threshold [4]. For tracking positively charged pions appearing in near–threshold reactions such as $pp \to pp\pi^+\pi^-$ with momenta by a factor of m_π/m_p smaller then the proton momenta it was necessary to extend the COSY-11 momentum acceptance towards smaller values.

Another important purpose was the detection of positively charged kaons prior to their decay which is especially important for measurement of the

$pp \to ppK^+K^-$ reaction due to small cross sections on the level of a few nbarn. For this, an additional drift chamber D3 was built and installed in the free space along the COSY–11 dipole magnet. The main requirement for the chamber was a shape of the chamber frame which would not interfere with high momentum particles that are registered in the chambers D1 and D2. This demand was fulfilled by choosing the frame in a rectangular form but with one vertical side missing called U–shaped frame since it resembles the character U turned by 90^o. The main design characteristics of the chamber are given in section 2. It was also essential, that the chamber allows for a three–dimensional track reconstruction in order to determine the momentum vectors of registered particles at the target by tracing back their trajectories in the magnetic field of the COSY–11 dipole magnet to the nominal target position. Therefore three different wire orientations were chosen and a track reconstruction program was developed. This program is described in section 3. The chamber calibration and results of the track reconstruction are presented in section 4.

2 The chamber construction

The chamber contains hexagonal cells (see Fig. 1) identical with the ones used in the central drift chamber of the SAPHIR detector [7]. In this type of cells the drift field has approximately cylindrical symmetry, and thus the distance–drift time relation depends only weekly on the particles' angles of incidence. In order to minimize the multiple scattering on wires, gold–plated aluminium [8] is used for the 110 μm–thick field wires, whereas the sense wires are made of 20 μm–thick gold–plated tungsten.

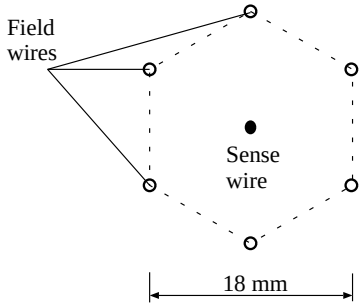

Figure 1: Hexagonal cell.

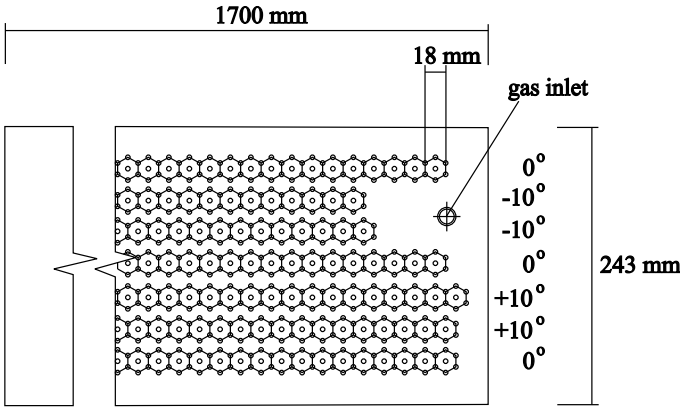

Figure 2: Upper end-plate with indicated positions of openings for feedthroughs used for mounting the wires.

The cells are arranged in seven detection planes as indicated in Fig. 2 showing one of two parallel aluminium endplates between which the wires are stretched. Three detection planes (1, 4 and 7) contain vertical wires, two planes (2, 3) have wires inclined at -10^o and the remaining two planes (5, 6) contain wires inclined at $+10^o$. This arrangement makes it possible to reconstruct particle trajectories in three dimensions, also in cases of multi-track events. The relatively small inclination of the wires was chosen since the measurement of particle trajectories in the horizontal plane needs to be much more accurate compared to the vertical plane. This is due to the fact that the particle momenta are determined on the basis of the deflection of their trajectories in an almost uniform vertical magnetic field in the 6 cm gap of the COSY-11 dipole magnet.

Each endplate contains Ø=4 mm openings with inserted feedthroughs for mounting the wires. The openings were drilled with a digitally programmable machine tool assuring a positioning accuracy better than ± 0.01 mm. The openings for the filed wires form equilateral hexagons with a width of 18 mm. In the middle of these hexagons there are the openings for the sense wires. The resulting spacing of the sense wires in the planes with vertical wires is again equal to 18 mm and in the detection planes with wires inclined by $\pm 10^o$ the spacing of sense wires is equal to 18 mm x $\cos 10^o = 17.73$ mm.

The chamber contains 3x80=240 cells with vertical wires, 2x76=154 cells with wires inclined by -10^o and 2x77=152 cells with wires inclined by $+10^o$. The disturbance of the electric field in the drift cells of a given plane by the cells of the neighboring planes was studied by calculations of the electric field

with the Garfield code [9]. With the chosen spacing of the detection planes equal to 28.8 mm (see Fig. 2) the resulting corrections to the distance–drift time relation determined as a function of position along the sense wires are smaller than 0.05 mm [10] for distances from the sense wire smaller then half of the cell width (9 mm) and were neglected in view of the expected precision of track reconstruction of the order of 0.1 mm. Thus one can assume that the distance–drift time relation is the same for all cells in a give detection plane simplifying the chamber calibration.

The two aluminium endplates for mounting the wires are 15 mm thick and are supported by two U-shaped frames made out of 20 mm thick aluminium and displayed in a three-dimensional view in Fig. 3. The frames hold the total load of 236.8 kG originating from the mechanical tension of 17 kG (= 548x0.031 kG) of the sense wires and 219.8 kG (= 2198x0.1 kG) of the field wires. Prior to mounting the wires, the frames were prestressed with a force corresponding to the tension of wires using led bricks uniformly distributed on the upper endplate. This caused a deflection of the endplates at the free ends of 0.7 mm each. The ends of the prestressed endplates were fixed together using a steel plate and the bricks were taken away. After mounting the wires the steel plate was removed and we checked that the distance between the ends of the endplates did not change.

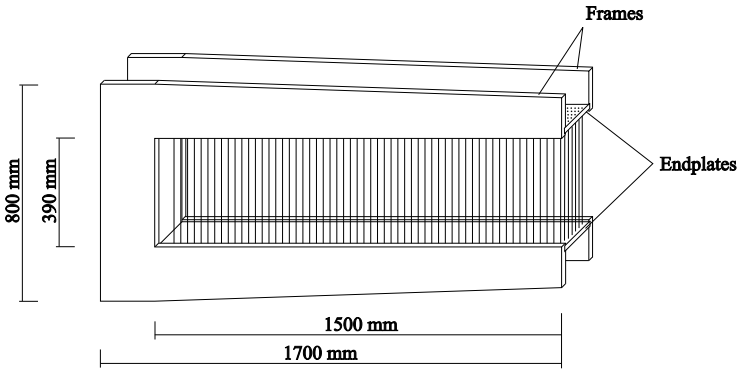

Figure 3: Schematic three-dimensional view of the chamber frame for mounting the wires. The window for particles is 1500 mm wide and 390 mm high.

For mounting the field wires brass feedthroughs with a $\emptyset = 150$ μm inner opening are used. Since all field wires should have the same ground potential electrical contact of the feedthroughs with the aluminium endplates is assured by usage of a conductive glue. For the sense wires we used isolating feedthroughs made of Delrin with inserted brass feedthroughs containing

$\emptyset = 50$ μm openings for the positioning of the wires. The wires were strung between pairs of feedthroughs and were fixed by means of copper crimp pins. For sealing the feedthroughs and the crimp pins epoxy resin was used. The high voltage was connected to the sense wires through 1 MΩ resistors soldered directly to the crimp pins on the lower endplate. The signals were read out through 1 nF coupling capacitors connected to the sense wires on the upper endplate. The capacitors and resistors were enclosed in hermetical volumes which were dried out with silica aerogel allowing to reduce leakage currents.

The window for particles penetrating the chamber was made of 20 μm thick Kapton foil glued to an aluminium frame which was screwed on the support frame and tightened with $\emptyset = 3$ mm rubber seal.

Each of the detection planes is equipped with five 16-channel preamplifier-discriminator cards based on the Fujitsu MB13468 amplifier chip and the Le Croy MVL407S comparator chip [11]. The cards are mounted directly on the chamber. The output pulses in the ECL standard are led by means of 30 m long twisted-pair cables to FASTBUS-TDCs of Le Croy 1879 type working in the common stop mode with the pulses from the discriminators as start signals and the trigger pulse as the common stop.

As the chamber gas, P10 mixture (90% argon and 10% methane) at atmospheric pressure is used. The gas flow through the chamber is about 12 l/h. The sense wire potential is +1800 V, whereas the field wires are all grounded. The gas amplification in the chambers is about 10^5 and the discrimination threshold set in the preamplifier-dicriminator cards corresponds to $3 \cdot 10^5$ electrons.

3 Track reconstruction algorithm

For the reconstruction of particle tracks a simple algorithm was developed and implemented as a computer code written in the C-language. The reconstruction proceeds in three stages:

- finding track candidates in two dimensions, independent for each orientation of the wires,
- matching the two-dimensional solutions in three dimensions,
- three-dimensional fitting in order to obtain optimal track parameters.

In the first stage, track candidates are found in two-dimensions using hits in the detection planes with the same inclination of the wires. For this, all

possible combinations of pairs of hits from two different detection planes are taken into account. Due to the left-right ambiguity of the track position with respect to the sense wire, for each pair of hits four straight-line solutions are possible. These solutions are determined using an iterative procedure. First, the track distance to the sense wire is calculated from the drift time to drift distance relation $d(t, \theta)$ using the measured drift time t and assuming the track entrance angle θ as equal to 0^o. The track is defined thus by a pair of points lying in the corresponding sense wire planes and indicated as P1 and P2 in Fig. 4. In the next step, the inclination of this track is taken for determining new values of the distances from the sense wires and constructing a new pair of points defining the track. These points are indicated as T1 and T2 in Fig. 4. This procedure can be repeated, however, we terminate it already after the second step since further steps give negligible corrections. For each track determined by this method one subsequently finds hits which are consistent with it within a certain corridor along the track. In this way, hits from neighboring cells with respect to the selected two cells and from other detection planes with the same orientation of wires are taken into account in the reconstruction. For the width of the corridor we take ± 1 mm which is a few times larger than the position resolution of a single detection plane. With this choice more than 90% of all hits are included in the reconstruction.

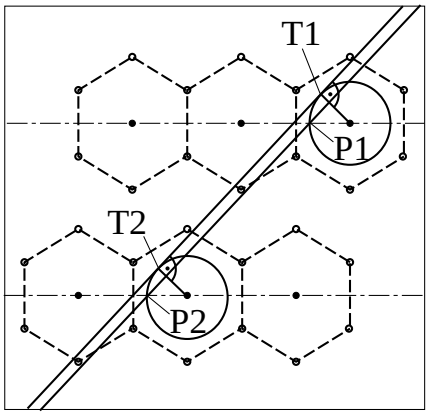

Figure 4: Illustration of iterative procedure of fitting a straight line to two hits.

In three dimensions a two-dimensional solution can be represented by a plane containing the track and parallel to the corresponding sense wires.

Planes representing the two-dimensional solutions for three different directions of sense wires used in the chamber should intersect along a common line corresponding to the particle track. However, due to the limited space resolution of the chamber, the planes intersect along three different lines (see Fig. 5). Two lines – l_1 and l_2 correspond to the intersections of the inclined planes with the vertical plane and the third line – l_3 is an intersection of the inclined planes. In order to quantify the consistency between the two-dimensional solutions, we determine the distances h_1 and h_2 between crossing points of the lines l_1, l_2 with the first and the seventh detection plane, respectively (see Fig. 5). For the three-dimensional reconstruction, we accept only the combinations of two-dimensional solutions for which the distances h_1 and h_2 are both smaller then a certain limit h which is adjusted as a reconstruction parameter. Too large values of h lead to an unnecessary increase of CPU time since too many non-matching combinations are taken into account. On the contrary, too small values of h cause losses of good combinations and consequently decreases the reconstruction efficiency. A typical value for h is 2 cm.

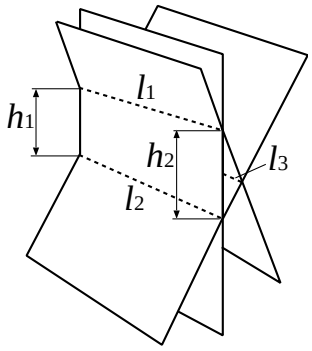

Figure 5: Crossing of planes representing two-dimensional solutions for three different orientations of wires.

The determination of track parameters in three dimensions proceeds via minimization of the χ^2 value calculated on the basis of the differences between the measured distances of tracks from sense wires d_i and the distances of the fitted tracks from the sense wires d_i^f:

$$\chi^2 = \sum_i \frac{(d_i - d_i^f)^2}{(\delta d_i)^2}, \tag{1}$$

where the summation proceeds over all hits taken for the fitting and δd_i is an uncertainty of the measured distance d_i. In the case of the two-dimensional

track reconstruction for wires oriented in one direction, the numerator in the above expression can be easily calculated in Cartesian coordinates using the formula:

$$(d_i - d_i^f)^2 = \frac{[x_i - (az_i + b)]^2}{(1 + a^2)}, \tag{2}$$

where a and b are parameters in the straight line equation: $x = az + b$ representing the track, x- and z are coordinates perpendicular to the sense wires and (x_i, z_i) is a point lying in the distance d_i from the sense wire in the location corresponding to the closest approach to the track (see Fig. 6). For the three-dimensional reconstruction, we use a coordinate system

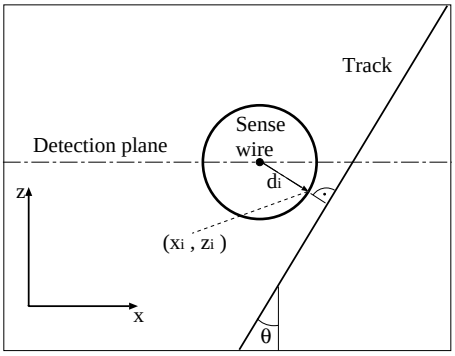

Figure 6: Definition of the point (x_i, z_i) used in the reconstruction.

with the y-axis parallel to the vertical wires and the z-axis perpendicular to the chamber. The beginning of the coordinate system is located in the first detection plane. Particle tracks are parametrized as straight lines in a conventional way:

$$x' = a'z' + b', \tag{3}$$
$$y' = c'z' + d', \tag{4}$$

where a', b', c', d' are the searched track parameters. They can be linked to the parameters a, b corresponding to the two-dimensional solutions using the linear transformation:

$$a = a' \cos\alpha_i + c' \sin\alpha_i, \tag{5}$$
$$b = b' \cos\alpha_i + d' \sin\alpha_i, \tag{6}$$

where α_i is the angle between the sense wires and the vertical direction. Inserting Eqs. (5), (6) into (2) and the result into (1), the expression for χ^2

takes the form:

$$\chi^2 = \sum_i \frac{[x_i - (a' \cos\alpha_i + c' \sin\alpha_i) z_i - (b' \cos\alpha_i + d' \sin\alpha_i)]^2}{[1 + (a' \cos\alpha_i + c' \sin\alpha_i)^2](\delta d_i)^2}. \qquad (7)$$

The derivative of the dimensionless term in the square bracket in the denominator is of the order of unity and is negligible compared with corresponding derivative of the numerator divided by $(\delta d_i)^2$ which is of the order of $z_i/\delta d_i$. Therefore, during the fitting procedure we regard the numerator just as a constant given by the initial values of the parameters and thus the minimization of χ^2 is reduced to a linear problem. The three-dimensional track fitting is performed for all combinations of two-dimensional track candidates and the solution with the minimal value of χ^2 is selected. The hits corresponding to this solution are then removed from the set of hits recorded in a given event and the reconstruction is repeated from the beginning until there are no further candidates of tracks. In this way multi-track events can be reconstructed.

4 Calibration and reconstruction results

The chamber is calibrated using the experimental data. In the first step an approximate drift time to drift distance relation is determined by integration of the drift time spectra as provided by the uniform irradiation method [12]. A typical spectrum obtained by summing up drift time spectra from all sense wires in one detection plane is shown in Fig. 7. The width of the drift time distribution is about 300 ns which corresponds roughly to half of the cell width equal to 9 mm. The space-time relationship obtained by integration of the drift time spectrum is not strictly linear; its slope increases slightly in the neighborhood of the sense wire. In the next step corrections are determined to this calibration using an iterative procedure. For this, the average deviations between the measured and fitted distances of the tracks from the sense wires are calculated. These deviations are determined as a function of the drift time t_j corresponding to the TDC channel j and the track entrance angle θ_k from the range (0, 90) divided into 9 intervals numerated by the index k:

$$\Delta d(t_j, \theta_k) = < d^f(t_j) > - d(t_j, \theta_k), \qquad (8)$$

where the average $<>$ is taken over all hits which were recorded in the TDC channel j and correspond to the track entrance angle interval k. The

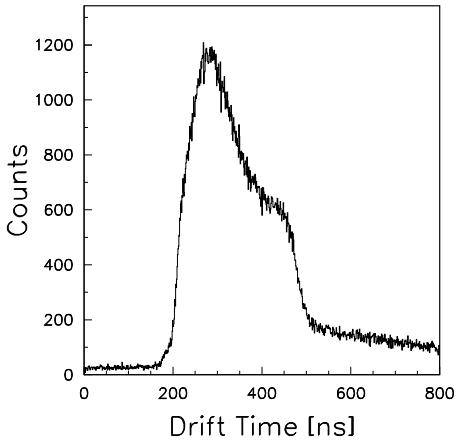

Figure 7: Drift time spectrum obtained by summing up spectra from all sense wires in the first detection plane.

space-time relation used in the first iteration is then corrected by the above deviation:

$$d'(t_j, \theta_k) = d(t_j, \theta_k) + \Delta d(t_j, \theta_k). \tag{9}$$

After performing the reconstruction of tracks with the new space-time relation new corrections are calculated and so on. This procedure is repeated until the corrections become smaller than the position resolution of the chamber. This occurs in our case after a few iterations. The preliminary value of the position resolution of the chamber is $\delta d = 0.2$ mm. Studies of various contributions to the position resolution are still carried out.

5 Conclusions

A drift chamber with a U-shaped frame was constructed for the COSY-11 experiment. The special shape of the frame allows for the detection of low momentum particles without disturbing the high momentum particles which are registered in other detector components of the COSY-11. This kind of chamber can be used in situations where no frame elements are allowed in the sensitive area of the detection system. An example of a possible further application besides the here discussed one could be the detection of particles scattered at small angles with respect to the beam. In this case, two such chambers placed symmetrically with respect to the beamline could be used for covering the forward angles. The chambers can be installed and removed

without dismounting the beam-pipe contrary to an alternative solution of one chamber with a central hole for the beam-pipe.

The track reconstruction algorithm which was developed for the chamber can also be used for other planar drift chambers containing cells with an electric field which has symmetry close to the cylindrical one. It is required, however, that the chamber contains wires oriented at least in three different directions and for each direction there are at least two detection planes.

Acknowledgments

The work has been supported by the European Community - Access to Research Infrastructure action of the Improving Human Potential Programme, by the DAAD Exchange Programme (PPP-Polen), and by the Polish State Committe for Scientific Research (grants No. 2P03B07123
and PB1060/P03/2004/26).

References

[1] R. Maier et al., Nucl. Instr. & Meth. **A 390** (1997) 1.

[2] S. Brauksipe et al., Nucl. Instr. & Meth. **A 376** (1996) 397.

[3] P. Moskal, M. Wolke, A. Khoukaz, W. Oelert,
Prog. Part. Nucl. Phys. **49** (2002) 1.

[4] C. Quentmeier et al., Phys. Lett. **B 515** (2001) 276.

[5] P. Moskal et al., Phys. Lett. **B 474** (2000) 416.

[6] H. Dombrowski et al., Nucl. Instr. & Meth. **A 386** (1997) 228.

[7] W. J. Schwille et al., Nucl. Instr. & Meth. **A 344** (1994) 470.

[8] California Fine Wire Company, Grover Beach, California, USA.

[9] R. Veenhof, GARFIELD, Simulation of gaseous detectors, Version 7.04, 2001, CERN Program Library Writeup W5050, CERN, Geneva, Switzerland.

[10] Ch. Kolf, Diploma Thesis, University of Bonn, Germany, January 2002.

[11] L. Jarczyk et al., Annual Report IKP-KFA 1990 (1991) p.219.

[12] A. Breskin et al., Nucl. Instr. & Meth. **119** (1974) 9.

Production of Σ^+ hyperon at COSY-11

Tomasz Rożek [a,b], Dieter Grzonka [a]
[a] *Institute of Nuclear Physics, FZ Jülich, Germany*
[b] *Institute of Physics, University of Silesia, Katowice, Poland*

Abstract: The Σ^+ production was measured at the COSY-11 installation via the $pp \to nK^+\Sigma^+$ reaction at Q = 13 MeV and Q = 60 MeV. These measurements continue the hyperon production studies at COSY-11 via $pp \to pK^+\Lambda/\Sigma^0$ where a strong decrease of the cross section ratio close to threshold was observed. The study of other isospin channels like the Σ^+ production will help to clarify the relevant dominant hyperon production mechanisms.

1 Introduction

The Σ^0 and Λ hyperon production near the kinematical threshold was studied by the COSY-11 collaboration in $pp \to pK^+\Lambda/\Sigma^0$ reactions. Data points, 16 for the Λ and 13 for the Σ^0 channel, were taken in the excees energy range between 0.68 MeV and 59.3 MeV for Λ (2.8 MeV and 59.1 MeV for Σ^0) [1, 2, 3].
The cross section ratio $\sigma(pp \to pK^+\Lambda)/\sigma(pp \to pK^+\Sigma^0)$ below excess energie of about 15 MeV was measured to be about 28 in contrast to the value of about 2.5 determined for excess energies above $Q = 300$ MeV [4]. The ratio of 2.5 is in good agreement with the Λ/Σ^0 isospin relation, which is 3.

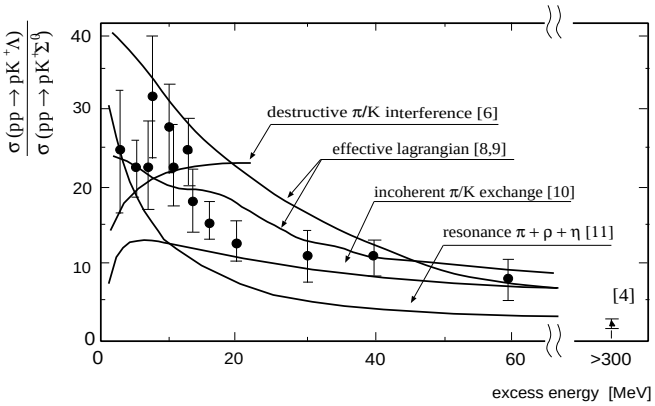

Figure 1: Cross section ratio for Σ^0 and Λ in the threshold region. The data are compared to different models.

To explain this unexpected threshold behaviour, various theoretical scenarios within meson exchange models were proposed. Calculations have been performed with pion and kaon exchange added coherently [6, 7] or incoherently [10], including the excitation of nucleon resonances [8, 9, 11] and heavy meson exchange (ρ, ω and K^*) [8, 9]. Although the various descriptions differ even in the dominant basic reaction mechanism, all more or less reproduce the trend of an increase in the cross section ratio in the threshold region, as can be seen fom Fig. 1. The present data are not sufficient to definitely exclude possible explanations. Further studies e.g. on the other isospin projections like the Σ^+ will help to understand the threshold hyperon production.

To be more specific let's consider the Jülich meson exchange model where calculations for other Σ production channels are available. This model includes π and K exchange and the large cross section ratio $\sigma(\Lambda)/\sigma(\Sigma^0)$ at threshold is achieved by a destructive interference of π and K exchange amplitudes [6, 7]. Calculations of the Σ^+ production in this model predict a factor of three higher cross section compared to the Σ^0 channel for the destructive and a factor of three lower for the constructive interference (see figure 2). Apart from this the ratio $\sigma(\Sigma^+)/\sigma(\Sigma^0)$ will also differ strongly if the dominant production mechanism runs via an intermediate N^* excitation or not. In order to check the cross section ratio between Σ^+ and Σ^0 production the Σ^+ production was recently measured at the COSY-11 installation via $pp \to nK^+\Sigma^+$ at Q = 13 MeV and Q = 60 MeV [5].

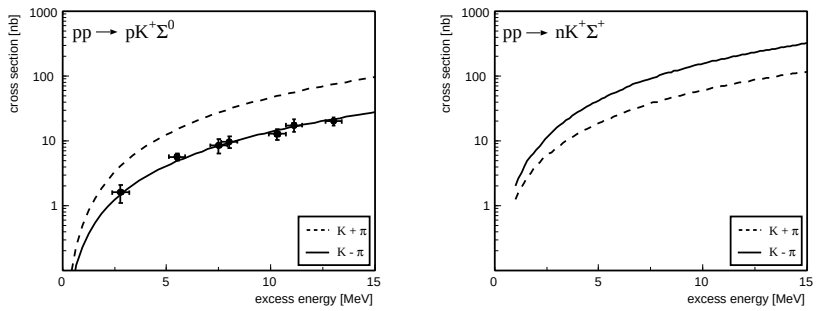

Figure 2: The theoretical predictions for Σ^0 and Σ^+ production according to the Jülich meson exchange model [6] and compared with the data [1, 2] (left figure).

2 Experiment

COSY-11 is an internal magnetic spectrometer experiment at the COoler SYnchroton and storage ring COSY in Jülich. It is equipped with scintillator hodoscopes and drift chambers for charged particle detection and a scintillator/lead sandwich detector for neutrons [12, 20].

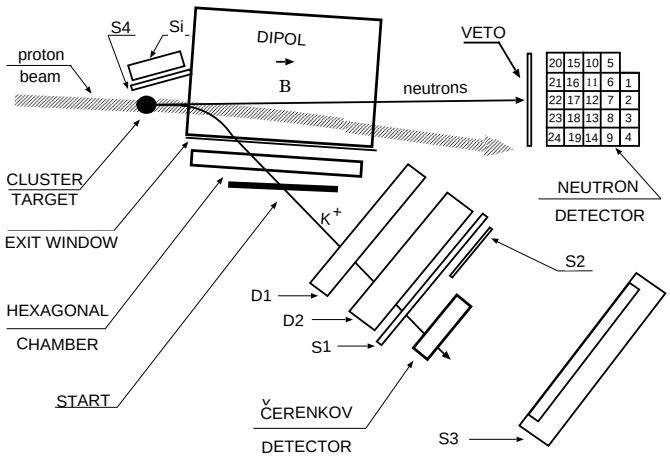

Figure 3: COSY–11 detection setup [12] with the emphasised neutron detector and superimposed tracks of Kaons and neutrons from the $pp \to nK^+\Sigma^+$ reaction. The neutron detector is drawn to a larger scale in comparison to the other detection components.

The Σ^+ hyperon is identified via the missing mass technique by detecting the remaining reaction products - K^+ and neutron. The experimental resolution of the missing mass determination depends on the reconstruction accuracy of the four-momentum vectors for the registered neutrons and kaons. The momentum vector of the K^+ meson can be established by tracking the K^+ trajectory reconstructed from signals registered in the drift chambers (D1 and D2 in the figure 3) through the magnetic field back to the target point.

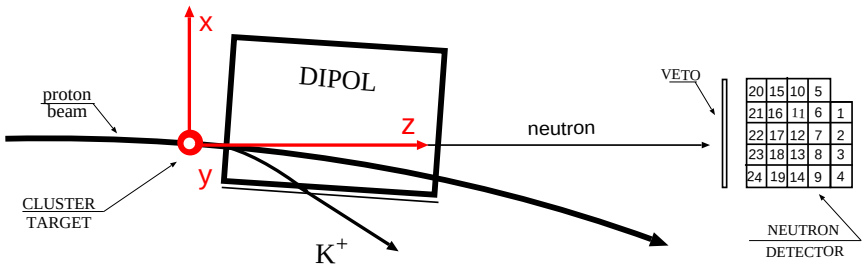

Figure 4: The four-vector of the neutron (n) is given by the measured velocity, the direction of the particle and the known mass; $\vec{P}_n = m_n \cdot \vec{v}_n \cdot \gamma_n$

Assuming a hit in the neutron detector being due to a neutron, the four-vector of the neutron is given by the measured velocity, the direction (given by the first hitted module) of the neutron which can be reconstructed with an accuracy of at least the size of the module (9.4 x 9.2 cm^2) and the known mass.

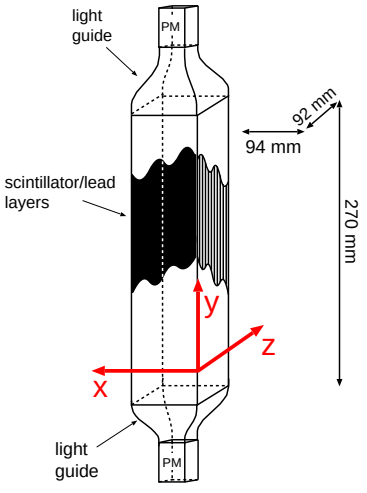

Figure 5: Single module of the neutron detector. Direction of the 'z' axis is the direction of neutrons.

The background from charged particles hitting the neutron detector is discriminated by veto scintillators (VETO in figure 4).

3 Neutron detector calibration

The precision of the time measurement of the neutron detector modules is the crucial factor for the resolution of the Σ^+ mass determination.

The neutron particle detector consists of 24 segments (9.4 x 9.2 cm^2 each) of scintillator/lead sheets positioned as depicted schematically in figure 4 and readout on both sides by photomultipliers. The first row of modules (front) is at a distance of 7.36 m from the target. The timing of the neutron detector modules is nearly independent on the hit position within a module since the timing (t^i_{TDC}) from the $i's$ module is taken from the average of the upper and lower photomultiplier signals [13]. In order to relate the time measurement of individual modules it is necessary to know the relative time offsets which are derived by comparing the signals of different modules. From the experimental data the distributions of time differences between neighbouring segments were generated and compared to the corresponding spectra from Monte Carlo simulations (MC). The example presented in figure 6 shows that the shape of the simulated distributions agrees very well with the experimental data. This confirms the correctness of the performed simulations. The mean of the distribution corresponds to the difference between the time offsets and its width reflects i) the time resolution of the involved modules, ii) the smearing of velocities of secondary particles and iii) the distribution of the positions at which they were created. A difference measured between $i'th$ and $j'th$ module can be expressed as:

$$\Delta_{ij} = t^i_{TDC} - t^j_{TDC} = t^i_{real} - t^j_{real} + off^i - off^j \qquad (1)$$

where t^i_{TDC} and t^j_{TDC} denote the time registered by a TDC (time-to-digital converter) in the $i'th$ and $j'th$ module of the neutron detector, respectively, t_{real} stands for the real time at which the secondary charged particles produced a light signal inside a scintillator and *off* summerises all delays between the module and the TDC. In the simulations the difference $off^i - off^j$ was set to zero.

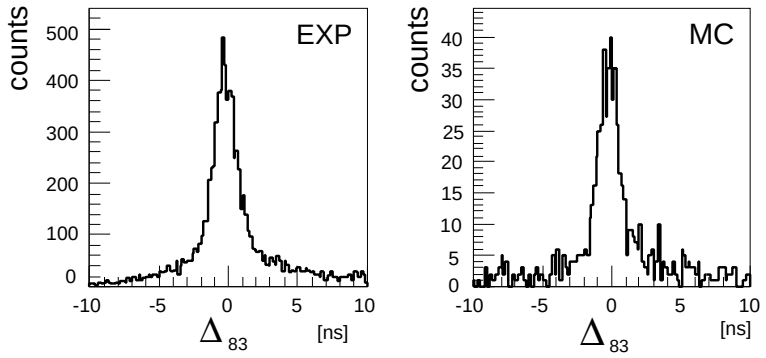

Figure 6: Distribution of the time difference between 8^{th} and 3^{th} (see also figure 4) modules of the neutron detector - (left side) experimental data, (right side) MC. A long tails of the distribution are caused by events where the secondary neutral particles with a significantly different velocity induce nuclear reactions in the neighbouring segments.

By the comparison of the experimental and simulated distributions of all possible combinations of Δ_{ij} the relative time offsets between the segments was established and the time resolution of a single module was found to be 0.4 ns [14](see also [15]).

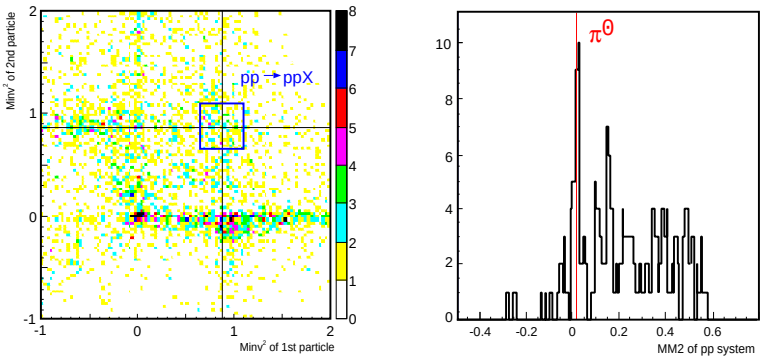

Figure 7: In the left part the invariant mass squared of the first particle vs. the second particle is shown. The $pp \rightarrow ppX$ "region" is marked. In the right part the square of the missing mass distribution from events out of the marked region (i.e. two track events identified as protons with a signal in the neutron detector) is shown. The π^0 peak is clearly seen.

In addition, the general time offset between the neutron production and the hit time in the neutron detector has to be determined. The global offset was found using the $pp \rightarrow pp\pi^0$ reaction. Two track events were selected and the four-momenta of both protons were determined by backtracking through the known magnetic field to the target and the π^0 was identified via the missing mass technique. The square of the missing mass distribution for two track events with a signal in the neutron detector is shown in figure 7. The statistics is very low due to the small detection acceptance but some $pp\pi^0$ events can be definitely identified. The π^0 meson decays with a $c\tau$ of 25 nm immediately in the target and the γs from the decay will reach the neutron detector with the speed of light without delay. Knowing the distance between the target and the first row of the modules of the neutron detector and the speed of light in air, one can adjust the general time offset for the neutron detector with high precision. In figure 8 the time distribution in the neutron detector for the selected π^0 events is shown. The total event number as well as the width of the discussed peak corresponds to the expectation from Monte Carlo.

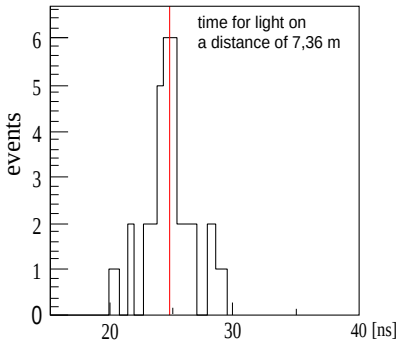

Figure 8: Time signal in the neutron detector for γs from the π^0 decay selected from experimental events in the $pp \rightarrow pp\pi^0$ area.

The global timing for the neutron detector is taken as the difference between the time of the reaction (taken from the backtracking of positively charge particles through the known magnetic field) and the shortest time in the neutron detector. The distribution of the modules with the first signal, i.e. where the γ conversion happened is shown in figure 9. It occurs mostly in the first row which is consistent with the expectation from the radiation length of 0.56 cm for γ's in lead. For neutrons, the distribution is more homogeneous with a maximum in the middle part of the neutron detector. For charged particles (figure 9**c)** - when the VETO detector was switched off - maximum of the distribution on the lower left part of the detector stems from the influence of nearby acceleration pipe (compare with the figure 3).

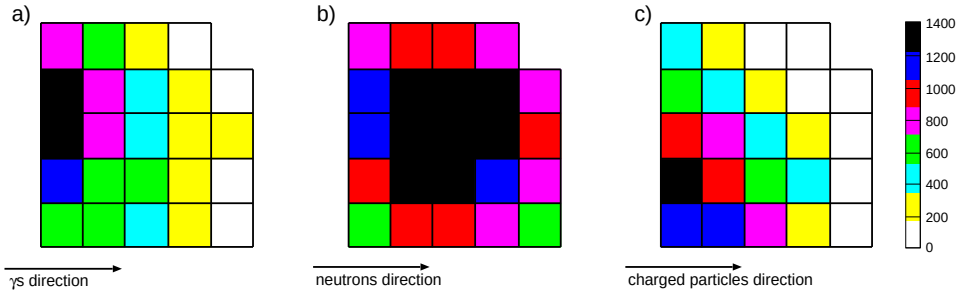

Figure 9: Conversion probability distribution in the neutron detector for γs, neutrons and charged particles from the left part of the figure to the right respectively. The module where the conversion happens was defined by the first signal.

4 Missing mass investigation

An event of Σ^+ production is characterized by the detection of a K^+ and a neutron and a calculated missing mass in the Σ^+ mass range. The kaon identification is performed via its measured mass. The invariant mass distribution of a second particle (where a neutron is the first one) determined from the reconstructed drift chamber tracks and the time of flight between kaon START and S1 scintillators is shown in Fig. 10. It can be calculated from the formula: $M_{inv} = p/(\beta \cdot \gamma)$, where p is the momentum, β the velocity of the particle and $\gamma = 1/\sqrt{1-\beta^2}$. An alternative signal for the particle identification is the energy loss when passing a detector material which is dependent on the velocity of the particle.

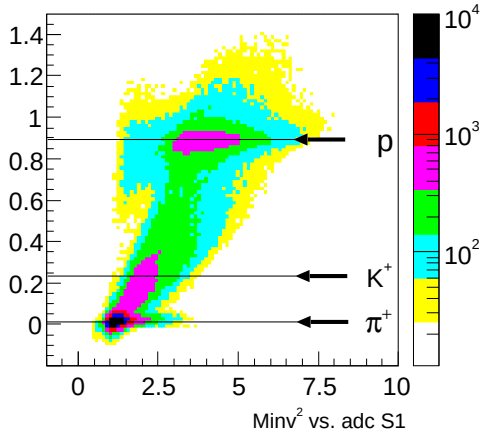

Figure 10: The squared invariant mass vs. energy loss in S1 for the second, positively charged particle.

The kaons were selected by two independent cuts namely on the invariant mass distribution and the energy loss in the S1 scintillator (see figure 10). The time of flight measurement allows due to the higher precision a much cleaner separation of different particle types compared to the energy loss signal but these nearly independent information is important as a further check of the correct particle identification. A neutron detection is defined by a hit in the neutron detector within the expected time window. By applying the cuts to select events with a detected K^+ and neutron the resulting missing mass distribution, gives an enhancement at the expected Σ^+ mass (see figure 11(c)). Extensive MC studies of possible background channels like $pp \to pnX$, $pp \to ppX$ and $pp \to pYX$ showed that $pp \to pK^+\Lambda$ and $pp \to pK^+\Lambda\gamma(\gamma's)$ are the dominant background channels in the Σ^+ region. The Λ hyperon decays with a $c\tau$ of 7.89 cm and a branching ratio of 35.8 $\pm$ 0.5 % to $n\pi^0$ [16]. Neutrons from this decay as well as kaons from the "primary production" can not be distinguished from neutrons and kaons from $pp \to nK^+\Sigma^+$ reaction. The missidentification of γs as a neutron are mostly removed by the cut on the neutron time of flight.The contribution of the Σ^0 hyperon which decays (with a $c\tau$ of $2.22 \cdot 10^{-11} m$ and a branching ratio of 100 %) to $\Lambda\gamma$ [16] is negligible due to the small detection acceptance and relatively small cross section.

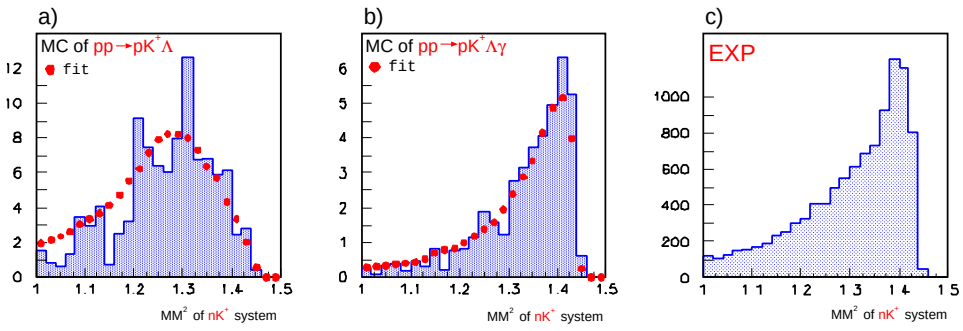

Figure 11: Missing mass distributions of the nK^+ system resulting from Monte Carlo studies of the $pp \to pK^+\Lambda$ and $pp \to pK^+\Lambda\gamma$ reactions and experiment (from the left part of the figure to the right, respectively). The simulations are continued to improve the statistics.

A clear separation of the background channels from the Σ^+ production

is not possible as can be seen from Fig. 11. But compared to the Σ^+ production events confined to the Σ^+ peak region the background channels results in much broader distributions with a tail to lower missing mass values. By adjusting the MC distributions of the background channels to the low missing mass region of the experimental spectrum the Σ^+ events can be separated from the background events.

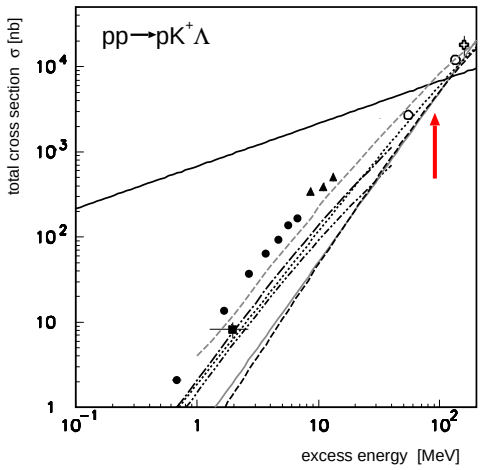

Figure 12: Total cross sections of the $pp \rightarrow pK^+\Lambda$ reaction compared with different theoretical descriptions. For details see [19]. The arrow points to the 88 MeV excess energy value for the $pp \rightarrow pK^+\Lambda$ reaction, which corresponds to $Q = 13$ MeV for the $pp \rightarrow nK^+\Sigma^+$ reaction.

Before an extraction of the number of Σ^+ events can be done, the background channel contributions on the resulting experimental missing mass distribution must be fully understood. 13 MeV excess energy for the $pp \rightarrow nK^+\Sigma^+$ reaction coresponds to about 88 MeV excess energy for the $pp \rightarrow pK^+\Lambda$ reaction (as well as $pp \rightarrow pK^+\Lambda\gamma(\gamma's)$). In this range cross section data for the $pp \rightarrow pK^+\Lambda\gamma$ are not available in contrary to $pp \rightarrow pK^+\Lambda$ reaction [17, 18]. A fit to the existing data of $pp \rightarrow pK^+\Lambda$ reaction gives a cross section value at Q = 88 MeV of $6 \cdot 10^3$ nb ($\pm 3 \cdot 10^3$nb). The error takes into account the differences in the gradient of the various models, see Fig. 12.
A preliminary adjustment of the Monte Carlo distributions to the experimental data is shown in Fig. 13. In the left part of the figure 13 the experimental distribution of nK^+ system is shown together with the smoothed distributions of the background channels. The amplitude of the $pp \rightarrow pK^+\Lambda$ distribution was taken from the known cross section. In this first adjustment the amplitude of the $pp \rightarrow pK^+\Lambda\gamma$ was taken as a free fit parameter. In the right part of figure 13 the sum of the background channels is subtracted from the experimental data resulting in a clear peak at the Σ^+ mass.

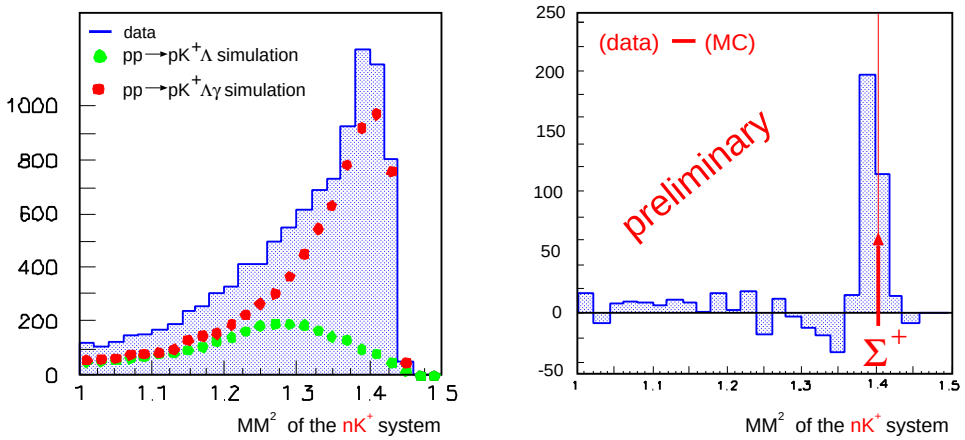

Figure 13: In the left part of the figure the experimental and simulated missing mass distributions of the nK^+ system are shown. In the figure right the sum of the background channels is subtracted from the data.

Although the amount of $pp \to pK^+\Sigma^+$ events is in the expected order of magnitude, more detailed studies and further checks are necessary to get a final number for the cross section.

References

[1] J. T. Balewski et al., Phys. Lett. **B 420** (1998) 211.

[2] S. Sewerin et al., Phys. Rev. Lett. **83** (1999) 682.

[3] P. Kowina et al., e-Print Archive nucl-ex/0402008, Eur. Phys. J. A, in print.

[4] A. Baldini et al., Total Cross-Section for Reactions of High-Energy Particles, Springer, Berlin, 1988.

[5] T. Rożek et al., COSY Proposal no. 117 (2002).

[6] A. Gasparian et al., Phys. Lett. **B 480** (2000) 273.

[7] A. Gasparian et al., Nucl. Phys. **A 684** (2001) 397-399.

[8] R. Shyam et al., Phys. Rev. **C 63** (2001) 022202.

[9] R. Shyam, e-Print Archive: hep-ph/0406297.

[10] A. Sibirtsev et al. Nucl. Phys. **A 646** (1999) 427-443

[11] A. Sibirtsev et al. nucl-th/0004022 v2 (2000).

[12] S. Brauksiepe et al., Nucl. Inst.& Meth. **A 376** (1996) 397-410.

[13] J. Przerwa, e-Print Archive: hep-ex/0408016; diploma thesis, Jagellonian University (2004), Berichte des FZ-Jülich, **Jül-4141** (2004).

[14] T. Rożek, P. Moskal, Ann. Rep. 2002, IKP FZ-Jülich, **Jül-4052**.

[15] P. Moskal, Ann. Rep. 2001, IKP FZ-Jülich, **Jül-3978**, 19.

[16] K. Hagiwara et al., Review of Particle Physics, Phys. Rev. **D 66**, (2002) 010001.

[17] R. Bilger et al., Phys. Lett. **B 420** (1998) 217.

[18] W. J. Fickinger et al., Phys. Rev. **125** (1962) 2082.

[19] M. Wolke, 'Hyperon production at the Cosy-11 facility' - Proceeding 'Hadrons in Dense Matter', GSI Darmstadt, **ISSN 0720-8715**, 27-34.

[20] P. Moskal et al., nucl-ex/0311003.

Molecule formation in the $K\bar{K}$- and DK-channels

F. P. Sassen

Institut für Kernphysik, Forschungszentrum Jülich, Germany

Abstract: We take a look at meson-meson scattering in the $K\bar{K}$- as well as the DK-channel emphasizing in particular the question of molecule formation. In this respect we first review results from the Jülich model [1, 2, 3] concerning the dynamics within the $K\bar{K}$-channel. Then we will assume $SU(4)$-symmetry to extend the Jülich model to the charmed sector. Using this model we investigate the dynamics of the coupled channel system consisting of the $D_s^+\pi^0$-, DK-, and $D_s^+\eta$-channels. We find that in the isoscalar channel a DK-molecule is formed due to the attraction of the t-channel meson exchange potentials. This may explain the observations by BaBar [10], Cleo [11], Belle [12] and others of a narrow D_{sJ} state at 2317 MeV. We thoroughly investigate the influence of isospin breaking via mass differences, $\rho\omega$- and $\pi\eta$-mixing on this molecule since within our model only isospin violating processes contribute to the width of the molecule. If the $D_{sJ}(2317)$ is assumed to be a pure molecule, we predict a width much smaller than the current experimental upper limit.

1 The Jülich model and its $SU(4)$ extension

Within the Jülich model [1, 2, 3] $SU(3)_{\text{flavour}}$-symmetry is used to relate the couplings g_{abc} of two pseudoscalars (a and b) and one vector (c) to the coupling $g_{\pi\pi\rho}$ of two pions and a ρ, which may be fixed from the pion decay constant via the KSFR-relation [4, 5]. With the same reasoning we use $SU(4)$-symmetry to relate the couplings in the charmed sector to the ones already known. This helps to keep the number of new parameters low, but since we know that $SU(4)$ is strongly broken when the mass sector is concerned, we need to ask whether it makes sense to use these relations for the coupling constants. So we compare experimentally observed decay widths to $SU(4)$-estimates. The results are shown in table (1). One should notice that, even though there is only rough agreement within the relative large errors, our results are robust regarding parameter changes of the order indicated by the differences between $SU(4)$-predictions and the experimental observations.

Decay process	Experimental width	Calculated width
$D^{*+} \to D^0\pi^+$	64 ± 18 keV [6]	38 keV
$D^{*+} \to D^+\pi^0$	29 ± 8 keV [6]	19 keV

Table 1: Comparison of decay widths calculated via $SU(4)$-relations and experimental observations.

2 The scattering equation and its kernels

In order to calculate the meson-meson dynamics we use the three dimensional reduction to the scattering equation suggested by Blankenbecler and Sugar [7] which is given in Eq. (1).

$$\begin{aligned} T_{ij}(\vec{k}', \vec{k}; E) &= V_{ij}(\vec{k}', \vec{k}; E) + \sum_l \int d^3k''\, V_{il}(\vec{k}', \vec{k}''; E) G_l(\vec{k}''; E) T_{lj}(\vec{k}'', \vec{k}; E) \\ G_l(\vec{k}''; E) &= \frac{\omega_1^l(k) + \omega_2^l(k)}{(2\pi)^3 2\omega_1^l(k)\omega_2^l(k)} \frac{1}{E^2 - (\omega_1^l(k) + \omega_2^l(k))^2} \end{aligned} \tag{1}$$

Here k denotes the relative momentum of the two mesons in their rest frame and $\omega_i = \sqrt{k^2 + m_i^2}$ denotes the energy of meson i. In the case of the $\pi\pi$-$K\bar{K}$ coupled channel system the kernel V_{ij} comprises s- and t-channel exchanges of ρ, ω, ϕ, K^*, f_0 and f_2. Here the K^* couples the two channels and the ρ-, ω- and ϕ-t-channel exchanges generate the attraction in the $K\bar{K}$-channel, which is responsible for the molecule formation in the isoscalar channel. In the isovector channel no molecule formation is observed, since the ρ t-channel exchange is repulsive here. This behavior is dictated by the Clebsch-Gordan coefficients.

When investigating the observation of the $D_{sJ}(2317)$ the kernel V_{ij} includes the K^* t-channel exchange to couple the $D_s^+\pi$ channel to the DK-channel and the ρ, ω t-channel exchanges in the DK-channel. These exchanges exhibit the same behavior as in the $K\bar{K}$-channel. i.e. in the isoscalar case both the ρ- and the ω-exchange generate attraction whereas in the isovector case the Clebsch Gordan coefficients dictate a repulsive behavior in the case of the ρ-exchange. Even though we calculated all potentials in the isospin symmetric limit we recoupled to the particle basis, which allows us to use the physical masses for charged and neutral particles, so that we may calculate the effects of isospin breaking introduced by them. Furthermore we included $\pi\eta$- as well as $\rho\omega$-mixing. To estimate the matrix elements

we used the values published in [8, 9], which we quote in Eq. (2).

$$\begin{aligned} \langle \rho | \, H \, | \omega \rangle &\approx -3480 \text{ MeV}^2 \\ \langle \pi | \, H \, | \eta \rangle &\approx -4400 \text{ MeV}^2 \end{aligned} \tag{2}$$

3 Isoscalar scalar resonances in pion pion scattering

Within the model described above it seems clear that a mesonic molecule is formed in the isoscalar $K\bar{K}$-channel. Nevertheless the prediction for the pole position varies from 20 MeV below to 30 MeV above the two kaon threshold. Even though there is a wealth of data available, this issue cannot be settled from data as can be seen in figure 1.

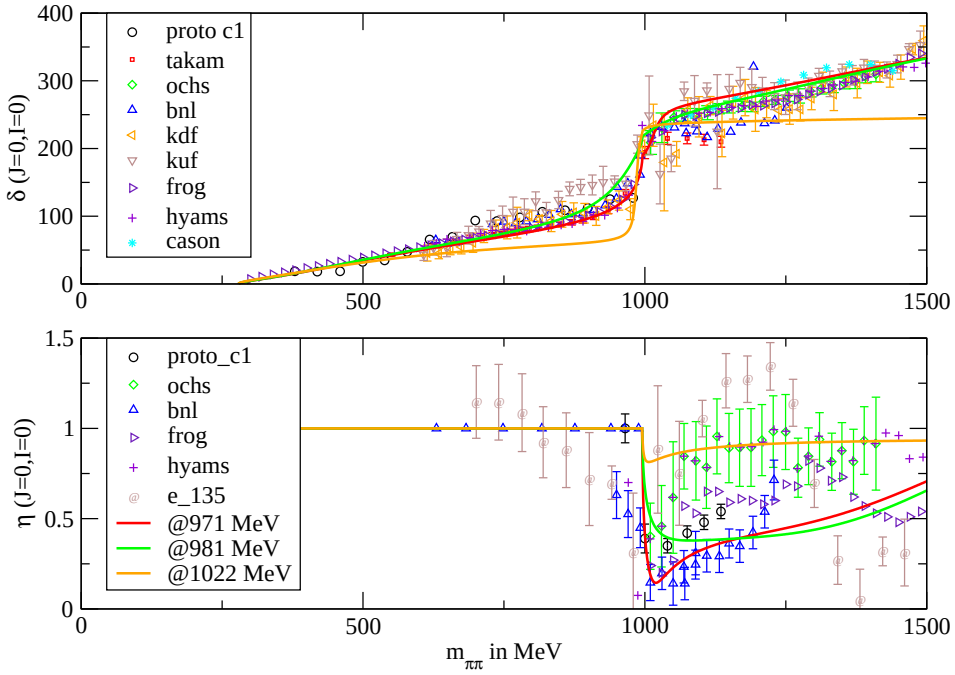

Figure 1: Pion-pion phase shifts and inelasticities in the scalar isoscalar channel are shown. The lines represent our model calculations representing pole positions at 971, 981 and 1022 MeV. The data sets shown have been chosen to give a representative overview of the available world data.

This even holds for the measurements from the BNL E852 and the GAMS collaboration which provide us with a measurement of the t-dependence in pion production. Sadly these two datasets are inconsistent, which makes it impossible to fix the coupling constants for the high lying scalar isoscalar states which is important since those states will certainly mix to the observed $f_0(980)$. Before looking at the charmed sector we would like to mention, that the width expected for the $K\bar{K}$-molecule is large since it may decay to the $\pi\pi$-channel.

4 The observation of the $D_{sJ}(2317)$ in the $D_s^+\pi^0$-channel

We model the $D_s^+\pi^0$ production by a constant production followed by FSI, which is calculated within the coupled channel framework described in section 2.

$$\begin{aligned} M = & \int d^3k''\, C^{prod}_{DK,I=1} G_l(\vec{k}''; E) T_{DK,I=1\to D_s^+\pi^0}(\vec{k}'', \vec{k}; E) \\ + & \int d^3k''\, C^{prod}_{DK,I=0} G_l(\vec{k}''; E) T_{DK,I=0\to D_s^+\pi^0}(\vec{k}'', \vec{k}; E) \end{aligned} \tag{3}$$

The results of the calculation are shown in figure 2. In the case of initial production in an isovector state(dotted) we see that the production is dominated by the opening DK-channel and only a small enhancement due to the formed molecule is seen, since the effect of the molecule is twice suppressed by isospin violation. So this possibility is excluded by data. The picture changes when isoscalar production is assumed. Even though the width of the molecule is very small(solid) due to isospin violation, the data can be reproduced. This can be seen when looking at the dashed line which includes the experimental resolution. One should notice that this is a key difference to the case of the $f_0(980)$, which has its mass much closer to the threshold and thus experiences an enhanced isospin breaking via the mass difference of the charged and neutral mesons, whereas the D_{sJ} does not profit from such an enhancement and thus stays very narrow. We also checked whether introducing a t-dependence to the $\pi\eta$- and $\rho\omega$-mixing might change this picture, but found no major changes.

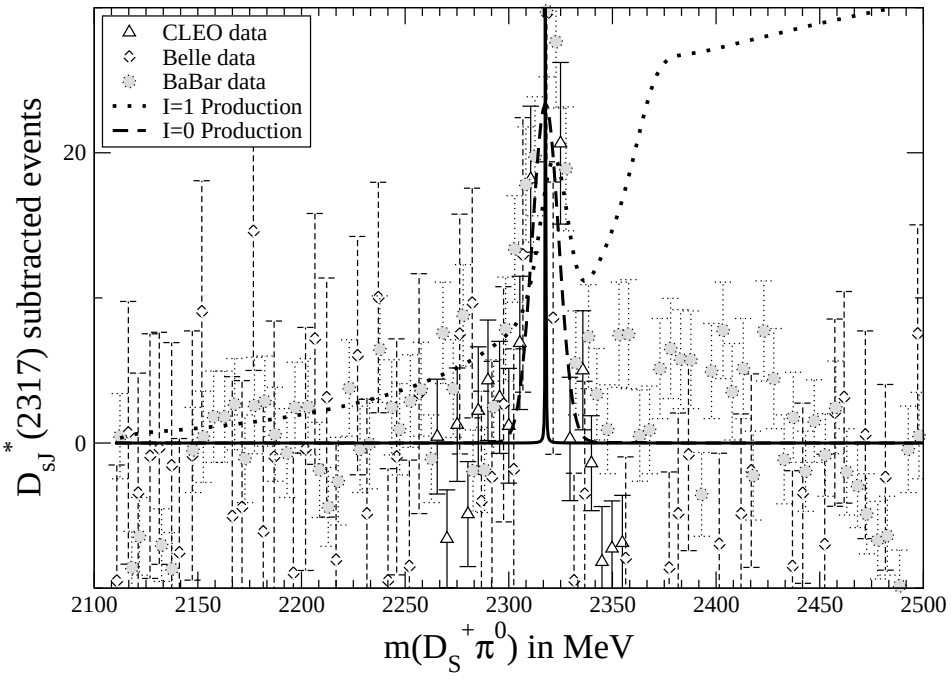

Figure 2: Invariant $D_s^+\pi^0$-mass spectrum with non D_{sJ} contributions subtracted. The data shown are from BaBar [10](circles), Cleo [11](triangles) and Belle [12](diamonds). The black line shows the result of our calculation(isoscalar production) with the actually predicted width. The dashed line is the same but folded with the experimental resolution. The dotted line shows an isovector production folded with the experimental resolution.

We conclude that so far a mesonic DK-molecule is able to reproduce the experimental observations, but this in no way excludes the possibility of an admixture of a pole from the mesonic spectrum to this state as the current upper limit of the width leaves much room for such an option as we have tested within our model. It is also worth to notice that such a genuine pole mixing to the dynamical pole generated within our model introduces a second scale to the physics which complicates a model independent analysis of the $D_{sJ}(2317)$ state.

References

[1] D. Lohse, J. W. Durso, K. Holinde and J. Speth,
Nucl. Phys. **A 516** (1990) 513.

[2] G. Janssen, B. C. Pearce, K. Holinde and J. Speth, Phys. Rev. **D 52** (1995) 2690.

[3] F. P. Sassen, S. Krewald and J. Speth, Phys. Rev. **D 68** (2003) 036003.

[4] K. Kawarabayashi and M. Suzuki, Phys. Rev. Lett. **16** (1966) 255.

[5] Riazuddin and Fayyazuddin, Phys. Rev. **147** (1966) 1071.

[6] K. Hagiwara et al. [Particle Data Group Collaboration], Phys. Rev. **D 66** (2002) 010001.

[7] R. Blankenbecler and R. Sugar, Phys. Rev. **142** (1966) 1051.

[8] S. Gardner and H. B. O'Connell, Phys. Rev. **D 57** (1998) 2716 [Erratum-ibid. **D 62** (2000) 019903].

[9] S. A. Coon and M. D. Scadron, Phys. Rev. **C 51** (1995) 2923.

[10] B. Aubert et al. [BABAR Collaboration], Phys. Rev. Lett. **90** (2003) 242001.

[11] D. Besson et al. [CLEO Collaboration], Phys. Rev. **D 68** (2003) 032002.

[12] K. Abe et al., Phys. Rev. Lett. **92** (2004) 012002. .

The $\Theta^+(1540)$ resonance and its influence on the reactions K^+N and K^+d

J. Haidenbauer

Institut für Kernphysik, Forschungszentrum Jülich, Germany

Abstract: Results on the impact of the $\Theta^+(1540)$ resonance on the KN isospin-zero cross section and on differential cross sections for the reaction $K^+d \to K^0pp$ in the relevant momentum range are presented. The investigation utilizes the Jülich KN model and extensions of it that include contributions from a $\Theta^+(1540)$ state. The evaluation of the reaction $K^+d \to K^0pp$ takes into account effects due to Fermi motion of the nucleons within the deuteron and the final three-body kinematics. The comparison with the available data allows to establish an upper limit of 1 MeV for the with of the Θ^+ resonance.

1 Introduction

The possible discovery of an exotic pentaquark baryon, the $\Theta^+(1540)$ [1], has led to an enormous increase in research activities covering various aspects of this state. First of all, of course, its existence has to be firmly established. Although the resonance is already listed in the recent compilation of the particle data group with a three-star rating [2] the statistical significance of the existing experiments is not too overwhelming and, moreover, there is also an increasing number of experiments where no signal of the $\Theta^+(1540)$ is seen [3]. Planned or already ongoing experiments will hopefully soon provide a conclusive answer here [4].

If one is optimistic and assumes that the $\Theta^+(1540)$ pentaquark indeed exists then there are further open questions that need to be resolved. For example, while its strangeness is fairly well established and the values of $S{=}+1$ clearly proves the exotic nature of this resonance, there is so far no information on its parity. This quantum number is a decisive quantity regarding the substructure of the Θ^+ resonance [5]. Specifically, in the chiral soliton model of Ref. [6] where such a state was predicted at almost exactly the energy where it was seen in the experiments a parity of $J^P{=}(1/2)^+$ is imperative. Several concrete and experimentally feasible suggestions for the determination of the Θ^+ resonance, in hadron- as well as in photon-

induced reactions, can be found in the literature, see e.g. Refs. [7, 8, 9], and are waiting on being taken up by experimentalists.

Another topic concerns the width of the Θ^+ resonance. Predicted in Ref. [6] to be in the order of 10 to 20 MeV the narrowness of the Θ^+ resonance was indeed confirmed in the experiments. As a matter of fact, the signal turned out to be so narrow that most of the experiments could only provide an upper limit for the width, $\Gamma_\Theta \approx 20$ MeV, which is basically given by available energy resolution [1]. Because of that the presently best constraints for the width are deduced from an entirely different empirical source, namely from kaon-nucleon (KN) and kaon-deuteron (Kd) scattering data. Since the Θ^+ resonance has S=+1 it can couple to and decay into the KN system (the kinematical threshold of the KN system is at roughly 1435 MeV). It should be emphasized, however, that this determination of the width is an indirect one because the available KN and Kd data in the relevant energy range show hardly any really obvious sign of the presence of the $\Theta^+(1540)$ resonance. As a consequence the deduced values for the width are to a significant extent influenced by the size of the energy intervals where there are no data at all and not only by the available data themselves.

Work along those lines has been performed by the theory group in Jülich [10, 11] but also by other authors [12, 13, 14, 15, 16], with varying degrees of sophistication. The unanimous outcome of those analysis was that the width of the Θ^+ must be in the order of 1 MeV or even less in order to be compatible with the existing KN and Kd data. Such a small value is presumably even outside of the range anticipated by the authors of Ref. [6] and rather surprising for a resonance that, in principle, can decay via ordinary hadronic channels even if one considers that the Θ^+ could be a P-wave resonance (in case of positive parity). As a benchmark one should compare the Θ^+ width of about 1 MeV with the corresponding value of the $\Lambda(1560)$ resonance which is 15.6$\pm$1.0 MeV – where one has to keep in mind that the latter is even a D-wave resonance. Thus, the $\Theta^+(1540)$ seems to be not only an exotic resonance with regard to its five-quark content but also, and may be even more, because of its extremely narrow width. Note that so far there is no plausible and generally accepted explanation for the narrow width of the Θ^+ resonance [4, 17, 18, 19, 20, 21, 22, 23, 24, 25, 26].

In the present paper I want to provide details about the analysis of the KN and Kd scattering data carried out in Jülich and its implications on the width of the $\Theta^+(1540)$ resonance. Starting point of the investigations by the Jülich group is a microscopic model of the KN interaction, derived in the meson-exchange picture, which was published about ten years ago. A detailed description of the Jülich KN model can be found in Refs. [27, 28].

However, for the ease of the reader we summarize its features briefly in Sect. II. In this section we also explain how the $\Theta^+(1540)$ resonance is included in this model and we present results for KN scattering based on the original model as well as on the variants including the contribution of a $\Theta^+(1540)$ assuming widths between 1 and 20 MeV [10].

Strictly speaking, the comparison with empirical KN cross sections is only meaningful for the isospin $I = 1$ channel where genuine data are available. The experimental information on the KN interaction in the isospin $I = 0$ channel has been inferred from data on the Kd reaction. In the extraction procedure it is implicitly assumed that the KN amplitude shows no sharp structure. Therefore, it is more conclusive to calculate explicitly observables for the reactions $K^+d \to K^+np$ and $K^+d \to K^0pp$, say, based on KN interaction models that include a $\Theta^+(1540)$ resonance so that a direct comparison with experimental data is possible. Then "medium" effects such as the broadening of the resonance by the Fermi motion of the nucleons in the deuteron and the interaction of the nucleons in the final state can be dealt with rigorously. Corresponding results are presented in Sect. III for the reaction $K^+d \to K^0pp$

The paper ends with a short summary.

2 The kaon-nucleon system

In the investigations presented in Refs. [10, 11] the Jülich meson-exchange model of the KN interaction is used to examine the effect of the presence of a Θ^+-like resonance structure on the description of the experimental data for KN and Kd scattering. A detailed description of this model is given in Refs. [27, 28]. It was constructed along the lines of the full Bonn NN model [29] and its extension to the hyperon-nucleon YN system [30]. Specifically, this means that one has used the same scheme (time-ordered perturbation theory) and the same type of processes. Moreover, most of the vertex parameters (coupling constants and cut-off masses of the vertex form-factors) appearing in the diagrams that contribute to the interaction potential V_{KN}, cf. Fig. 1 of Ref. [28], have been fixed already by the study of other reactions.

Once the KN interaction potential V_{KN} is derived, the corresponding reaction amplitude T_{KN} is then obtained by solving a Lippmann-Schwinger equation defined by time-ordered perturbation theory,

$$T_{KN} = V_{KN} + V_{KN} G_0 T_{KN} \ . \tag{1}$$

Taking the solution of such a scattering equation implies that the resulting reaction amplitude T_{KN} automatically fulfils the requirements of (two-body) unitarity. In the present investigation we use the KN model (I) described in Ref. [28]. In that reference one can also find pertinent results for phase shifts and as well as for differential cross sections and polarizations. Evidently the model (I) yields a good overall reproduction of all presently available empirical information on KN scattering. Specifically, it describes the data up to kaon laboratory momenta of $p_K \approx 1$ GeV/c, i.e. well beyond the region of the observed Θ^+ resonance structure which corresponds to the momentum $p_K \simeq 440$ MeV/c.

The Θ^+ resonance is included in the model by adding a pole diagram with a bare mass $\hat{M}_{\Theta^+}$ and a bare coupling constant $\hat{g}_{KN\Theta^+}$ to the other diagrams that contribute to V_{KN}, cf. Ref. [10] for details. When the total interaction potential is then iterated in the Lippmann-Schwinger equation the $KN\Theta^+$ vertex gets dressed by the non-pole part of the interaction and the Θ^+ acquires a width and also its physical mass via self-energy loops. Note that the bare mass and bare coupling constant are free parameters that are adjusted to obtain the desired physical mass and width of the Θ^+ resonance. The latter are adopted to be M_{Θ^+}=1540 MeV and, for exploring the sensitivity of the KN and Kd results to the width, Γ_{Θ^+}=1, 5, 10, and 20 MeV.

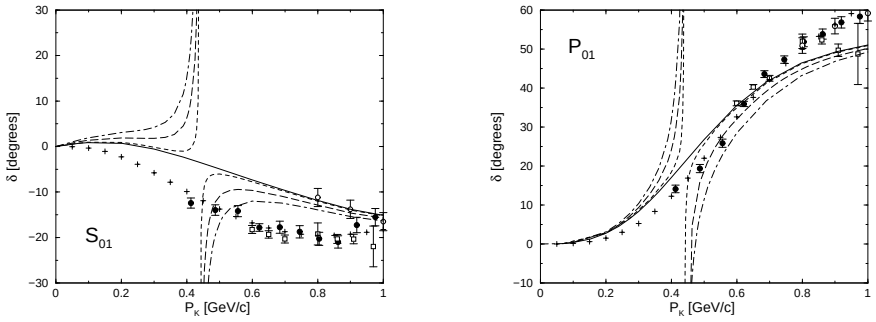

Figure 1: The S_{01} and P_{01} phase shifts for KN scattering as a function of the kaon momentum. The solid lines show the calculations without Θ^+ contribution. The short-dashed line is our calculation with Γ_{Θ^+}=1 MeV, the long-dashed line corresponds to Γ_{Θ^+}=5 MeV and the dash-dotted line to Γ_{Θ^+}=10 MeV. Note that the phases for the resonance cases are shown modulo π!

Depending on the parity of the Θ^+ the resonance will contribute to different partial waves of the KN interaction. If the Θ^+ is a $J^P = \frac{1}{2}^+$ state, as predicted by the chiral quark-soliton model [6], then it couples to the P_{01}

channel (we use the standard spectral notation $L_{I\,2J}$), if it has the opposite parity it will occur in the S_{01} partial wave. These two phases exhibit quite different characteristics as can be seen in Fig. 1. The S_{01} is small and basically repulsive. In fact $\delta_{S_{01}}$ is practically zero up to the momentum of p_K=440 MeV/c corresponding to the Θ^+ resonance mass. In contrast the P_{01} phase shift is large and attractive. As a consequence, the total KN cross section for isospin I=0 is dominated by the P_{01} partial wave while the contribution of the S_{01} partial wave is roughly given by the result on the very left side of Fig. 2.

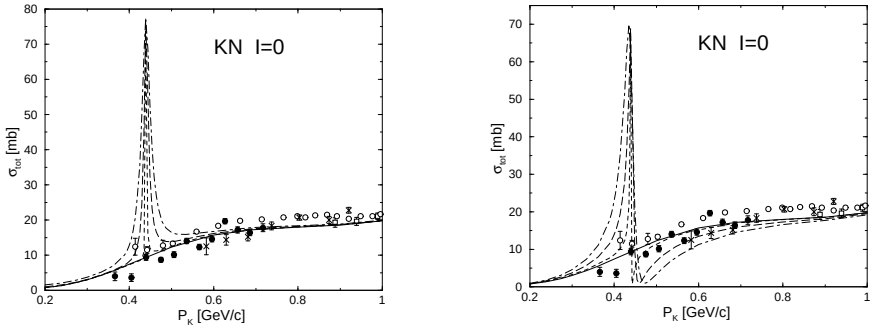

Figure 2: The KN reaction cross section for the $I = 0$ channel as a function of the kaon momentum. Results are shown for negative (left) and positive (right) parity of the Θ^+ resonance. The various curves correspond to different Θ^+ widths, Γ_{Θ^+}=1 MeV (short dashed), 5 MeV (long dashed), and 10 MeV (dash-dotted), while the solid line is the prediction without a Θ^+ contribution. Data are taken from Refs. [31] (filled circles), [32] (squares), [33] (open circles), and [34] (crosses).

Adding a resonance in these two partial waves generates again quite different characteristics. In the S_{01} partial wave we obtain basically a Breit-Wigner type structure because the non-resonant background is rather small. In the P_{01} partial wave, on the other hand, there is an interference of the background phase with the added resonance structure. In particular, the phase will not only rise beyond 90^0 (because of the resonance) but even beyond 180^0 (because of the large background). For momenta around the region where the phase shift passes through 180^0 there will be practically no contribution of this partial wave to the total cross section because $\sigma_{P_{01}} \propto \sin^2(\delta_{P_{01}})$. As a consequence, a resonance in the P_{01} partial wave causes a rather striking bump-dip structure in the KN I=0 cross section.

Fig. 3 shows the cross section for the charge-exchange reaction $K^+n \rightarrow K^0p$ as a function of the kaon momentum. Obviously, here the characteristic differences between the S_{01} and P_{01} resonances have basically disappeared.

Since the charge-exchange cross section is given by the difference of the isospin $I = 1$ and $I = 0$ amplitudes we now get an interference of the (larger) S_{11} partial wave with the resonant S_{01} partial wave and that leads to a similar bump-dip structure in the cross section as produced by the interference of the resonance with the background in the P_{01} case. Still one can see that for the negative parity case the dip after the resonance energy is somewhat less pronounced, cf. the two cases in Fig. 3.

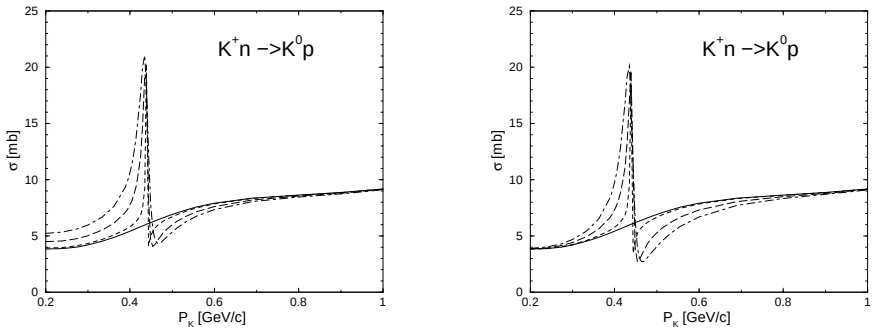

Figure 3: The $K^+n \to K^0p$ reaction cross section as a function of the kaon momentum. Same description of curves as in Fig. 2.

This specific behaviour of the elementary KN and $K^+n \to K^0p$ cross sections will be reflected in the reaction Kd, as we will see in the next section, but, of course, it should be also present in all of those reactions where the Θ^+ was experimentally observed because there too the complete KN amplitude enters [35].

3 The kaon-deuteron system

There are no data on the elementary $K^+n \to K^0p$ process. However, the charge-exchange channel has been measured on a deuteron target, i.e. in the reaction $K^+d \to K^0pp$. In Ref. [11] we have investigated this reaction employing the Jülich KN model and the extensions including a Θ^+ resonance discussed above. For the calculation of the reaction $K^+d \to K^0pp$ we follow, in general, the theoretical procedure which was originally developed by Stenger et al. [36]. A detailed description of the formalism can be found in Ref. [37].

The amplitude T_d for the deuteron breakup reaction is

$$T_d = \sqrt{16\pi^3 m_d}[T_{KN}(q)u(p) + T_{KN}(p)u(q)], \qquad (2)$$

where m_d is the deuteron mass, p and q are the momenta of the two final nucleons, u is the (S-wave) deuteron wave function and T_{KN} is the elementary KN amplitude. In the present calculation we used the deuteron wave function of the CD-Bonn potential. Exploratory calculations based on other wave functions (Paris, Hulthen) indicated, however, that the results are rather insensitive to the specific choice. Note that throughout we neglect the deuteron D-state. The differential cross section for the $K^+d \to K^0pp$ reaction is then given as [36, 37]

$$\frac{d\sigma}{d\Omega} = (|f_x|^2 + |g_x|^2)[I(\theta) - J(\theta)] + \frac{2}{3}|g_x|^2 J(\theta), \tag{3}$$

where f_x and g_x are the elementary spin-non-flip and spin-flip $K^+n \to K^0p$ amplitudes and I and J are the deuteron inelastic form factors, respectively. They are explicitely given by [36, 37]

$$\begin{aligned} I &= F\int \frac{k^2 dk}{E_K}\frac{d^3p}{E_p}\frac{d^3q}{E_q}\delta^4(k_0 + P - k - p - q)\frac{u^2(p) + u^2(q)}{2}, \\ J &= F\int \frac{k^2 dk}{E_K}\frac{d^3p}{E_p}\frac{d^3q}{E_q}\delta^4(k_0 + P - k - p - q)u(p)u(q), \end{aligned} \tag{4}$$

where k_0, k and P are the momenta of the initial and final kaon and of the deuteron, respectively. E_k, E_p and E_q are the total energies of particles in the final state. The factor F accounts for the transformation of the kaon scattering angle θ from the laboratory deuteron rest frame to the center-of-mass frame of the KN two-body system. It is usually evaluated in the stationary spectator configuration, i.e. by assuming that the reaction takes place on the neutron at rest.

In the derivation of the expression for the $K^+d \to K^0pp$ differential cross section one encounters three-body phase space integrals of the KN amplitudes over the momentum distribution of the nucleons within the deuteron. The form factor approximation rests on the assumption that the elementary amplitudes f_x and g_x and the kinematic factors vary only slightly over the integration range and therefore can be taken out of the integrands and evaluated for a fixed typical nucleon momentum. The remaining integrals are then the form factors I and J. However, in the presence of the Θ^+ resonance the amplitudes f_x and g_x depend strongly on the kaon energy and can not be removed from the I and J integrands. Therefore, in our analysis we integrate the KN amplitude over the final three-body phase space. Furthermore we do not use the stationary spectator approximation but compare our calculations directly to the differential cross sections measured in the deuteron rest frame.

It is worthwhile to mention that for the $K^+d \to K^0pp$ three-body final-state the invariant mass m_{Kp} of the K^0p system is integrated over the range from m_K+m_p to $\sqrt{s}-m_p$, where m_K and m_p stand for the masses of the K^0-meson and the proton, respectively, and

$$s = m_K^2 + m_d^2 + 2m_d\sqrt{m_k^2 + k_0^2}. \tag{5}$$

Therefore, for a fixed initial kaon momentum, k_0, the deuteron experiment samples the elementary $K^+n \to K^0p$ amplitude over the m_{Kp} range given above. This situation substantially differs from the "free neutron target" approximation, where the invariant mass m_{Kp} is fixed by k_0 through Eq. (5).

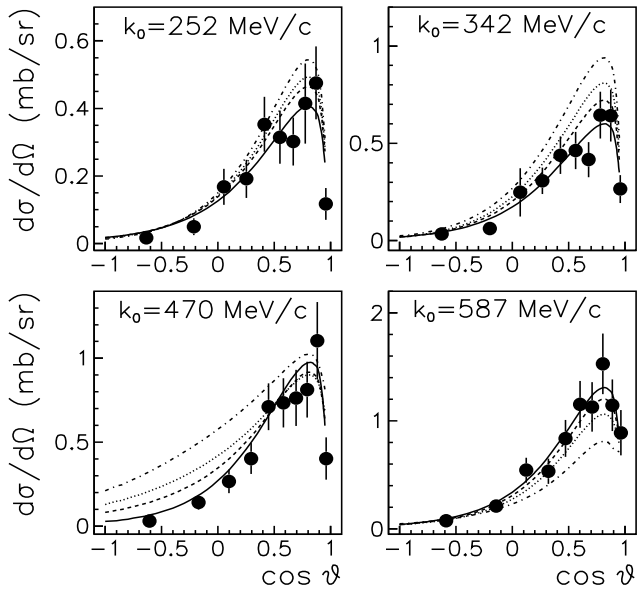

Figure 4: The K^0-meson angular spectra from the $K^+d \to K^0pp$ reaction for different K^+ momenta. The curves show our results for the original Jülich KN model without the Θ^+ resonance (solid line) and the variants with a $\Theta^+(1540)$ and with different widths (Γ_Θ=5 MeV - dashed; 10 MeV - dotted; and 20 MeV - dash-dotted). The data are from Glasser et al. [40].

For the "free target" measurements the Θ^+ mass of 1530 MeV corresponds to incident kaon momentum of k_0=417 MeV/c and only the data around that momentum can be sensitive to the Θ^+ resonance. If one does not make the assumption of a free target, all $K^+d \to K^0pp$ observables above k_0=417 MeV/c will be influenced by the presence of the Θ^+ resonance,

which will show up in the K^0p mass distribution. Note that the m_{Kp} spectrum is affected by the deuteron wave function, since the maximal K^0p mass corresponds to the minimal spectator momentum, while the minimal m_{Kp} probes high spectator momenta. In addition the Θ^+ resonance occupies only a small fraction of the K^0p mass distribution, while the overall m_{Kp} integration includes large part of the "non-resonant background". Therefore it might be that the Θ^+ signal in the invariant K^0p mass spectrum becomes invisible after m_{Kp} integration. The arguments given above are confirmed by our explicit calculations of the K^0p mass spectra for different kaon momenta [11].

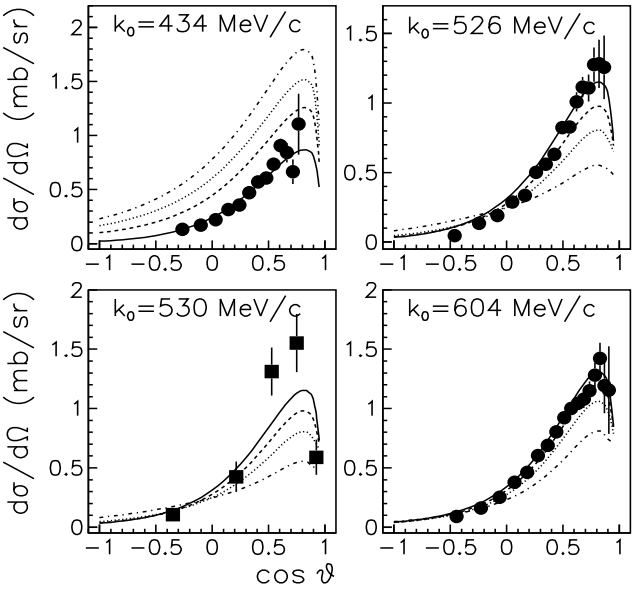

Figure 5: The K^0-meson angular spectra from $K^+d\to K^0pp$ reaction at different K^+ momenta. For notations, see Fig. 4. The data from Damerell et al. [41] (circles) and Stenger et al. [36] (squares).

Results for the K^0-meson angular spectra for the reaction $K^+d\to K^0pp$ are compared with a selection of available experimental spectra [38, 39, 40, 41] that have kaon momenta below 610 MeV/c in Figs. 4 and 5. The lines correspond to calculations with the original Jülich KN model (i.e. without a Θ^+) and with the variants with different Θ^+ widths. Recall that the resonance energy is always the same and was assumed to be 1540 MeV. For the parity only the case $J^P = 1/2^+$ is considered. It is interesting to see that the calculations with a Θ^+ increase the differential $K^+d\to K^0pp$ cross sections

at momenta $k_0 \leq 470$ MeV/c and decrease them at higher momenta as compared to those obtained without a Θ^+ resonance. This effect is caused by the interference of the Θ^+ and the non-resonant P_{01} contribution, discussed in the last section. Note also that at large kaon momenta the integration over the K^0p invariant mass does not allow to distinguish between the situation with $\Gamma_\Theta \leq 10$ MeV and that without a Θ^+ resonance.

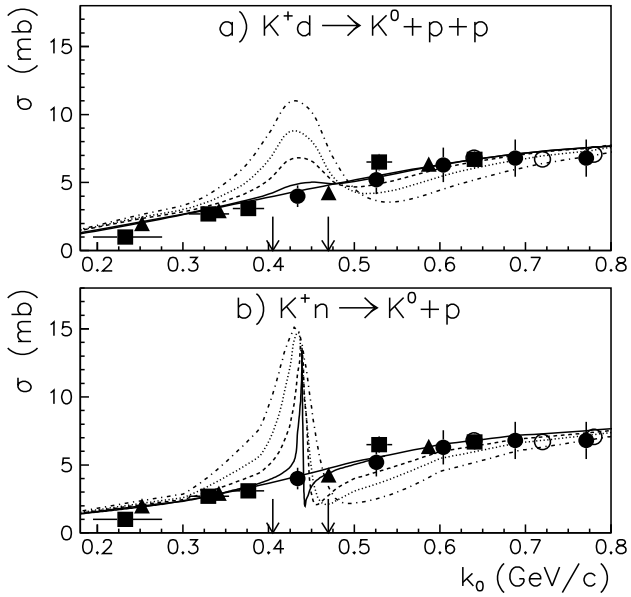

Figure 6: Total $K^+d \to K^0pp$ cross section as a function of the kaon momentum. The curves in a) show our full results for the original Jülich KN model without the Θ^+ resonance (solid line) and the variants with a Θ^+ and with different widths (Γ_Θ=1 MeV - solid with bump; 5 MeV - dashed; 10 MeV - dotted; and 20 MeV - dash-dotted). The curves in b) correspond to a calculation for the reaction $K^+n \to K^0p$ assuming that the neutron target is at rest. Data are from Refs. [41] (filled circles), Ref. [38] (squares), [40] (triangles) and [39, 42] (open circles). The vertical arrows indicate the range of kaon momenta corresponding to the smallest and the largest values found experimentally for the mass of the Θ^+ resonance.

A detailed inspection of the available differential $K^+d \to K^0pp$ cross sections clearly indicates that the measurement by Glasser et al. [40] at the K^+-meson momentum k_0=470 MeV/c and of Damerell et al. [41] at k_0=434 MeV/c are the most crucial ones for the determination of the Θ^+ width. In Fig. 6a we present results for the integrated $K^+d \to K^0pp$ cross section as a function of the kaon momentum in comparison to the available experimental infor-

mation. Again, it is evident that the data of Glasser et al. [40] and Damerell et al. [41] provide the most restrictive constraints for the Θ^+ width.

Thus, it is certainly fortunate that there are two independent measurements in the critical energy range. One can see from Fig. 6a that none of the model calculations with a Θ^+ width larger than 1 MeV is compatible with the data. Widths of 1 MeV or less can be certainly accommodated though we should say here that we did not explore the effect of such narrow widths in detail. If we disregard those two data points there is a larger gap in the data base just at those energies where the Θ^+ is supposed to be located (the largest and smallest resonance masses reported so far [1] are indicated by bars in Fig. 6 and that allows to fit in such a resonance with a width of $\Gamma_\Theta \approx 5$ MeV without increasing the χ^2/data by more than 10% as was demonstrated in Ref. [11].

In order to illustrate the impact of the stationary neutron approximation we show here also calculations for the two-body reaction $K^+n \to K^0p$, cf. Fig. 6b. Comparing the two panels of the figure one can see to which extend the resonance is broadened by the Fermi motion of the nucleons in the deuteron and by the integration over the three-body phase space.

Further studies, exploring also the influence of a negative parity $\Theta^+(1540)$ resonance on the reaction $K^+d \to K^0pp$ as well as an extension of the analysis to the reaction channels $K^+d \to K^+np$ and $K^+d \to K^+d$ are presently in preparation.

4 Summary

We have examined the impact of the $\Theta^+(1540)$ resonance on the reactions KN and $K^+d \to K^0pp$ by comparing results of a concrete model calculation with available experimental information in those reaction channels in the relevant momentum range. The investigation utilizes the Jülich KN model and extensions of it that include contributions from a $\Theta^+(1540)$ state with different widths. The evaluation of the reaction $K^+d \to K^0pp$ takes into account effects due to Fermi motion of the nucleons within the deuteron and the final three-body kinematics. The comparison with existing data on differential and integrated cross sections suggests that there is no room for a Θ^+ resonance with a width of more than 1 MeV.

Acknowledgments

I would like to thank G. Krein, S. Krewald, Ulf-G. Meißner, and A. Sibirtsev for collaboration on the topics presented here.

References

[1] For a recent review see, e.g., E. Klempt, hep-ph/0404270.

[2] S. Eidelman et al., Phys. Lett. **B 592** (2004) 1.

[3] For references see, e.g., M. Karliner and H.J. Lipkin, hep-ph/0405002.

[4] For a recent outlook see, e.g., K. Hicks, hep-ph/0408001.

[5] B.K. Jennings and K. Maltman, Phys. Rev. **D 69** (2004) 094020.

[6] D. Diakonov, V. Petrov, and M. Polyakov, Z. Phys. **A 359** (1997) 305.

[7] A. W. Thomas, K. Hicks, and A. Hosaka,
Prog. Theor. Phys. **111** (2004) 291.

[8] K. Nakayama and K. Tsushima, Phys. Lett. **B 583** (2004) 269.

[9] C. Hanhart et al., Phys. Lett. **B 590** (2004) 39; hep-ph/0407107.

[10] J. Haidenbauer and G. Krein, Phys. Rev. **C 68** (2003) 052201(R).

[11] A. Sibirtsev, J. Haidenbauer, S. Krewald and Ulf-G. Meißner,
hep-ph/0405099, Phys. Lett. **B**, in print.

[12] S. Nussinov, hep-ph/0307357.

[13] R.A. Arndt, I.I. Strakovsky and R.L. Workman,
Phys. Rev. **C 68** (2003) 042201(R).

[14] R.N. Cahn and G.H. Trilling, Phys. Rev. **D 69** (2004) 011501.

[15] R.L. Workman et al., Phys. Rev. **C 70** (2004) 028201.

[16] W. R. Gibbs, nucl-th/0405024.

[17] A. Casher and S. Nussinov, Phys. Lett. **B 578** (2004) 124.

[18] M. Karliner and H.J. Lipkin, Phys. Lett. **B 586** (2004) 303.

[19] D. Melikhov, S. Simula, and B. Stech, Phys. Lett. **B 594** (2004) 265.

[20] D.K. Hong, Y.J. Sohn, and I. Zahed, Phys. Lett. **B 596** (2004) 191.

[21] F. Buccella and P. Sorba, Mod. Phys. Lett. **A 19** (2004) 1547.

[22] C.E. Carlson et al., hep-ph/0312325.

[23] X.-C. Song and S.-L. Zhu, hep-ph/0403093.

[24] D. Diakonov, V. Petrov, and M. Polyakov, hep-ph/0404212.

[25] S.-L. Zhu, hep-ph/0406204.

[26] R.L. Jaffe and A. Jain, hep-ph/0408046.

[27] R. Büttgen et al., Nucl. Phys. **A 506** (1990) 586.

[28] M. Hoffmann et al., Nucl. Phys. **A 593** (1995) 341.

[29] R. Machleidt, K. Holinde, and Ch. Elster, Phys. Rep. **149** (1987) 1.

[30] B. Holzenkamp, K. Holinde and J. Speth, Nucl. Phys. **A 500** (1989) 485.

[31] T. Bowen et al., Phys. Rev. **D 2** (1970) 2599.

[32] R.L. Cool et al., Phys. Rev. **D 1** (1970) 1887.

[33] A.S. Carroll, et al., Phys. Lett. **45B** (1973) 531.

[34] T. Bowen et al., Phys. Rev. **D 7** (1973) 22.

[35] A. Sibirtsev, J. Haidenbauer, S. Krewald, and U.-G. Meißner, nucl-th/0407011.

[36] V.J. Stenger et al., Phys. Rev. **134** (1964) B1111.

[37] K. Hashimoto, Phys. Rev. **C 29** (1984) 1377.

[38] W. Slater et al., Phys. Rev. Lett. **7** (1961) 378.

[39] G. Giacomelli et al., Nucl. Phys. **B 42** (1972) 437.

[40] R.G. Glasser et al., Phys. Rev. **D 15** (1977) 1200.

[41] C.J.S. Damerell et al., Nucl. Phys. **B 94** (1975) 374.

[42] G. Giacomelli et al., Nucl. Phys. **B 37** (1972) 577.

On the possibility of studying properties of the exotic Θ^+ baryon using WASA at COSY

J. Złomańczuk

[a] *Department of Radiation Sciences, Uppsala University, Uppsala, Sweden*

Abstract: The feasibility of studying properties of the exotic Θ^+ baryon using WASA at COSY is investigated. Phase space Monte Carlo simulation shows that $pd \to p\Lambda\Theta^+$ reaction fits well into the WASA detector acceptance. For the 200 nb Θ^+ production cross section and $10^{31}/\mathrm{cm}^2\mathrm{s}$ luminosity, one may expect 10^4 Θ^+ events to be collected in less than 200 hours.

1 Introduction

Quantum Chromodynamics (QCD) is believed to be the underlying theory of strong interactions. Indeed, in the high energy regime it has been tested up to 1% level. However, in the low energy sector, QCD is highly nonperturbative due to the non-abelian $SU_c(3)$ color group structure. Therefore, various models, which are QCD based, were proposed to explain the low-energy properties of strong interactions. Among them the quark model is the most successful one. According to this model, mesons are composed of a quark and anti-quark pair while baryons are composed of three quarks. Both mesons and baryons are color singlets. Any state with the quark content other than $q\bar{q}$ or qqq is beyond the quark model, and is termed non-conventional or exotic.

It should be pointed out that QCD itself does not exclude the existence of the non-conventional states such as glueballs (gg, ggg,...), hybrid mesons ($q\bar{q}g$), and other multi-quark states ($qq\bar{q}\bar{q}$, $qqqq\bar{q}$, $qqq\bar{q}\bar{q}\bar{q}$, $qqqqq\bar{q}$,...). However none of these states has been pinned down without controversy until the surprising discovery of pentaquarks by the LEPS collaboration [1].

Early in 2003, the LEPS Collaboration at the SPring-8 facility in Japan observed a sharp resonance, Θ^+, at 1.54±0.01 GeV with a width smaller than 25 MeV and a statistical significance of 4.6 σ in the reaction $\gamma n \to K^+K^-n$ [1]. This resonance decays into K^+n, hence carries strangeness $S = +1$.

Later, many other groups have claimed the observation of this state [2]. Since all known baryons with $B = +1$ carry negative or zero strangeness, such a resonance must have a minimum quark content $uudd\bar{s}$, a structure which is clearly beyond the conventional quark model. This experimental discovery triggered a lot of theoretical activity and up to now over 250 papers appeared trying to interpret this exotic state [3].

There is preliminary evidence that the Θ^+ is an iso-scalar because no enhancement was observed in the pK^+ invariant mass distribution [4]. All the other quantum numbers including its angular momentum and parity remain undetermined. Most of theoretical work postulated its angular momentum to be one half, because of its low mass, but the possibility of $J = 3/2$ still cannot be excluded completely.

It is important to point out that many other experimental groups reported negative results [5]. A long list of experiments yielding negative results, including those unpublished, can be found in Ref. [6].

With both positive and null evidence for the Θ^+ from a variety of experiments, it is difficult to conclude whether the Θ^+ exists or not. Furthermore, the theoretical difficulties to explain a possible narrow width, perhaps as small as 1 MeV, suggest that if the Θ^+ exists, it is very unusual indeed. Guidance from lattice gauge theory is not helpful, as some calculations show evidence for a negative parity resonance, some indicate a positive parity, and some do not see a resonance in either parity. So the job of proving or disproving the Θ^+ existence is currently an experimental task.

WASA at COSY with its very good mass resolution and large acceptance can make a decisive contribution to this field by providing high statistics data on the differential cross sections of Θ^+ production in elementary reactions. While there are several elementary reactions with the Θ^+ in the final state within the COSY energy range, the $pd \to p\Lambda\Theta^+$ reaction is of special interest since it suits well the WASA acceptance. Recent theoretical estimation of the Θ^+ production cross section in this reaction shows that it may rise from about 30 nb at 1360 MeV beam energy to about 200 nb at 1450 MeV, as shown in the figure 1 [8]. Feasibility of studying this reaction using WASA at COSY is briefly discussed in the next section.

2 Feasibility study

Out of the two decay modes of the Θ^+, the K^0p channel gives the best experimental conditions for being measured in the WASA detector, so we shall concentrate on this decay branch.

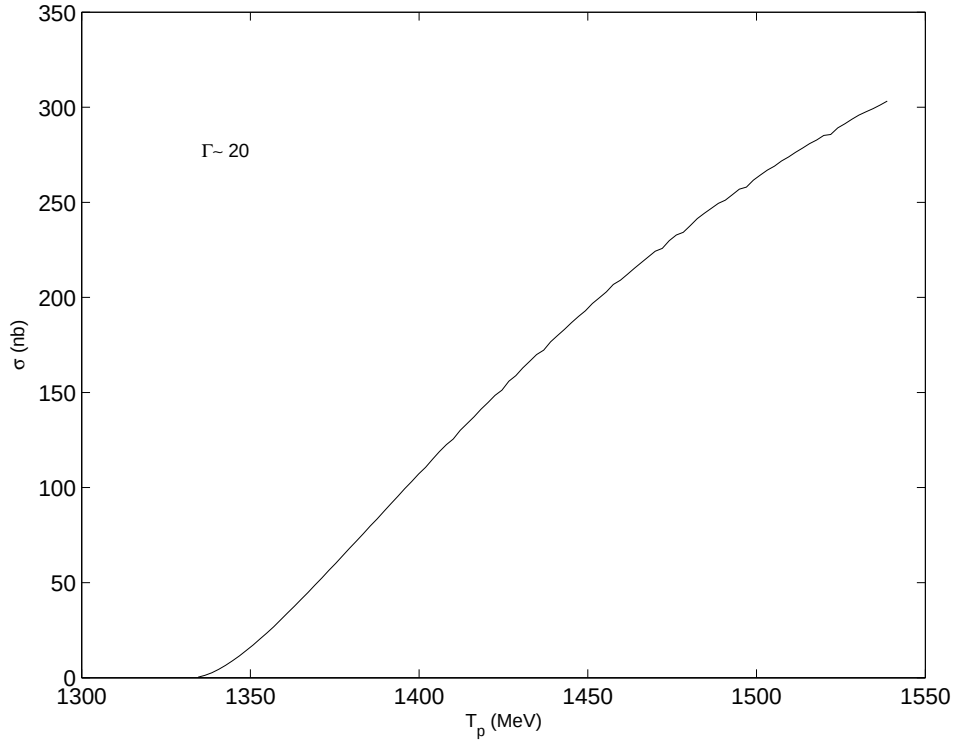

Figure 1: Cross section for the Θ^+ pentaquark production. The production amplitude has been calculated at threshold assuming J^P=1/2$^+$ and Γ=20 MeV. The energy dependence is from phase space.

For the Λ there are only two important decay modes, $p\pi^-$ and $n\pi^0$ with branching ratios of 63.9 % and 35.8 %, respectively. The choice of using the charged decay mode to identify the Λ is advantageous due to the following reasons:

- the energy resolution of the WASA for charged particles is generally better than for photons,
- the combination of the forward tracker and the MDC provides a clean identification of the Λ by reconstruction of its decay vertex,
- both decay products are measured,
- higher branching ratio.

Regarding the kaon decay, half of the events are lost due to K_L^0 having $c\tau$=15.5 m and thus escaping detection. For the K_S^0 two modes are important, $\pi^+\pi^-$ (BR = 68.6%) and $\pi^0\pi^0$ (BR = 31.4%). Selecting the charged mode has the advantage of higher rate. However, it leads to a final state with six charged particles. It might be difficult to distinguish between the π^- produced in the Λ decay and the K_S^0 decay, which could impair the reconstruction of the Λ. Therefore, the neutral decay mode will be used.

Putting all branching ratios together gives the overall branching ratio, or efficiency of detecting Θ^+ using this particular final state, of $0.5\times0.639\times0.314 = 0.1$.

This final state with four charged particles, π^- and three protons, and the four photons from $\pi^0\pi^0$ provides a well defined trigger as well as favorable analysis conditions.

A rough estimate of the WASA acceptance for the $pd \to p + \Lambda + \Theta^+ \to p + p\pi^- + p\gamma\gamma\gamma\gamma$ reaction has been obtained using phase space Monte Carlo simulation. The first things needed are the energies and angles of all charged final state particles. They are shown in the figure 2 below. The proton produced directly is denoted p while those produced in the decays of the Λ and Θ^+ are denoted p_Λ and p_Θ respectively. It is seen that the maximum energies for p and p_Λ are below 300 MeV, which is the highest energy deposited by protons in the FD. For such protons one may expect a very good energy resolution.

Assuming that reconstruction of the Λ requires the p_Λ proton to be detected in the FD ($2.5^0<\theta_{p\Lambda}<18^0$) and the π^- either in the FD or MDC ($22^0<\theta_\pi<158^0$) one finds that this requirement is fulfilled in $\sim$85% of cases. This is roughly the efficiency of the Λ reconstruction, eff_Λ. It should be noted that the resolution of the MDC is limited at the forward and backward angles due to a reduced number of wire planes being crossed by the particles. All 17 layers are crossed only for angles between 44^0 and 134^0. For the π^- going into the FD or into this limited angular range of the MDC, the eff_Λ is reduced to 55%.

The requirement that the proton p_Θ from Θ^+ enters the FD or the plastic barrel is fulfilled in $eff_{p\Theta}$=87% of cases.

Finally, the requirement of the four photons (from the K_S^0 decay into $\pi^0\pi^0$) to fall into the angular range of the electromagnetic calorimeter is fulfilled with an efficiency $eff_{4\gamma}$=62%. This gives the overall acceptance of $\sim$45% for eff_Λ=85% and 29% for eff_Λ=55%.

Remembering that the resolution of the WASA detector is far better for charged particles than for photons one would like the Θ^+ mass to be calculated as the missing mass to the reconstructed p, p_Λ and π^- (for π^- only

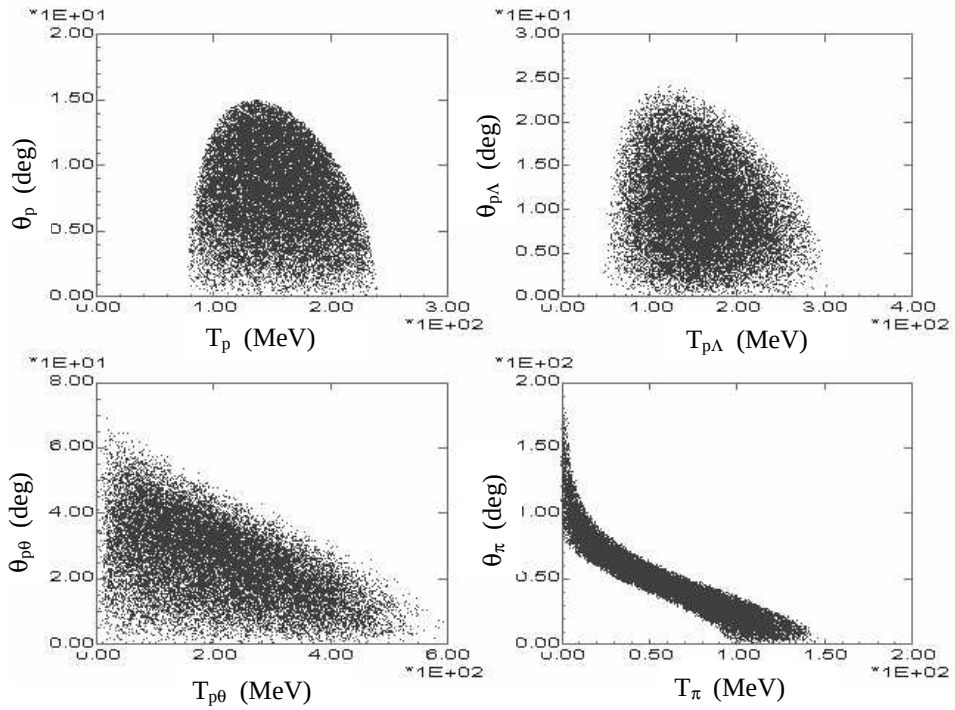

Figure 2: Energy and angular ranges of the four final state charged particles in the reaction $pd \to p + \Lambda + \Theta^+ \to p + p\pi^- + p\gamma\gamma\gamma\gamma$ at 1360 MeV proton beam energy.

angles will be used – see below). In such a case one has to take into account losses of protons due to nuclear interactions with the detector material, which is expected to reduce the acceptance by, roughly, a factor of two.

As already mentioned, the Θ^+ mass will be found as the missing mass calculated for the p and p_Λ reconstructed in the FD and π^- either in the FD or MDC. Measurement of the energy and angle of the p proton is straightforward since the reaction vertex is at the known target position. This is not the case for the p_Λ because of the Λ's $c\tau$=7.89 cm. In order to reconstruct the Λ momentum one has to find the Λ decay vertex using either the forward tracker, when both p_Λ and π^- enter the FD, or the forward tracker and the MDC. Reconstruction of the vertex requires finding two tracks which, together with the target point, are in the same plane. When two tracks fulfilling the above criteria are found, one can calculate the absolute value of the π^- momentum, k, from the condition:

$(\sqrt{m_\pi^2 + k^2} + E)^2 - (k\hat{u} + \vec{p})^2 = m_\Lambda^2$,

where E, $\vec{p}$ represent the proton total energy and momentum, $\hat{u}$ is the unit

vector representing direction of the presumed π^- and m_Λ is the Λ mass. One should verify that the reconstructed Λ-momentum points to the target area.

Further check is provided by the ΔE-E method when the pion enters the FD (see figure 3) and extracting the momentum from the measurement of the track curvature in the magnetic field, when the pion enters the MDC.

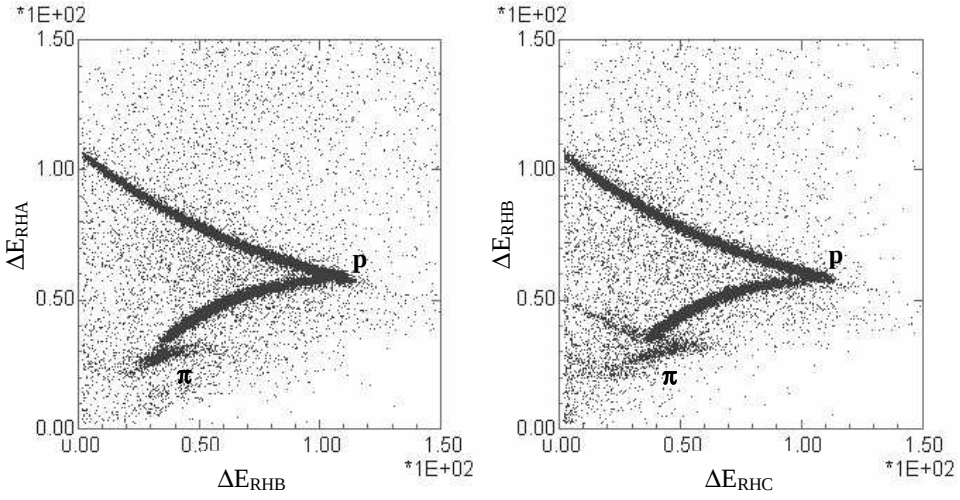

Figure 3: ΔE-E plots for three consecutive layers of the range hodoscope in the FD as obtained in the M-C simulation of the reaction $pd \to p + \Lambda + \Theta^+ \to p + p\pi^- + p\gamma\gamma\gamma\gamma$ at 1360 MeV proton beam energy.

At present the position resolution of the forward tracker amounts to $\sim$2 cm in x-y plane (perpendicular to the beam) [7] so one can estimate the resolution in angle to be of the order of $\arctan(2/140) \approx 1$ degree, where 140 is the distance between the target position and the FD tracker. For the proton p, the resolution in angle is given by the size of the beam-target overlap and accuracy of the FD tracker. For the π^-, which in most cases enters the MDC, one can expect the resolution in θ to be of the order of $\arctan(1/22) = 2.6$ degree.

A rough estimate of the resolution in M_{Θ^+} can be obtained by smearing the energies of the p, p_Λ and angles of the p, p_Λ and π^- with the experimental resolutions. Taking for the energy resolution 3%, and 1.0, and 3.0 degrees for the angular resolution for protons and π^- respectively, leads to the results shown in the figure 4 (solid line). The width of the peak at half maximum amounts to 4.5 MeV, which is nearly five times better than the resolution quoted in Ref. [1]. This is a valuable feature which could improve

our knowledge of the true width of the Θ^+ resonance expected to be much smaller than the 20 MeV measured in the experiments so far. The wide background seen in the figure corresponds to the phase space simulation of the non-resonant reaction $p + d \rightarrow p + \Lambda + K^0 + p$.

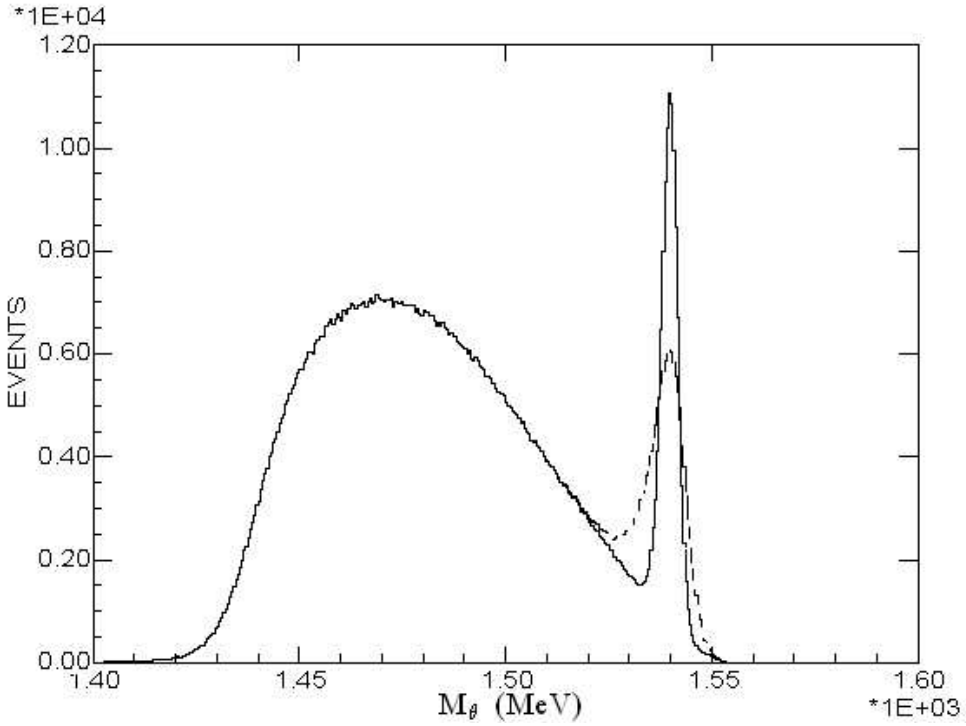

Figure 4: Phase space Monte Carlo simulation of the reaction $p + d \rightarrow p + \Lambda + \Theta^+$ at 1360 MeV beam energy. The Θ^+ peaks are seen on a wide background from non-resonant $p + d \rightarrow p + \Lambda + K^0 + p$ reaction, which has been assumed to be 10 stronger than the Θ^+ production. For both peaks the energy resolution for protons has been assumed to be equal to 3% and the π^- angular resolution to amount to 3 degrees. The narrower peak, fwhm=4.6 MeV, corresponds to the proton angular resolution of 1 degree and for the wider one the resolution of 3 degrees has been assumed. The fwhm obtained in this case amounts to 9.6 MeV.

For the Θ^+ cross section of 30 nb, the beam-target luminosity of $10^{31}/\mathrm{cm}^2\mathrm{s}$ and the acceptance of 1.5% (with the overall branching ratio of 10% included) one would expect the Θ^+ event rate of $30{\times}10^{-33}{\times}10^{31}{\times}0.015/\mathrm{s} = 0.0045/\mathrm{s}$ at the beam energy of 1360 MeV. Simulation shows that the detector acceptance depends rather weakly on the beam energy. Thus increasing the beam energy to 1450 MeV would increase the event rate by a factor of

$\sim$7 due to the change of the cross section [8]. With the duty factor of 50% obtaining 10^4 events would then take less than 200 hours.

References

[1] T. Nakano et al., Phys. Rev. Lett. **91** (2003) 012002.

[2] V. V. Barmin et al., hep-ex/0304040; S. Stepanyan et al., hep-ex/0307018; J. Barth et al., hep-ph/0307083; A. E. Aratayn, A. G. Dololenko and M. A. Kubantsev, hep-ex/0309042; V. Kubarovsky et al., hep-ex/0311046; A. Airapetian et al., hep-ex/0312044; A. Aleev et al., hep-ex/0401024; COSY-TOF Collaboration, hep-ex/0403011; P. A. Aslanyan et al., hep-ex/0403044; ZEUS Collaboration, hep-ex/0403051; S. V. Chekanov, hep-ex/0404007.

[3] Shi-Lin Zhu, hep-ph/0406204 and references therein.

[4] J. Barth et al., hep-ph/0307083; V. Kubarovsky et al.,hep-ex/0311046; A. Airapetian et al., hep-ex/0312044; S. V. Chekanov, hep-ex/0404007.

[5] J.Z. Bai et al., hep-ex/0402012; K. T. Knopfle et. al., hep-ex/0403020; C. Pinkenburg, nucl-ex/0404001.

[6] M. J. Longo, talk at 2004 International Conference on Quarks and Nuclear Physics, Indiana University, May 23, 2004.

[7] J. M. Dyring, Detailed Studies of the Reaction $pp \to pp\eta$ Using a Straw Chamber Tracking Device, PhD thesis, Uppsala University, 1997.

[8] G. Fäldt, private communication.

The puzzle of apparent narrowing of widths of meson[1] resonances produced at or near maximum momentum transfer

Bogdan C. Maglić
Serbian Academy of Sciences & Arts, Belgrade, Serbia Montenegro and HiEnergy Technologies, Inc.,1601 Alton Parkway Irvine, California 92606

Abstract: Measured widths, Γ, of the meson resonances produced deep inside hadron matter at maximum |t| values, $\sim$0.2 (GeV/c)^2 (impact parameter Δx=0.1f) appear narrower than their true values observed in peripheral production, Δx=1.2f, |t|<0.005 (GeV/c)^2. Velocity of the resonances in hadron matter is lower, v=βc/H (H= ad hoc hadron matter constant) and uncertainty in the transition time, Δt, greater than in peripheral production; this, coupled with ΔEΔt>$\hbar$, requires a lower ΔE=Γ. Experiments on Γ vs. |t| dependence would reveal physical constant, H, of hadron matter, which from the current observation is 10<H<100.

Ever since the discovery of ω^0 [1], a number of experimentalists have been reporting the observation that the widths, Γ, of the mesons produced at *very high* momentum transfer near the kinematic maximum, |t|$\geq$0.2 (GeV/c)^2, appear to be significantly narrower than the widths of the very same mesons when produced in the peripheral collisions, at |t|<0.005 (GeV/c)^2 [2]. The Γ values at near max-|t| were found to be in the 2-10 MeV range, compared to the 100-400 MeV observed in peripheral collisions and expected from the strong interaction coupling constant. No statistically significant experimental study of Γ vs. |t| dependence in between the two extreme |t| regions has been reported; since the meson production cross section is inversely proportional to |t| most of the data available have been either at the lowest |t| or at the max-|t| in a few experiments. To explain the effect, it was postulated that the true widths are narrow and become broader via the multiple scattering in the passage through hadron matter [2, 3, 4, 5, 6].

An alternate explanation is presented here. The true widths of the resonances are broad, as dictated by the strong interaction coupling constant and observed at low |t|. Narrow widths of the mesons produced at near

[1]Terms 'meson(s)' and 'meson resonances(s)' are synonymous and interchangeable in this paper.

max-$|t|$ are an *observational artifact*. It arises from their creation deep inside the hadron matter, at impact parameters $\Delta x << r_0$=1.2f, coupled with the fact that they are observable only if they reach the periphery, $\Delta x \geq r_0$, before decay. Referring to Fig. 1, the resonances that are both produced and decayed inside the hadron matter are unobservable (Case A), because in their transit through the hadron matter the momentum–energy correlation of the decay products cannot give the unique mass.

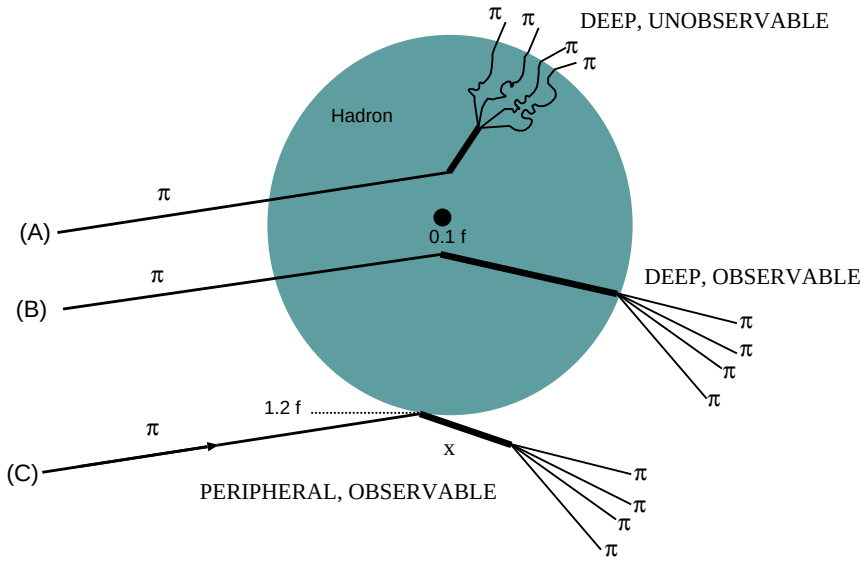

Figure 1: 3 cases of production of resonance X in $\pi N \rightarrow N + X$:
(A) Both produced and decays deep inside hadron matter, (t)$\leq$ 0.2.
(B) Produced deep but decays at the periphery and
(C) Both produced and decayed at periphery (t) $\leq$ 0.005

Only the fraction produced at $x << r_0$ that decayed <u>outside</u> the hadron, at $x > r_0$, will have the 4-momenta unperturbed and be observable as a particle (Case B). In contrast, all resonances that are produced and decayed at the periphery (vacuum), $|t| < 0.005$, are unperturbed and are observable (Case C). The true widths must exhibit an apparent narrowing at high $|t|$ because their velocity in the passage through hadronic matter is lower than when they are created at the periphery in vacuum. As a result, the time uncertainty, Δt, for it to be observed must be greater, which in turns, means that the observable $\Delta E = \Gamma$ must be narrower, according to the Uncertainty Principle.

Assuming that the peripherally produced meson moves in free space out-

side the hadron volume with velocity βc, where β of the meson is determined by the kinematics, we can write down:

$$\Delta E \Delta t = \frac{\Gamma \Delta x}{\beta c} \geq \hbar \tag{1}$$

where Δx is the collision impact parameter and $\hbar$=6.6x10^{-22}MeV s. For peripheral collisions, $\Delta x \geq r_0 \geq 1.2$ f, and $\beta \approx 1$, we expect Γ=ΔE $\geq$ $\beta c\hbar/r_0$ = 165MeV, which is in agreement with most observations (except for those that are narrower via the centrifugal barrier, e.g. ω).

What is the meson velocity in hadronic medium? In analogy with propagation of the light in macroscopic matter, to obtain the meson velocity in the hadron medium, the vacuum velocity should be divided by the product of 3 constants of the hadron matter: the dielectric constant, diamagnetic constant and a new unknown constant that characterizes propagation of charged hadrons through the hadron matter. Lets define the triple product by a non-dimensional parameter H, the ad hoc 'overall hadronic matter constant'. Meson velocity through the hadron matter becomes:

$$\beta c \rightarrow \frac{\beta c}{H} \tag{2}$$

By so replacing β in Eq.(1), we get ΔEΔt = Γ(ΔxH)/(βc)$\geq\hbar$, and with Δx= r_0, we get

$$\Gamma \geq \frac{\beta c \hbar}{H r_0} = \frac{165 MeV}{H} \tag{3}$$

For peripheral decay in vacuum r_0= 1.2f and H=1, and we get $\Gamma > 165$ MeV, as observed and expected. For H=10-50, we get 16> Γ >3MeV. Hence, Eq. (3) opens the way for determination of the overall hadronic matter constant, H, by measuring Γ vs. $|t|$. From the reportedly observed widths at max [t], Γ= 2-10 MeV, we obtain an order of magnitude limits to the ad hoc overall hadronic matter constant to be:

$$10 < H < 100. \tag{4}$$

We need Γ vs. $|t|$ experiments and a quantitative theoretical connection between the hadron matter constant, H, and the 3 physics parameters of the hadron matter as a function of $|t|$, the hadron constant and the diaelectric and diamagnetic constants.

The author would like to thank Yuval Ne'eman for his reading of an early version of this paper.

References

[1] B. C. Maglić, L. W. Alvarez, L. Stevenson, A. Rosenfeld,
Phys. Rev. Lett **1** (1961) 178.

[2] B. C. Maglić, *Contradictions about fine Structures in Meson Spectra and Proposed High-Resolution Hadron Spectrometer using "Interactive" Solid-State Hydrogen Target*, Hadron 2003: 10^{th} International Conference on Hadron Spectroscopy, AIP Conf. Proc. **No. 717** (2004) 37.

[3] M. Focacci et al., Phys. Rev. Lett. **17** (1967) 49.

[4] B. Levrat et al., Phys. Lett. **22** (1966) 714;
L. Dubal et al., Nucl. Phys. **B 3** (1967) 435.

[5] D. R. Bowen et al., Phys. Rev. Lett. **26** (1971) 1663.

[6] J. Seguinot et al., Phys. Lett. **19** (1966) 712. Now named π_2 (1670).

Polarized Proton and Deuteron Beams at COSY

H. Stockhorst for the COSY spin team
Institut für Kernphysik, Forschungszentrum Jülich, Germany

Abstract: Aim of this paper is to present a brief and basic introduction to polarized beams and the behaviour of a particle's spin in an electromagnetic field. It is not intended to give a complete presentation of the spin dynamic theory. Instead the most important features are given without proof and details not absolutely necessary are left out. Spin depolarizing mechanisms are discussed and the cures against depolarizing especially during acceleration as utilized at COSY are outlined. A list of references is given at the end to help the reader to find more deep details on spin dynamic theory [1].

1 Introduction

The particle spin is an important feature of nuclei and subnuclear particles. In general, the particle interactions depend to various degrees on their spin states. It is thus not surprising that the experimentalists demand on polarized beams at COSY [2] became important rather early. Polarized proton beams at COSY are now routinely delivered to internal and external experiments since 1996. The polarized beams from the ion source are pre-accelerated in the cyclotron JULIC [3], injected and accelerated in COSY without significant loss of polarization. Imperfection resonances are increased in strength by means of vertical orbit distortions, leading to a complete polarization reversal (spin flip). Intrinsic resonances are overcome by means of a fast ramping air core quadrupole magnet inducing a rapid change in tune and therefore preservation of the polarization (tune jump).

The polarization during acceleration is observed utilizing parts of the former EDDA [4] detector system as polarimeter. Only the fast online polarization measurements during the COSY acceleration cycle made possible by the EDDA setup allows an efficient correction of the up to 16 first order depolarizing resonances encountered.

Polarized deuterons were accelerated for the first time early in 2003 and are also now routinely available for internal and external experiments. Because of the lack of depolarizing resonances in the COSY energy range,

preservation of the polarization is less involved for deuterons as compared to protons. However, a polarization measurement technique for vector and tensor polarization has to be developed. Also in this case the EDDA detector turned out to be the most important and efficient tool to measure the polarization even in the accelerating ramp of COSY.

Polarized proton beams with intensities above 10^{10} stored protons with a degree of polarization of up to 0.80 are now routinely delivered to internal experiments [5, 6]. For external experiments polarized protons can be slowly extracted from COSY via stochastic extraction without loss of polarization by keeping the extraction momentum far enough away from depolarizing resonances and careful adjustment of the betatron tunes during the extraction process.

2 Polarization

2.1 Polarization of spin-1/2 particle beams

Along a quantization axis z the spin $\vec{S}$ of a proton can only be found in two eigenstates of $\vec{S_z}$ with eigenvalues of the spin component $S_z = +\hbar/2$ ("up" or "+" state) or $S_z = -\hbar/2$ ("down" or "-" state). The degree of polarization is defined as the ratio

$$P \;=\; \frac{N_+ - N_-}{N_+ + N_-}, \tag{1}$$

where $N_\pm$ are the number of particles in the two spin states "up" and "down". For a 100% polarized beam ($P = \pm 1$) the spin states of all particles are aligned along a polarization axis. In general three parameters are needed to specify the polarization of spin-1/2 particles. Two for the direction of the quantization axis and one for the ratio $\frac{N_+}{N_-}$. Thus the polarization of a spin-1/2 particle is a vector characterized by a direction and magnitude. This type of polarization is therefore called *vector polarization*. The polarization of a bunch of particles is found by an ensemble average.

2.2 Polarization of spin-1 particle beams

For a spin-1 system, e.g. deuterons, there are three spin states along a quantization axis as depicted in figure 1.

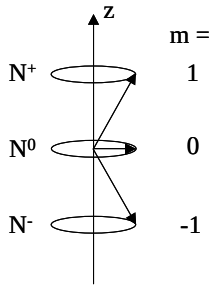

Figure 1: Spin states for a spin-1 particle.

Particles having their spin in a $m = 0$ state have zero vector polarization *but* they are still aligned, i.e. are polarized. Thus the polarization of spin-1 particles is characterized by vector polarization *and* an alignment. This is called *tensor polarization*. The vector polarization is given by the ratio

$$P_z = \frac{N_+ - N_-}{N_+ + N_0 + N_-}, \tag{2}$$

where N_+, N_0, N_- particles are aligned along the axis with $m = 1, 0, -1$ respectively. The tensor polarization is determined from

$$P_{zz} = \frac{N_+ + N_- - 2N_0}{N_+ + N_0 + N_-}, \tag{3}$$

with $-2 \leq P_{zz} \leq 1$.

There are several possibilities for vector and tensor polarization. If all states were equally populated the polarization would be zero. Some special polarization states are:

- maximum vector polarization $P_z = \pm 1$ with tensor polarization $P_{zz} = 1$
- pure vector polarization ($P_{zz} = 0$) with $P_z = \pm 2/3$
- pure tensor polarization with $P_{zz} = -2$ or 1 and $P_z = 0$
- $P_z = \pm 1/3$ with $P_{zz} = -1$

The polarized source of COSY is capable to deliver these states as required from the experiment.

The polarization of a particle $\vec{P}$ is the quantum average of the spin operator $\vec{S}$, $\vec{P} = \frac{2}{\hbar} < \psi|\vec{S}|\psi >$. According to the Ehrenfest theorem the evolution of the polarization vector (which is called $\vec{S}$ in the following) is governed by a classical equation of motion.

3 Spin Precession in an Electromagnetic Field

3.1 Non-relativistic particles

For non-relativistic non-radiating particles in a magnetic field $\vec{B}$ the spin motion in the particles' rest frame is governed by the equation

$$\frac{d\vec{S}}{dt} = \vec{\mu} \times \vec{B} \tag{4}$$

that gives the time change of the spin as the torque on the magnetic moment $\vec{\mu}$ exerted by the magnetic field. The magnetic moment $\vec{\mu}$ is associated to the spin by

$$\vec{\mu} = g\frac{e}{2m_0}\vec{S} \tag{5}$$

with the rest mass m_0 and the elementary charge e. The gyromagnetic ratio g is 2 for a point-like spin-1/2 particle. For real particles its deviation from 2 is expressed by the gyromagnetic anomaly $G = (g-2)/2$. For protons this value is $G = 1.79$ and for deuterons $G = -0.143$. If we insert the magnetic moment into eq. 4 the equation of motion of the spin vector is found

$$\frac{d\vec{S}}{dt} = \vec{S} \times \vec{\Omega}_L \tag{6}$$

around the direction of the rotation vector (angular velocity)

$$\vec{\Omega}_L = \frac{ge}{2m_0}\vec{B} \tag{7}$$

which is collinear to the magnetic field, see figure 2. The magnitude of the rotation vector gives the time rate of change $d\phi/dt$ of the angle ϕ covered by the spin projetion onto the plane perpendicular to the magnetic field,

$$\frac{d\phi}{dt} = |\vec{\Omega}_L|, \tag{8}$$

as shown in figure 2.

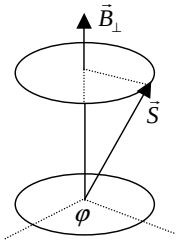

Figure 2: Precession of the spin vector around the magnetic field.

3.2 Relativistic particles

So far we considered a particle at rest. However in COSY particles are moving with a speed close to the velocity of light and also experience an acceleration when they are bent by the dipole magnets. It turns out that eq. 6 is then still valid albeit with a different rotation vector if the electromagnetic fields in the laboratory frame are properly Lorentz transformed into a co-ordinate system that moves with the particle around the ring (moving frame). If for simplicity the particles move in the horizontal plane they experience an acceleration that is perpendicular to the velocity and the vertical magnetic field (dipole fields of COSY). This is the reason of the Thomas precession which contributes an angular velocity in the moving frame. Thus the angular velocity $\vec{\Omega}$ in eq. 6 will contain two parts, one component results from the Lorentz transformation and the other one from the Thomas precession term. The correct form of eq. 6 for moving particle bears the name from $Thomas$, $Bargman$, $Michel$ and $Telegdi$ ($Thomas - BMT\ equation$) and is given by

$$\frac{d\vec{S}}{dt} = \vec{S} \times \vec{\Omega}_{BMT} \tag{9}$$

with the angular velocity vector

$$\vec{\Omega}_{BMT} = \frac{e}{m_0\gamma}[(1+\gamma G)\vec{B}_\perp + (1+G)\vec{B}_\parallel - (\gamma G + \frac{\gamma}{1+\gamma})\vec{\beta} \times \frac{\vec{E}}{c}] \tag{10}$$

in which the magnetic field $\vec{B}$ (see figure 3) in the laboratory frame has been decomposed into a componet $\vec{B}_\parallel$ parallel to the particle velocity $\vec{\beta} = \vec{v}/c$ and perpendicular to it, $\vec{B}_\perp$. The electric field is $\vec{E}$ and the kinematic factor is given by $\gamma = \frac{1}{\sqrt{1-\beta^2}}$.

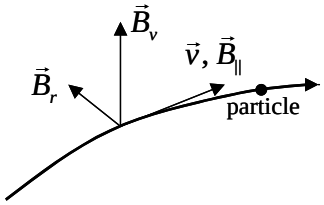

Figure 3: Decomposition of the magnetic field into a component parallel $\vec{B}_\parallel$ to the beam's velocity and orthogonal to it $\vec{B}_\perp$, in this case a radial and vertical component.

The spin precession has the following properties:

- An electric field **E** is equivalent to a magnetic field **B**=**E**/c. An electric field of $3 \cdot 10^8$V/m has the same strength as a magnetic field of 1 T. In general no such electric field is present. *In the following electric fields are therefore neglected.*

- Comparison of longitudinal ($\parallel$) and transverse ($\perp$) magnetic fields: According to eq. 8 and 10 the spin vector will rotate in longitudinal fields by $d\phi = \Omega_{BMT} dt$ in the time interval dt. Using $ds/dt = \beta c$ we see that the spin rotates by $d\phi = \Omega_{BMT} ds/(\beta c)$ while the particle moves the distance ds. Thus the total spin rotation in a longitudinal field is

$$\Delta\phi = \frac{e}{p}(1+G)\int B_\parallel ds, \tag{11}$$

  where we have used that the momentum of the particle is given by $p = m_0 \beta\gamma c$. Similarly, for transverse fields the spin rotation is determined from

$$\Delta\phi = \frac{e}{p}(1+\gamma G)\int B_\perp ds = \frac{e}{m_0\beta\gamma c}(1+\gamma G)\int B_\perp ds. \tag{12}$$

  The spin rotation by longitudinal fields becomes less effective at large momenta and the spin rotation by transverse fields becomes nearly independent of momentum ($\gamma G \ll 1$).

From eq. 11 and 12 we can directly calculate that

- to rotate the spin of 3.3 GeV/c protons around the *longitudinal* axis by an angle π a *longitudinal* field with 12.4 Tm is needed at COSY and for deuterons: 40.3 Tm (!!)

- to rotate the proton spin at 3.3 GeV/c in the *moving frame* by an angle π around the *vertical* axis one needs a vertical magnetic field with $\int B_\perp ds = \pi \frac{m_0 \beta c}{eG} = 5.3\ Tm$, and for deuterons $\approx$ 118 Tm.

Thus the deuterons spin is about 20 times harder to manipulate with magnetic fields. On the other hand their spin direction is less sensitive to field errors.

4 Spin Precession and Resonances in a Circular Particle Accelerator

We first consider an ideal accelerator or storage ring in which all components (dipoles quadrupoles etc.) lie in the horizontal plane. The particles will then also move in the horizontal plane on the ideal (circular) path guided by the vertical dipole fields. The particle frame rotates with angular velocity (cyclotron frequency)

$$\vec{\Omega}_C = \frac{e}{m_0\gamma}\vec{B}_\perp. \tag{13}$$

The spin will precess around the vertical axis and remains constant in the straight sections as long as the particle passes the quadrupoles on axis. The difference in frequency of spin and velocity precession, eq. 10 and eq. 13, yields

$$\vec{\Omega} = \vec{\Omega}_{BMT} - \vec{\Omega}_C = \gamma G\vec{\Omega}_C. \tag{14}$$

The *number of spin precession during one turn* in the ring follows from eq. 14 and is called *spin tune*

$$\nu = \gamma G. \tag{15}$$

From eq. 10 it is clear that the vertical spin component is preserved while the two other components rotate in the moving frame with the angular frequency given by eq. 14 around the vertical axis. As the particle completes one revolution, the coordinate system rotates by 2π and the spin has precessed around the vertical axis by $2\pi\gamma G$. As a result, in a ring where particles experience only vertical magnetic fields the only stable (or invariant) spin direction is along the vertical axis. The spin rotation around the vertical axis after one turn in the ring can be expressed by the matrix

$$\begin{pmatrix} \cos(2\pi\gamma G) & 0 & \sin(2\pi\gamma G) \\ 0 & 1 & 0 \\ -\sin(2\pi\gamma G) & 0 & \cos(2\pi\gamma G) \end{pmatrix} \tag{16}$$

Now consider that at one location in the ring there is a static *radial* magnetic field component (along the x-axis) as shown in figure 3. When the particle passes this disturbing magnetic field the spin is rotated around the

x-axis by an angle (given by eq. 12). The spin rotation around the x-axis due to the disturbing field is then given by the matrix

$$\begin{pmatrix} 1 & 0 & 0 \\ 0 & \cos\theta & \sin\theta \\ 0 & -\sin\theta & \cos\theta \end{pmatrix} \tag{17}$$

The total spin rotation matrix for one turn is then given by the product M of eq. 16 and eq. 17. The stable spin direction outside the disturbing field region can be found by determining the eigenvectors of M with eigenvalue 1, i.e. solving the equation $M\vec{u} = \vec{u}$. One finds that the vertical spin component is:

$$y = \frac{S_y}{\sqrt{1 + \tan^2(\theta/2)/\sin^2(\pi\gamma G)}}. \tag{18}$$

Clearly, $y = S_y$ if there is no disturbing field, i.e. $\theta = 0$. However polarization along the vertical axis is completely lost if the spin tune equals an integer, $\nu = \gamma G = k \in \mathbb{N}$. One can say that the spin motion is in *resonance* with the radial magnetic field: every time the particle passes the field the spin vector is bent more and more away from the vertical axis until polarization is lost. Resonances of this type are called *imperfection resonances* or *integer resonances*. They arise e.g. if magnets are slightly misaligned or if there are vertical orbit distortions. The particles then experience radial magnetic fields (e.g. from vertical focussing quadrupoles). Thus it is impossible to operate the accelerator with a polarized beam at energies where imperfection resonances occur. However they can be crossed with (almost) no polarization loss during acceleration as is discussed below.

The term "resonance" might become more clear in another view: Each time the particle passes the disturbing radial field the spin may point in a different direction with respect to the magnetic field if the spin tune is not an integer. One can think of a rotation of the radial magnetic field around the vertical axis with resonance frequency $\nu_R\Omega_C$. While the spin is rotating around the vertical axis with spin tune ν (not an integer) it rotates with frequency $\delta = (\nu - \nu_R)\Omega_C$ in the frame of the disturbing field as shown in figure 4. If the spin tune is not an integer these rotations are out of phase and the disturbing effect of the field averages out. No polarization loss occurs.

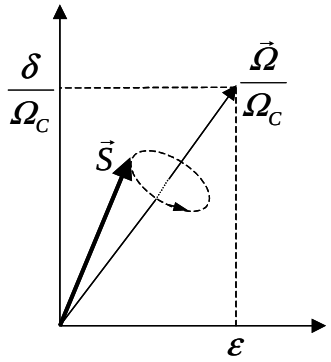

Figure 4: Explanation see text.

The radial component is according to eq. 10 given by

$$\vec{\Omega}_\perp = \frac{e}{m_0\gamma}(1+\gamma G)\vec{B}_\perp = \epsilon\vec{\Omega}_C, \tag{19}$$

where ϵ is proportional to the *resonance strength*. It is clear that the larger the field is the larger the resonance strength will be. Large vertical closed orbit errors enhances the imperfection resonance strength. The resonance strength can also be interpreted as the *width of the resonance* since in the tune interval $(\nu_R - \epsilon, \nu_R + \epsilon)$ the angle of $\vec{\Omega}$ with vertical axis is larger then 45 degrees. On top of the resonance, i.e. $\delta = 0$, as shown in figure 5, the spin rotates around the radial direction and on average the vertical component is zero and the vertical polarization is lost.

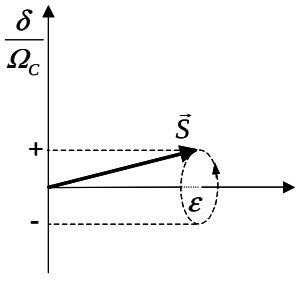

Figure 5: On resonance the vertical polarization is lost.

So far we assumed that the particles move, apart from the straight sections, on a circle in the horizontal plane. If the particles execute *horizontal*

betatron oscillations the spin rotation is no longer given by the rotation matrix eq. 16 since the path length during one turn of a particle now depends on the betatron amplitude and betatron tune Q_x. The spin precession is *modulated* by the betatron motion and the spin tune has two additional values which are in the case of COSY $\gamma G \pm (Q_x - 2)$. A *horizontal spin resonance* can occur if $\gamma G \pm (Q_x - 2)$ equals an integer. These resonance are not important (except when there is coupling between the horizontal and vertical betatron motion) at COSY with its vertically polarized beams since the horizontal betatron motion is driven by vertical magnetic fields of the quadrupoles (see eqs. 9 and 10). In addition to the horizontal betatron motion the particles also execute a vertical betatron motion with betatron tune Q_y induced by the radial magnetic fields of the vertical focussing quadrupoles. In this case eq. 17 is no longer valid since, besides a possible static radial magnetic field, the spin precession experiences, or is driven by a force that is evoked by the vertical betatron motion. Similarly, a resonance occurs if $\gamma G \pm (Q_y - 2)$ equals an integer. These resonances are named *vertical spin* resonances or more frequently, *intrinsic resonances*. Their strength is proportional to the square root of the vertical beam emittance (proportional to beam size). Resonances of this type are dangerous in COSY because they produce a severe polarization loss if they are not avoided or compensated. As in the case of imperfection resonances the spin resonances driven by the betatron motion are energy dependent but in addition depend also on the vertical tune of the machine. Among these resonances there are higher order resonances as well those that can be excited by the synchrotron motion of the particles as induced by an rf-cavity (bunched beam). These cases play however a minor role at COSY and will therefore not be discussed here. There are also resonances that can be excited by longitudinal magnetic fields (solenoids). For this type of resonance the reader is referred to the literature.

5 Resonance Crossing

Suppose we are away from a single resonance. Then $\delta = (\nu - \nu_R)\Omega_C \neq 0$. If the beam is accelerated linearly through the resonance one can write $\nu = \nu_R + \alpha\Theta$ for the linear variation of the tune with azimuth Θ. For the spin rotation frequency on resonance we have $\Omega_\perp = \epsilon\Omega_C$ which shows that the change in the spin rotation angle within the "time" $\Delta\Theta$ is $\Delta\phi = \epsilon\Delta\Theta$. Since the "time" needed to cross the resonance is $\Delta\Theta = 2\epsilon/\alpha$ the spin rotation angle changes by $\Delta\phi = 2\epsilon^2/\alpha$ during resonance crossing. Thus we

can distinguish two regimes:

- **Fast crossing** ($\Delta\phi \ll 1$) means either a small resonance strength or a large crossing speed. There is no time to bent away the spin $\vec{S}$ from the vertical and polarization is conserved.

- **Slow crossing** ($\Delta\phi \gg 1$) means either a large resonance strength or a slow crossing speed. The spin vector rotates much faster around the rotation vector $\vec{\Omega}$ than the latter moves. The spin vector $\vec{S}$ follows the motion of $\vec{\Omega}$ and is completely reversed. The polarization has changed its sign but there is no depolarization (*adiabatic spin flip*).

Between these two cases polarization may be completely lost. A quantitative estimate of the final vertical spin component S_y compared to the initial value before crossing the resonance is given by the Froissart-Stora formula

$$\frac{S_{y,initial}}{S_{y,final}} = 2e^{\frac{\pi\epsilon^2}{2\alpha}} - 1, \tag{20}$$

which includes the two cases of fast crossing, $S_{y,final} = +S_{y,initial}$, and adiabatic spin flip, $S_{y,final} = -S_{y,initial}$.

6 Polarized Proton and Deuteron Beams at COSY

6.1 Proton beams

At COSY vertically polarized proton beams are available in the momentum range up to 3650 MeV/c for *internal* and *external* experiments. At flat top about $1.0 \cdot 10^{10}$ protons with a polarization of more than 80% can be achieved. During acceleration to flat top energy up to sixteen depolarizing resonances have to be cured for polarized protons. The following graphics shows the imperfection and intrinsic resonances in the momentum range of COSY. In this figure the imperfection resonances appear as horizontal lines since they are independent of tune. The horizontal axis is the fractional vertical tune q_y (Q_y=*integer part* + q_y, for COSY the integer part always equals 3).

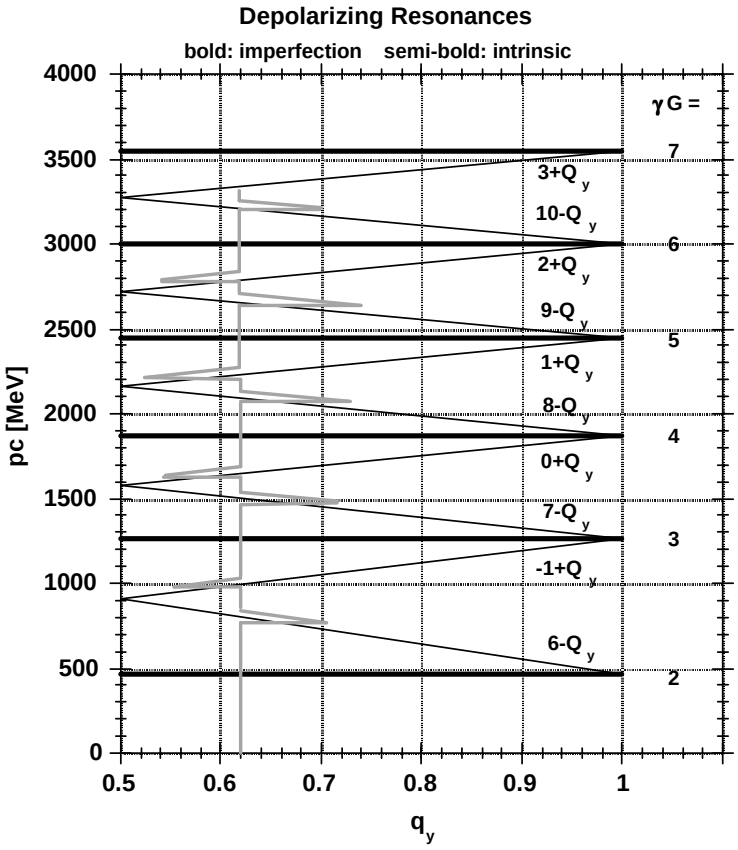

Figure 6: Depolarizing resonances during acceleration of protons in COSY as a function of the vertical fractional tune. Bold: imperfection resonances, semi-bold: intrinsic resonances. The shaded zigzag line at $q_y = 0.62$ symbolizes the change in working point (not in scale) during acceleration of the beam (tune jump).

There are six imperfection resonances. A loss of polarization at these resonances is avoided by artificially increasing the resonance strength, such that the polarization direction is completely reversed (adiabatic spin flip, slow crossing) when protons are accelerated across the resonance. A vertical correction dipole located at a position with a large vertical beta-function is used to increase the orbit distortion that enhances the resonance strength. One method to conserve polarization at up to ten intrinsic resonances is a rapid vertical tune change (fast crossing). For this a fast tune jump system consisting of one air coil quadrupole with a length of 0.6 m and a gradient of 0.43 T/m is installed in one arc of COSY. It allows a rapid tune change

of about 0.06 within 10 μs. Double crossing of resonances is avoided by a slow fall time of 40 ms. Polarization and particle losses due to an emittance increase can be kept low during acceleration if the beam position is carefully aligned in the acceleration ramp. In addition electron cooling at injection energy of COSY has been successfully applied to reduce the beam emittances in the transverse as well as in the longitudinal phase space. This increases not only the fast crossing (chapter 5) by reducing the resonance strength but also lowers beam losses visibile in figure 5 caused by the fast tune jumps. At injection the vertical tune is below 3.66. Therefore it is fixed close to 3.62 during acceleration in order to have enough time for consecutive tune jumps (figure 6). The dynamic tune measurement allows adjusting the tune during acceleration as well as the time and amplitude of the tune jumps. Figure 7 shows online measurements of the vertical steerer and fast quadrupole currents in comparison with the beam current (BCT). The beam is accelerated in 2.6 s from injection, 0.294 GeV/c, up to 3.1 GeV/c. Particle losses due to the steerer and fast quadrupole actions are less than 10%. Electron cooling was not applied in this case. In this example $4 \cdot 10^9$ polarized protons are accelerated to flat top.

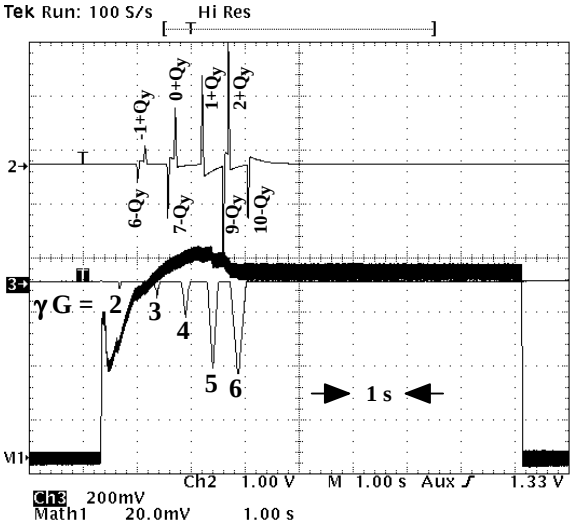

Figure 7: Trace M1 shows the beam current versus time measured with a beam current transformer (BCT). Trace 3 represents the current of the vertical steerer magnet that excites a total spin flip at the imperfection resonances. The current of the fast quadrupole is given by trace 2.

Figure 8 shows a polarization measurement versus momentum during acceleration to 3.3 GeV/c. The initial polarization is 80% and drops to 75% at flat top momentum. The loss of about 6 resonance.

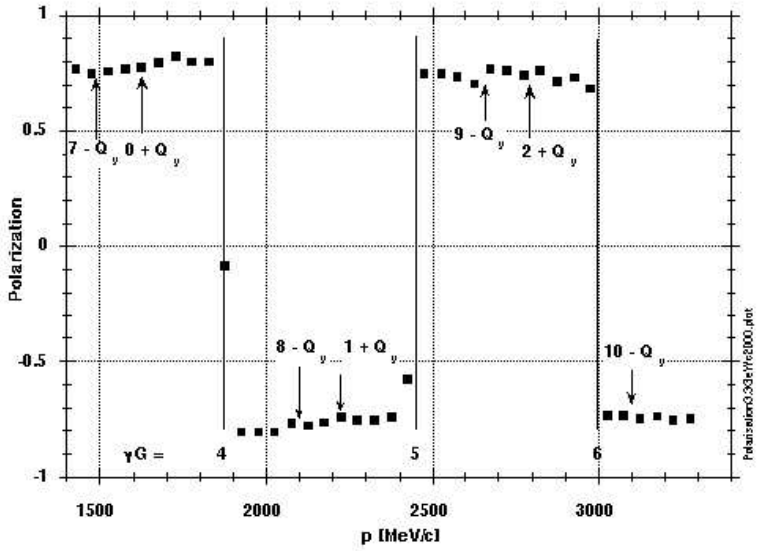

Figure 8: Online polarization measurement starting about 1.3 GeV/c. The arrows mark the intrinsic resonances which are compensated with almost no polarization loss by fast tune jumps. A total spin flip is created with a vertical steerer for the imperfection resonances.

On-line polarization measurements are carried out during acceleration with the high precision detector EDDA, designed to measure pp-scattering excitation functions during the acceleration of the COSY beam. This detector is a double layered scintillation hodoscope and in conjunction with a CH_2 or C fiber target well suited to function as a polarimeter. The great advantage of this online measurement is that the behavior of the polarization at every resonance is clearly visible in only a few ten minutes, depending on the desired measurement statistics.

6.2 Deuteron beams

As was pointed out in chapter 3.2 the deuterons spin is about 20 times harder to manipulate with magnetic fields. Due to the deuterons G factor the lowest imperfection resonance that can occur is $\gamma G = 7$ corresponding

to a momentum $p = 13$ GeV/c which is well above COSYs working range. Furthermore there are no intrinsic resonances at COSY in the normal tune range $3.5 < Q_y < 3.65$. Stochastic extraction to the experiment GEM [7] of a tensor and vector polarized deuteron beam at 2.4 GeV/c flat top momentum has been carried out successfully.

Acknowledgment

I would like to thank the organizers around P. Moskal to invite me for this talk. It was not only a great pleasure to participate in this well prepared and stimulating workshop but also I enjoyed the kind hospitality very much, at the workshop in the impressive premises of the Collegium Maius building and in the splendid neighborhood of Cracow.

References

[1] J. Buon, "*Polarization in Electron and Proton Beams*", CERN Accelerator School CERN 87-03, Vol. II, p. 647;
J. Buon and J.P. Koutchouk, "*Polarization in Electron and Proton Beams,*", CERN Accelerator School CERN 95-06, Vol. II, p. 879;
A.W. Chao, "*Polarization of a stored electron beam*", AIP Conference Proceedings No. 87, 1982, p. 395;
S.Y. Lee, "*Spin Dynamics and Snakes in Synchrotrons*", World Scientific Publishing 1997, ISBN 9810228058;
A. Lehrach, "*Erarbeitung und Umsetzung eines Konzepts zur Beschleunigung polarisierter Protonen im Khlersynchrotron COSY*", Berichte des Forschungszentrums Jülich 3501;
A. Lehrach et al., Nucl. Instr. and Meth. **A 439** (2000) 26;
H. Stockhorst et al., "*The Medium Energy Proton Synchrotron COSY*", 7^{th} European Particle Conference, EPAC2000, 26-30 June 2000, Vienna.

[2] R. Maier, Nucl. Instr. and Meth. **A 390** (1997) 1;
D. Prasuhn et al., Nucl. Instr. and Meth. **A 441** (2000) 167.

[3] H. Beuscher et al., "*The Characteristics of the cyclotron JULIC as injector for COSY*", Berlin 1989, Proceedings, Cyclotrons and their application (1989) 66.

[4] D. Albers et al., nucl-ex/0403045, submitted to EPJ;
M. Altmeier et al., Phys. Rev. Lett. **85** (2000) 1819.

[5] R. Czyżykiewicz et al., AIP. Conf. Proc. **717** (2004) 858;
e-Print Archive: nucl-ex/0312006.

[6] P. Winter et al., Phys. Lett. **B 544** (2002) 251;
erratum-ibid. **B 553** (2003) 339.

[7] M. Betigeri et al., Nucl. Instr. and Meth. **A 421** (1999) 447.

COSY-11 as a polarimeter

R. Czyżykiewicz
Institut für Kernphysik, Forschungszentrum Jülich, Germany
Institute of Physics, Jagellonian University, Kraków, Poland

Abstract: Good quality polarised beams at the cooler synchrotron COSY render precise measurements of the polarisation observables possible. Determination of this observables requires the accurate monitoring of the polarisation degree. For this purpose, when measuring the spin observables at the COSY-11 setup, up to now internal facilities like EDDA or COSY polarimeter have been used. In this paper the feasibility of using the COSY-11 detection setup as the polarimeter is discussed and different techniques to determine the polarisation degree are pointed out.

1 Introduction

With the improvement of the quality of the polarised proton beams [1] at the COSY accelerator [2], polarisation experiments started to be performed at the COSY-11 facility [3]. In January '01 first measurement ever of the proton analysing power for the $\vec{p}p \to pp\eta$ reaction have been performed at the excess energy of Q=40 MeV [4]. Since within the next two years the degree of proton beam polarisation had significantly increased from 50% up to 75%, two new measurements of the analysing power had been performed at the excess energies of Q=10 MeV and Q=37 MeV, corresponding to the proton beam momenta p_{beam} = 2010 MeV/c and 2085 MeV/c, respectively. These measurements aim at the determination of the production mechanism of the η meson. So far there are two models of the η meson creation close to the reaction threshold [5, 6] that predict completely different behaviour of the analysing power in that region. Since the models contradict with regard to the excitation mechanism of the S_{11} resonance, a precise determination of the analysing power may point up the way the S_{11} is created and also may bring up more information on its nature. Angular dependence of the analysing power may be helpful in distiguishing contributions from different partial waves responsible for the η meson production in the close–to–threshold region [5].

For the February '05 it is planned to measure the analysing power of the $\vec{p}p \rightarrow pK^+\Lambda$ reaction in the close to threshold region, in order to have a better access to the hyperon-nucleon scattering length [7].

A precise monitoring of the beam polarisation is a crucial point of the analysing power's determination for all mentioned reactions. For the COSY-11's experiments the polarisation monitoring is possible utilizing its own standard detection setup [3] in combination with a so called luminosity monitoring system [8, 9] described in section 3.1. In the past in order to prove the correctness of the utilized method in parallel to the COSY-11 operation the polarisation of the beam was measured also by the EDDA detection setup [10, 11] or by the COSY polarimeter [12]. The comparison of the obtained results will be presented in the subsequent sections.

2 Determination of the averaged degree of polarisation

For the experiment with a vertically polarised proton beam (polarisation along the y axis) we have the following formula for the analysing power determination:

$$A_y = \frac{\epsilon}{P}, \tag{1}$$

where

$$\epsilon = \frac{N_L - N_R}{N_L + N_R} \tag{2}$$

is the left-right assymetry and P is the beam polarisation ($\vec{P} = [0, P, 0]$). The error of the analysing power scales with the $\frac{1}{P^2}$. Therefore, in order to achieve the good acuracy of a measurement, a high degree of polarisation is desirable.

Since COSY-11 is one arm detector, in order to make possible the registration of events scattered to the left and to the right side with respect to the polarisation plane, in the neighbouring cycles the spin of the proton beam had been flipped. The fact that subsequent cycles had inversed polarisation decreased possible systematical uncertainities due to the variation of the target densities. The duration of the cycle was equal to 300 s which is significantly less than the time scale (10 hours) for the substantial changes of the density of the target. The areal target density has no direct influence on the differential distributions observed for the elastically scattered protons, yet due to the energy losses of the beam and nonvanishing dispersion at the

target place it causes variations of the beam characteristics and hence alters the distribution of the reaction points [13].

In the horizontal plane, perpendicular to the plane containing the polarisation vector, the elastically scattered events were registered by means of the detection subsystem presented in figure 1.a, consisting of a scintillator S1 made of 16 modules and a stack of granulated silicon detectors Si_{mon} [1].

Figure 1.b depicts the relation between the centre-of-mass scattering angles and the position in the S1 detector for the $pp \rightarrow pp$ reaction at the beam momentum of $p_{beam} = 2010$ MeV/c. The scattering angles for which both protons may still be measured in coincidence by S1 and Si_{mon} ranges from around 35 to circa 80 degrees. However, the practical partition of the CM scattering angles that may be used for the polarisation evaluation is squeezed to the range (37÷49) degrees. This is due to the strong dependence of the cross section upon the scattering CM angle and also due to the worsening of the momentum determination for protons passing the dipole only on its edge.

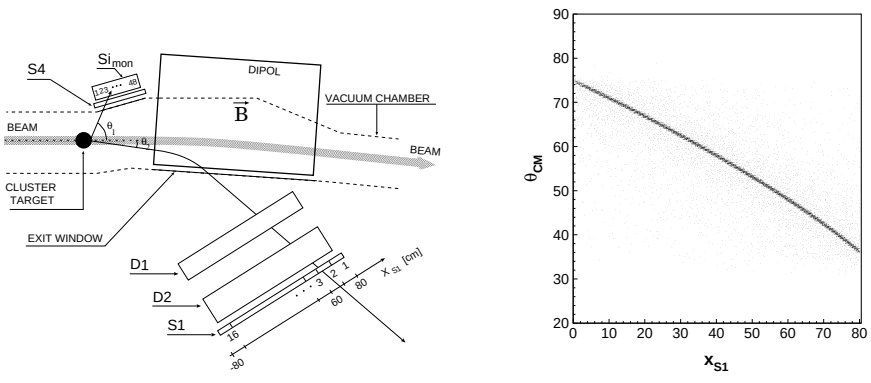

(a) (b)

Figure 1: (a) Schematic view of the COSY-11 detection setup. Only detectors used for the measurement of the proton-proton elastic scattering are shown. Figure is adopted from [14]. (b) Relation between the centre of mass scattering angle and the position in the S1 detector for the $pp \rightarrow pp$ elastic scattering at $p_{beam} = 2010$ MeV/c.

[1] For a detailed description of elastic event analysis the reader is referred to [13, 14].

This range was divided into three sections of 4 degrees width: (37÷41), (41÷45) and (45÷49) degrees. The analysing powers for these ranges have been chosen as the mean values of the $pp \to pp$ analysing powers measured at $p_{beam} = 1995$ MeV/c and $p_{beam} = 2025$ MeV/c by the EDDA collaboration [10] at the corresponding centre-of-mass angles (figure 2). The obtained mean values are given in table 2.

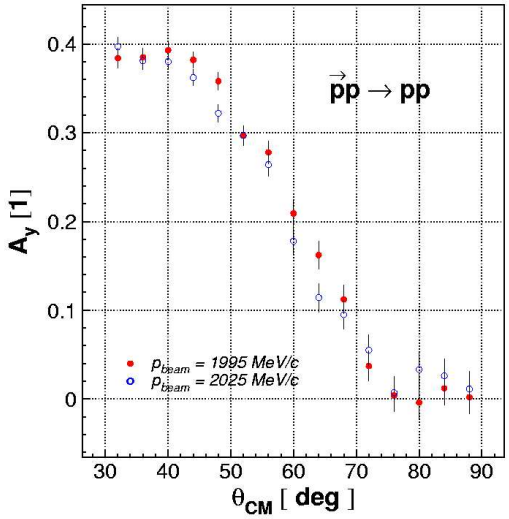

Figure 2: Analysing powers for the $pp \to pp$ elastic scattering as measured by the EDDA collaboration at the beam momenta of $p_{beam} = 1995$ MeV/c and $p_{beam} = 2025$ MeV/c. In the COSY-11 experiment the beam momentum was equal to $p_{beam} = 2010$ MeV/c, which is the middle of the range of beam momenta presented in this figure.

i	θ_{CM} range [deg]	A_y
1	(37÷41)	0.385 ± 0.013
2	(41÷45)	0.376 ± 0.013
3	(45÷49)	0.348 ± 0.013

Table 1: Analysing power values for the corresponding ranges of the CM scattering angle.

The number of scatterings to the right (N_R) and to the left side (N_L) with respect to the polarisation plane have been determined for the periods of 20 cycles, corresponding to circa 1.5 h of measurement. Within this time there might have occured slight change of the luminosity, which was roughly taken into account by normalizing N_R and N_L to the number of coincidences between small scintillators installed in the plane that contained the polarisation vector: N_0^{up} (during the spin "up" cycle) and N_0^{dn} (while spin "down"). Thus, we used the following formula to calculate the polarisation degree:

$$|P| = \sum_{i=1}^{3} P_i, \tag{3}$$

where

$$P_i = \frac{1}{A_{y,i}} \frac{N_{R,i}/N_0^{up} - N_{L,i}/N_0^{dn}}{N_{R,i}/N_0^{up} + N_{L,i}/N_0^{dn}} \tag{4}$$

are the three polarisations calculated for the three θ_{CM} ranges mentioned in table 2. In order to determine N_0^{up} and N_0^{dn} the luminosity system [8, 9] depicted in figure 3 had been used.

For the description and the working principle of this detection subsystem the reader is referred to section 3.1. Here we will only mention that for N_0^{up} and N_0^{dn} determination we had chosen the number of coincidences of a following type:

$$(SC_1 \wedge SC_2) \vee (SC_3 \wedge SC_4), \tag{5}$$

where the individual scintillators are labeled in figure 3.b. One should mention that this method needs to be improved, since the coincidence 5 apart from $pp \rightarrow pp$ reaction may also originate from other reactions, like for instance $pp \rightarrow np\pi^+$ or $pp \rightarrow pp\pi^0$ [2].

[2]The contribution from $pp \rightarrow d\pi^+$, which is the only two-body reaction other then elastic proton-proton scattering is negligible, since the total cross section for this reaction is about 100 times smaller at $p_{beam} = 2010$ MeV/c than the one for elastic scattering.

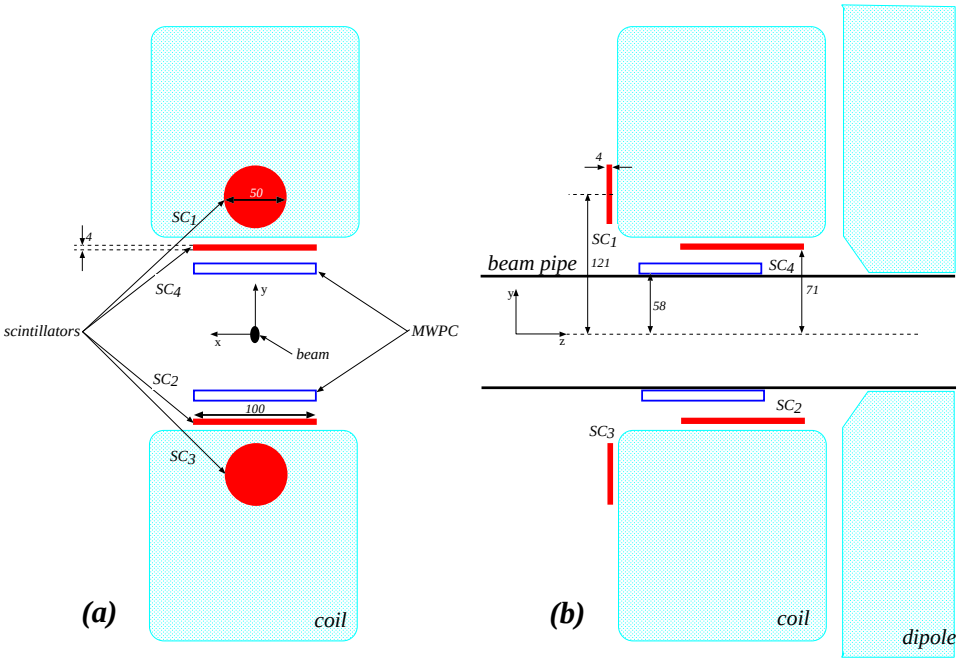

Figure 3: Schematic view of the detection subsystem for registration of the elastically scattered events in the polarisation plane as mounted at the COSY-11 facility. (a) Front view. (b) Side view. Beam is circulating along the z-axis and target is along the y axis.

At the present stage, we assumed that the coincidence rate is proportional to the rate of the $pp \rightarrow pp$ reactions. The exact analysis with the identification of the elastically scattered events will be done in the further data evaluation, after improvement of the identification of the $pp \rightarrow pp$ reaction in the polarisation plane. Problems regarding the latter are sketched in section 3.2.

In figure 4 the full circles are the COSY-11 results on the polarisation degree, determined by means of the method described in this section. The gap in the third day of measurement is caused by the lack of data in that period, which was due to the techinical problems during the beamtime. COSY-11 polarisation values are compared with the results of the COSY spin team [15] (open circles) as measured with an internal COSY polarimeter [12]. In the latter the similar method to determine the polarisation had been used, however the data were averaged over 4 cycles only (2 cycles with spin "up" and 2 with spin "down") [3].

[3] Achievement of the sufficient statistics within the 4 cycles was possible by using the

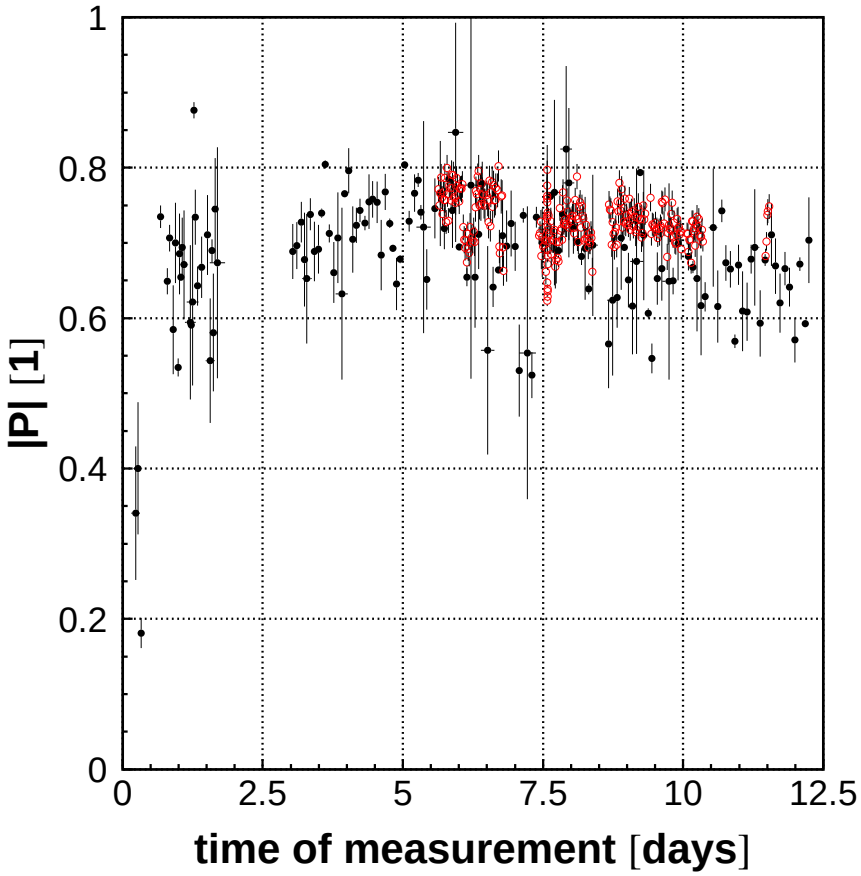

Figure 4: Polarisation degree versus the time of the measurement as obtained during the COSY-11 experiment with polarized beam in April 2003. Open circles denote results obtained by means of the COSY polarimeter [15] and full points were determined using a simplified analysis of the data from the COSY-11 setup.

In the first order the results obtained by the COSY-11 setup and Hamburger polarimeter are in good agrrement except the discrepancy in the ninth day of the measurement. Therefore, the determination of the polarisation by means of the COSY-11 polarimeter needs to be improved in order to achieve the better differential agreement of both stacks of data. The improvement of the technique is in the progress. It must be stated however, that this

CH_2 fiber target and a two-arm polarimeter

preliminary estimation was done only to check roughly a correctness of the method and therefore the results are still burdened by the assumption that the ratio between the coincidence rate of the scintillators in the polarisation plane and the rate of the $pp \rightarrow pp$ reaction was unaltered during the whole measurement period. The results are also biased by the implicit assumption made in equation 3 that the polarisation degree was the same for both spin projections. The final analysis will be performed without these two suppositions.

3 Determination of the absolute value of polarisation

Since the incident beam consisted of vertically polarised protons – which means that we deal with spin 1/2 particles and the polarisation vector has the form $\vec{P} = [0, \mathbb{P}, 0]$ – the differential cross section for an elastic scattering into the scattering angles θ and ϕ can be written as:

$$\frac{d\sigma}{d\Omega}(\theta, \phi) = \frac{d\sigma_0}{d\Omega}(\theta, \frac{\pi}{2})(1 + \mathbb{P}A_y(\theta)cos(\phi)). \tag{6}$$

In the above equation θ is a polar angle of scattered proton, ϕ is an angle which defines the orientation of the reaction plane, namely it is an angle between the polarisation vector and the vector perpendicular to the plane in which the final state protons are emerging. Therefore, $\frac{d\sigma_0}{d\Omega}(\theta, \frac{\pi}{2})$ corresponds to the differential cross section for an elastic scattering into the plane which contains the polarisation vector, which is consistent with the differential cross section for the elastic scattering of unpolarised protons. Analysing power functions – $A_y(\theta)$ – for the elastic proton-proton scattering have been measured by the EDDA collaboration [10] and are accessible within a wide range of energies. The differential cross sections of equation 6 can be written in terms of the number of events $\Delta N(\theta, \phi)$ registered in the small solid angle $\Delta\Omega(\theta, \phi)$ oriented in the direction given by the angles θ and ϕ:

$$\frac{d\sigma}{d\Omega}(\theta, \phi) = \frac{\Delta N(\theta, \phi)}{\Delta\Omega(\theta, \phi)E(\theta, \phi)L}, \tag{7}$$

where L is the luminosity integrated over the time of the measurement and $E(\theta, \phi)$ is the efficiency for detecting and reconstructing the elastically scattered events into that solid angle. Similarily for the other cross section we have:

$$\frac{d\sigma_0}{d\Omega}(\theta, \frac{\pi}{2}) = \frac{\Delta N_0(\theta, \frac{\pi}{2})}{\Delta\Omega_0(\theta, \frac{\pi}{2})E_0(\theta, \frac{\pi}{2})L}, \tag{8}$$

where $\Delta\Omega_0(\theta, \frac{\pi}{2})$ may be different from the corresponding value in equation 7. Assuming that the efficiencies $E(\theta, \phi) = 1 = E_0(\theta, \frac{\pi}{2})$, which at COSY-11 holds for the considered range of angles Θ, and putting equations 7 and 8 into equation 6 we obtain the following formula for proton beam's polarisation calculated from the solid angle around the angle θ:

$$\mathbb{P} = \frac{[\Delta N(\theta, \phi)/\Delta N_0(\theta, \frac{\pi}{2})][\Delta\Omega_0(\theta, \frac{\pi}{2})/\Delta\Omega(\theta, \phi)] - 1}{A_y(\theta) cos(\phi)}. \tag{9}$$

The important feature of this method of polarisation determination is that we are able to obtain the absolute values of polarisation for both "up" and "down" orientations of the vector of polarisation, which is desirable for minimizing the systematical error in the analysing power calculation. The only values that remain to be determined from experiment are the sizes of the solid angles $\Delta\Omega(\theta, \phi)$ and $\Delta\Omega_0(\theta, \frac{\pi}{2})$ and the numbers of event scattered in the horizontal ($\Delta N(\theta, \phi)$) and vertical plane ($\Delta N_0(\theta, \frac{\pi}{2})$). Elastically scattered events in the horizontal plane will be identified by means of the detection subsystem presented in figure 1.a, and in the vertical plane by the subsystem shown in figure 3. The latter will be described in the subsequent section.

3.1 Luminosity monitoring system

In order to register the elastically scattered events in the vertical plane, the COSY-11 facility has been extended with the luminosity monitoring system [8, 9] schematically presented in figure 3. The system consists of two round plastic scintillators of a diameter of 50 mm and the width of 4 mm mounted vertically on a dipol's coil as depicted in figure 3, two flat scintillators of dimensions $100 \times 100 \times 4\text{mm}^3$ placed horizontally, in the plane perpendicular to the polarisation plane, and two multi wire proportional chambers (MWPC) [8, 16]. The chambers consist of three planes of wires: an anode plane, made out of 36 parallel wires lying in a distance of 3 mm and two cathode planes, containing 72 wires. The distance between the cathode wires is 1.5 mm. All planes are separated by 6 mm space. All the wires were made out of gold-plated tungsten. The thickness of the cathode wires is 0.05 mm, whereas the anode plane wires thickness is 0.02 mm. Signals were read out from the cathode planes only. For a better position determination in the x-z plane, the wires in one cathode plane were oriented perpendicularly to the wires in the other plane. Delay between the neighbouring wires of

the cathode planes, was equal to 5 ns [4], resulting in the total delay of the line equal to 360 ns. The gas mixture filling the volume of the MWPC used in the experiment was Argon (50%) and C_2H_6 (50%).

3.2 Position determination in the MWPC chambers

Let's consider one of the cathode planes of the chamber. We will refer to that plane as to the plane "1". Suppose that the charged particle on its way trough the chamber created an avalanche of cations which subsequently induce signals in a cluster of wires, as the one between x_1 and x_2 position in figure 5.

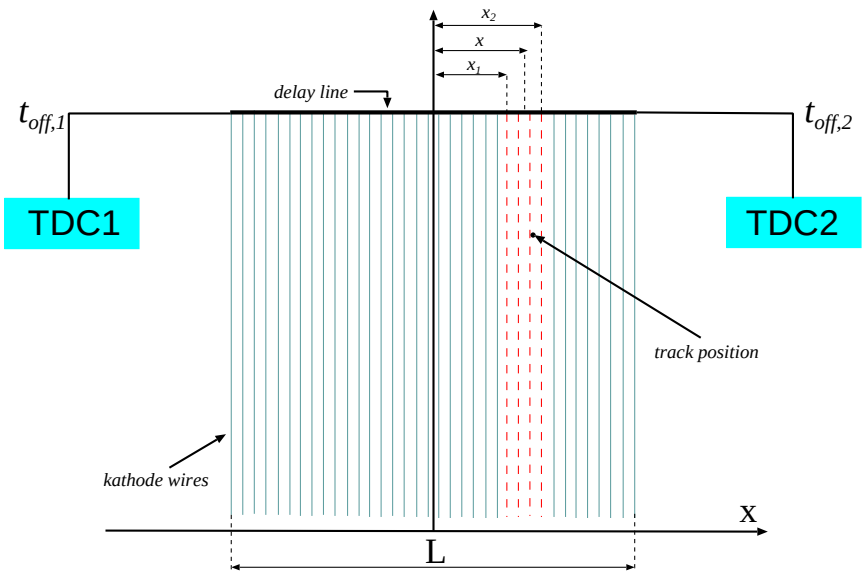

Figure 5: Principle of position determination in the cathode plane of the chamber. Meaning of symbols is explained in the text.

Let's denote the distance between the "left" edge of the cluster and the centre of the chamber by x_1 and the distance between the "right" edge of the

[4]Since the cells of the delay line contain the non-linear electronic elements, the delay of each cell is a function of the magnetic field in which the chamber is positioned. Due to the vicinity of the dipole, the magnetic field inside a chamber is not negligible. However, in the experiment we measured signals from the MWPC only in the period of time when the magnetic field was constant [18].

cluster to the centre of the chamber by x_2 as shown in figure 5. Naturally, we are not able to judge which wire out of those that fired is the one lying in the closest distance to the trajectory of particle. Therefore, the best assumption that one can make is that the centre of the cluster defines the line that lies closest to the particle track. In our case, the distance between that line and the centre of the chamber is equal to:

$$x = \frac{x_1 + x_2}{2}. \tag{10}$$

In the ideal case, if only one wire fired we would have: $x_1 = x_2 = x$. In what follows we will search for the x position. Signals from the wires that fired are emerging in both directions through the delay line towards the TDC1 and TDC2. However, the signal that will set the TDC1 value is the one originating from the wire on the left edge of the cluster, since this signal will reach the TDC1 earlier than the signal from the right edge of the cluster. Similarily, the signal which will define the TDC2 value is the one from the right edge of the cluster of wires that fired. We notice from figure 5 that the time registered in TDC1 is equal to:

$$t_1 = \frac{L/2 + x_1}{v_{sig}} + t_{off,1} - t_{real}, \tag{11}$$

where L is the length of delay line, v_{sig} is the velocity of the signal in the delay line, $t_{off,1}$ is the total time offset of the signal between the left end of the delay line and TDC1 unit, and t_{real} is the time when the avalanche was created. Similarily for the time registered by TDC2 we may write:

$$t_2 = \frac{L/2 - x_2}{v_{sig}} + t_{off,2} - t_{real}. \tag{12}$$

Therefore, dividing by 2 the equations 11 and 12, and by substracting them we obtain:

$$x = \frac{x_1 + x_2}{2} = A(t_1 - t_2) + B, \tag{13}$$

where A and B are the constants that need to be determined from the data. These parameters may be established from the distribution of events on the x-axis, which should be limited to the dimension of the active area of the chamber and be centered in zero according to the notation of equations 11 and 12. $A = v_{sig}/2$ is responsible for scaling of the picture of hit position in plane "1" whereas $B = (t_{off,1} - t_{off,2})\ v_{sig}/2$ is responsible for the shift in the x-direction of the position of the picture.

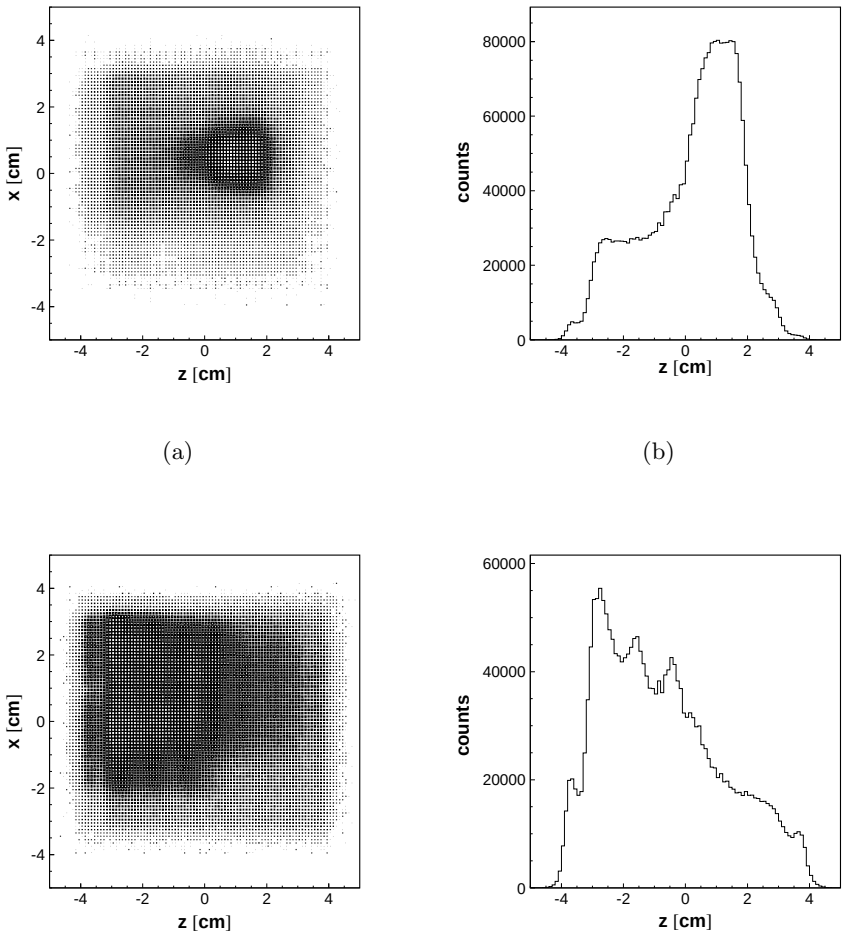

Figure 6: (a) Distribution of events in the upper chamber of the COSY-11 luminosity system as registered during the measurement of the $\vec{p}p \to pp\eta$ reaction at $p_{beam} = 2085$ MeV/c. The position x in the direction perpendicular to the beam is drawn versus the position z along the beam direction. x and z correspond to those from figure 3. (b) Projection of previous data onto a z axis. Panels (c) and (d) correspond to (a) and (b) but here position in the lower chamber is sketched.

In figure 6 the distributions of the events in the upper and lower chambers of the COSY-11 luminosity detection subsystem are presented. One

can see that while in the case of the upper chamber data tend to be gathered in a small part of the chamber, it's not the case of the lower chamber, where the data are spread over the wide part of the detection volume. The enhancement seen in figure 6.a we would like to assign to the elastic scattering events which due to the two body kinematics of the $pp \to pp$ reaction should reflect the shape of the SC1 scintillator used for the triggering. Yet, first of all we need to understand a significant difference between spectra observed in upper and lower detector.

In order to explain that effect, the luminosity system have been implemented into the simulation program, based on GEANT code. Results of the Monte-Carlo calculations are presented in figure 7, where the differential distribution of the elastic $pp \to pp$ scattering [17], as well as the analysing powers [10] have been taken into account. Also the background from the $pp \to np\pi^+$, $pp \to pp\pi^0$ and $pp \to d\pi^+$ reactions have been added. Background from the multi-pion production have been omitted, due to the significantly lower cross section.

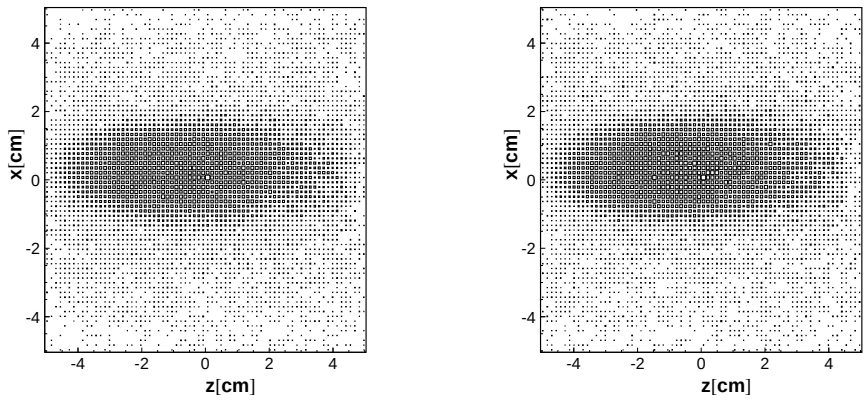

(a) (b)

Figure 7: Monte-Carlo calculations of the respond of COSY-11 luminosity system. Pictures (a) and (b) correspond to the figures (a) and (c) of figure 6. The interaction point was set in the simulations to be at the position [0,0,0] as shown in figure 3.

Distribution of events as obtained in Monte-Carlo simulation is different

than the one from experiment. Explanation of that effect requires further studies. At the present stage of understanding one can explain a shift of the experimental events towards the higher x values as originating in the shift of the beam along the x direction (figure 8).

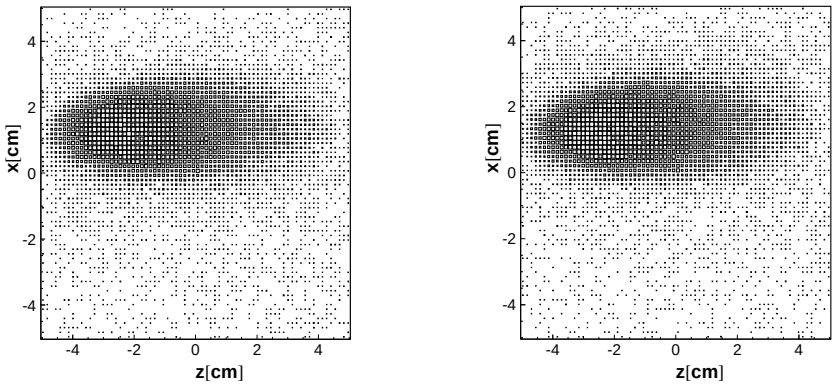

(a) (b)

Figure 8: As figure 7, but only $pp \to pp$ distribution is shown and the interaction point is shifted to the position [7.5;0;0] mm. The coordinates are introduced in figure 3.

One can notice from figure 6 that the distribution of elastically scattered events in the lower chamber is wider than the distribution in the upper one. This effect is due to the shift of the beam position in the y direction towards the higher values of y. This shifting causes for the upper chamber the decreasing of the surface of area of intersection of the chamber plane and the solid angle that the elastically scattered events are emerging. Similarily for the lower chamber the surface of this area will increase. The Monte-Carlo distribution of events is shown in figure 9 for the case when the interaction point was shifted to the position [7.5;7.5;0] mm.

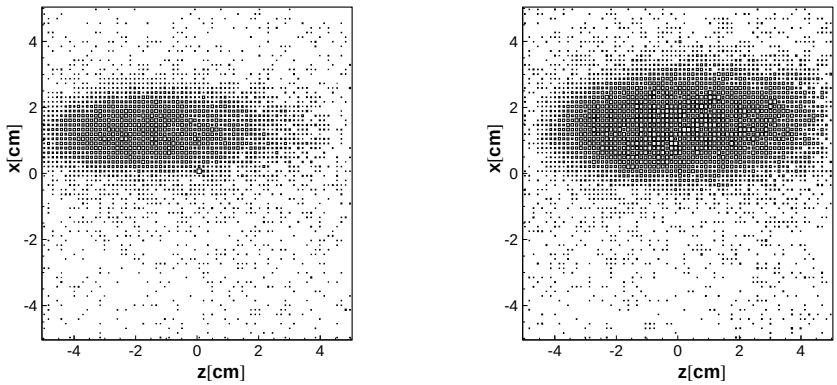

(a) (b)

Figure 9: As figure 8, but the interaction point is shifted to the position [7.5;7.5;0] mm.

Further investigation of the COSY-11 luminosity system is required and when ready it will allow to perform the accurate determination of the absolute polarisation values. The presented examples of simulations indicate the sensitivity of the shape of the observed patterns to the relative settings of the target and the detectors. In figure 9 we observe that shifting a beam towards one of the detector makes that the form of the spectrum in upper chamber differes significantly from the spectrum determined by the lower detector. We still need to check how the target dimensions, beam geometrical emittance and also the relative beam-target adjustment are related to the form of the studied spectra. The analysis is in progress.

Acknowledgments

I am enormously grateful to dr Paweł Moskal – my colleague and supervisor – for lots of valuable ideas concerning the polarisation determination which were described in this paper and also for giving me posibility to participate in this extremely interesting meeting.

References

[1] H. Stockhorst, contribution to this proceedings.

[2] R. Maier, Nucl. Instr. and Meth. **A 390** (1997) 1;
D. Prasuhn et al., Instr. and Meth. **A 441** (2000) 167.

[3] S. Brauksiepe et al., Nucl. Instr. and Meth. **A 376** (1996) 397.

[4] P. Winter et al., Phys. Lett. **B 544** (2002) 251;
erratum-ibid. **B 553** (2003) 339.

[5] K. Nakayama et al., Phys. Rev. **C 68** (2003) 045201.

[6] G. Fäldt, C. Wilkin, Phys. Scripta **64** (2001) 427.

[7] D. Grzonka and T. Rożek, COSY Proposal #143 (2004).

[8] I.-A. Pellmann, Diploma Thesis (1999), Berichte des FZ-Jülich, Jül-3686.

[9] P. Kowina et al., contribution to the Annual Report of IKP (2001) 14, Berichte des FZ-Jülich, Jül-3978.

[10] M. Altmeier el al., Phys. Rev. Lett. **85** (2000) 1819.

[11] K. Ulbrich, Bonn University, private communication (2003).

[12] F. Bauer and K. Büsser, Nucl. Instr. and Meth. **A 431** (1999) 385.

[13] P. Moskal et al., Nucl. Instr. and Meth. **A 466** (2001) 448.

[14] P. Moskal, PhD Thesis (1999), Berichte des FZ-Jülich, Jül-3685.

[15] B. Lorentz, FZ-Jülich, private communication (2003).

[16] A. Manarin and G. Vismara, "*The Delay Wire Chamber Description*", LEP/BI-TA/Note 85-3 (1985).

[17] D. Albers et al., nucl-ex/0403045, accepted for publication in Eur. Phys. J. **A**.

[18] T. Sefzick, FZ-Jülich, private communication (2004).

Spin-observables in meson production in nucleon-nucleon collisions

P. N. Deepak[a], G. Ramachandran[b] and C. Hanhart[a]
[a] *Institut für Kernphysik, Forschungszentrum Jülich, D-52425 Jülich, Germany*
[b] *Indian Institute of Astrophysics, Bangalore-560 034, India*

Abstract: In the first part of the report, we define channel-spin cross sections for $NN \to NNx$, x being any meson with spin s_x, at the *double differential level itself.* Numerical values for these cross sections for the reaction $\vec{p}\vec{p} \to pp\pi^\circ$ near threshold are also provided, using the IUCF data of Meyer et al. In the second part, we show how one can extract the values for the partial-wave amplitudes for the reaction $\vec{p}\vec{p} \to pp\pi^\circ$, near threshold, using the IUCF data of Meyer et al.

1 Introduction

Spin-observables have always played a crucial rule in our understanding of the hadronic interactions by allowing for a selective test of the theoretical models. In this context, it is of interest to note that an analysis of the total cross section into its singlet and triplet components were attempted in several $\vec{p}\vec{p} \to pp\pi^0$ measurements [1] using the theoretical results of Bilenky and Ryndin [2]. Since the reaction involves only a few lowest-order partial-waves in the final state at threshold, which in turn limit the initial partial-waves through parity and total angular momentum conservation, these observables filter out particular aspects of the reaction. It is perhaps also interesting to note here that the measurements of the channel-spin cross sections for the reaction $\vec{p}\vec{p} \to \Sigma^+\Theta^+$ were suggested [3] to unambiguously determine the parity of the Θ^+. We now present here a model-independent partitioning of the cross section for reactions of the type $\vec{N}\vec{N} \to NNx$ (x being a meson with spin s_x) at the *double differential level* itself and show how one can extract their values for the case of $\vec{p}\vec{p} \to pp\pi^0$, using the data of Meyer et al. [4]. These results have been published [5].

In the later part of the report we also discuss how one can extract the partial-wave amplitudes themselves for the reaction $\vec{p}\vec{p} \to pp\pi^0$, near threshold, using the data of Meyer et al. [4]. The preliminary results obtained will be presented.

2 Channel-spin differential cross sections

If $\overrightarrow{p_i}$, $\overrightarrow{p}$ denote respectively the relative momenta, in c. m., of the two nucleons in the initial and final states, $\overrightarrow{q}$ the c. m. momentum of the meson and ϵ the relative kinetic energy of the two nucleons in the final state, the kinematically-complete unpolarized differential cross section can be written in terms of the on-energy-shell T matrix as

$$\frac{\mathrm{d}\sigma_0}{\mathrm{d}\Omega_p \mathrm{d}\Omega_q \mathrm{d}\epsilon} = \frac{1}{4}\mathrm{Tr}\left(\boldsymbol{T}\boldsymbol{T}^\dagger\right). \tag{1}$$

Introducing now a complete set

$$\sum_{s_i=0,1}\sum_{\mu_i=-s_i}^{s_i} |s_i\mu_i\rangle\langle s_i\mu_i| = 1$$

of (initial) channel-spin states between $\boldsymbol{T}$ and $\boldsymbol{T}^\dagger$ in (1), we obtain

$$\frac{\mathrm{d}\sigma}{\mathrm{d}\Omega_p \mathrm{d}\Omega_q \mathrm{d}\epsilon} = \frac{1}{4}\sum_{s_i=0,1}\sum_{\mu_i=-s_i}^{s_i} \frac{^{2s_i+1}\mathrm{d}\sigma_{\mu_i}}{\mathrm{d}\Omega_p \mathrm{d}\Omega_q \mathrm{d}\epsilon}, \tag{2}$$

where

$$\frac{^{2s_i+1}\mathrm{d}\sigma_{\mu_i}}{\mathrm{d}\Omega_p \mathrm{d}\Omega_q \mathrm{d}\epsilon} \equiv \mathrm{Tr}\left(\boldsymbol{T}|s_i\mu_i\rangle\langle s_i\mu_i|\boldsymbol{T}^\dagger\right) \tag{3}$$

are the kinematiacally-complete *channel-spin differential cross sections*, which project out the contribution of the initial channel-spins to the unpolarized differential cross section. To proceed further, we expand the channel-spin projection operators $|s_i\mu_i\rangle\langle s_i\mu_i|$ in terms of the Pauli spin matrices $\overrightarrow{\boldsymbol{\sigma}}_1$, $\overrightarrow{\boldsymbol{\sigma}}_2$ of the two nucleons, using explicit matrix representations for the spinors and the Pauli matrices as[1]

$$|00\rangle\langle 00| = \frac{1}{4}\left(1 - \overrightarrow{\boldsymbol{\sigma}_1}\cdot\overrightarrow{\boldsymbol{\sigma}_2}\right), \tag{4a}$$

$$|1\pm 1\rangle\langle 1\pm 1| = \frac{1}{4}\left(1 \pm \boldsymbol{\sigma}_{1z} \pm \boldsymbol{\sigma}_{2z} + \boldsymbol{\sigma}_{1z}\boldsymbol{\sigma}_{2z}\right), \tag{4b}$$

$$|10\rangle\langle 10| = \frac{1}{4}\left(1 + \boldsymbol{\sigma}_{1x}\boldsymbol{\sigma}_{2x} + \boldsymbol{\sigma}_{1y}\boldsymbol{\sigma}_{2y} - \boldsymbol{\sigma}_{1z}\boldsymbol{\sigma}_{2z}\right). \tag{4c}$$

[1]It may be noted that channel-spin projection operators for reactions involving higher spins, say, $\vec{p}\,\vec{d}$ collisions, can be expressed in a very elegant way in terms of the individual spin operators, by employing irreducible tensorial techniques [6].

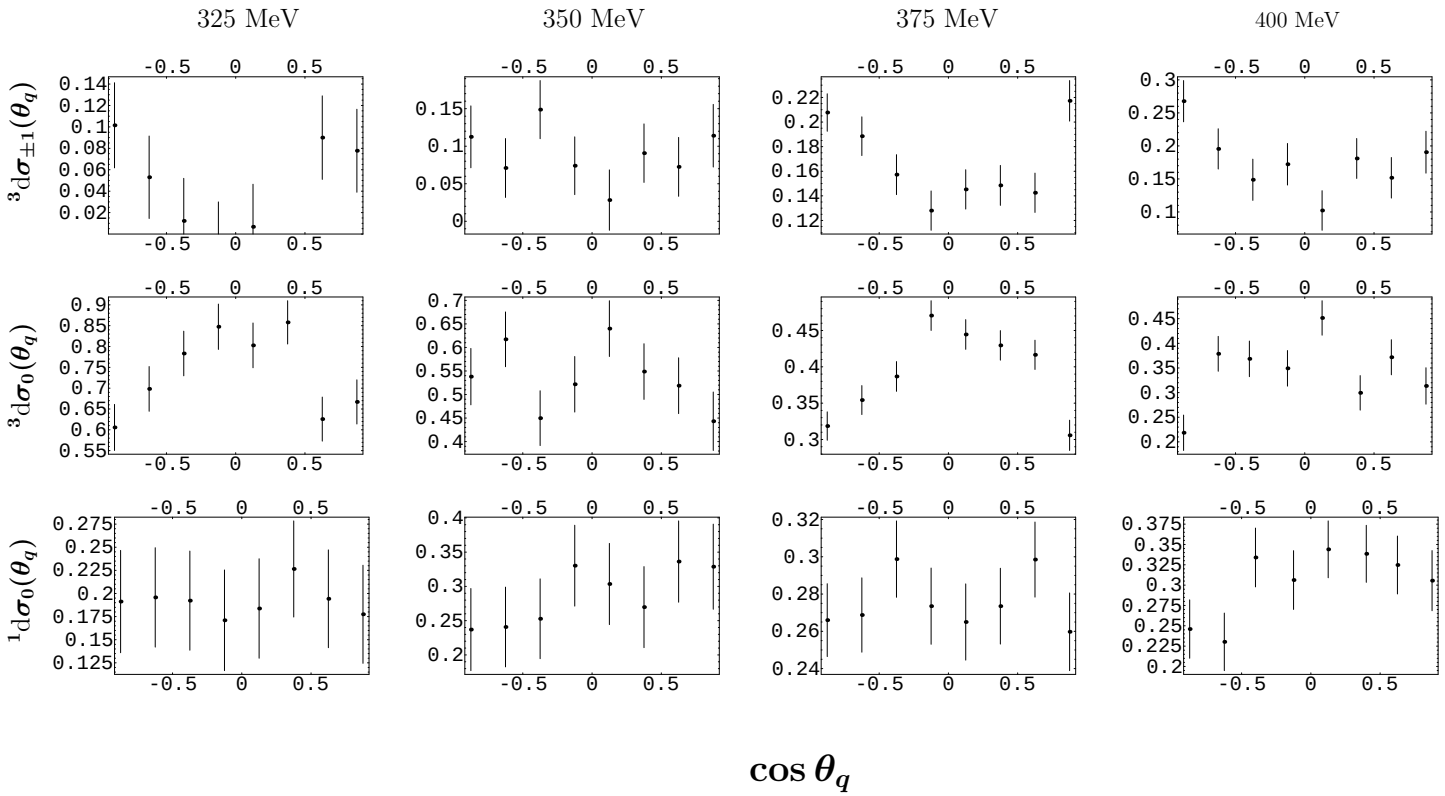

Figure 1: Estimates for $^{2s_i+1}\mathrm{d}\sigma_{\mu_i}(\theta_q)$ as functions of $\cos\theta_q$, based on the results of Meyer et al. [4].

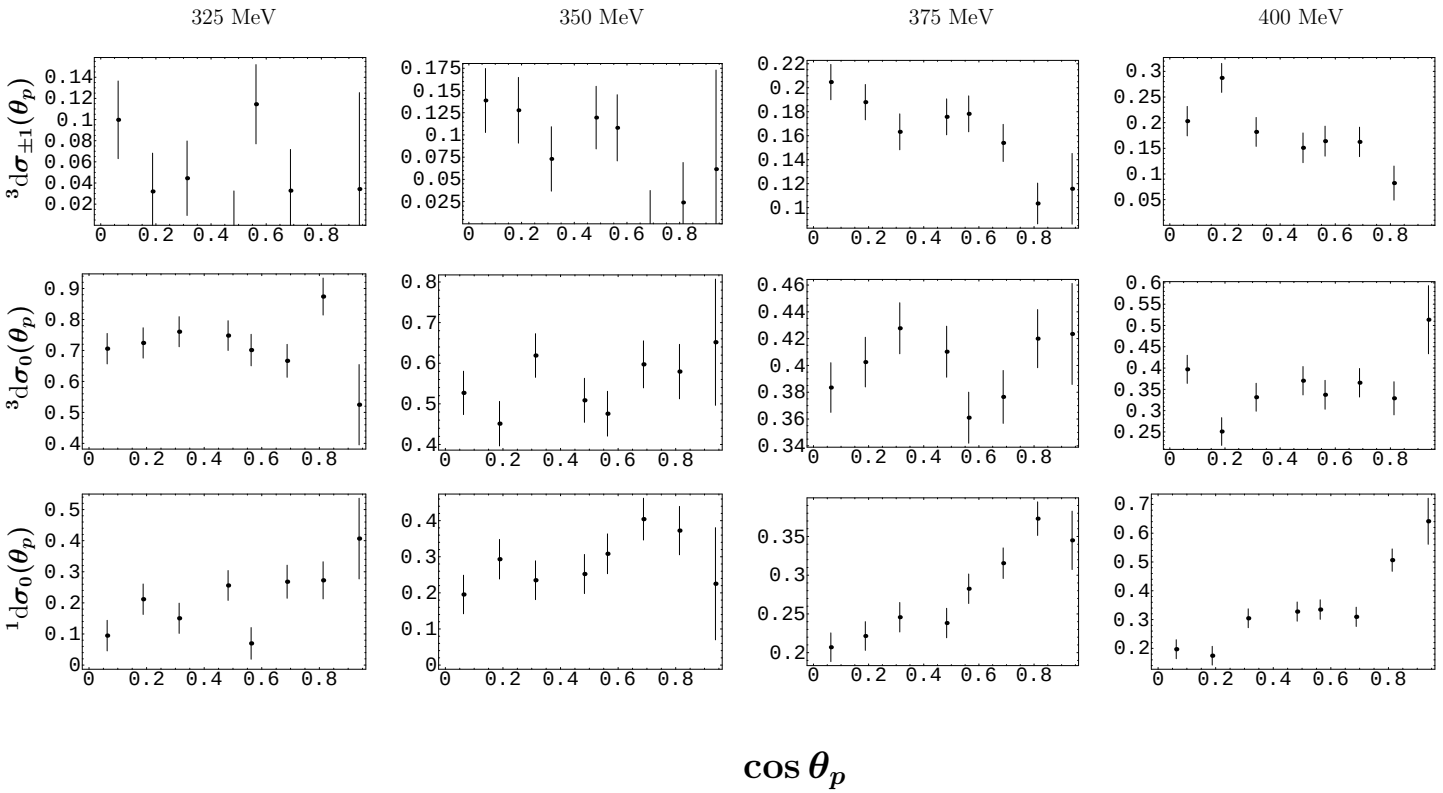

Figure 2: Estimates for $^{2s_i+1}d\sigma_{\mu_i}(\theta_p)$ as functions of $\cos\theta_p$, based on the results of Meyer et al. [4].

Adding eqs. (4b), (4c), we recover the well known triplet projection operator

$$\sum_{\mu_i=-1}^{1} |1\mu_i\rangle\langle 1\mu_i| = \frac{1}{4}\left(3 + \overrightarrow{\boldsymbol{\sigma}_1}\cdot\overrightarrow{\boldsymbol{\sigma}_2}\right). \tag{5}$$

To relate the channel-spin cross sections to the experimentally measured spin-observables, we note that the analyzing powers and the spin-correlations are defined through

$$\frac{\mathrm{d}\sigma_0}{\mathrm{d}\Omega_p\mathrm{d}\Omega_q\mathrm{d}\epsilon}\,A_{ij} \equiv \mathrm{Tr}\Big(\boldsymbol{T}\boldsymbol{\sigma}_{1i}\boldsymbol{\sigma}_{2j}\boldsymbol{T}^{\dagger}\Big), \quad i,j = 0,x,y,z \tag{6}$$

with $\boldsymbol{\sigma}_{10} = 1$; $\boldsymbol{\sigma}_{20} = 1$ and thus by using eqs. (3), (4) we obtain

$$\frac{{}^3\mathrm{d}\sigma_{\pm1}}{\mathrm{d}\Omega_p\mathrm{d}\Omega_q\mathrm{d}\epsilon} = \frac{\mathrm{d}\sigma_0}{\mathrm{d}\Omega_p\mathrm{d}\Omega_q\mathrm{d}\epsilon}\left(1 \pm A_{z0} \pm A_{0z} + A_{zz}\right), \tag{7a}$$

$$\frac{{}^3\mathrm{d}\sigma_0}{\mathrm{d}\Omega_p\mathrm{d}\Omega_q\mathrm{d}\epsilon} = \frac{\mathrm{d}\sigma_0}{\mathrm{d}\Omega_p\mathrm{d}\Omega_q\mathrm{d}\epsilon}\left(1 + A_{xx} + A_{yy} - A_{zz}\right), \tag{7b}$$

$$\frac{{}^1\mathrm{d}\sigma_0}{\mathrm{d}\Omega_p\mathrm{d}\Omega_q\mathrm{d}\epsilon} = \frac{\mathrm{d}\sigma_0}{\mathrm{d}\Omega_p\mathrm{d}\Omega_q\mathrm{d}\epsilon}\left(1 - A_{xx} - A_{yy} - A_{zz}\right). \tag{7c}$$

In order to estimate the channel-spin cross sections for the reaction $\vec{p}\vec{p} \to pp\pi^\circ$, using the data of Meyer et al. [4], we define the one-dimensional channel-spin cross sections

$${}^{2s_i+1}\mathrm{d}\sigma_{\mu_i}(\theta_p/\theta_q) \equiv \frac{\int \frac{{}^{2s_i+1}\mathrm{d}\sigma_{\mu_i}}{\mathrm{d}\Omega_p\mathrm{d}\Omega_q\mathrm{d}\epsilon}\,\mathrm{d}\Omega_{q/p}\mathrm{d}\varphi_{p/q}\mathrm{d}\epsilon}{\int \frac{\mathrm{d}\sigma_0}{\mathrm{d}\Omega_p\mathrm{d}\Omega_q\mathrm{d}\epsilon}\mathrm{d}\Omega_{q/p}\mathrm{d}\varphi_{p/q}\mathrm{d}\epsilon} \tag{8}$$

and we plot the same in figure 1 and figure 2.

3 Extraction of partial-wave amplitudes for $\vec{p}\vec{p} \to pp\pi^\circ$ from the IUCF data

Ignoring the participation of any D-waves in the final state, as in [4], a set of 12 partial-wave amplitudes participate in the reaction, given explicitly, following the notations of Meyer et al. [4], by

Type	$^{2s_i+1}l_J \to {}^{2s_f+1}l_{pj}, l_q$
Ss	$^3P_0 \to {}^1S_0, s$
Ps	$^1S_0 \to {}^3P_0, s$
	$^1D_2 \to {}^3P_2, s$
Pp	$^3P_0 \to {}^3P_1, p$
	$^3P_2 \to {}^3P_1, p$
	$^3P_2 \to {}^3P_2, p$
	$^3F_2 \to {}^3P_1, p$
	$^3F_2 \to {}^3P_2, p$
	$^3P_1 \to {}^3P_0, p$
	$^3P_1 \to {}^3P_1, p$
	$^3P_1 \to {}^3P_2, p$
	$^3F_3 \to {}^3P_2, p$

Since an overall phase is not determinable, we may choose the amplitude $^1S_0 \to {}^3P_0, s$ to be real. If we ignore the participation of D-waves in the final state, Ss does not mix with any of the other amplitudes in either the analyzing power or spin-correlations. This leaves 22 real numbers to be determined. To this end, we specifically make use of the values of the coefficients (which are sums of bilinears in the partial-wave amplitudes) given in table IV of Meyer et al. [4]. Since these coefficients have been integrated over ϵ, we parametrize the integrated partial-wave amplitudes as:

$$\int_0^{\epsilon_{\max}} T_i(\epsilon)\, T_j^*(\epsilon)\, q(\epsilon)\, p(\epsilon)\, \mathrm{d}\epsilon = z_i\, z_j^*\, \eta^x \quad i,j = 2,\ldots,12, \tag{9}$$

where T_i is the i^{th} partial-wave amplitude in the table above, z_i, z_j are the energy-independent complex quantites to be determined from the data and $\eta = q_{\max}/m_\pi$, $q_{\max}$ being the largest possible value of pion momentum for a given incident energy and m_π is the pion mass. In (9) we use the non-relatavistic phase-space volume, proportional to $q(\epsilon)\, p(\epsilon)\, \mathrm{d}\epsilon$. This parametrization is based on the assumption that near threshold when q, p are small, all the ϵ-dependence of the amplitudes comes from the radial part of the wave functions which is proportional to $q^{l_q} p^{l_p}$. Thus it can be shown that x in (9) is respectively equal to 6,7 and 8 for $PsPs$, $PsPp$ and $PpPp$ interfering terms.

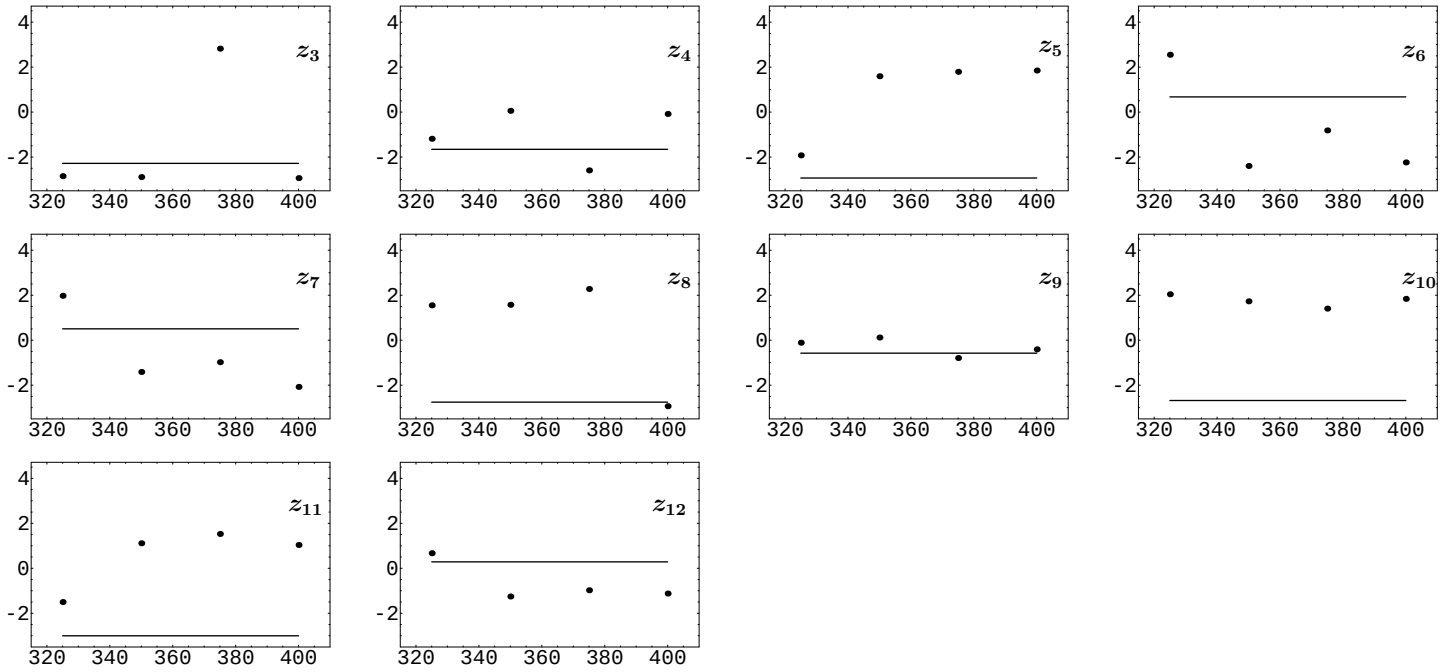

Figure 3: Plots of the phases (in radians) of the z_i, $i = 3, \ldots, 12$. The solid line indicates the value obtained by assuming the z_i's to be energy-independent, while the dots indicate the values obtained by making them energy-dependent.

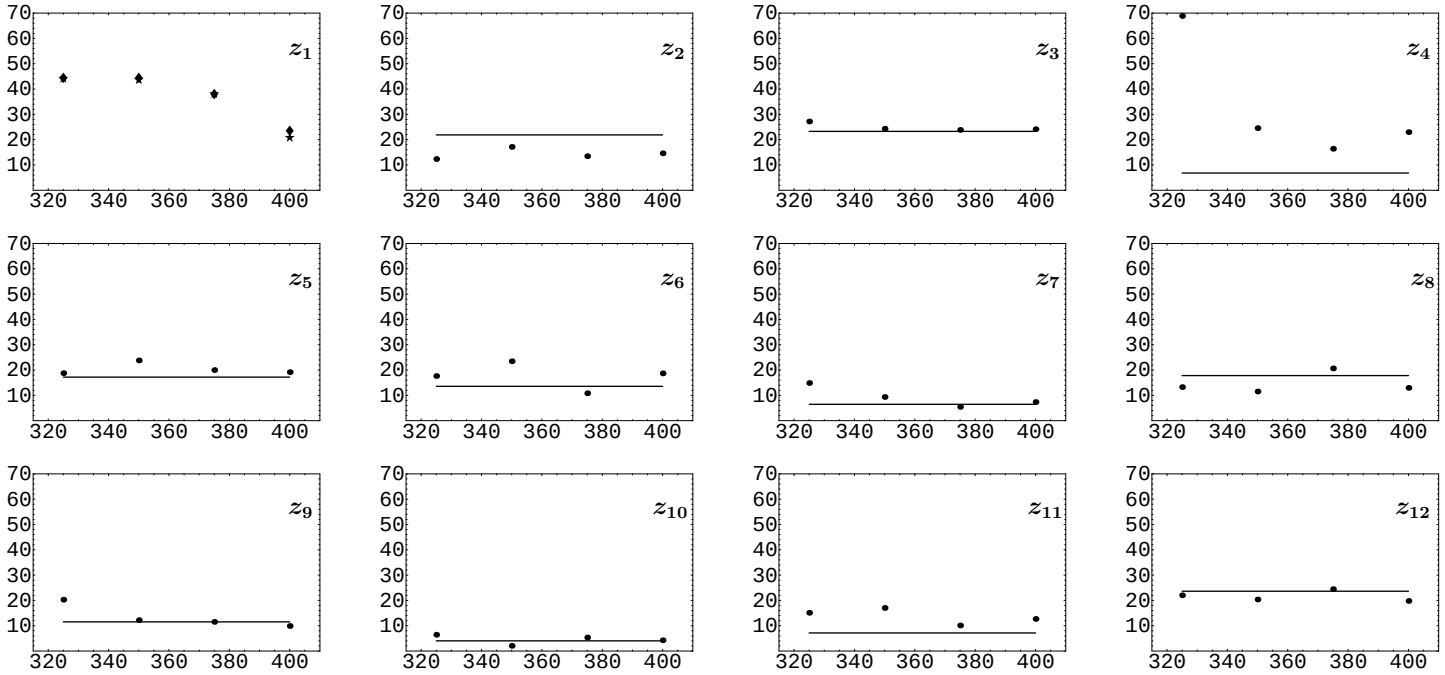

Figure 4: Plots of moduli (in $(\mu\mathrm{b})^{1/2}$) of the $z_i,\ i = 1, \ldots, 12$. The solid line indicates the value obtained by assuming the $z_i,\ i = 2, \ldots, 12$ to be energy-independent, while the dots indicate the values obtained by making them energy-dependent. For z_1, the stars, rhombi indicate the values which were obtained by making respectively the remaining $z_i,\ i = 2, \ldots, 12$ energy-dependent and energy-independent.

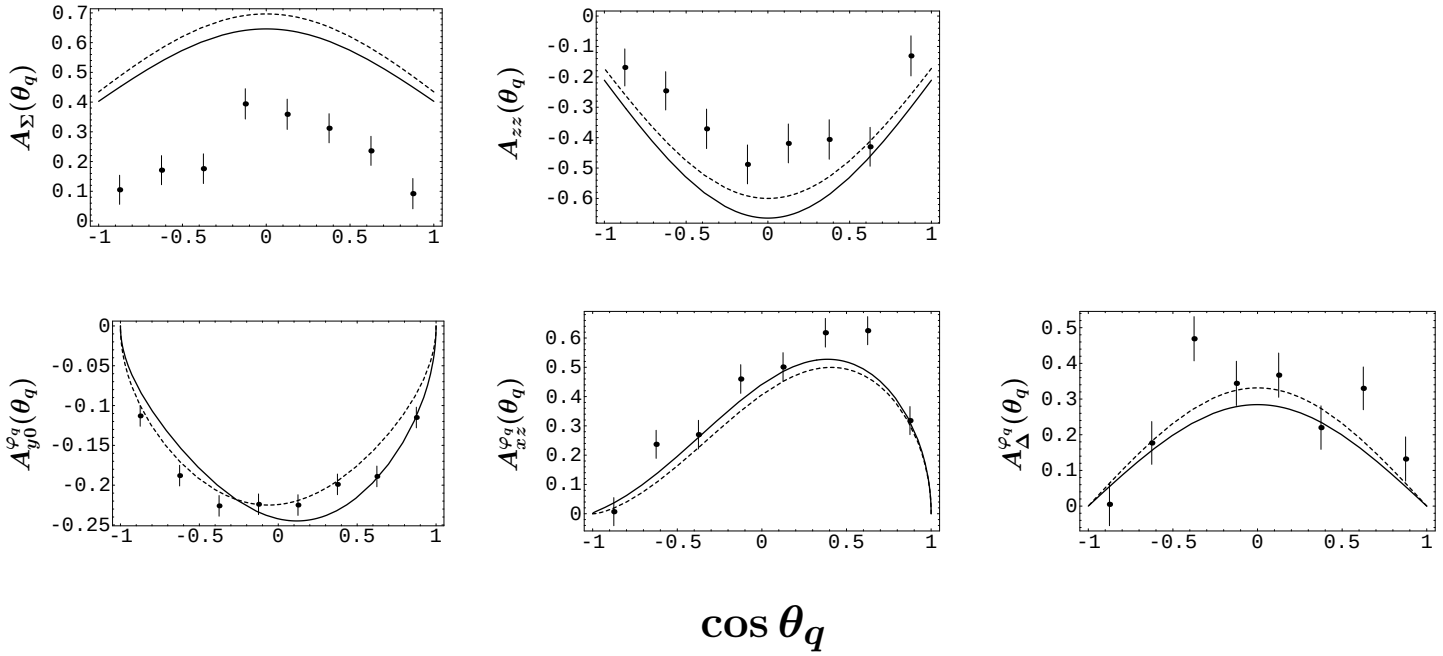

Figure 5: Plots of the estimates for some of the observables measured in [4] at 375 MeV, the energy with the best statistics. The solid line is obtained for an energy-independent fit, while the dashed line is obtained for an energy-dependent fit.

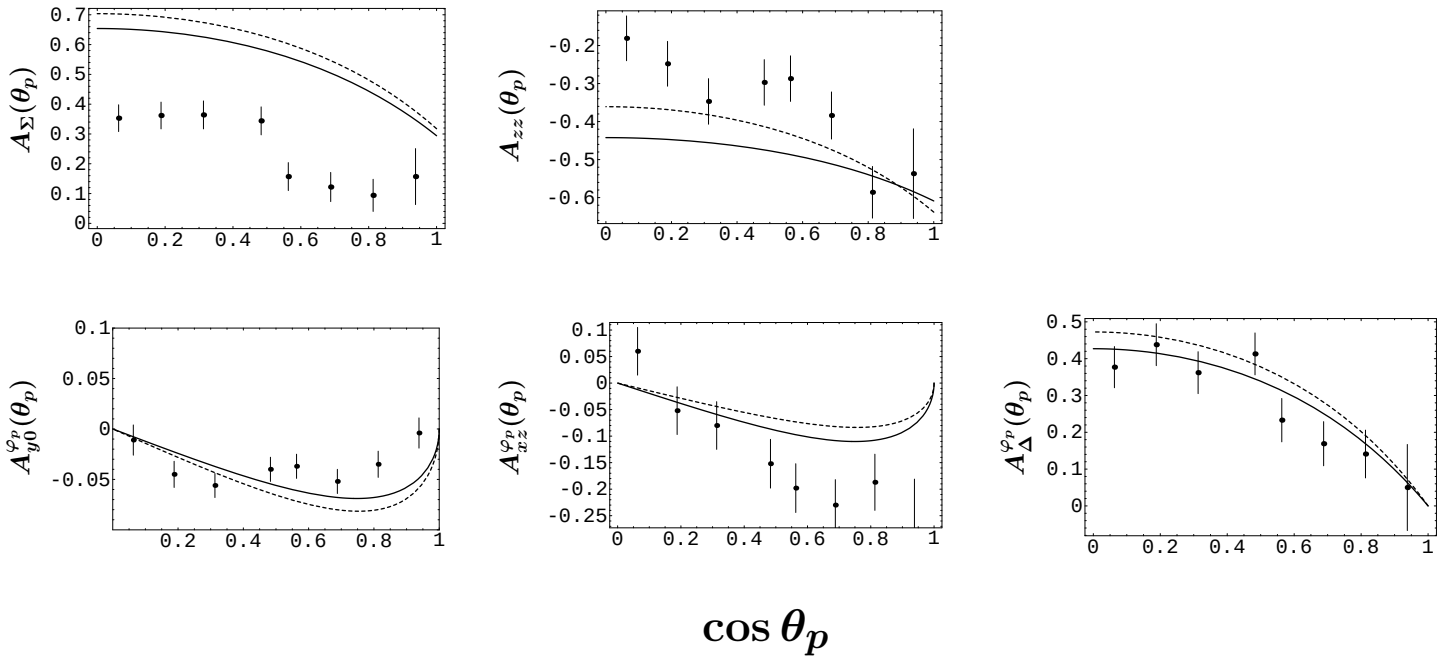

Figure 6: Plots of the estimates for some of the observables measured in [4] at 375 MeV, the energy with the best statistics. The solid line is obtained for an energy-independent fit, while the dashed line is obtained for an energy-dependent fit.

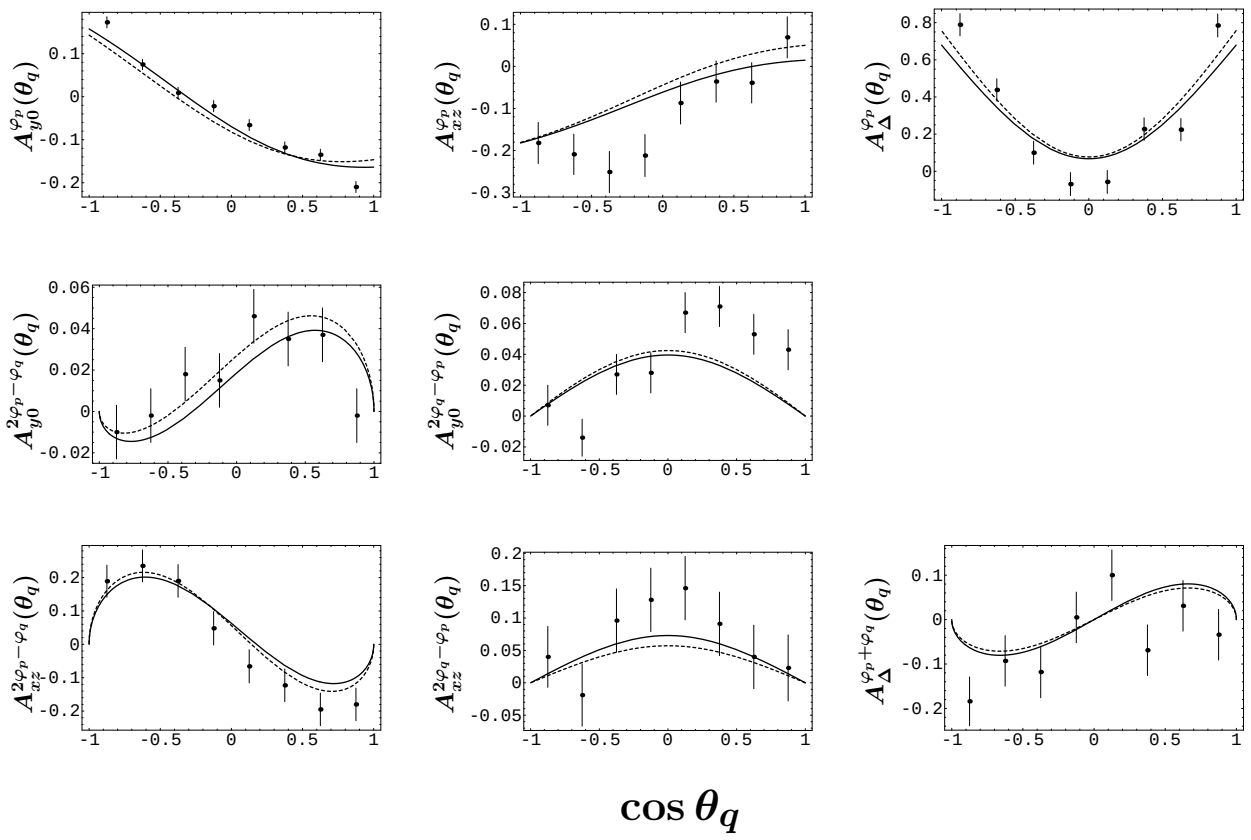

Figure 7: Plots of the estimates for some of the observables measured in [4] at 375 MeV, the energy with the best statistics. The solid line is obtained for an energy-independent fit, while the dashed line is obtained for an energy-dependent fit.

Since Ss does not interfere with any other partial-wave, we parametrize it as: $\int_0^{\epsilon_{\max}} |T_1(\epsilon)|^2\, q(\epsilon)\, p(\epsilon)\, \mathrm{d}\epsilon = |z_1|^2$. At each incident energy there are 39 equations and since the data was measured at four bombarding energies, we have a total of 156 equations in 25 (real) unknowns. This nonlinear-overdetermined-system of equations can only have approximate solutions, which were obtained by least squares minimization. The validity of the ansatz (9) was also checked by solving for the z_i's at each energy. We need to mention here that the partial-wave amplitudes used here are obtained by multiplying the ones given in [7] by a factor, $(4\pi)^3(\mathrm{i})^{l-l_q-l_p}$. In figures 3-4, the obtained values for the z_i are plotted, while figures 5-7 show estimates, using these values, for some of the observables measured in [4].

Acknowledgments

P. N. D. would like to thank the Alexander von Humboldt Foundation for support, G. R. thanks Professors B. V. Sreekantan, R. Cowsik and J. H. Sastri for research facilities.

References

[1] H. O. Meyer et al., Phys. Rev. Lett. **81** (1998) 3096; H. O. Meyer et al., Phys. Rev. Lett. **83** (1999) 5439; P. Thörngren-Engblom et al., nucl-ex/9810013; P. Thörngren-Engblom et al., Nucl. Phys. **A 663-A 664** (2000) 447.

[2] S. M. Bilenky and R. M. Ryndin, Phys. Lett. **6** (1963) 217.

[3] A. W. Thomas, K. Hicks and A. Hosaka, Prog. Theor. Phys. **111** (2004) 291; C. Hanhart et al., Phys. Lett. **B 590** (2004) 39.

[4] H. O. Meyer et al., Phys. Rev. **C 65** (2001) 027601.

[5] G. Ramachandran and P. N. Deepak, Phys. Rev. **C 63** (2001) 051001(R); P. N. Deepak and G. Ramachandran, Phys. Rev. **C 65** (2002) 027601.

[6] G. Ramachandran and P. N. Deepak, Nucl. Phys. **A 695** (2001) 177.

[7] G. Ramachandran, P. N. Deepak and M. S. Vidya, Phys. Rev. **C 62** (2000) 011001(R).

η' meson production in gamma-nucleon and nucleon-nucleon collisions

K. Nakayama

Department of Physiscs and Astronomy, University of Georgia, USA
Institut für Kernphysik, Forschungszentrum Jülich, Germany

Abstract: The production of η' mesons in the reactions $\gamma p \to p\eta'$ and $pp \to pp\eta'$ is described consistently within a relativistic meson exchange model of hadronic interactions. The photoproduction can be described quite well over the entire energy range of available data by considering an S_{11} and a P_{11} resonance, in addition to the t-channel mesonic current. The controversial conclusions reached by different authors on the dynamics of this reaction are addressed. Also the preliminary data from the CLAS collaboration are analyzed. As for the $pp \to pp\eta'$ reaction, different current contributions are constrained by a combined analysis of this and the photoproduction reaction. Difficulties to simultaneously account for the 47-MeV and 144-MeV angular distributions measured by the COSY-11 and DISTO collaborations, respectively, are addressed.

1 Introduction

The study of the intrinsic properties of the η' meson as well as its production processes in elementary particle and hadron physics is of particular interest for various reasons. The properties of η' are largely governed by the dynamics of the QCD $U_A(1)$ axial vector anomaly [1, 2, 3, 4, 5, 6]. Expressed in the (pseudoscalar) quark-flavor basis, the physically observed η and η' mesons may be written as

$$\begin{pmatrix} \eta \\ \eta' \end{pmatrix} = \begin{pmatrix} \cos\alpha & -\sin\alpha \\ \sin\alpha & \cos\alpha \end{pmatrix} \begin{pmatrix} \eta_q \\ \eta_s \end{pmatrix} \ , \tag{1}$$

where $\eta_s \equiv s\bar{s}$ and $\eta_q \equiv (u\bar{u} + d\bar{d})/\sqrt{2}$ describe the strange and nonstrange quark-antiquark states, respectively. The $U_A(1)$ anomaly mediates η_q–η_s transitions and therefore plays a central role in understanding the η–η' mixing [7]. The mixing angle α is shown to be fairly constant [8, 7], and a

weighted average value of $\alpha = 39.3^\circ \pm 1.0^\circ$ has been extracted [9]. Quite recently, the KLOE collaboration [10] has reported a value of $\alpha = 41.8^{\circ +1.9^\circ}_{-1.6^\circ}$. As can be seen from Eq. (1), such a value of the mixing angle results in a considerable amount of $s\bar{s}$ in both the η and η' mesons. By contrast, the corresponding mixing angle for the vector mesons ω and ϕ is quite small ($\approx 3.4^\circ$ [11, 12, 13]), providing an ω with nearly no $s\bar{s}$ and a ϕ being almost a pure $s\bar{s}$ state.

Therefore, instead of using the vector mesons ω and ϕ, production processes involving η' and η offer an alternative way of probing the strangeness content of the nucleon. Due to the fact that both η and η' contain a significant amount of $s\bar{s}$, but of opposite phase with respect to the nonstrange $u\bar{u} + d\bar{d}$ component, significant interference effects involving the strange-quark piece of the nucleon wave function are possible [14]. In fact, it has been proposed that the relative cross sections for the reactions induced by pseudoscalar mesons, $\eta p, \eta' p \to \eta p, \eta' p, K^+\Lambda$ and $\pi^- p \to \eta n, \eta' n$, provide a sensitive test for the presence of the $s\bar{s}$ component in the nucleon wave function [14].

Due to its nontrivial properties, the QCD vacuum exhibits strong gluonic fluctuations with pseudoscalar quantum numbers to which the $\eta_{q,s}$ states can couple via the $U_A(1)$ axial anomaly. The nonperturbative gluon dynamics and the axial anomaly [3, 4, 5, 15] are thought to be responsible for the generation of the much larger mass of η' as compared to the masses of other members of the $SU(3)$ pseudoscalar meson nonet known as the Goldstone bosons. The masses of the Goldstone bosons are generated by the spontaneous breaking of chiral symmetry [2, 6, 16]. The η' meson is, therefore, thought to couple strongly to gluons via the $U_A(1)$ axial anomaly coupling [17, 18]. The unexpectedly large branching ratio measured recently for the inclusive decay of beauty particles, $B \to \eta' + X$ [19], has been interpreted as possible experimental evidence in this respect [20]. To date, the KLOE collaboration has recently found that the gluonium content in the η' is consistent with a fraction below 15% [10]. In any case, if there is a strong coupling of η' meson to gluons, it would be conceivable that short-range reaction processes such as $pp \to pp\eta'$ might reveal the gluonic degrees of freedom in the low energy interactions involving nucleons and η' [21].

One of the properties of the η' meson of extreme importance is its yet poorly known coupling strength to the nucleon. This has attracted much attention in connection with the so-called "nucleon-spin crisis" in polarized deep inelastic lepton scattering [22]. In the zero-momentum limit, the $NN\eta'$ coupling constant $g_{NN\eta'}$ is related to the flavor singlet axial charge G_A through the flavor singlet Goldberger-Treiman relation [23] (see also Refs.

[24, 25])

$$2m_N\, G_A(0) = F\, g_{NN\eta'}(0) + \frac{F^2}{2N_F}\, m_{\eta'}\, g_{NNG}(0)\ , \tag{2}$$

where $F \sim \sqrt{2N_F}F_\pi$ is a renormalization-group invariant decay constant; N_F and F_π denote the number of flavors and the pion decay constant, respectively. g_{NNG} describes the coupling of the nucleon to the gluons arising from contributions violating the Okubo-Zweig-Iizuka rule [26]. The EMC collaboration [22] has measured an unexpectedly small value of $G_A(0) \sim 0.20$–0.35. The first term on the right-hand side of the above equation corresponds to the quark contribution to the "spin" of the proton, and the second term to the gluon contribution [25, 27]. Therefore, if $g_{NN\eta'}(0)$ is known, Eq. (2) may be used to extract the coupling $g_{NNG}(0)$. However, unfortunately, there is no direct experimental measurement of $g_{NN\eta'}(0)$ so far. Reaction processes where the η' meson is produced directly off a nucleon, such as $\gamma p \to p\eta'$ and $pp \to pp\eta'$, may thus offer a unique opportunity to extract this coupling constant. Of course, other production mechanisms, such as meson exchange and nucleon resonance currents, must be taken into account before a quantitative determination of $g_{NN\eta'}$ is possible.

Yet another interesting aspect in studying η' production processes is that they may provide an alternative tool to extract information on nucleon resonances, N^*. Current knowledge of most of the nucleon resonances is mainly due to the study of πN scattering and/or pion photoproduction off the nucleon. Reaction processes such as η' photoproduction provide opportunities to study those resonances that couple only weakly to pions, especially, in the less explored higher N^* mass region of "missing resonances" [28]. Missing resonances are those predicted by quark models but not found in more traditional pion-production reactions [28].

In the present work, we concentrate on the reactions $\gamma p \to p\eta'$ and $pp \to pp\eta'$. So far there exists only a limited number of studies of the η' photoproduction both experimentally [29, 30] and theoretically [31, 32, 33, 34]. Zhang *et al.* [31], in their theoretical investigation using an effective Lagrangian approach, have emphasized the role of the $D_{13}(2080)$ resonance in the description of the, then, existing data [29], while Li [32] has described those data within a constituent quark model with the off-shell $S_{11}(1535)$ excitation as the dominant contribution. The authors of Ref. [30] described their data — obtained with much higher statistics than the previous measurements [29] — in the energy region from threshold to 2.6 GeV under the assumption of resonance dominance. They considered an S_{11} and a P_{11} resonance with extracted masses of 1897 and 1986 MeV, respectively. The former

resonance was needed to explain the energy dependence of the total cross section which exhibits a steep rise and falloff close to threshold. The $P_{11}(1986)$ resonance was needed to account for the measured forward rising angular distributions. In a calculation similar to that in Ref. [32], Zhao [34] introduced also a P_{13} and an F_{13} resonance to describe the SAPHIR data [30]. In both these quark model calculations, no (t-channel) vector meson exchange contribution was considered. Based on a $U(3)$ baryon chiral perturbation theory, Borasoy [33] introduced the off-shell $P_{11}(1440)$ and $S_{11}(1535)$ resonances, in addition to the Born and vector meson exchange contributions, to describe the data [30]. Quite recently, Chiang *et al.* [35] have put forward a model for η' photoproduction that considers the t-channel vector meson exchanges in terms of Regge trajectories to comply with high energy behavior. In their calculation, which was applied to the SAPHIR data [30] (that cover an energy region $< 2.6\,\mathrm{GeV}$), the interference of the Regge trajectories with an S_{11} resonance is the underlying mechanism responsible for reproducing the data and no need of any P_{11} resonance contribution was found. In contrast, also in a quite recent calculation, Sibirtsev *et al.* [36] have described the SAPHIR data by considering the t-channel ρ- and ω-meson exchange contributions with an exponential form factor at the $\gamma\eta' v$ vertex ($v = \rho, \omega$). The observed forward rise of the angular distribution is then largely accounted for by the (t-dependent) exponential form factor. In addition, the $S_{11}(1535)$ resonance is introduced in order to account for the energy dependence of the total cross section. Sibirtsev *et al.* [36] have also speculated that the η' photoproduction at high energies and large t may be useful in determining the $NN\eta'$ coupling constant $g_{NN\eta'}$. New experimental investigations of η' photoproduction are currently being carried out at ELSA by the Crystal Barrel collaboration [37] and JLab by the CLAS collaboration [38] (see contribution by B. Ritchie to this meeting where the preliminary CLAS data were made public for the first time).

The $pp \to pp\eta'$ reaction has been a subject of increasing attention in the last few years. Experimental data on total cross section exist for excess energies up to $Q \sim 24$ MeV [39], in addition to the total cross section and the angular distribution at $Q = 143.8\,\mathrm{MeV}$ from the DISTO collaboration [40]. The new total cross section data in the excess energy range of $Q = 26$–$47\,\mathrm{MeV}$ and an angular distribution at $Q = 46.6\,\mathrm{MeV}$ have been just reported by the COSY-11 collaboration [41], filling in partly the gap between the near threshold [39] and higher energy DISTO data [40]. Theoretically, the $pp \to pp\eta'$ reaction has been investigated by a number of authors [42, 43] within meson-exchange approaches of varying degrees of sophistication. In particular, in Ref. [43], we have explored the possible role of

the nucleonic, mesonic, and resonance current contributions. The $S_{11}(1987)$ and $P_{11}(1986)$ resonances as determined by the SAPHIR collaboration [30] have been considered for the resonance current. Due to the scarcity of the then available data (total cross sections up to $Q \approx 10\,\mathrm{MeV}$), it was not possible to quantitatively constrain each of these currents. With the increase of the data base since then, we are now in a much better position to learn about this reaction than was possible before.

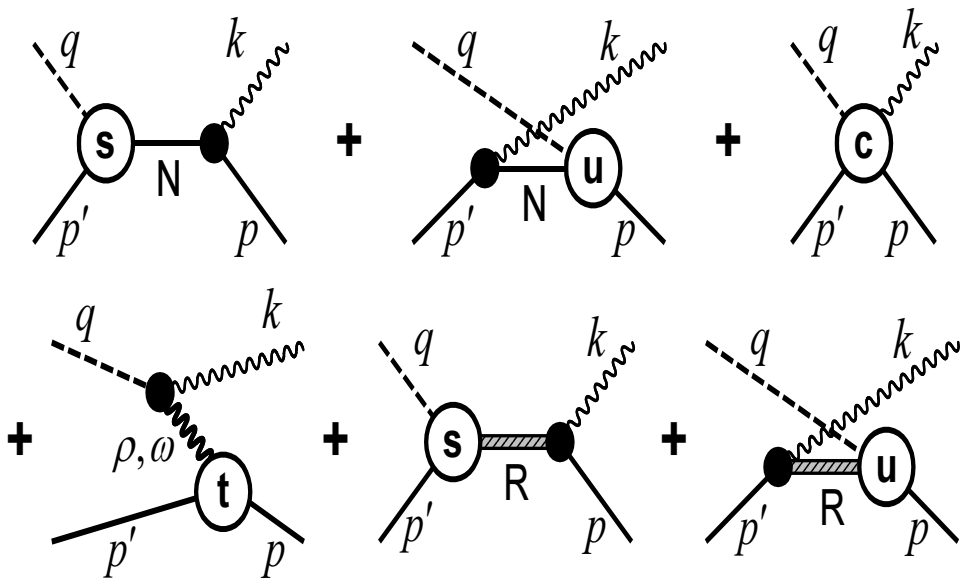

Figure 1: Diagrams contributing to $\gamma p \to \eta' p$. Time proceeds from right to left. The intermediate baryon states are denoted N for the nucleon, and R for the S_{11} and P_{11} resonances. The intermediate mesons in the t-channel are ρ and ω. The external legs are labeled by the four-momenta of the respective particles and the labels s, u, and t of the hadronic vertices correspond to the off-shell Mandelstam variables of the respective intermediate particles. The three diagrams in the lower part of the diagram are transverse individually; the three diagrams in the upper part are made gauge-invariant by an appropriate choice (see text) of the contact current depicted in the top-right diagram. The nucleonic current (nuc) referred to in the text corresponds to the top line of diagrams; the meson-exchange current (mec) and resonance current contributions correspond, respectively, to the leftmost diagram and the two diagrams on the right of the bottom line of diagrams.

The major purpose of the present work is to perform a combined analysis of the $\gamma p \to p\eta'$ and $pp \to pp\eta'$ reactions within a relativistic meson-exchange model of hadronic interactions (see Figs. 1 and 2).

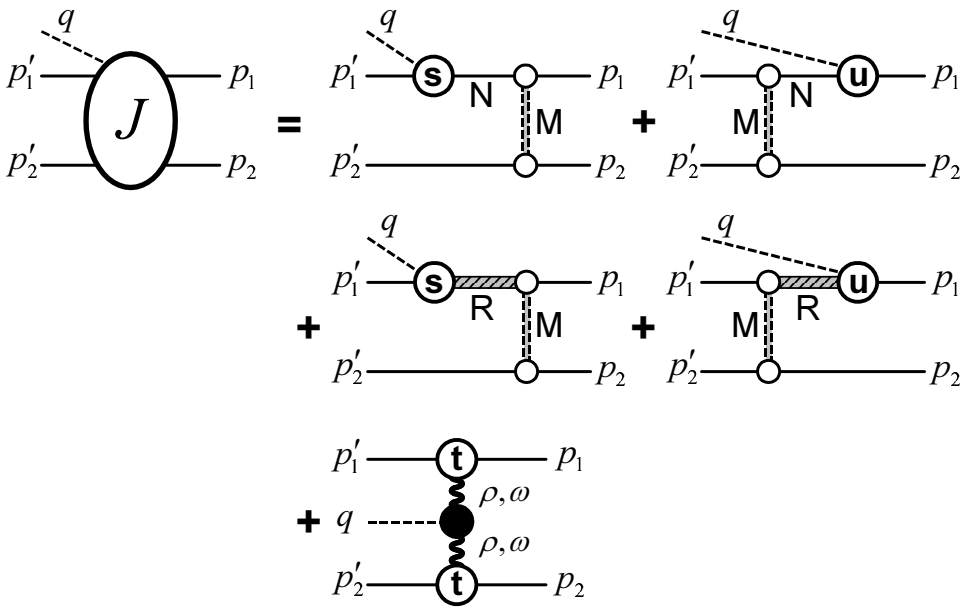

Figure 2: Basic production mechanisms for $pp \to pp\eta'$. Time proceeds from right to left. As in Fig. 1, N and R denote the intermediate nucleon and resonances, respectively, and M incorporates all exchanges of mesons π, η, ρ, ω, σ, and a_0 ($\equiv \delta$) for the nucleon graphs and π, ρ, and ω for the resonance graphs. External legs are labeled by the four-momenta of the respective particles; the hadronic vertices s, u, and t here correspond to the same kinematic situations, respectively, as those identified similarly in Fig. 1. The nucleonic, resonance, and meson-exchange contributions referred to in the text correspond, respectively, to the first, second, and third lines of the diagrams on the right-hand side.

For the η' photoproduction, in the s and u channels, we consider contributions due to the intermediate nucleon and the nucleon resonances and in the t-channel, we take into account ρ and ω meson exchanges. Since we employ the physical coupling constants and physical masses for all intermediate particles in all the channels, the s-channel diagrams also account for the pole part of the $N\eta'$ final-state interaction (FSI) [44]. For the nonpole part of the FSI, the u and t channels correspond to the Born approximation of the corresponding $N\eta'$ T-matrix. Phenomenological form factors are attached to each vertex in all channels. The total amplitude is constrained to obey gauge invariance following the prescription of Refs. [45, 46, 47]. The photoproduction amplitude thus obtained is then used in the construction of the basic η' production amplitude in $pp \to pp\eta'$ by replacing the photons with relevant mesons which, in turn, are attached to the second nucleon (see

Fig. 2). Hereafter, the basic η' production amplitude is referred to as the η' production current following the nomenclature employed in Ref. [43]. The $pp \to pp\eta'$ reaction is then described in a Distorted-Wave Born Approximation (DWBA) which includes both the nucleon-nucleon (NN) final-state interaction and the initial-state interaction (ISI). Further details of our approach may be found in Ref. [48].

2 $\gamma + p \to p + \eta'$

The basic strategy of our model approach is to first fix the free parameters of the photoproduction reaction and then go to the hadronic process to fix the remaining parameters.

The results for coupling constants and resonance masses, etc., given here were obtained by standard best-fit procedures. At present, however, the quality of the data is not good enough to provide really stringent constraints for the fits. As discussed also in detail below, in many instances, therefore, the parameters obtained here may be changed within certain limits without affecting the overall quality of the fits. In this situation, χ^2 values for the fits carry little information and were omitted from the tables.

The steep rise and fall of the measured total cross section in $\gamma p \to p\eta'$ close to threshold [29, 30] suggests the presence of an S_{11} nucleon resonance contribution. Of course, one should always keep in mind that there is also the possibility of a threshold cusp effect, as discussed in Ref. [54], that might explain the observed behavior of the photoproduction total cross section close to threshold in the absence of any resonance. This requires further careful considerations. Here we assume the observed behavior of the cross section to be due to the nucleon resonance. Therefore, we first consider the $N^* = S_{11}$ resonance current. The mass of the resonance as well as the product of the coupling constants, $g_{NN^*\gamma}g_{NN^*\eta'}$, and the ps-pv mixing parameter at the $NN^*\eta'$ vertex are free parameters to be fitted to the measured angular distributions from 1.49 to 2.44 GeV [30]. In addition to the S_{11} resonance, we also consider the ρ and ω meson-exchange currents in the t-channel. For this current, the coupling constants at the production vertices $\eta' v\gamma$ ($v = \rho, \omega$) are known from the radiative decay of η', $\eta' \to v + \gamma$. Also, since the relevant hadronic vertices NNv are known from other studies, the only unknown parameter in the mesonic current is the cutoff parameter in the form factor at the $\eta' v\gamma$ vertex. Together with the free parameters of the S_{11} resonance, it has also been fitted to the data. The resulting angular distributions are shown in Fig. 3(a).

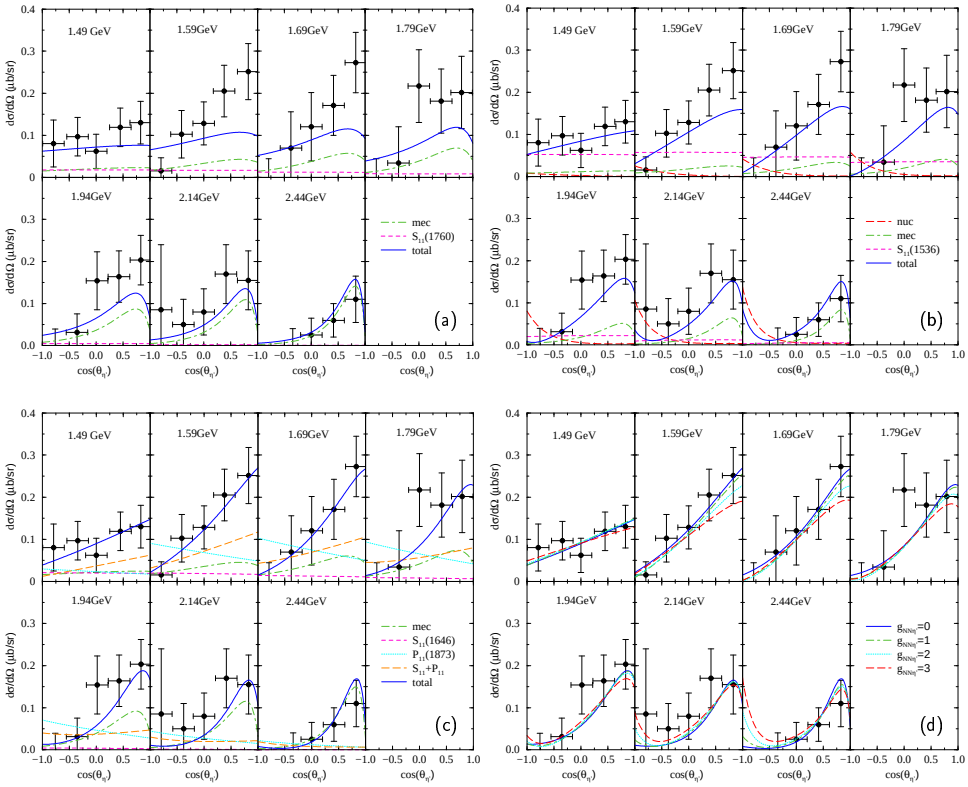

Figure 3: Differential cross section for $\gamma p \to p\eta'$ according to the mechanisms shown in Fig. 1. Panel (a) includes only the meson-exchange current (mec) and the S_{11} resonance. Adding either the nucleonic (nuc) contribution or a P_{11} resonance produces the results of panels (b) and (c), respectively. In (d), successively stronger (as indicated by the values of the $g_{NN\eta'}$ coupling constant) nucleonic contributions are added to the results shown in panel (c). In each case, the model parameters are determined by best fits. The meaning of the corresponding lines is indicated in the panels. The data are from Ref. [30].

Here, the mass of the S_{11} resonance results to be $m_{S_{11}} = 1760\,\mathrm{MeV}$; however, inclusion of other currents into the fitting procedure will change its value as we shall show below. As one can see from the figure, the $S_{11}(1760)$ current contribution decreases as the energy increases while the mesonic current contribution increases with the energy and rises at forward angles. At lower energies, the constructive interference between the two currents is important in enhancing the cross section, although it is not sufficient to reproduce the forward rise exhibited by the data. At higher energies, the mesonic current dominates almost completely and describes nicely the observed angular distribution. Therefore, the mesonic current is fixed to a

large extent by the forward angle data at higher energies.

Fig. 3(b) shows the results when the nucleonic current is added to the S_{11} resonance and mesonic currents. In the nucleonic current, both the $NN\eta'$ coupling constant $g_{NN\eta'}$ and the corresponding ps-pv mixing parameter $\lambda_{NN\eta'}$ are fitted to the data. The parameters in the mesonic and S_{11} resonance currents are refitted to the data altogether. The nucleonic current contribution (long-dashed curves) is small at lower energies but increases with energy at backward angles due to the u-channel diagram, a feature that has been also realized in Ref. [36]. Therefore, measurements at high energy and backward angles (large t) will help constrain the poorly known $NN\eta'$ coupling constant $g_{NN\eta'}$. We will come back to further discussion of this issue later. The S_{11} resonance contribution (dashed curves) is larger than that shown in Fig. 3(a) at lower energies which improves the description of the data in this energy region. It also exhibits a stronger energy dependence. The fitted value of the resonance mass is now $m_{S_{11}} = 1536\,\mathrm{MeV}$. A comparison with the value of $m_{S_{11}} = 1760\,\mathrm{MeV}$ obtained in Fig. 3(a) illustrates how this parameter value changes with the inclusion of different production mechanisms. Due to a constructive interference between the nucleonic plus resonance current and the mesonic current in the forward angle region at higher energies, the latter contribution is somewhat smaller than in Fig. 3(a). The overall description of the data is improved with respect to that in Fig. 3(a).

Fig. 3(c) illustrates the effect of the P_{11} resonance in $\gamma p \to p\eta'$. The mass of the P_{11} resonance as well as the product of the coupling constants, $g_{NN^*\gamma}g_{NN^*\eta'}$, and the ps-pv mixing parameter at the $NN^*\eta'$ vertex ($N^* = P_{11}$) are free parameters to be fitted to the data together with the parameters in the other currents. Here, the nucleonic current has been switched off [it will be considered in the results shown in Fig. 3(d)]. As can be seen, the P_{11} resonance contribution (dotted curves) rises at backward angles; it also rises and falls with energy. The S_{11} resonance contribution (dashed curves) is relatively small, but its interference with the P_{11} resonance contribution results in a total resonance current contribution (long-dashed curves) that rises at forward angles. Again, the mesonic current (dash-dotted curves) dominates at higher energies. The solid curves correspond to the total contribution. The overall agreement with the data is excellent, showing that the P_{11} resonance may be required for a quantitative description of the data. For a more definite conclusion about the role of the P_{11} resonance more accurate data are called for. The fitted masses of the S_{11} and P_{11} resonances are $m_{S_{11}} = 1646\,\mathrm{MeV}$ and $m_{P_{11}} = 1873\,\mathrm{MeV}$, respectively. At this point, we might identify the S_{11} resonance with the known

$S_{11}(1650)$ resonance [12], whose quoted width is $\Gamma_{S_{11}} = 180\,\mathrm{MeV}$. (Recall that, in this work, we have used a constant width of $\Gamma_{N^*} = 150\,\mathrm{MeV}$ for all the resonances.) The P_{11} resonance does not correspond to any known resonance; it is tempting to identify it with one of the missing resonances with $m_{P_{11}} = 1880\,\mathrm{MeV}$ and with the corresponding width of $\Gamma_{P_{11}} = 155\,\mathrm{MeV}$, predicted by quark models [28, 55]. Recently, an evidence for this resonance has been found in a three-channel unitary model analysis [56]. However, we emphasize that such an identification from the present analysis is premature as we shall show later in connection with the results in Fig. 4.

The role of the nucleonic current is illustrated in Fig. 3(d). Here, each curve corresponds to a given value of the $NN\eta'$ coupling constant $g_{NN\eta'}$ as indicated. The pseudovector coupling ($\lambda_{NN\eta'} = 0$) is adopted. We mention that we have also considered the pseudoscalar coupling ($\lambda_{NN\eta'} = 1$), but the fits do not support this choice and prefer to have a small value of $\lambda_{NN\eta'}$ close to zero. For each value of $g_{NN\eta'}$, the parameters of the resonance and mesonic currents have been refitted to best reproduce the data. Here, the mass of the S_{11} resonance is fixed at 1650 MeV. The solid curves corresponding to the choice $g_{NN\eta'} = 0$ are the same results as shown in Fig. 3(c). As one can see again, the major effect of the nucleonic current shows up at higher energies and backward angles in the photoproduction reaction. Accurate measurements in these kinematic regions are called for. In any case, judging from the overall results, the existing data do not support values much larger than $g_{NN\eta'} = 3$. In fact, they seem to prefer smaller value of $g_{NN\eta'}$, compatible with 0. This is considerably smaller than the value of $g_{NN\eta'} = 6.1$ used in our previous work [43] on $pp \to pp\eta'$, and it is more in line with estimates based on the dispersion method [57].

As discussed in the Introduction, such a small value of the $NN\eta'$ coupling would have an important implication in connection to the "spin puzzle" of the nucleon. A recent estimate [7] of $g_{NN\eta'}$ based on an alternative formula to Eq. (2) (neglecting the higher excited pseudoscalar states or glueballs which are assumed to be negligible) in conjunction with the measured value of the singlet axial charge yields a value of $g_{NN\eta'}(0) = 1.4 \pm 1.1$. It should be noted that the $NN\eta'$ coupling constant entering in Eq. (2) is at zero momentum squared, $g_{NN\eta'}(q^2 = 0)$, while the coupling constant $g_{NN\eta'}$ in the present work is defined at the on-shell momentum squared, $q^2 = m_{\eta'}^2$. We emphasize that the relatively small value of $g_{NN\eta'}$ found here is a model-dependent result. In particular, what is relevant in our model is the product of the $NN\eta'$ coupling constant and the corresponding off-shell form factor. Since the intermediate nucleon in the nucleonic current is far off-shell due to the large mass of the produced η' meson, the result is sensitive to the

choice of the form factor. As mentioned in the preceding section, the form factor used at the $NN\eta'$ vertex is the same as that used consistently in our investigation of other meson production processes.

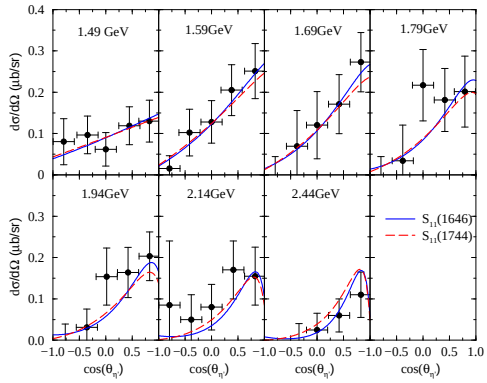

Figure 4: Two fits resulting in different sets of the extracted resonance mass values. Both fits include the S_{11} and P_{11} resonances as well as the meson-exchange currents. The solid curves are the same ones shown in Fig. 3(c) with the mass values of $(m_{S_{11}}, m_{P_{11}}) = (1646, 1873)\,\mathrm{MeV}$. For the dashed curves, the corresponding mass values are $(1744, 1879)\,\mathrm{MeV}$.

In Fig. 4 we show a comparison of two fit results for $\gamma p \to p\eta'$, in which both the S_{11} and P_{11} resonance currents were considered in addition to the meson exchange current. The solid curves are the same results shown in Fig. 3(c) with the resulting resonance masses of $m_{S_{11}} = 1646\,\mathrm{MeV}$ and $m_{P_{11}} = 1873\,\mathrm{MeV}$. The dashed curves correspond to a fit with the resulting resonance masses of $m_{S_{11}} = 1744\,\mathrm{MeV}$ and $m_{P_{11}} = 1879\,\mathrm{MeV}$. For this fit, the values of the remaining fit parameters are very close to the corresponding values obtained in the case of Fig. 3(c) , except for the value of $g_{NN^*\gamma}g_{NN^*\eta'}$ for $N^* = S_{11}$ which compensates for the change in the value of $m_{S_{11}}$. As one can see, the quality of the fit is essentially the same in both cases; yet, the extracted values of $m_{S_{11}}$ differ by $\sim 100\,\mathrm{MeV}$ from each other. (See also the results of a Regge trajectory calculation in Fig. 6, where the mass of the P_{11} resonance varies substantially.) This illustrates the order of uncertainties involved in the identification of the resonances from the differential cross section data only (at least from those currently available and from the type of analysis employed here). For a more definitive identification of the resonances, one probably needs more exclusive data than the cross sections, such as the spin observables, which can impose more stringent constraints. A further investigation of this issue is certainly required.

Recently, Chiang *et al.* [35] have also investigated the $\gamma p \to p\eta'$ reaction. They concluded that the consideration of t-channel vector-meson exchanges in terms of Regge trajectories is crucial in describing the available data and that the ρ and ω meson exchanges are unable to reproduce the data. In contrast to the present work, they have not introduced a form factor at the $\eta' v\gamma$ vertex ($v = \rho, \omega$). In their calculations, the observed forward rise of

the cross section is due to the interference between the Regge and the S_{11} resonance contributions. Furthermore, no need for any P_{11} resonance was found in order to describe the data. In our opinion, the application of Regge trajectories — designed for high energies and low t [60] — in the low energy regime of the SAPHIR data [30] is debatable. Moreover, such an approach cannot be used (at least not straightforwardly) in the $pp \to pp\eta'$ reaction due to the important NN FSI which has to be included in any model describing this process. This involves a loop integration for which the Regge propagator as given in Ref. [35] cannot be used. The Regge theory is a theory designed for amplitudes. Of course, with respect to our approach, one may criticize the use of a form factor at the $\eta' v\gamma$ vertex in the mesonic current, whereas we do not use any form factor at any other electromagnetic vertex. However, the use of such a form factor may be defended based on the results for the radiative decay process $\eta' \to \rho + \gamma \to \pi^+\pi^- + \gamma$. One may speculate that the relatively strong form factor needed at the $\eta' v\gamma$ vertex simulates effects of the FSI ignored in the present approach.

In any case, we have also performed the calculation of the photoproduction reaction by replacing the t-channel vector meson exchanges by the Regge trajectories following Ref. [35]. Apart from the obvious differences in the details of the treatment of the resonance current, our calculation also differs in the sign of the $\eta'\omega\gamma$ coupling constant from that employed in Ref. [35]. In the present work the signs of the $\eta' v\gamma$ couplings are inferred from a systematic analysis [43] of the pseudoscalar and vector meson radiative decays based on an $SU(3)$ Lagrangian in conjunction with the sign of the coupling constant $g_{\pi v\gamma}$ determined from a study of pion photoproduction in the 1 GeV energy region [52]. Our results using the Regge trajectories are shown in Fig. 5. We see that, overall, the results are basically the same as those of Fig. 3(c) using the conventional ρ and ω meson exchanges. In particular, here also the interference between the mesonic and resonance currents is the underlying mechanism responsible for reproducing the observed angular distribution. This corroborates the findings of Ref. [35]. However, the resulting resonance masses of $m_{S_{11}} = 1932\,\text{MeV}$ and $m_{P_{11}} = 1710\,\text{MeV}$ differ considerably from those obtained in Fig. 3(c). It is natural to ask whether this discrepancy is related to the uncertainties in the determination of the resonance mass using only the cross section data as illustrated in Fig. 4 or whether it is due to different approaches used in the treatment of the t-channel exchange contribution. To address this question, in Fig. 6 we show the results of three different fits using the Regge trajectories. The solid curves are the same results shown in the left panel of Fig. 5. The dashed curves correspond to another fit resulting in the resonance masses of

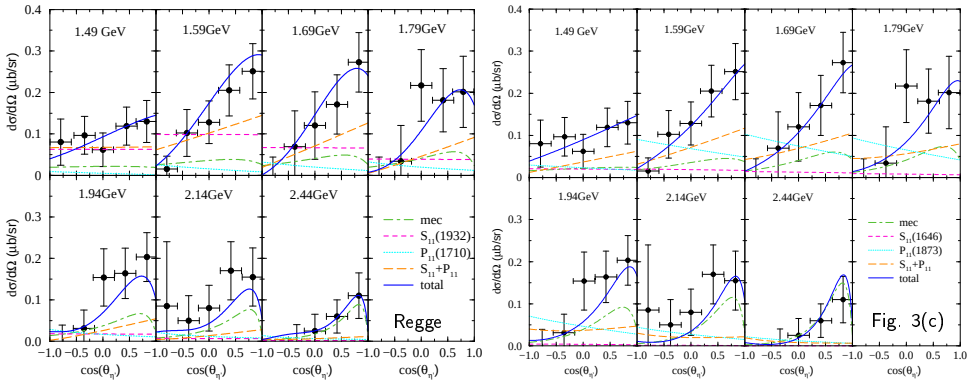

Figure 5: Comparison of differential cross sections for $\gamma p \to p\eta'$ using Regge trajectories (left), similar to the treatment of Ref. [35], and conventional meson-exchange currents (right) for the t-channel vector meson exchange. [The figure on the right-hand side is identical to Fig. 3(c); it is repeated here to allow for a better side-by-side comparison.]

$(m_{S_{11}}, m_{P_{11}}) = (1932, 1950)$ MeV. One sees that the qualities of both fits are comparable to each other but the corresponding values of $m_{P_{11}}$ differ by more than 200 MeV, revealing once more (cf. Fig. 4) that the cross section data alone are insufficient to constrain accurately the resonance masses. However, we were unable to fit the data (with a comparable quality) with the mass of the S_{11} resonance much smaller than $m_{S_{11}} = 1932$ MeV. The dash-dotted curves in Fig. 6 correspond to a fit with a fixed mass of $m_{S_{11}} = 1650$ MeV. This yields a fitted mass of $m_{P_{11}} = 1811$ MeV for the P_{11} resonance. This set of the resonance masses $(m_{S_{11}}, m_{P_{11}}) = (1650, 1811)$ MeV is more in line

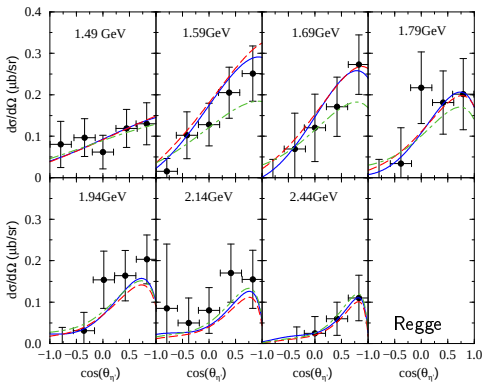

Figure 6: Three fits based on Regge trajectories resulting in different sets of the extracted resonance mass values. All the fits include the S_{11} and P_{11} resonances as well as the mec. The solid curves are the same ones shown in Fig. 5 with the mass values of $(m_{S_{11}}, m_{P_{11}}) = (1932, 1710)$ MeV. For the dashed curves, the corresponding mass values are $(1932, 1950)$ MeV. The dash-dotted curves correspond to a fit with the mass values $(1650, 1811)$ MeV.

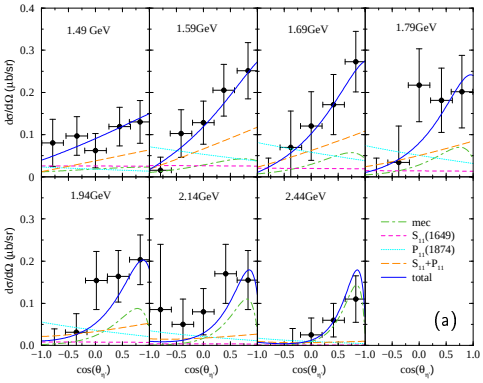

Figure 7: Fig. (a) here corresponds to Fig. 3(c), the difference being that now the $\gamma v \eta'$ vertex functions of dipole form have been replaced by exponential form factors, $F_v(t) = \exp\left[(t - m_v^2)/\Lambda^2\right]$, similar to Ref. [36] (however, with a different normalization; see text).

with the set $(1646, 1873)$ MeV obtained using the conventional vector meson exchanges in the t-channel. Here, however, the quality of the fit is inferior to that achieved in Fig. 3(c), although the data are still reproduced within their uncertainties. These considerations indicate that the determination of the resonance masses is also quite sensitive to different approaches used. Further studies of this issue are needed before a more unambiguous identification of the resonances can be made from the η' photoproduction process. It should also be noted that our calculations based on Regge trajectories differ in details from the results obtained in Ref. [35]. As mentioned above, these differences should, in part, be due to the different treatment (in detail) of the resonance current contributions.

Sibirtsev *et al.* [36] have also reported their study of the $\gamma p \to p\eta'$ reaction quite recently. In contrast to Ref. [35] and the present work, they describe the forward rise of the angular distribution basically by the ρ and ω meson exchanges in the t-channel. They achieve this by including a (t-dependent) exponential form factor at the $\eta' v \gamma$ vertex. Moreover, the $S_{11}(1535)$ resonance was introduced in order to describe the steep rise and fall of the total cross section close to threshold. We have also repeated our calculation employing an exponential form factor at the $\eta' v \gamma$ vertex instead of the dipole form factor. The results are shown in Fig. 7 which again exhibits the same features observed in the calculation using the dipole form factor [see Fig. 3(c)]. We were not able to reproduce their results using only the mesonic and $S_{11}(1535)$ resonance currents. The chief difference between the results shown in Fig. 7 and those in Ref. [36] is that we have used an exponential form factor normalized to unity at the on-mass-shell point $q^2 = m_v^2$, consistent with the kinematics at which the coupling constant $g_{\eta' v \gamma}$ is extracted. In Ref. [36], the form factor is normalized at $q^2 = 0$ instead.

The above considerations show that we arrive at the same conclusion,

namely, that the interference between the meson exchange and resonance currents is the mechanism responsible for the angular distribution exhibited by the photoproduction data, irrespective of whether one uses the ρ and ω meson exchanges in the t-channel (with either dipole or exponential form factor) or Regge trajectories. Certainly, the problem of the Regge trajectory versus form factor is an extremely important issue that needs to be addressed. Judging from our findings so far, it may well be that both simulate the same physics not accounted for explicitly in these calculations.

It should be mentioned that, as we shall discuss in sect.4, the preliminary data from JLab by the CLAS collaboration [38] are quite different from the SAPHIR data [30] analyzed in the present section. However, the qualitative aspects of the results and the major conclusions reached here will remain unchanged.

3 $p + p \to p + p + \eta'$

Since most of the parameters of our model were fixed by the photoproduction reaction in the previous section, we now turn our attention to the $pp \to pp\eta'$ process. The results are shown in Fig. 8. The calculations shown here incorporate *all three* data sets in the determination of the hadronic resonance coupling parameters (in contrast to the results shown in Fig. 9 below). The two panels labeled (a) include the $S_{11}(1760)$ resonance and the mesonic currents; they correspond to the photoproduction results of Fig. 3(a). All the relevant parameters for the latter reaction are taken over unchanged. Thus, the additional parameters to be fitted for the hadronic reaction concern the three products of the coupling constants, $g_{NN^*\pi}g_{NN^*\eta'}$, $g_{NN^*\rho}g_{NN^*\eta'}$, and $g_{NN^*\omega}g_{NN^*\eta'}$ [where $N^* = S_{11}(1760)$], corresponding to the three mesons exchanged between the two interacting nucleons in the resonance current (see Fig. 2). As can be seen here, the dominant contribution is the $S_{11}(1760)$ resonance current (dashed curves). The mesonic current is relatively small.

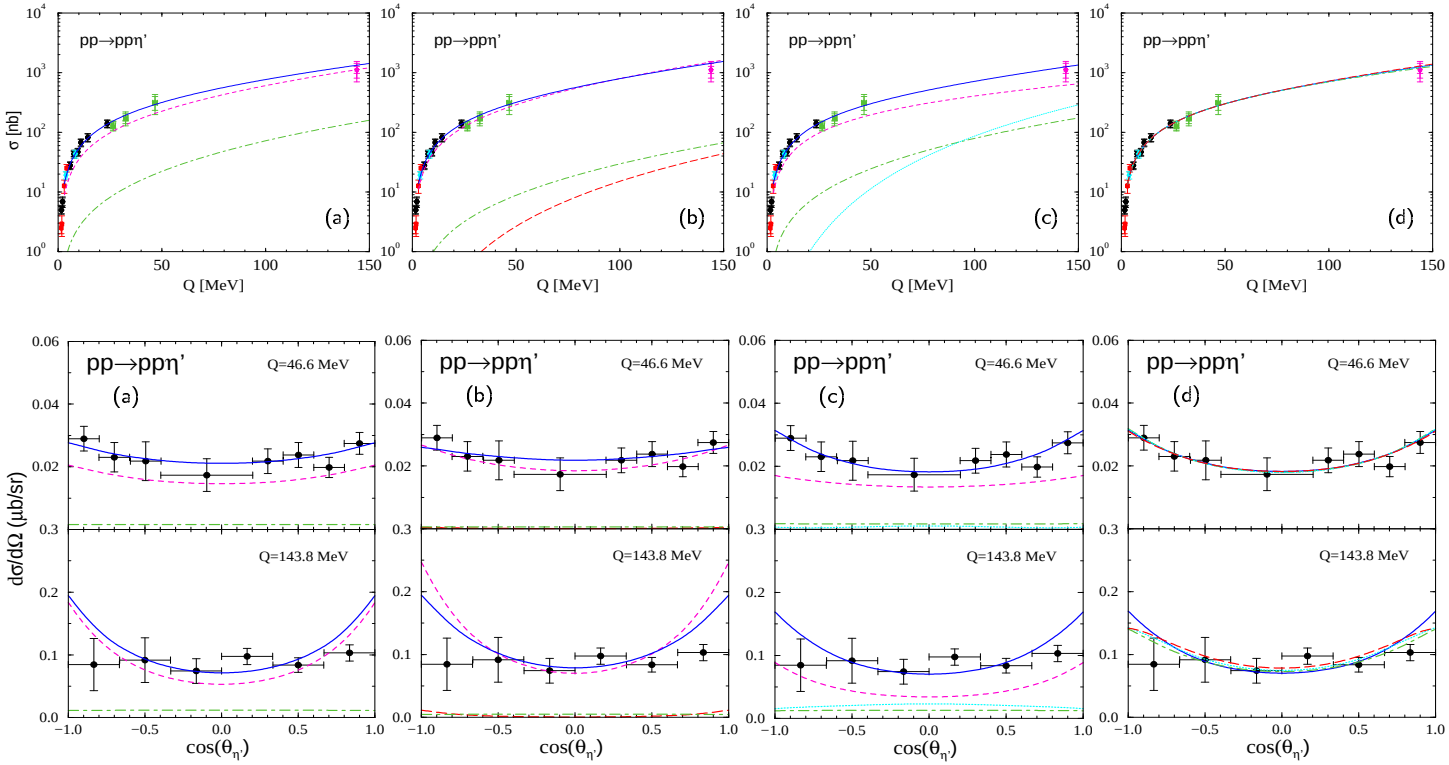

Figure 8: Total cross section as a function of excess energy Q and angular distributions at $Q = 46.6$ and 143.8 MeV in the c.m. frame of the system for $pp \to pp\eta'$. The panels labeled (a)–(d) in both rows correspond to the respective panels (a)–(d) in Fig. 3, and all line styles are explained there. The total cross section comprise data from Refs. [39, 40, 41]; the angular distribution data are from the COSY-11 collaboration (47 MeV) [41] and from DISTO (144 MeV) [40].

The total cross section is nicely reproduced, as well as the measured angular distribution at $Q = 47\,\mathrm{MeV}$. The latter exhibits some angular dependence although it might be compatible with a flat shape within the given experimental uncertainties. The completely flat angular distribution measured at $Q = 144\,\mathrm{MeV}$, however, is not reproduced. As one can see, the calculated angular dependence is introduced by the S_{11} resonance and it arises due to the recoil of this resonance in the overall center-of-mass (c.m.) frame.

Fig. 8(b) shows the results for $pp \to pp\eta'$ which include the nucleonic, $S_{11}(1536)$ resonance, and mesonic currents. Some of the parameters are fixed from the photoproduction reaction corresponding to Fig. 3(b). As before, the remaining parameters are fitted to the $pp \to pp\eta'$ data. Here, for the purpose of consistency, one could, in principle, employ the coupling constants at the MNN^* vertex ($M = \pi, \eta, \rho, \omega$) for $N^* = S_{11}(1535)$ resonance as determined from our recent study of the $pp \to pp\eta$ reaction [58]. We would then have the coupling constant $g_{NN^*\eta'}$ as the only free parameter to be fitted. However, we have opted not to do so because Ref. [58] did not aim for a quantitative determination of those coupling constants. As can be seen here, the $S_{11}(1536)$ resonance current (dashed curves) gives nearly the whole contribution to the cross sections. The mesonic current is small followed by the nucleonic current. This is in contrast to the results in our previous work [43], where due to the scarcity of the then available data, it had not been possible to constrain the individual current contributions. The solid curves correspond to the total contribution. They exhibit similar features to those shown in Fig. 8(a). Here, the model tends to overestimate the total cross section at high energies although it still lies within the experimental uncertainties. We may conclude, therefore, that the addition of the nucleonic current at this stage does not improve the agreement with the data.

Next, we add the $P_{11}(1873)$ resonance to the mesonic and $S_{11}(1646)$ resonance contributions. The results are shown in Fig. 8(c). Again, all parameters relevant for the corresponding photoproduction reaction results of Fig. 3(c) are taken over. The remaining parameters are fitted to the hadronic reaction. It is interesting to note that, unlike in the photoproduction, here the $P_{11}(1873)$ contribution is much smaller than that from $S_{11}(1646)$. The latter is the dominant current. The angular distribution at $Q = 144\,\mathrm{MeV}$ is somewhat improved; however, still in disagreement with the data. This issue is further discussed in Fig. 9.

Fig. 8(d) illustrates the influence of the nucleonic current in the $pp \to pp\eta'$ reaction. The relevant parameters for the corresponding photoproduction reaction results of Fig. 3(d) are taken over. The remaining parameters

are fitted to the As one can see, this reaction is rather insensitive to the nucleonic current contribution. This corroborates the statement in our earlier work [43].

In order to investigate the discrepancy between our model results and the measured flat angular distribution at $Q = 144\,\mathrm{MeV}$ for $pp \to pp\eta'$, we have repeated the calculation shown in Fig. 8 excluding the COSY-11 angular distribution data at $Q = 47\,\mathrm{MeV}$ from fitting. The resulting cross sections are displayed in Fig. 9. Although the total cross sections are reproduced with the same quality as in Fig. 8, the angular distributions shown in panels (a)–(d) at $Q = 144\,\mathrm{MeV}$ are now much flatter and bring the model results in better agreement with the data at this energy. Here, the less pronounced angular distribution is due to a flatter S_{11} resonance contribution which, in turn, is due to the change in the excitation mechanism of this resonance, in particular, due to interference effects among the exchanged meson (π, ρ, ω) contributions in the S_{11} resonance current. The predicted angular distributions at $Q = 47\,\mathrm{MeV}$ in panels (a)–(d) are now practically isotropic. They may be considered as being still compatible with the data given the experimental error bars. However, the overall results in Figs. 8 and 9 may also indicate that the COSY-11 and DISTO angular distribution data could be incompatible with each other. In this connection, it is interesting to note that the angular distribution measured recently in $pp \to pp\eta$ at $Q = 41\,\mathrm{MeV}$ is completely isotropic [59]. There, the dominant η-production mechanism is the $S_{11}(1535)$ resonance current [58]. Since in the present model, the dominant η'-production mechanism is the $S_{11}(1650)$ resonance current, it is natural to expect a similar feature for the angular distribution in both reactions. Possible differences may, however, originate from the eventual difference in the excitation mechanism of these two S_{11} resonances as mentioned above. For this purpose, it would be very interesting to measure other observables, such as the invariant mass distribution, which are more sensitive to excitation mechanisms of nucleon resonances [58]. In any case, independent measurements of the angular distribution for energies $Q > 50\,\mathrm{MeV}$ would help resolve the issue as far as the shape of the angular distribution is concerned.

4 $\gamma + p \to p + \eta'$: preliminary data from JLab

In this section we briefly analyze the newly obtained (preliminary) data on the $\gamma + p \to p + \eta'$ reaction at JLab by the CLAS collaboration [38]. The

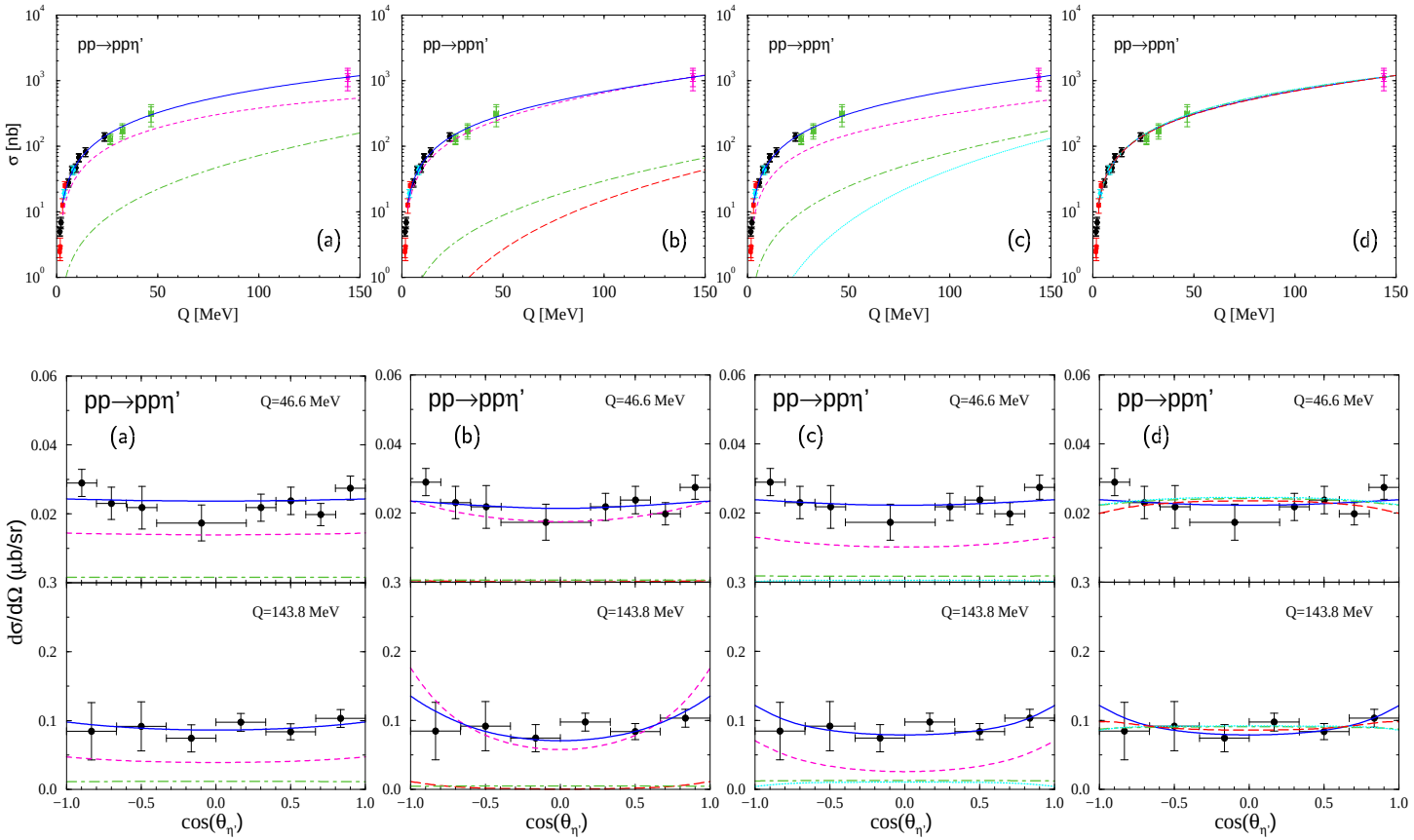

Figure 9: Same as Fig. 8, except that now the 47-MeV angular distribution data set is excluded when fitting the hadronic parameters.

result we show below is a part of the on going analysis of the new data and, therefore, by no means complete and final. First of all, as can be seen from the contribution by B. Ritchie to this meeting, the accuracy of the new CLAS data is impressive which allows a much more quantitative analysis then was possible until now. Secondly, the new data differ considerably from the SAPHIR data [30] both in the absolute normalization and the shape of the angular distributions. This will change considerably the parameter values extracted in sect.2 using the SAPHIR data. However, the qualitative features discussed there remain unchanged.

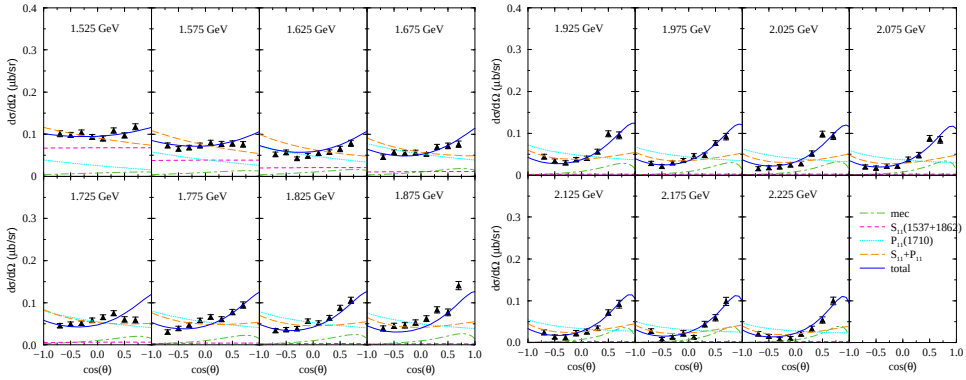

Figure 10: Fit results to the (preliminary) differential cross sections for $\gamma p \to p\eta'$ obtained by the CLAS collaboration [38].

Fig.10 shows our fit results to the preliminary CLAS data [38]. Here, we follow the same fitting procedure applied in sect.2. In contrast to the SAPHIR data [30] discussed in sect.2, here the new data require at least two S_{11} resonances, in addition to a P_{11} resonance and the t-channel meson exchange contributions, in order to achieve the fit quality as shown in Fig.10. The nucleonic current worsen the fit quality, i.e., the data prefer no nucleonic current. The resulting masses of the resonances are $m_{P_{11}} = 1710$ MeV and, $m_{S_{11}} = 1537$ and 1862 MeV for the two S_{11} resonances. The lowest mass S_{11} and the P_{11} resonances may be identified with the known $S_{11}(1535)$ and $P_{11}(1710)$ resonances, respectively [12]. The higher mass S_{11} resonance in the present work is compatible with the one-star (*) resonance with $J^P = 1/2^-$ around 1.9 GeV [12]. Also, a quark model by Metsch [61] predicts a $J^P = 1/2^-$ resonance in the same mass region. Overall, the data are reproduced quite well both in angular shape and in absolute normalization, except at the incident energy of 1.875 GeV, where they are underestimated by a factor of ~ 1.3. This might suggest a narrow bump in the data (note that the data are taken in steps of 50 MeV energy bin). In fact, a three

dimensional plot of the data shows a bump structure at about 1.875 GeV and for forward scattering angles. Whether such a bump structure is actually present in the final data or not remains to be confirmed. At the moment, it is too premature to make any definite statement about it.

5 Summary

We have described consistently the $\gamma p \to p\eta'$ and $pp \to pp\eta'$ reactions within an approach based on a relativistic meson-exchange model of hadronic interactions. The model includes the nucleonic and the mesonic, as well as the nucleon-resonance currents. The photoproduction process is made gauge-invariant by adding a phenomenological contact current that parametrizes the effect of the final-state interactions. The $pp \to pp\eta'$ is described within the distorted-wave Born approximation in which both the initial and final state NN interactions are taken into account explicitly.

For η' photoproduction, we have shown that the mesonic as well as the S_{11} and P_{11} resonance currents are important to describe the existing data. Our analysis, where the widths of the resonances were set to $\Gamma_{N^*} = 150\,\mathrm{MeV}$, yields a position close to 1650 MeV and 1870 MeV for the S_{11} and P_{11} resonances, respectively. This suggests that the former resonance may well be identified with the known $S_{11}(1650)$ resonance [12], whose quoted width is $\Gamma_{S_{11}} = 180\,\mathrm{MeV}$. The P_{11} resonance, in contrast, does not correspond to any known resonance. It is tempting to identify it with one of the missing resonances predicted at 1880 MeV with the correspond width of $\Gamma_{P_{11}} = 155\,\mathrm{MeV}$ [28, 55]. We emphasize, however, that one should be cautious with such an identification of the resonances. As we have seen, the cross section data alone do not impose enough constraints for an unambiguous determination of the resonances. To do so probably requires more exclusive data than just the cross sections. Moreover, the extracted values of the resonance masses are quite sensitive to the model used in the description of the photoproduction process. In particular, the issue of Regge trajectories versus conventional vector meson exchanges (with form factors) is of extreme importance. These points require further investigation before a conclusive identification of the resonances can be made.

Our study also shows that the nucleonic current should be relatively small. Indeed, the available photoproduction data prefer this current to be compatible with zero. In any case, the $NN\eta'$ coupling constant cannot be much larger than $g_{NN\eta'} = 3$. The η' photoproduction reaction may impose a more stringent constraint on $g_{NN\eta'}$, provided one measures the cross sections

at higher energies and backward angles. In this respect, as we have also shown, spin observables such as the photon asymmetry might be suited better than the cross sections. It should be noted that the result pertaining here to the $NN\eta'$ coupling constant is, of course, a model dependent one. Indeed, what is relevant in our calculations is the product of $g_{NN\eta'}$ and the associated form factor.

We have also addressed the contradictory conclusions as to the underlying reaction mechanisms arrived in the recent work by two independent groups [35, 36]. In our consistent calculations, whether introducing a form factor at the electromagnetic vertex in the t-channel meson-exchange current or using the Regge trajectories instead, one arrives at the same conclusion; namely, the observed angular distribution is due to the interference between the t-channel and the nucleon resonance s- and u-channel contributions, irrespective of the particular approach one uses. It is conceivable, therefore, that the phenomenological aspects of the various approaches (including the present one) may be simulating the same physics not taken into account explicitly.

As for the $pp \to pp\eta'$ reaction, the present study yields the S_{11} resonance as the dominant contribution to the production current. The P_{11} resonance, mesonic and nucleonic currents are much smaller than the S_{11} resonance current. The combined analysis of this and the photoproduction reaction was crucial for these findings. The details of the excitation mechanism of the S_{11} resonance, however, are not constrained by the currently existing data. To learn more about the relevant excitation mechanism, observables other than the cross sections, such as the invariant mass distribution, are necessary [58], in addition to measuring the $pn \to pn\eta'$ and/or $pn \to d\eta'$ process. This process will help disentangle the isoscalar and isovector meson-exchange contributions.

The present model cannot describe the flat angular distribution in $pp \to pp\eta'$ measured by the DISTO collaboration [40] at $Q = 144\,\mathrm{MeV}$, once the recently measured angular distribution by the COSY-11 collaboration [41] at $Q = 47\,\mathrm{MeV}$ is included in a global fitting for the relevant hadronic coupling parameters. The calculated result exhibits a pronounced angular dependence. If we wish, however, a flatter angular distribution at $Q = 144\,\mathrm{MeV}$ — compatible with the DISTO data within the given experimental uncertainties — can be achieved provided the $Q = 47\,\mathrm{MeV}$ angular distribution data is excluded from fitting. Doing so, the predicted angular distribution at $Q = 47\,\mathrm{MeV}$ comes out to be nearly completely isotropic. Although this seems still compatible with the COSY-11 data, the latter exhibits some angular dependence which is too disturbing to be ignored. Independent

measurements of the angular distribution for excess energies $Q > 50\,\mathrm{MeV}$ will help resolve this issue.

The new high precision data from the CLAS collaboration will certainly allow a much more quantitative analysis of the η' photoproduction reaction than was possible before. These new data differ considerably from the SAPHIR data both in the normalization and in the shape of the angular distribution. As a consequence, the fitted values of the resonance masses differ from those found from the analysis of the SAPHIR data. The bump structure observed in the preliminary CLAS data needs to be confirmed before any definite statement can be made about it.

Finally, the results of the present work should provide useful information for further investigations, both experimentally and theoretically, of the $\gamma N \to N\eta'$ and $NN \to NN\eta'$ reactions.

Acknowledgments

I would like to thank the organizers of this meeting for giving me the opportunity to present this material and for their kind hospitality. I thank Helmut Haberzettl for the collaboration which resulted in the material presented here. I also would like to thank Mike Dugger and Barry Ritchie for providing the preliminary CLAS data. The financial support from COSY (Grant No.41445282 (COSY-58)) is also acknowledged.

References

[1] J. Kogut and L. Susskind, Phys. Rev. **D 10** (1974) 3468; Phys. Rev. **D 11** (1975) 3594; E. Witten, Nucl. Phys. **B 149** (1979) 285; Ann. Phys. **128** (1980) 363; G. 't Hooft, Phys. Rep. **142** (1986) 357.

[2] S. Weinberg, Phys. Rev. **D 11** (1975) 3583.

[3] G. 't Hooft, Phys. Rev. Lett. **37** (1976) 8.

[4] E. Witten, Nucl. Phys. **B 156** (1979) 269.

[5] G. Veneziano, Nucl. Phys. **B 159** (1979) 213.

[6] G. Christos, Phys. Rep. **116** (1984) 251.

[7] T. Feldmann, P. Kroll, and B. Stech, Phys. Rev. **D 58** (1998) 114006; Phys. Lett. **B 449** (1999) 339; T. Feldmann, Int. J. Mod. Phys. **A 15** (2000) 159; T. Feldmann and P. Kroll, Phys. Scripta **T 99** (2002) 13.

[8] H. Leutwyler, Nucl. Phys. Proc. Suppl. **64** (1998) 223; R. Kaiser and H. Leutwyler, Eur. Phys. J. **C 17** (2000) 623.

[9] T. Feldmann and P. Kroll, Eur. Phys. J. **C 5** (1998) 327.

[10] KLOE Collaboration, Phys. Lett. **B 541** (2002) 45.

[11] H. H. Jones and M. D. Scadron, Nucl. Phys. **B 155** (1979) 409.

[12] Particle Data Group, Eur. Phys. J. **C 15** (2000) 1.

[13] A. Cordier *et al.*, Nucl. Phys. **B 172** (1980) 13; S. I. Dolinsky *et al.*, Phys. Rep. **202** (1991) 99.

[14] C. B. Dover and P. M. Fishbane, Phys. Rev. Lett. **64** (1990) 3115.

[15] G. 't Hooft, Phys. Rev. **D 14** (1976) 3432.

[16] A. De Rújula, H. Georgi, and S. L. Glashow, Phys. Rev. **D 12** (1975) 147.

[17] P. Ball, J.-M. Frere, and M. Tytgat, Phys. Lett. **B 365** (1996) 367;

[18] B. Diekmann, Phys. Rep. **159** (1988) 99; J. Jousset *et al.*, Phys. Rev. **D 41** (1990) 1389.

[19] B. H. Behrens *et al.*, CLEO Collaboration, Phys. Rev. Lett. **80** (1998) 3710; T. E. Browder *et al.*, CLEO Collaboration, *ibid.* **81** (1998) 1786.

[20] D. Atwood and A. Soni, Phys. Lett. **B 405** (1997) 150; Phys. Rev. Lett. **79** (1997) 5206; W.-S. Hou and B. Tseng, *ibid.* **80** (1998) 434; M. R. Ahmady, E. Kou, and A. Sugamoto, Phys. Rev. **D 58** (1998) 14015; E. Kou, *ibid.* **63** (2001) 054027.

[21] S. D. Bass, Phys. Lett. **B 463** (1999) 286.

[22] J. Ashman *et al.*, Phys. Lett. **B 206** (1988) 364.

[23] G. M. Shore and G. Veneziano, Nucl. Phys. **B 381** (1992) 23.

[24] T. Hatsuda, Nucl. Phys. **B 329** (1990) 376; A. V. Efremov, J. Soffer, and N. A. Törnqvist, Phys. Rev. Lett. **64** (1990) 1495; Phys. Rev. **D 44** (1991) 1369.

[25] G. M. Shore and G. Veneziano, Phys. Lett. **B 244** (1990) 75.

[26] S. Okubo, Phys. Lett. **5** (1963) 165; G. Zweig, CERN Report No. TH412, 1964; J. Iizuka, Prog. Theor. Phys. Suppl. **37–38** (1966) 21.

[27] G. Altarelli and G. G. Ross, Phys. Lett. **B 212** (1988) 391; R. D. Carlitz, J. C. Collins, and A. H. Müller, *ibid.* **B 214** (1988) 229.

[28] S. Capstick and N. Isgur, Phys. Rev. **D 34** (1986) 2809; S. Capstick and W. Roberts, *ibid.* **47** (1993) 1994; **49** (1994) 4570; **57** (1998) 4301; **58** (1998) 074011.

[29] ABBHHM Collaboration, Phys. Rev. **175** (1968) 1669; Nucl. Phys. **B 108** (1976) 45.

[30] R. Plötzke *et al.*, Phys. Lett. **B 444** (1998) 555; J. Barth *et al.*, Nucl. Phys. **A 691** (2001) 374c.

[31] J. F. Zhang, N. C. Mukhopadhyay, and M. Benmerrouche, Phys. Rev. **C 52** (1995) 1134.

[32] Z. P. Li, J. Phys. **G 23** (1997) 1127.

[33] B. Borasoy, Eur. Phys. J. **A 9** (2000) 95.

[34] Q. Zhao, Phys. Rev. **C 63** (2001) 035205.

[35] W. T. Chiang, S. N. Yang, L. Tiator, M. Vanderhaeghen, and D. Drechsel, Phys. Rev. **C 68** (2003) 045202.

[36] A. Sibirtsev, Ch. Elster, S. Krewald, and J. Speth, nucl-th/0303044.

[37] Crystal Barrel Collaboration (see http://www.cb.uni-bonn.de).

[38] M. Dugger and B. R. Ritchie, private communication (see contribution by B. Ritchie to this meeting).

[39] F. Hibou *et al.*, Phys. Lett. **B 438** (1998) 41; P. Moskal *et al.*, Phys. Rev. Lett. **80** (1998) 3202; P. Moskal *et al.*, Phys. Lett. **B 474** (2000) 416; P. Moskal *et al.*, Phys. Lett. **B 482** (2000) 356.

[40] F. Balestra *et al.*, Phys. Lett. **B 491** (2000) 29.

[41] A. Khoukaz *et al.*, Eur. Phys. J. **A 20** (2004) 345.

[42] A. Sibirtsev and W. Cassing, Eur. Phys. J. **A 2** (1998) 333; V. Bernard, N. Kaiser, and U. Meißner, *ibid.* **A 4** (1999) 259; E. Gedalin, A. Moalem, and L. Razdolskaja, Nucl. Phys. **A 650** (1999) 471; V. Baru, J. Haidenbauer, C. Hanhart, A. Kudryavtsev, and J. Speth, Eur. Phys. J. **A 6** (1999) 445.

[43] K. Nakayama, H. F. Arellano, J. W. Durso, and J. Speth, Phys. Rev. **C 61** (1999) 024001.

[44] B. C. Pearce and I. R. Afnan, Phys. Rev. **C 34** (1986) 991.

[45] H. Haberzettl, Phys. Rev. **C 56** (1997) 2041.

[46] H. Haberzettl, C. Bennhold, T. Mart, and T. Feuster, Phys. Rev. **C 58** (1998) R40.

[47] R. M. Davidson and R. Workman, Phys. Rev. **C 63** (2001) 025210.

[48] K. Nakayama and H. Haberzettl, Phys. Rev. **C 69** (2004) 065212.

[49] K. Nakayama, J. Speth, and T.-S. H. Lee, Phys. Rev. **C 65** (2002) 045210.

[50] Ch. Hanhart and K. Nakayama, Phys. Lett. **B 454** (1999) 176.

[51] R. Machleidt, Adv. Nucl. Phys. **19** (1999) 189.

[52] H. Garcilazo and E. Moya del Guerra, Nucl. Phys. **A 562** (1993) 521.

[53] K. Nakayama, A. Szczurek, C. Hanhart, J. Haidenbauer, and J. Speth, Phys. Rev. **C 57** (1998) 1580.

[54] G. Höhler, πN Newsletter **14** (1998) 168.

[55] S. Capstick *et al.*, Phys. Rev. **C 59** (1999) R3002.

[56] M. Batinić *et al.*, Phys. Rev. **C 51** (1995) 2310; *ibid.* **57** (1998) 1004.

[57] W. Grein and P. Kroll, Nucl. Phys. **A 338** (1980) 332.

[58] K. Nakayama, J. Haidenbauer, C. Hanhart, and J. Speth, Phys. Rev. **C 68** (2003) 045201.

[59] M. Abdel-Bary *et al.*, Eur. Phys. J. **A 16** (2003) 127.

[60] See, e.g., J. K. Storrow, in *"Electromagnetic Interactions of Hadrons"*, edited by A. Donnachie, and G. Shaw, (Plenum Press, 1978), Vol. I, p. 263.

[61] B. Metsch, hep-ph/0403118.

Recent results on η and η' photoproduction on the proton

B. G. Ritchie
Arizona State University
for the CLAS Collaboration

Abstract: The experimental situation on η and η' photoproduction on the proton is reviewed, emphasizing progress made since 2001. New preliminary results for η' photoproduction on the proton from Jefferson Lab are presented. Experimental results are compared with several theoretical approaches, with an emphasis on consequences for understanding baryon spectroscopy.

1 Introduction

Much of this meeting has concerned itself with the properties of the η and η' mesons themselves. However, in this contribution, I will take a different vantage point by focusing on baryon spectroscopy. This is, in part, because the ASU Meson Physics Group and many of my colleagues at Jefferson Lab are excited about the prospects of using our results on meson photo- and electro-production to gain a better understanding of the quark structure of the nucleon.

What is the ultimate goal of taking this approach? We want to understand in detail the structure of the nucleon in terms of its quark composition. Such an understanding will require, among other things, identification of the excited states of the nucleon, determining the photon coupling strengths of those excitations, measuring branching ratios for various final state decay modes, and developing a consistent overall theoretical picture of those decay modes. All this represents a very demanding "shopping list"!

Within this shopping list, my group at ASU has been particularly interested in focusing on eta meson photoproduction because the η and η' mesons form a unique tool for helping unravel the puzzles of nucleon structure. As pseudoscalar mesons, the eta mesons complement the large database that exists for pion photo- and electroproduction, from which most of our current

knowledge of the nucleon excited states has been gleaned. While both eta mesons contain a strange quark contribution, the relative size of that component is different for η and η', providing a "selectable strangeness" probe. Finally, as isoscalar mesons, the η and η' mesons, to first order, only couple to the isospin 1/2 nucleon resonances, unlike the pion which couples to the isospin 1/2 and 3/2 resonances. Eta meson photoproduction thus provides an "isospin filter" for the nucleon resonance spectrum.

Even though these are very good reasons for pursuing eta meson production experiments, the dataset until recently has been quite limited and puzzling. I will divide the relatively short history of exploration of the eta mesons into several eras. Prior to the end of 2001, there was a period of initial exploration quite limited by experimental facilities, the "classical era." From 2002 onward, the "modern era," data from much more capable facilities have begun to roll in, providing a much broader view of the process. In the "future," we will be seeing more extensive datasets of polarization observables that will provide a much more detailed view of the production process than permitted by differential cross sections alone. The remainder of this contribution will follow those divisions, with the emphasis on the modern era.

2 The Classical Era: Before 2002

Prior to 2002, the earlist published experimental results [1, 2, 3, 4, 5, 6, 7, 8] on η photoproduction were primarily differential cross sections, usually either close to threshold and/or with rather sparse angular coverage. Even within this limited dataset, however, the dominance of the photoproduction process by the $S_{11}(1535)$ resonance was well-established. Attempts to extract the photon helicity amplitude for this resonance were greatly handicapped by uncertainties in how to treat contributions to the process other than the $S_{11}(1535)$ resonance. Thorough angular coverage of the reaction with high statistics became available from the TAPS collaboration [9], but those data were limited to energies from threshold up to the maximum where the total cross section is dominated by the $S_{11}(1535)$. Within this limited dataset, nonetheless, were indications or suggestions of contributions from other resonances (such as the $D_{13}(1520)$).

With respect to spin observables, early results from ELSA [10] and GRAAL [11] provided data on Σ and T, respectively. These studies not only provided evidence for contributions from the $S_{11}(1535)$ and $D_{13}(1520)$ resonances, but also suggested possible contributions from, for instance, the

$P_{13}(1720)$ and $D_{15}(1675)$. While these data were very useful, they also included some puzzles that various theoretical approaches found very difficult to address [12].

The situation with respect to η' photoproduction prior to 2001 was even less promising. No polarization observable data were available for η' photoproduction. Aside from those differential cross sections gleaned from a dozen or so events detected in early bubble chamber experiments (when the η' was called the X^0), the only differential cross sections for η' photoproduction on the proton were those from the SAPHIR collaboration [13]. From the approximately 300 events detected over the photon energy range from 1.44 to 2.64 GeV, angular distributions were obtained that hinted at resonances near threshold, though the uncertainties were quite large, and the results were somewhat clouded by indications of problems with the absolute normalization of the dataset. Because even the lowest energy bin suggested evidence of a non-isotropic angular distribution, these data hinted that, like the situation for η photoproduction, η' photoproduction on the proton might also be dominated at theshold by a resonance. The resonance fit provided by the SAPHIR group for their data produced masses and widths for two possible resonance, but the parameters for those resonances were difficult to relate to any well-known resonances.

With this rather limited dataset, theoretical attempts to describe η and η' photoproduction on the nucleon were severely handicapped, often restricted to simply "bump-hunting." Even in the case of η photoproduction near threshold, where a single resonance dominates the process, extracting information about that resonance was very problematic, with large uncertainties in the parameters extracted. The overlap of the η photoproduction dataset with the existing pion photoproduction dataset remained very small, so that coupled channels approaches were limited. Approaches to the limited dataset on spin observables for η photoproduction called for additional data to resolve the puzzles uncovered. The dataset with respect to η' photoproduction was simply too limited to provide much insight. To be useful for baryon spectroscopy, these sparse data on η and η' photoproduction needed to be greatly supplemented if coupled channels approaches were to be constrained in any useful way. Such approaches are demanded if one wishes to move to a constituent quark description of the nucleon.

3 Experimental capabilities at Jefferson Lab

Improvements in the database for a reaction channel generally arise from extensions of the capabilities of experimental facilities. This is certainly true for the case of eta meson photoproduction. Here, a brief overview of the salient features of the facility in Hall B at Jefferson Lab is presented to provide some idea of the possibilities there.

The electron accelerator at Jefferson Lab, located in Newport News, Virginia, provides up to three continuous electron beams with energies selectable in the range of 0.8 to 5.7 GeV. Currents up to 200 μA are available, with polarization up to 75%. The electron beams can be delivered simultaneously to 3 experimental halls, and, with some constraints, the three beams may have different energies.

Experimental Hall B at Jefferson Lab contains a pair of instruments particularly useful for photoproduction studies: a bremsstrahlung photon tagger and the CEBAF Large Acceptance Spectrometer (CLAS). Both have been described in some detail elsewhere [16, 17], so only the elements of particular interest here are mentioned.

The photon tagger provides tagged photons with energies of 20-95% of the incident electron beam energy. With the electron energy ranges noted above, this permits a choice of a range of energies from 160 MeV up to about 5.5 GeV. Portions of the tagger focal plane can be switched off or prescaled to emphasize particular photon energy ranges. Polarization of the photons can be either circular (using a longitudinally polarized electron beam) or linear (using an oriented diamond crystal for coherent bremsstrahlung). Photon fluxes up to a few times 10^7/s are possible.

The major CLAS subsystems are shown in Figure 1. Here we focus only on those systems of interest for the photoproduction experiments described herein. The detector is built around a six-sectored toroidal superconducting magnet. Each sector is instrumented for tracking and time-of-flight measurement. A cryogenic liquid hydrogen target is located at the center of the detector. A set of scintillators, the "start counter" (not shown in the figure) surrounds this target to provide a timing signal for charged particles passing into the magnetic field of a sector. Within each sector is a set of three drift chambers for tracking information (with a total of 35,000 cells in the detector volume). At the outer region of each sector, a scintillator array (with 114 photomultiplier tubes per sector), in conjunction with the start counter, provides the time-of-flight through the sector.

The tagger-CLAS combination provides very good particle identification, as can be seen in Figure 2. The kinematical information available from

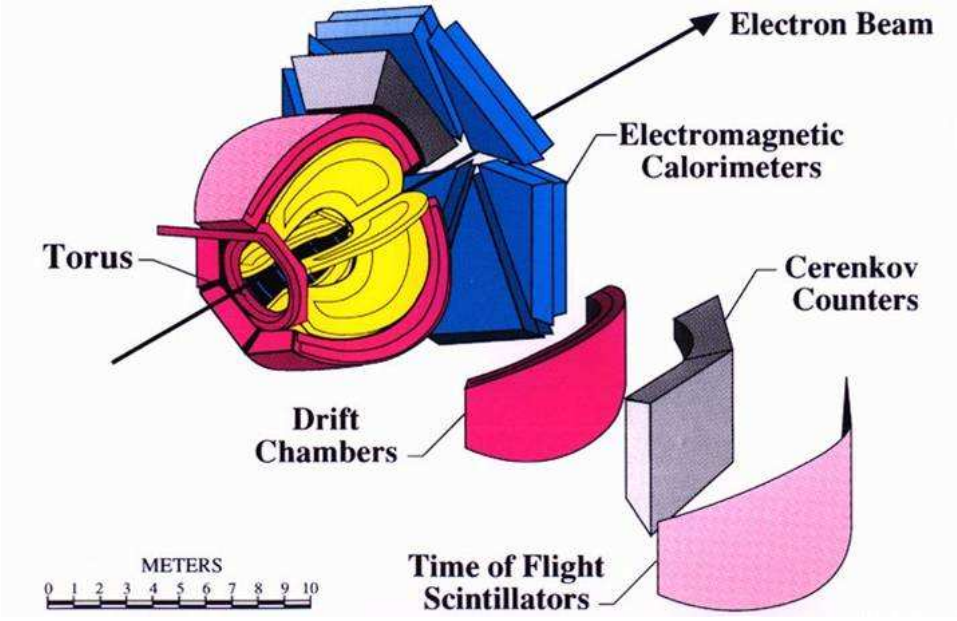

Figure 1: A cutaway view showing the major systems of the CEBAF Large Acceptance Spectrometer in Hall B at Jefferson Lab.

the tagger, tracking, and time-of-flight systems, coupled with the large acceptance of the system, permits the use of missing mass reconstruction by using the kinematical information from the recoiling proton to identify the mesons photoproduced in the final state. An example of this missing mass reconstruction for the $\gamma + p \rightarrow p + X$ is shown in Figure 3. One can clearly and cleanly identify peaks for the π^0, η, the bump corresponding to the ρ and ω, the η', and even the ϕ.

Because of the large solid angle subtended by CLAS, the detection efficiency for the recoil proton can be measured empirically with the reaction $\gamma + p \rightarrow \pi^+\pi^- p$. By triggering on two charged particle events, and using solely the kinematical information from the pions to reconstruct the proton, one can then look to see if the proton was indeed detected in the CLAS. This empirically measured detector response agrees very well with the simulated response. For the cross sections presented here for Jefferson Lab, the empirical detector response is used.

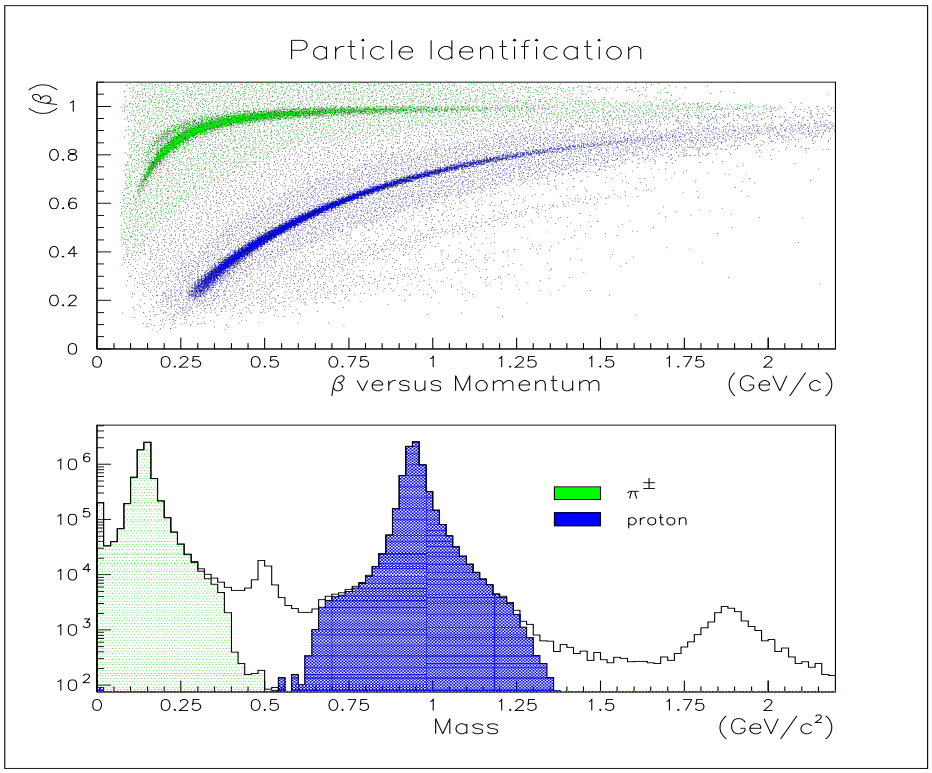

Figure 2: Particle identification performance of tagger-CLAS combination.

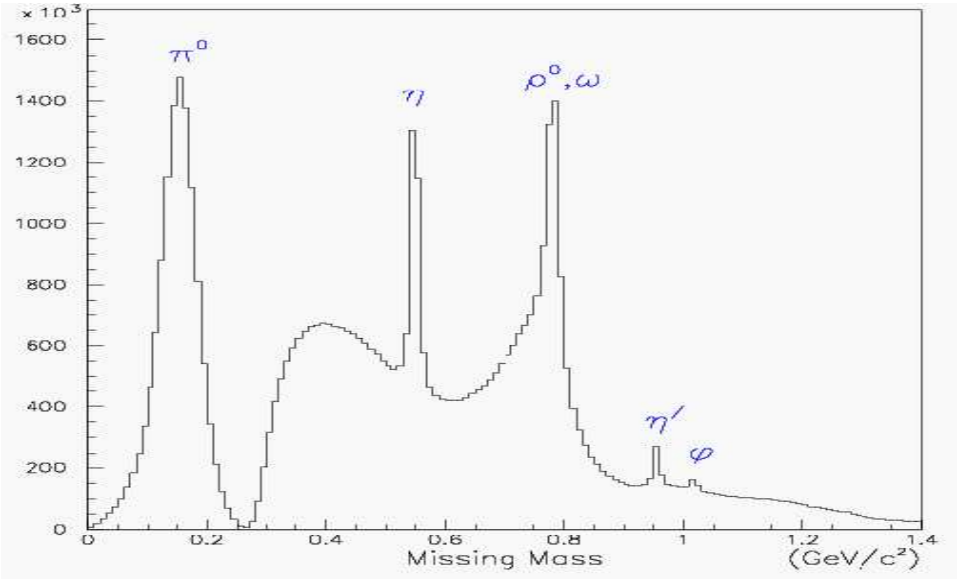

Figure 3: Reconstructed missing mass spectrum using tagger and CLAS kinematical information for the recoil proton assuming the reaction $\gamma + p \rightarrow p + X$.

4 The Modern Era: 2002 to present

In 2002, the database for η and η' photoproduction began to enlarge considerably with the publication of the first results from GRAAL [14]and Jefferson Lab [15]. These new facilities have tremendous capabilities for unraveling the details of nucleon structure.

The results of the 2002 publications are shown in Figures 4 and 5, with comparisons to the earlier TAPS data [9] in Figure 4. Where they overlap the TAPS data, the GRAAL and Jefferson Lab data are in very good agreement. However, for the energies shown in Figure 4, the GRAAL and Jefferson Lab data overlap each other and map out the previously unmeasured upper portion of the $S_{11}(1535)$ region and extend beyond it. Furthermore, as seen in Figure 5, the Jefferson Lab data extend up to E_γ 1.95 GeV ($W \approx 2.1$ GeV). What is clear from the Jefferson Lab data is, as one goes to higher incident photon energies, the cross sections begin to show strong forward peaking, usually a signal indicating a growing importance for $t-$channel meson exchange.

To obtain total cross sections for these Jefferson Lab data, an extrapolation to unmeasured angles was required. In Ref. [15], an isobar model for η photo- and electroproduction (ETA-MAID) [18] was extended and

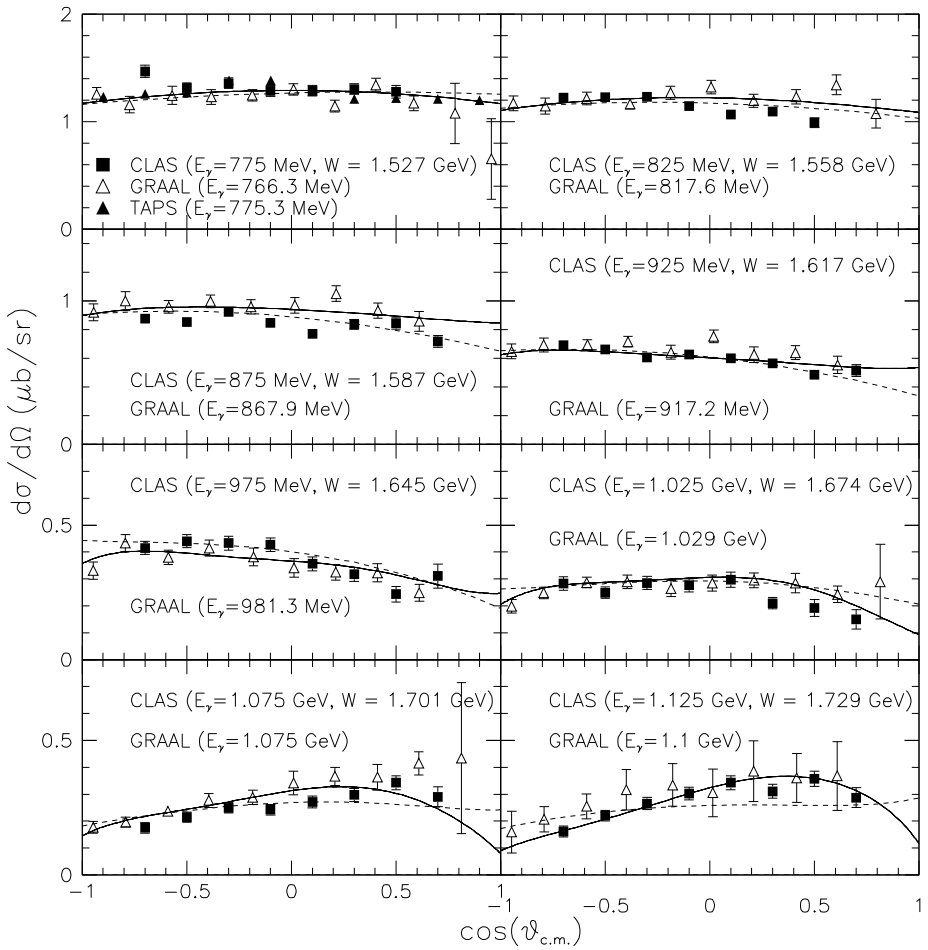

Figure 4: Differential cross sections for the reaction $\gamma + p \rightarrow p + \eta$ from TAPS [9] (solid triangles), from GRAAL [14] (open triangles), and Jefferson Lab [15] (squares). Calculations shown are the re-fit ETA-MAID calculation ([22], solid curve) and the chiral quark model ([29], dashed line).

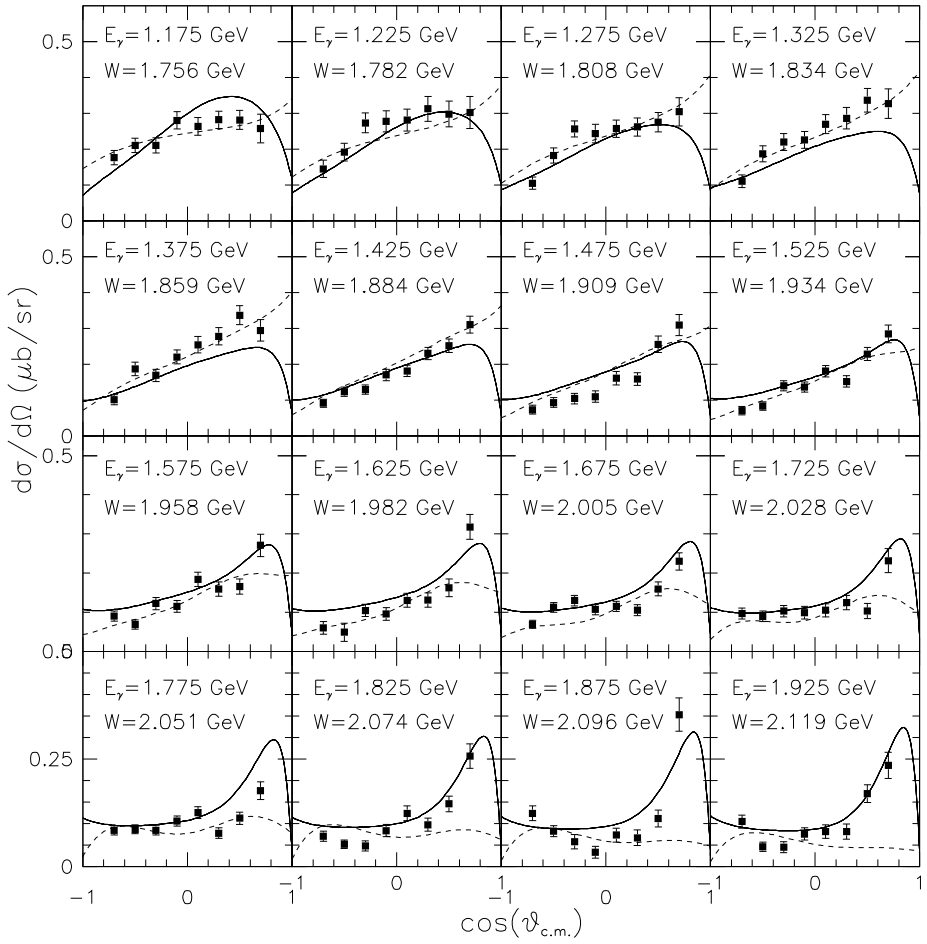

Figure 5: Differential cross sections for the reaction $\gamma + p \to p + \eta$ from Ref. [15]. Curve labels as in Figure 4.

used for the extrapolation of the CLAS data to unmeasured angular regions. The previous version of ETA-MAID used the differential cross sections for η photoproduction reported in Refs. [9, 14], polarization observable measurements on the same reaction [11], and electroproduction measurements reported in Refs. [19, 20], to arrive at parameters for their multiple $s-$channel resonance model, which included contributions from Born terms and vector meson exchange. Those earlier data were described well using the $D_{13}(1520)$, $S_{11}(1535)$, $S_{11}(1650)$, $D_{15}(1675)$, $F_{15}(1680)$, $D_{13}(1700)$, $P_{11}(1710)$, and $P_{13}(1720)$ resonances, with values for masses and widths of the resonances in good agreement with accepted values [21].

For Ref. [15], the ETA-MAID fit was performed again [22], with these CLAS differential cross sections added to the data set used previously. The results of this re-fit are compared with the data in Figs. 4 and 5 (solid lines). This re-fit ETA-MAID model (REM) generally reproduces the shapes of the observed cross sections quite well, including the forward peak seen at the highest energies, usually interpreted to be due to $t-$channel processes. However, while the predicted shapes mimic those observed, the new calculations fall below the differential cross sections reported here around W=1.85 GeV, and are above the data at $W \geq$1.9 GeV.

Since the differential cross section shapes from REM were similar to those observed by CLAS, these shapes were used in Ref. [15] to approximate the differential cross section shape for regions beyond the CLAS data angular coverage in order to make total cross section estimates σ_{est} at each photon energy. These are shown in Figure 6. Again, the total cross section estimates from GRAAL, TAPS, and CLAS agree quite well, with the exception of the region around W =1.7 GeV, where the GRAAL data show a precipitous rise in the total cross section. Since the differential cross sections for CLAS and GRAAL are in agreement in this region, this difference is solely attributable to the extrapolation to unmeasured angles. It is unlikely the total cross section rises as sharply as the extrapolations reported in Ref. [14] suggest.

As noted above, the overarching goal is a description of these data in terms of the quark constituents of the nucleon. As an example, Saghai and Li [23, 24] used a chiral constituent quark model (χQM), based on $SU(6)\otimes O(3)$ symmetry broken by gluon exchange interactions, to determine nucleon resonance quark wave functions and to study decays to various channels. Their approach has been applied to η photoproduction [23], using the set of resonances noted above in the ETA-MAID model and the $P_{11}(1440)$, $P_{13}(1900)$, and $F_{15}(2000)$ resonances. The dataset investigated included the data used for the original ETA-MAID work, plus polarized target asymmetry data for η photoproduction from ELSA [25].

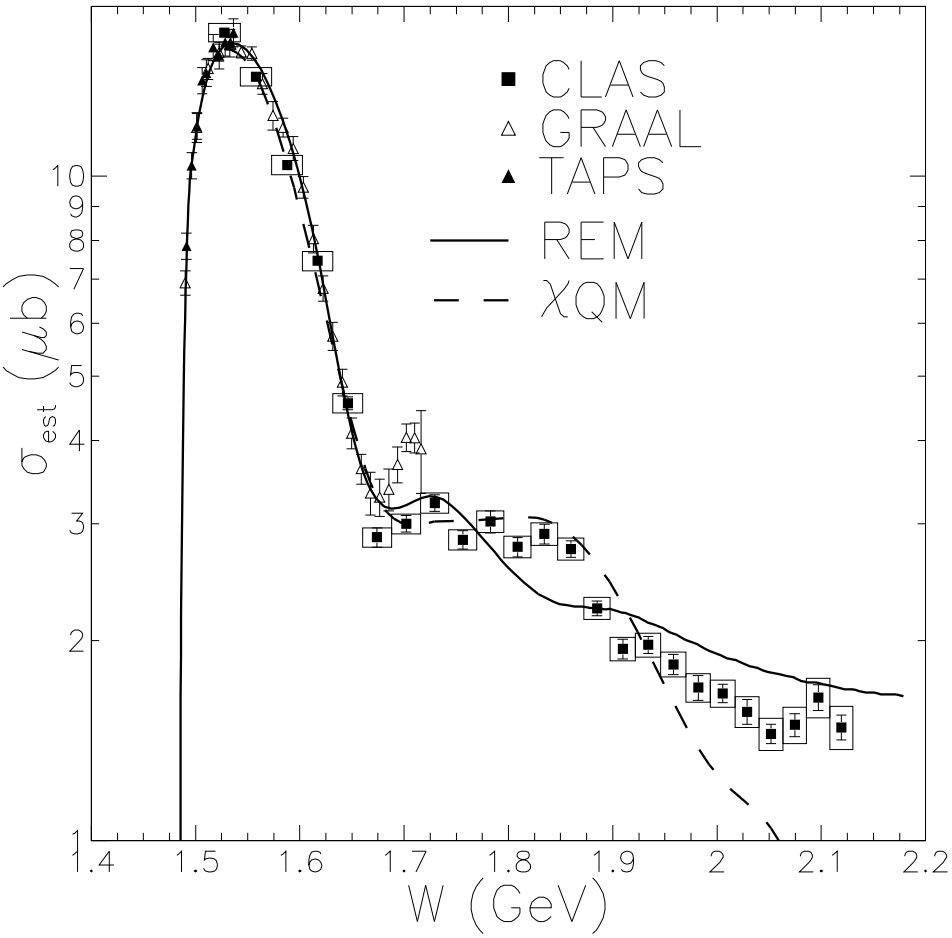

Figure 6: Total cross section estimates for the reaction $\gamma + p \rightarrow p + \eta$ from CLAS([15]), GRAAL ([14]) and TAPS ([9]). Calculations shown are the re-fit ETA-MAID calculation (Ref. [22], REM, solid curve) and the chiral quark model (Ref. [29], χQM, dashed line).

Good agreement with this data set was obtained, but the results were consistent with the broken $SU(6)\otimes O(3)$ symmetry only if an additional S_{11} resonance, not predicted by the quark model, was present at W=1.7-1.8 GeV. A third S_{11} resonance near W=1.8 GeV has been suggested by others [26, 27, 28], though the evidence is not strong. Interestingly, this resonance is near where the REM predictions fall below the data of Ref. [15].

In Ref. [15], preliminary calculations [29] used the χQM to fit their original dataset and the CLAS results. The resulting fit is shown in Figs. 4-6 (dashed curve). These preliminary results are generally in good agreement

with data for $W \leq 1.9$ GeV. Again, interestingly, including the third S_{11} resonance noted above in these preliminary calculations, with a mass 1.79 GeV and width of 250-350 MeV, markedly improved the fit to the CLAS data [29]. The χQM agreement with the CLASdata around W=1.85 GeV is considerably better than with the REM calculation, which lacks this third S_{11} resonance. However, above W=1.9 GeV, the χQM shapes are inconsistent with the peak at forward angles in the differential cross section as the energy increases.

The CLAS differential cross section data taken with the χQM predictions, thus, also provide hints of a third S_{11} resonance, with a mass near 1.8 GeV coupling to the ηN channel. However, a stronger case for that resonance must include simultaneous predictions of more observables for this reaction and other channels. Lastly, the failure of the χQM above 1.9 GeV to match the CLAS data here also provides evidence that resonances beyond those presently included in the χQM calculations may also couple to the ηN channel.

5 The Future

5.1 Near future: 2004 to 2005

Within the very near future, GRAAL should release new differential cross section data on the photoproduction of η mesons, improving the statistical accuracy of their previous measurements and extending those in energy up to about E_γ =1.4 GeV [30]. Preliminary versions of these cross sections are in very good agreement with the data shown in Figs. 4 and 5. The CB-ELSA group also has recently uploaded preliminary results on η photoproduction up to about 3 GeV [32]. Those data will cover the region from resonance behavior to a regime where Regge approaches might prove more successful.

Within the next year, the CLAS collaboration should be releasing the differential cross sections up to E_γ =2.25 GeV for η' photoproduction. Preliminary results for those cross sections are shown in Figure 7. In that same figure are shown the published SAPHIR data [13]. While the error bars on the SAPHIR data are quite large, an absolute normalization discrepancy between our preliminary CLAS data and the SAPHIR data is obvious. We obtained neutral pion photoproduction cross sections on the proton at the same time as those shown in Figure 7, using the same recoil proton technique. Those π^0 photoproduction cross sections are in excellent agreement with the SAID parametrization, with typical overall differences of 2% or so. Thus, the absolute normalization of the SAPHIR data does indeed appear

to be incorrect, but it does not appear to be a consistent discrepancy as a function of energy.

Since many of the theoretical approaches to η' photoproduction have been limited to explaining the older SAPHIR data, the predictions of those approaches perform poorly on the new CLAS data. Nakayama and Haberzettl have used these new preliminary cross sections in refining their formalism; Kanza Nakayama will fully describe this approach and their results elsewhere in these proceedings [31]. We show the results of their predictions as solid lines in Figure 7.

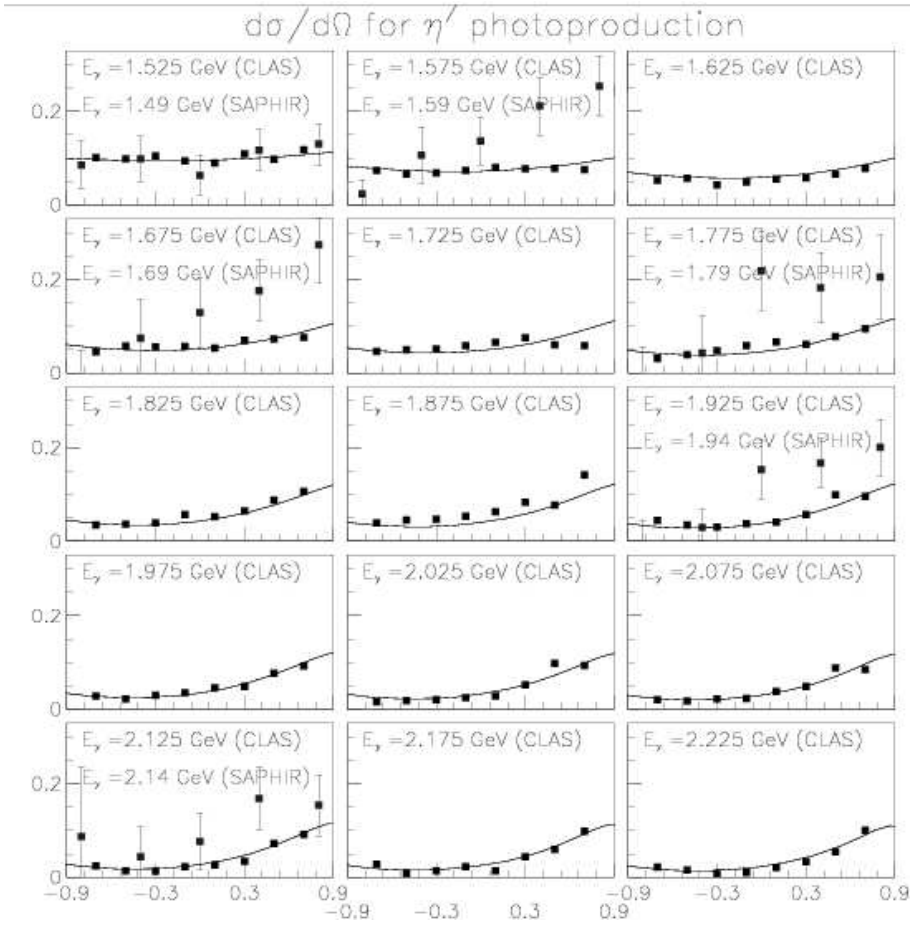

Figure 7: Preliminary CLAS differential cross sections for the reaction $\gamma+p \rightarrow p+\eta'$ compared with published results from SAPHIR [13]. Cross sections are given in μb/sr as a function of the cosine of the center-of-mass meson angle. Solid curves are results from Nakayama and Haberzettl [31].

The agreement between their predictions and our preliminary results is generally very satisfactory. But even more interesting is that the resonances they needed to describe the data are the $S_{11}(1535)$ and the $P_{11}(1710)$, two resonances long known to have significant couplings to the η. If this preliminary conclusion from their work is correct, then the combination of η and η' photoproduction for the $S_{11}(1535)$ and the $P_{11}(1710)$ resonances should provide an excellent testing ground for constituent quark models, particularly those probing the strangeness content of the nucleon.

5.2 More distant future: Plans

What's next? With regard to eta meson photoproduction, I believe we are at "childhood's end." We should recall the goal mentioned above: We want to understand in detail the structure of the nucleon in terms of its quark composition. The previously crippling limitations of the dataset are disappearing as the dataset is becoming more and more complete; baryon spectroscopy is maturing rapidly. "Simple" single-channel approaches will soon become dinosaurs. This trend will accelerate in 2005 and beyond.

On the experimental side, beyond the very near future, the ASU group is working on improving the statistical accuracy of the previous CLAS measurements on η photoproduction and to extend those in energy to just above incident photon energies of 3 GeV. We are also analyzing photon beam asymmetry data up to 2 GeV on the proton.

The ASU group is analyzing CLAS deuterium data to provide coherent photoproduction cross sections for η and η'. While some data is available for coherent photoproduction of η mesons from deuterium, our preliminary data show a clear signal for η' coherent photoproduction for the first time.

Both CLAS and GRAAL collaborations have polarized target plans for those facilities. The GRAAL efforts are very far along, with data already taken on their target, while target construction is just beginning at Jefferson Lab. When the data from those efforts become available, the results from those polarized beam, polarized target experiments on eta meson photoproduction should provide a very stringent laboratory for models of the photoproduction process.

On the theoretical side, I am hopeful we are entering a transition period. As the quality of the dataset has improved, single-channel analyses are becoming more ambiguous and less fruitful. My hope is that competing, multi-channel, quark-motivated approaches will be developed, perhaps even becoming the norm.

6 Acknowledgements

Most of the η and η' photoproduction work at CLAS is the result of the determined efforts of my colleagues in the ASU Meson Physics Group, particularly Mike Dugger. I also gladly acknowledge the assistance of other members of the CLAS Collaboration. I appreciate the cooperation and useful discussions extended during the analysis of our data and the preparation of this talk by Annalisa D'Angelo, Dominique Rebreyend, W.-T. Chiang, Charlotte Elster, Helmut Haberzettl, Kanza Nakayama, Bigan Saghai, and their colleagues. Finally, I greatly appreciate the hospitality provided by the conference organizers, particularly Pawel Moskal and Joanna Przerwa.

The ASU Meson Physics Group is supported by the National Science Foundation.

References

[1] B. Delcourt *et al.*, Phys. Lett. **B 29** (1967) 75.

[2] C. Bacci *et al.*, Phys. Rev. Lett. **20** (1968) 571; Nuovo Cimento **45** (1966) 983.

[3] Aachen-Berlin-Bonn-Hamburg-Muenchen Collaboration, Phys. Rev. **175** (1968) 1669.

[4] Cambridge Bubble Chamber Group, Phys. Rev. **169** (1968) 1081.

[5] E. D. Bloom *et al.*, Phys. Rev. Lett. **21** (1968) 1100.

[6] C. A. Heusch *et al.*, Phys. Rev. Lett. **25** (1970) 1381.

[7] S. Homma *et al.*, J. Phys. Soc. Jpn. **57** (1988) 828.

[8] S. Dytman *et al.*, Phys. Rev. **C 51** (1995) 2710.

[9] B. Krusche, *et al.*, Phys. Rev. Lett. **74** 3736 (1995).

[10] A. Bock *et al.*, Phys. Rev. Lett. **81** (1998) 534.

[11] J. Ajaka *et al.*, Phys. Rev. Lett. **81** (1998) 1797.

[12] For example, L. Tiator, D. Drechsel, G. Knoechlein, and C. Bennhold, Phys. Rev. **60**, (1999) 035210.

[13] R. Plotzke, *et al.*, Phys. Lett. **B 444** (1998) 555.

[14] F. Renard, *et al.*, Phys. Lett. **B 528** (2002) 215.

[15] M. Dugger, *et al.*, Phys. Rev. Lett. **89** (2002) 222002.

[16] D. I. Sober, *et al.*, Nucl. Instr. Meth. **A 440** (2000) 263.

[17] B. Mecking, *et al.*, Nucl. Instr. Meth. **A 503** (2003) 513.

[18] W.-T. Chiang, S.-N. Yang, L. Tiator, and D. Drechsel, Nucl. Phys. **A 700** (2002) 429.

[19] C. S. Armstrong, *et al.*, Phys. Rev. **D 60** (1999) 052004.

[20] R. Thompson, *et al.*, Phys. Rev. Lett. **86** (2001) 1702.

[21] D. E. Groom, *et al.*, Eur. Phys. J. **C 15** (2000) 1.

[22] W.-T. Chiang, private communication.

[23] B. Saghai and Z. Li, Eur. Phys. J. **A 11** (2001) 217.

[24] Z. Li and B. Saghai, Nucl. Phys. **A 644** (1998) 345.

[25] A. Bock, *et al.*, Phys. Rev. Lett. **81** (1998) 534.

[26] Z. Li and R. Workman, Phys. Rev. **C 53** (1996) R549.

[27] M. Batinić, *et al.*, Phys. Scripta **58** (1998) 15.

[28] T. P Vrana, S. A. Dytman, and T.-S. H. Lee, Phys. Reports **328** (2000) 181.

[29] B. Saghai, nucl-th/0202007.

[30] A. DeAngelo and D. Rebreyend, private communication (2003).

[31] H. Haberzettl and K. Nakayama, private communication (2004), and K. Nakayama, elsewhere in this volume.

[32] V. Crede, *et al.* (CB-ELSA Collaboration), hep-ex/0311045.

Total and Differential Cross Sections for the pp → ppη' Reaction Near Threshold

A. Khoukaz

Institut für Kernphysik, Westfälische Wilhelms-Universität Münster, Germany

Abstract: The η' meson production in the reaction $pp \to pp\eta'$ has been studied at excess energies of Q = 26.5, 32.5 and 46.6 MeV using the internal beam facility COSY-11 at the cooler synchrotron COSY. The total cross sections as well as one angular distribution for the highest Q-value are presented. The excitation function of the near threshold data can be described by a pure s-wave phase space distribution with the inclusion of the proton-proton final state interaction and Coulomb effects. The obtained angular distribution of the η' mesons is also consistent with pure s-wave production.

1 Introduction

Recently, detailed measurements on the η' meson production in the reaction channel $pp \to pp\eta'$ have been performed in the previously unexplored region close to threshold up to an excess energy of Q = 24 MeV [1, 2, 3, 4] as well at a higher excess energy of Q = 144 MeV [5]. Here we present new results on this reaction channel at intermediate excess energies of Q = 26.5, 32.5 and 46.6 MeV [6], filling the gap between the available data sets.

Due to the small relative momenta of the ejectiles in the region of low excess energies, only partial waves of the lowest order participate in the exit channel. Therefore, total and differential cross section data yield nearly unscreened information on relevant production mechanisms and allow to study final state interactions (FSI) of the participating particles. Consequently, these new data became subject of several model calculations and comparisons with the related reaction channels on the π^0 and η meson production [7, 8, 9].

In contradistinction to the corresponding η meson production channel, whose production amplitude is assumed to be dominated by the excitation of the S_{11} nucleon resonance $N^*(1535)$, the relevance of possible production diagrams to describe the η' meson formation is still controversially discussed.

2 Experiment

Measurements on the reaction $pp \rightarrow pp\eta'$ have been performed at the internal beam facility COSY-11 [10] at COSY-Jülich [11], using a hydrogen cluster target [12] in front of a COSY-dipole magnet, acting as a magnetic spectrometer. The event selection for the reaction $pp \rightarrow pp\eta'$ was performed by accepting events with two reconstructed tracks in the drift chambers, requiring both particles being identified as protons [13]. The four-momentum determination of the positively charged ejectiles yields a full event reconstruction for the reaction type $pp \rightarrow ppX$ and allows an identification of the X-particle using the missing mass method and to study angular distributions of the ejectiles. This situation is demonstrated in figure 1 for a beam momentum of $p_{beam} = 3.356$ GeV/c, corresponding to an excess energy of Q = 46.6 MeV above the η' meson production threshold.

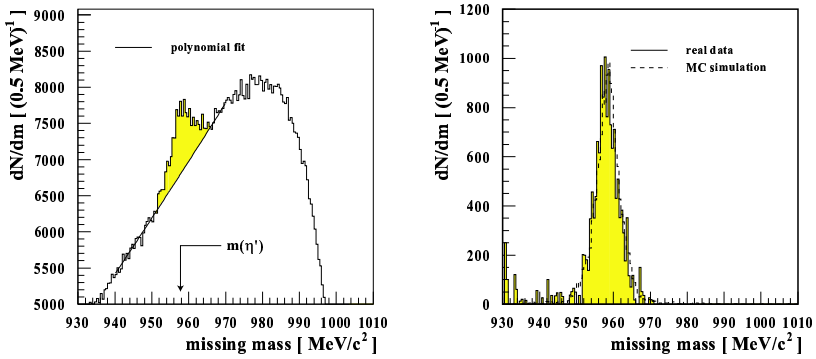

Figure 1: Missing mass distribution of the selected two track events with both particles identified as protons (Q = 46.6 MeV). The figure on the right hand side presents the experimental data after subtraction of the background (see figure on the left hand side). In addition, the resulting η' signal (solid line) is compared with expectations according to Monte-Carlo simulations (dashed line).

In the raw spectrum (left hand figure) a signal of the η' meson production is clearly visible on a background arising from multi pion production channels. The spectrum on the right hand side presents the η' missing mass peak with a content of N $\sim$ 13000 events after subtraction of the background, which was fitted by a first order polynomial. The observed mean position of the missing mass peak, $m_X = 958.1$ MeV/c^2, differs by 0.3 MeV/c^2 from the nominal value ($m_{\eta'} = 957.78 \pm 0.14$ MeV/c^2 [14]), reflecting the precision of the experimental method and the quality of the accelerator beam. The missing mass resolution amounts to $\sigma = 3$ MeV/c^2.

3 Results

In figure 2 the resulting angular distribution of the emitted η' mesons in the overall center of mass system is presented for an excess energy of Q = 46.6 MeV.

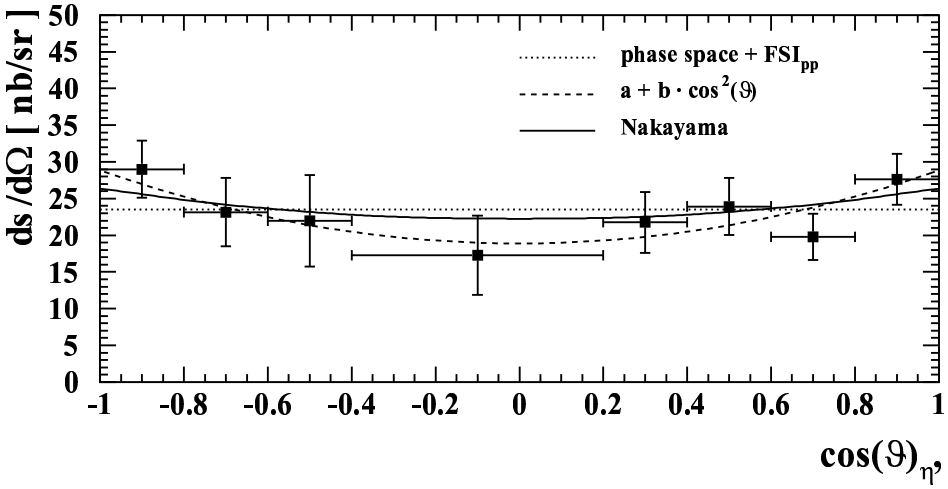

Figure 2: Angular distribution of the emitted η' meson in the center of mass system at an excess energy of Q = 46.6 MeV.

The quoted errors include statistical and systematical errors except contributions from overall systematical uncertainties (e.g. luminosity determination). The differential cross sections are compatible with an isotropic emission (dotted line), indicating a dominance of S-waves in the final state, consistent with results obtained from the DISTO collaboration at an excess energy of Q = 144 MeV [15]. However, figure 2 might also indicate contributions of higher partial waves, i.e. D-waves. An inclusion of a $\cos^2(\vartheta)$ term to account for higher partial waves leads to an adequate description of the angular distribution as demonstrated by the dashed line.
In figure 3 the results (filled circles) are compared with existing data. The solid line represents an s-wave phase space calculation (meson production matrix element $|M_0|^2$ = const.) modified by the proton-proton final state interaction (FSI) and Coulomb effects, scaled to fit the data [7]. Within the experimental errors this fit is able to describe the whole set of existent data. Therefore, one can conclude that no further assumptions like a significant η'-proton final state interaction are needed in order to describe the excitation function. In particular, distinct effects of higher partial waves can be

rejected due to the isotropy of the presented angular distribution and the one from DISTO at Q = 144 MeV [15]. The dotted curve of figure 3 represents calculations from Sibirtsev et al. [16] based on a one-pion exchange diagram including the pp final state interaction. While for excess energies below Q = 25 MeV the observed excitation function is described well, the new data from COSY-11 (filled circles) as well as the cross section from DISTO are somewhat overestimated.

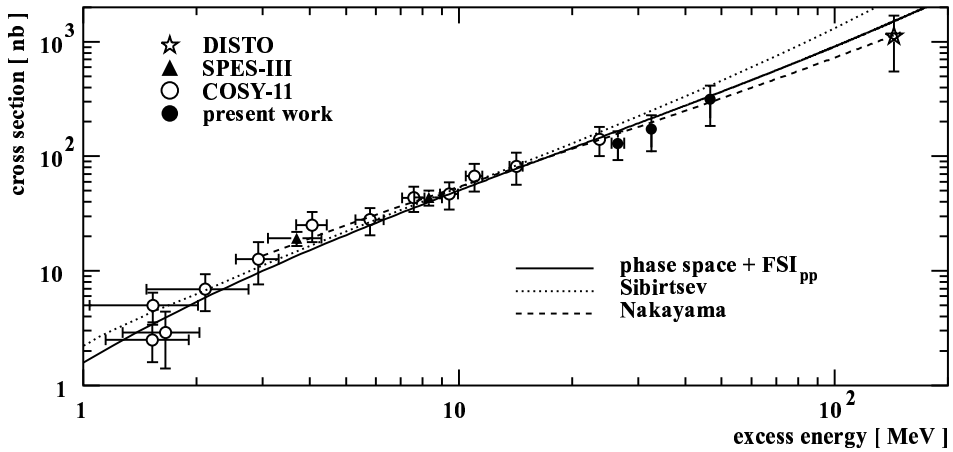

Figure 3: Total cross sections for the reaction $pp \to pp\eta'$ as a function of the excess energy Q. Filled circles correspond to the data presented in this paper and triangles, open circles and stars correspond to data from [1, 2, 3, 15], respectively. The curves are explained in the text.

Additionally, figure 2 and figure 3 show the newest calculation from Nakayama [17] for the near threshold η' meson production in proton-proton collisions (dashed lines), based on a relativistic meson exchange model. Since the relative strengths as well as the absolute scales of the considered mesonic, nucleonic and nucleon resonance currents are not known, different combinations reproducing the available total cross sections are possible. However, in a combined analysis of the η' meson production in pp and γp interactions Nakayama succeeded to describe both reactions within his model consistently [17]. In this approach the contribution of the mesonic exchange current has been fixed by the photoproduction data and appeared to be much smaller than assumed in earlier calculations [18]. On the contrary, contributions of at least an S_{11} nucleon resonance in the mass region of 1650 MeV/c^2

and probably a P_{11} resonance in the mass region of 1880 MeV/c^2 were found to be necessary in order to describe the energy dependence of the total cross sections of both the γp an pp data. Furthermore, in proton-proton collisions contributions of the nucleonic exchange current were estimated to be comparatively small in order to describe within the given uncertainties both the excitation function a well as the observed angular distributions of emitted η' mesons presented in [15] and in this work (figure 2).

4 Summary

At the COSY-11 facility the near threshold η' meson production in the reaction channel $pp \to pp\eta'$ has been studied at excess energies of Q = 26.5, 32.5 and 46.6 MeV. The obtained total cross section data fill the region of intermediate excess energies between the low energy data [1, 2, 3, 4, 5] and one data point at a high excess energy [15]. It was demonstrated that within the quoted errors the complete available excitation function can be adequately described by calculations on basis of the three body phase space behaviour including effects of the pp FSI only, and no distinct contributions from the η'-proton interaction or higher partial waves are necessary for the interpretation of the data.

References

[1] F. Hibou et al., Phys. Lett. **B 438** (1998) 41.

[2] P. Moskal et al., Phys. Rev. Lett. **80** (1998) 3202.

[3] P. Moskal et al., Phys. Lett. **B 474** (2000) 416.

[4] P. Moskal et al., Phys. Lett. **B 482** (2000) 356.

[5] Y. Bedfer et al., Acta Phys. Pol. **B 29**(1998) 2973.

[6] A. Khoukaz et al., Eur. Phys. J. **A 20** (2004) 345.

[7] P. Moskal, M. Wolke, A. Khoukaz, W. Oelert, Prog. Part. Nucl. Phys. **49** (2002) 1.

[8] G. Fäldt et al., Phys. Scripta **T 99** (2002) 146.

[9] H. Machner, J. Haidenbauer, J. Phys. **G 25** (1999) R231.

[10] S. Brauksiepe et al., Nucl. Instr. & Meth. **A 376** (1996) 397.

[11] U. Bechstedt et al., Nucl. Instr. & Meth. **B 113** (1996) 26;
R. Maier, Nucl. Instr. & Meth. **A 390** (1997) 1.

[12] H. Dombrowski et al., Nucl. Instr. & Meth. **A 386** (1997) 228.

[13] C. Quentmeier, doctoral thesis, Universität Münster, (2001).

[14] K. Hagiwara et al., Phys. Rev. **D 66** (2002) 010001.

[15] F. Balestra et al., Phys. Lett. **B 491** (2000) 29.

[16] A. Sibirtsev and W. Cassing, Eur. Phys. J. **A 2** (1998) 333.

[17] K. Nakayama, private communication, and Phys. Rev. **C 69** (2004) 065212.

[18] K. Nakayama et al., Phys. Rev. **C 61** (1999) 024001.

Production of η meson in NN collisions

V. Baru[1], A. M. Gasparyan[1], J. Haidenbauer[2], C. Hanhart[2], A. Kudryavtsev[1] and J. Speth[2]

[1] *Institute of Theoretical and Experimental Physics, 117259, B.Cheremushkinskaya 25, Moscow, Russia*

[2] *Institut für Kernphysik, Forschungszentrum Jülich, D-52425 Jülich, Germany*

Abstract: A model calculation for the reaction $NN \to NN\eta$ near-threshold is presented. The η meson production is described by elementary rescattering processes via $MN \to \eta N$, with $M = \pi$, ρ, η and σ. Corresponding amplitudes are taken from a multi-channel meson-exchange model of the πN system developed by the Jülich group. Effects of the NN interaction in the final as well as in the initial state are taken into account microscopically.

1 Introduction

Meson production in nucleon-nucleon (NN) collisions is a rather attractive research field in hadron physics at intermediate energies. The revived interest in such reactions was initiated by the arrival of a new accelerator generation (e.g., the IUCF Cooler at the Indiana University, CELSIUS in Uppsala or COSY at the Forschungszentrum Jülich) which allowed not only to measure such reactions with much higher precision than before but also to carry out experiments very close to the production thresholds.

Among those reactions the production of the η meson is certainly rather interesting, especially, because the η production near threshold is closely linked with the properties of the S_{11} $N^*(1535)$ resonance. Furthermore, this reaction might provide information about the strength of the ηN (S-wave) interaction. This strength plays a crucial role in the present controversy about the possible existence of η-nuclear quasibound states. Also, there is already a wealth of rather accurate data on η meson production near threshold [1, 2, 3, 4, 5, 6] providing a sensible testing ground for model calculations.

In the present contribution we report results of our investigation of η production in NN collisions [7]. The goal is a combined theoretical analysis of all measured channels of the reaction $NN \to NN\eta$, namely $pp \to pp\eta$,

$pn \to pn\eta$ and $pn \to d\eta$, by taking into account consistently the interaction between the nucleons in the final as well as in the initial state [8] and by utilizing a microscopic model of meson-nucleon (MN) scattering [9] for the description of the η-meson production process. Specifically, we present results for the total cross sections in the different NN channels and for the invariant mass distributions in the reaction $pp \to pp\eta$.

2 The model

We study η-meson production in distorted wave Born approximation (DWBA). This means that the transition amplitude from the initial to the final state, $M_{2\to3}$, is given by the expression

$$M_{2\to3} = \langle\, \chi_f \,|\, (1 + T_{NN}^{FSI} G_0) A_{2\to3} (1 + G_0 T_{NN}^{ISI}) \,|\chi_i\rangle. \qquad (1)$$

where $A_{2\to3}$ is the (elementary) production operator (cf. Fig. 1) and T_{NN}^{ISI} and T_{NN}^{FSI} are the NN reaction amplitudes in the initial and final states.

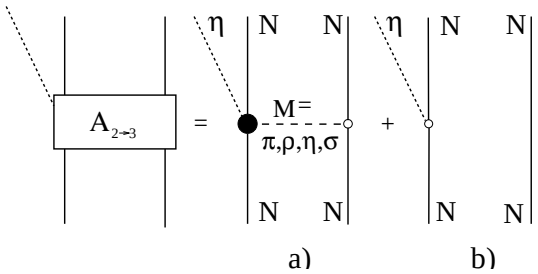

Figure 1: Production mechanisms for the reaction $NN \to NN\eta$ taken into account in our model: (a) η production via $MN \to \eta N$ rescattering; (b) direct η production.

The production amplitude $A_{2\to3}$ consists of re-scattering diagrams with π, ρ, η, and σ meson exchanges (Fig. 1a) plus the direct η emission (Fig. 1b). One of the principal novelties of our study is the utilization of a realistic microscopic model for the elementary reaction amplitudes $MN \to \eta N$ entering in $A_{2\to3}$ (Fig. 1a), namely a coupled-channels model for πN scattering that has been developed recently by the Jülich group [9]. The interactions in and between the various channels (πN, ηN, ρN, σN, and $\pi\Delta$) are derived in the meson-exchange picture starting out from effective chiral Lagrangians. The model includes the $N^*(1535)$ resonance as essential contribution but in

addition also various (t–channel) meson and (u–channel) baryon exchange diagrams. The parameters of the model are fixed by requiring a simultaneous description of the πN phase shifts and inelasticities as well as of the transition cross sections for the reactions $\pi N \to \eta N$ and $\pi N \to \rho N$ over an energy range that extends well beyond the ηN threshold. The reaction amplitudes are obtained from solving a coupled-channels relativistic scattering equation of Lippmann-Schwinger type. Clearly, in such a model not only the $\pi N \to \eta N$ amplitude is determined by empirical data, but also the transition amplitudes involving heavier mesons are to a large extend constrained by the phase shifts and inelasticity parameters of πN scattering. This is also true for the relative phases between the various amplitudes.

Another merit of our model study of η production in NN collisions consists in the full and consistent treatment of effects from the NN FSI as well as ISI by employing an NN model that describes the relevant NN phase shifts reasonably well up to energies around the η production threshold [7, 8].

We focus on the description of η-meson production in the near-threshold region, i.e. for excess energies Q up to around 50 MeV. Therefore, we restrict our investigation mainly to S-wave contributions. However the influence of P-wave NN contributions on the invariant mass distributions is also investigated.

3 Results

Results for the reactions $pp \to pp\eta$, $pn \to pn\eta$ and $pn \to d\eta$ are presented in Fig. 2 and compared with empirical information from the Uppsala/Celsius [1, 2, 3, 4] and Jülich/COSY [5, 6] accelerator facilities. The solid curves correspond to the calculation based on the modified Jülich MN model [9, 7] for the elementary η-production amplitude and the CCF NN model [8] for the ISI and FSI. Evidently, the calculation yields a reasonable overall description of the experimental data. This has to be certainly considered as success because there are no adjustable parameters in our calculation of $NN \to NN\eta$.

In order to examine the sensitivity of our results to differences in the NN interaction in the final state we also performed a calculation where the OBE potential Bonn B [10] was utilized. Corresponding results are presented in Fig. 2 by dashed-dotted lines. As one can see from this figure, for the $pp \to pp\eta$ channel the predictions of both NN models lie basically on top of each other. However, for the $pn \to pn\eta$ channel the results based on the Bonn B potential are about 20% larger and, indeed, are practically in

agreement with the experiment. At the same time the cross section for the $pn \to d\eta$ channel is also enhanced by about 20% and now slightly overshoots the data.

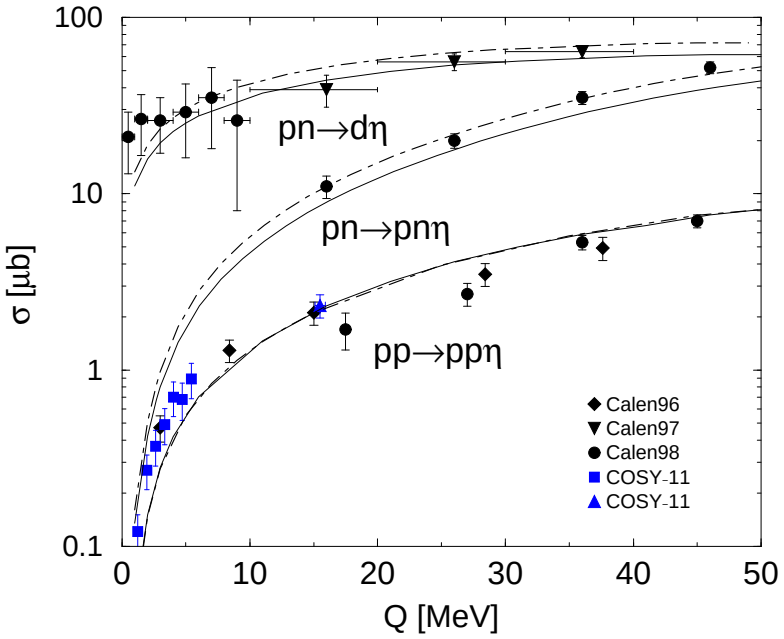

Figure 2: Total cross sections of the reactions $pp \to pp\eta$, $pn \to pn\eta$ and $pn \to d\eta$. The solid lines represent the results of our calculation with the CCF NN model of Ref. [8], whereas the dashed-dotted lines are based on the Bonn B NN model utilized for the FSI. Data are taken from Refs. [1, 2, 3, 4, 5, 6].

In any case, the differences between the results for the two considered NN models are not that large. But let us emphasize here an interesting by-product of the above comparison. Obviously it is not possible to achieve a simultaneous description of all three measured η production channels. Either we have agreement for the reactions $pp \to pp\eta$ and $pn \to d\eta$ (for CCF) and then $pn \to pn\eta$ is off, or $pp \to pp\eta$ and $pn \to pn\eta$ are reproduced (Bonn B) and then the results for $pn \to d\eta$ deviate from the data. Let us remind the reader that, close to threshold, there are only two independent amplitudes that determine those three reaction channels. The same incompatibility is also seen in the results of Fäldt and Wilkin, cf. Fig. 5 of Ref. [11], and, therefore, we believe that it is not due to the specific production mechanism employed in our study. In any case, we want to mention that a similar incompatibility exists also for near-threshold pion production, cf. the results in Fig. 3 of Ref. [12] and also in Ref. [13].

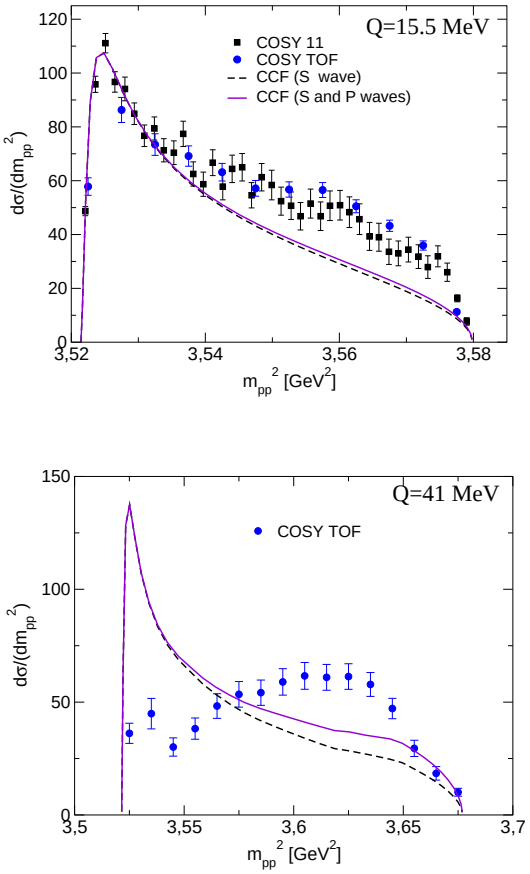

Figure 3: Invariant mass distributions. Experimental data are from Refs. [14, 15].

Let us now consider the other observables that have been measured in the near-threshold region. The angular distributions in the reaction $pp \to pp\eta$ exhibit an isotropic structure at the excess energies Q=15 MeV as well as at Q=41 MeV [14, 15]. The analyzing power, measured at Q=40 MeV [16], is rather small and basically consistent with zero. Thus, these observables are consistent with pure S-wave contributions and indeed are satisfactory described by our model. However, the invariant-mass distributions reported in [14, 15] can not be described by S-waves plus pp FSI alone as represented by the dashed lines in Fig. 3. This could be an indication for the presence of a considerable ηN FSI [17] but also that at least at the higher energy P-waves already play a role [18]. However at least in our particular model calculation NN P-waves play only a minor role, i.e. they can not significantly improve

agreement with the experiment as shown by the solid lines in Fig. 3.

We would like to note in this context that so far the most efforts both of the theory and experiment are focused on the study of the isotriplet reaction $pp \to pp\eta$. However the experimental study of the invariant-mass distributions in the reaction $pn \to pn\eta$, which is dominated by isospin zero, would be also very helpful in order to understand the role of NN higher partial waves. This is based on the fact that P-wave contributions between protons, specifically $^3P_0$ and $^3P_2$ partial waves, which might be of importance for the reaction $pp \to pp\eta$, are not allowed by quantum numbers for the isosinglet channel of the reaction $pn \to pn\eta$ (only $^1P_1$ is possible here). Thus, the reaction $pn \to pn\eta$ contains information about the NN FSI in different partial waves complementary to the pp channel.

4 Summary

We performed a detailed theoretical calculation of the reactions $pp \to pp\eta$, $pn \to pn\eta$ and $pn \to d\eta$ in the near-threshold region, i.e. for excess energies up to about 50 MeV. The production mechanisms which have been included consist of re-scattering processes with $M = \pi, \rho, \eta, \sigma$ meson exchanges and the direct η production. Effects of the final and initial state interaction between the nucleons are fully taken into account. A quantitative agreement of calculated total cross sections with the experimental data is achieved for all considered η production channels. Recent data on the invariant-mass distributions in the reaction $pp \to pp\eta$, however, can not be described. The influence of P-wave NN contributions on these observables is found to be minor in our model. This could be a sign for the presence of a considerable ηN FSI, which was not taken into account in our present model calculation.

Further measurements of the invariant-mass distributions, especially in the pn channel, are very desirable in order to allow a combined theoretical analysis of the invariant-mass distributions in the different NN channels.

References

[1] H. Calén et al., Phys. Lett. **B 366** (1996) 366.

[2] H. Calén et al., Phys. Rev. Lett. **79** (1997) 2642.

[3] H. Calén et al., Phys. Rev. Lett. **80** (1998) 2069.

[4] H. Calén et al., Phys. Rev. **C 58** (1998) 2667.

[5] J. Smyrski et al., Phys. Lett. **B 474** (2000) 182.

[6] P. Moskal et al., πN Newsletter **16** (2002) 367.

[7] V. Baru, A. M. Gasparyan, J. Haidenbauer, C. Hanhart, A. E. Kudryavtsev, and J. Speth, Phys. Rev. **C 67** (2003) 024002.

[8] J. Haidenbauer, K. Holinde, and M. B. Johnson, Phys. Rev. **C 48** (1993) 2190.

[9] O. Krehl, C. Hanhart, S. Krewald, and J. Speth, Phys. Rev. **C 62** (2000) 025207.

[10] R. Machleidt, Adv. Nucl. Phys. **19** (1989) 189.

[11] G. Fäldt and C. Wilkin, Phys. Scr. **64** (2001) 427.

[12] C. Hanhart, J. Haidenbauer, O. Krehl, J. Speth, Phys. Lett. **B 444** (1998) 25.

[13] G. Fäldt and C. Wilkin, Phys. Rev. **C 56** (1997) 2067.

[14] M. Abdel-Bary et al. Eur. Phys. J. **A 16** (2003) 127 .

[15] P. Moskal et al., Phys. Rev. **C 69** (2004) 025203

[16] P. Winter et al., Phys. Lett. **B 544** (2002) 251 [Erratum-ibid. **B 553** (2003) 339]

[17] A. Fix and H. Arenhovel, Phys. Rev. **C 69** (2004) 014001.

[18] K. Nakayama, J. Haidenbauer, C. Hanhart and J. Speth, Phys. Rev. **C 68** (2003) 045201.

Three-pair final-state interaction in the pp $\rightarrow$ ppη reaction close to threshold

A. Deloff

Institute for Nuclear Studies, Hoża 69, 00-681 Warsaw, Poland

Abstract: We present a three-body formalism describing the final-state interaction effects in the $pp \rightarrow pp\eta$ reaction close to threshold. We derive a three-body enhancement factor devised in such a way that all three pair-wise interactions are regarded on equal footing. The enhancement factor is obtained by expanding the three-particle wave function in hyperspherical harmonics. It has been shown that close to threshold the $p-p$ interaction strongly dominates whereas the $\eta - p$ interaction gives almost negligible contribution to the calculated effective mass spectra. Within the presented three-body approach it has been possible to reproduce the effective mass distributions at the excitation energy Q=15.5 MeV in good accord with the data.

1 Introduction

The last decade has seen major advances in the experimental investigation of the near threshold meson production reactions in nucleon-nucleon collisions (for a review cf. [1] and [2]). In the recent measurements of the $pp \rightarrow pp\eta$ reaction a very accurate determination of the four-momenta of both outgoing protons allowed for the full reconstruction of the kinematics of the final ηpp state. In consequence, these measurements provided in addition to the η and the proton angular distributions, also the pp and ηp effective mass distributions [3, 4]. The common feature of the near-threshold meson production in proton-proton collisions is the dominance of the very strong proton-proton final state interaction (FSI). This effect is clearly visible in the invariant mass distributions: as a prominent peak close to threshold in the (pp)-mass distribution, or as a bump near the end-point in the (ηp)-mass spectrum. For sufficiently low excitation energies the $^3P_0 \rightarrow {}^1S_0\, s$ transition amplitude becomes necessarily the sole contributor to the cross section as it is the only amplitude surviving at threshold. The supposition that this happens at the lowest available excitation energy equal Q=15.5

MeV [4] appears to be quite plausible, especially that in a similar experiment [3] at Q=15 MeV the measured angular distributions were consistent with isotropy. The description in terms of a simple model in which a constant η production amplitude is multiplied by pp FSI enhancement factor, although qualitatively correct, is not fully satisfactory in quantitative terms. The calculated invariant mass distributions are presented in Fig. 1 (dashed curves). In order to improve the agreement with experiment two possibilities have been considered. The most obvious explanation admits the contribution from the p-waves, or, more precisely, from the $^1S_0 \to {}^3P_0 s$ and $^1D_2 \to {}^3P_2 s$ amplitudes. These amplitudes have the best chance to show up when the relative momenta of the final-state protons take the largest values allowed by the phase space. Since at Q=15.5 MeV this sector still overlaps with the peak region of the $^1S_0$ enhancement factor, the s-wave also receives there maximal amplification. Therefore, the relative strength of the p-wave amplitudes to be discernible has to be quite substantial which in general should be reflected by a pronounced angular dependence of the cross section. This difficulty has been thoroughly examined by Nakayama et al. [5] who pointed out that the unwanted angular dependence might still be suppressed under two circumstances: (i) if the $^1D_2 \to {}^3P_2 s$ amplitude was negligibly small so that the angular dependent term was absent, or, (ii) if the lack of angular dependence resulted from cancellations – from a destructive interference between $^1S_0 \to {}^3P_0 s$ and $^1D_2 \to {}^3P_2 s$ amplitudes. Thus, a model basing upon a strong p-wave needs additionally somewhat fortuitous coincidences. According to the second proposition presented in [6], the s-wave amplitude dominates because it is proportional to the huge FSI enhancement factor whilst the p-wave amplitudes are not. Therefore, the latter might be neglected explaining in a natural way the lack of angular dependence. Instead, a weak energy dependence is admitted in the production amplitude. Both models are capable of improving the agreement with experiment at the expense of introducing an adjustable parameter. The best fit from [6] is depicted in Fig. 1 by the full line. Since the agreement with experiment presented in [5] is of similar quality, polarization experiments are required to discriminate between these two models. The prediction of the s-wave model [6] is that all polarization observables are bound to vanish. Any non-zero value for the analyzing power reveals the presence of higher partial waves [5].

In the above considerations final-state ηp interaction has been ignored and an interesting question arises how much its inclusion can change the resulting invariant mass spectra. The ηp interaction is poorly known but there have been suggestions that the corresponding scattering length might

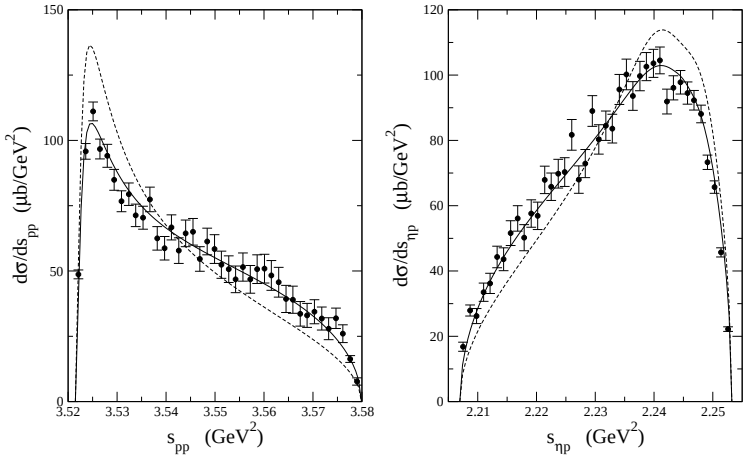

Figure 1: Invariant mass distributions at Q=15.5 MeV; left panel: (pp)-mass plot; right panel: (ηp)-mass plot. The data are from [4] the calculated curves are from [6].

be as large as about 1 fm. This is still one order of magnitude smaller than the pp scattering length but the discrepancies in the invariant mass distribution in Fig. 1 are not large either. The purpose of this work is to shed some light on the possible role of the ηp final-state interaction but to be able to do that we need a formalism in which all pair-wise interactions would be regarded on equal footing.

The plan of our presentation is as follows. In the next Section we start with the well known two-body case recalling the arguments leading to the derivation of the FSI enhancement factor. In Section 3 we generalize these ideas to the three-body case by utilizing the hypersherical harmonics approach. Finally, in Section 4 we verify our model by confronting the obtained results with the experimental data.

2 Two-body final-state interaction

Since the proton-proton final-state interaction is believed to be the dominant ingredient in the description of the $pp \to pp\eta$ reaction close to threshold, it is logical to begin with the two-body FSI problem. The basic idea how to account for final state interaction was put forward 50 years ago by Fermi, Watson, Migdal [7] and others (for a review cf. [8]) and is based on the observation that in many processes the interaction responsible for carrying the system from the initial to the final state is of such a short range that in

the first approximation may be regarded as point like. As a prototype one may consider a meson (x) production reaction $NN \to NNx$. To generate the meson mass m in nucleon-nucleon collision a large momentum transfer is required between the initial and the final nucleons, which is typically of the order $\sqrt{Mm}$, with M being the nucleon mass. The corresponding "range" of the production interaction is therefore much shorter than the range of the interaction between the two final state nucleons. Although it is perfectly true that the final state NN interaction significantly distorts the NN wave function but in the transition matrix element the contribution from all but the smallest NN separations will be strongly suppressed and the main effect may be attributed to the change of the normalization of the wave function at zero separation. If the non-interacting NN pair is described by a plane wave $\mathrm{e}^{-\imath\,\boldsymbol{k}\cdot\boldsymbol{r}}$, where $\boldsymbol{k}$ is the relative NN momentum ($\hbar = c = 1$ units are used hereafter), to account for final state interaction the latter must be replaced in the transition matrix element by the complete NN wave function $\Psi^-(\boldsymbol{k},\boldsymbol{r})^\dagger$ satisfying outgoing spherical wave boundary condition at infinity. Nevertheless, for a *point-like interaction*, we may set

$$\Psi^-(\boldsymbol{k},\boldsymbol{r})^\dagger \approx \mathrm{e}^{-\imath\,\boldsymbol{k}\cdot\boldsymbol{r}}\, C(k) \tag{1}$$

in the matrix element so that the final state interaction will be accounted for by multiplying the transition matrix element by the enhancement factor, defined as

$$C(k) \equiv \lim_{r\to 0}\ \Psi^+(-\boldsymbol{k},\boldsymbol{r})/\mathrm{e}^{-\imath\,\boldsymbol{k}\cdot\boldsymbol{r}}. \tag{2}$$

The factor $|C(k)|^2$ that appears in the cross section represents the ratio of two probabilities: one of finding the interacting NN pair at zero separation, while the other probability is associated with non-interacting particles. By construction, when the final state interaction is turned off, the enhancement factor will be equal to unity. Expanding both, the numerator and the denominator on the right hand side of (2) in partial waves, we have

$$C(k) = \lim_{r\to 0} \frac{\sum_{\ell=0}^{\infty} (2\ell+1)\,\imath^{-\ell}\,\psi_\ell(k,r)/r\ P_\ell(\hat{\boldsymbol{k}}\cdot\hat{\boldsymbol{r}})}{\sum_{\ell=0}^{\infty} (2\ell+1)\,\imath^{-\ell}\ j_\ell(kr)\,P_\ell(\hat{\boldsymbol{k}}\cdot\hat{\boldsymbol{r}})}, \tag{3}$$

where $\psi_\ell(k,r) \sim r^{\ell+1}$ for small r, $j_\ell(kr)$ is spherical Bessel function and $P_\ell(\hat{\boldsymbol{k}}\cdot\hat{\boldsymbol{r}})$ denotes Legendre polynomial. Clearly, in the limit $r \to 0$ in (3), all higher partial waves will be suppressed by the centrifugal barrier, and only the contribution the from s-wave survives. Thus, we obtain a simple formula

$$C(k) = \psi_0(k,0)'/k, \tag{4}$$

where prime denotes derivative with respect to r, and, as apparent from (4), the enhancement factor is determined by the slope of the wave function at the origin. To find this slope we must know the NN s-wave interaction and for simplicity we shall in the following assume that the latter takes the form of a spherically symmetric radial potential. The shape of this potential may be arbitrary but it must be of a short range. Given the NN potential, we can integrate outward the appropriate wave equation, containing both the nuclear and the Coulomb potential, generating numerically a regular solution $u_0(k,r)$ (i.e. vanishing at the origin) whose derivative for later convenience is selected to be

$$u_0(k,0)' = C_0(\eta)\, k, \tag{5}$$

where η denotes the Sommerfeld parameter and $C_0(\eta)^2 = 2\pi\eta/[\exp(2\pi\eta)-1]$ is the Coulomb barrier penetration factor. The sought for physical solution $\psi_0(k,r)$ occurring in (4) which is also regular, is necessarily proportional to $u_0(k,r)$, and, more explicitly, we have

$$\psi_0(k,r) = [C(k)/C_0(\eta)]\; u_0(k,r). \tag{6}$$

Now, all we need to calculate $C(k)$ is the asymptotic expression for the physical wave function. For $r = R$ with R much bigger than the range of the nuclear potential, the physical wave function takes the form

$$\psi_0(k,R) = F_0(\eta,kR) + f_0(k)\, H_0^+(\eta,kR), \tag{7}$$

where $H_0^+(\eta,kR) = G_0(\eta,kR) + \imath\, F_0(\eta,kR)$ with $G_0(\eta,kR)$ and $F_0(\eta,kR)$ being the standard Coulomb wave functions defined in [9], and $f_0(k) = \sin\delta\, \mathrm{e}^{\imath\delta}$ denotes the s-wave scattering amplitude with δ being the s-wave Coulomb distorted phase shift. The differentiation of (7) with respect to R, provides us with a second condition for the derivatives but it should be noted that $u_0(k,R)$ and $u(k,R)'$ occurring in these two matching conditions are to be regarded as known quantities. Indeed, they are fully specified by the boundary condition at the origin (5) and can be either calculated analytically, or obtained by numerical methods. Therefore, we end up with two algebraic equations in which the two unknowns are the enhancement factor $C(k)$ and the scattering amplitude $f_0(k)$ and the respective solutions, can be conveniently written as

$$C(k) = \frac{k\, C_0(\eta)}{w[H_0^+(\eta,kR), u_0(k,R)]}, \tag{8}$$

and

$$f_0(k) = -\frac{w[F_0(\eta, kR), u_0(k, R)]}{w[H_0^+(\eta, kR), u_0(k, R)]}, \tag{9}$$

where the symbol $w[f, g]$ denotes the Wronskian defined as $w[f, g] \equiv fg' - f'g$. The specific Wronskian occurring in the denominators of (8)–(9) has been referred to as the Jost function [8]. Thus, given the potential, the two-body enhancement factor can be obtained from (8).

3 Three-body final-state interaction

We wish now to extend the ideas outlined above to the three-body case. We assume that the pair-wise short range interaction between the particles is strong but the system is Borromean, i.e. *no binary bound state may exist in the three-body system under consideration.* A formal theory of the continuum in a Borromean system was developed in [10] using the same hyperspherical harmonics method which has been widely employed for the investigation of bound states and specifically the halo nuclei [11]. In this paper we follow this approach to derive the enhancement factor for three interacting particles. The wave functions in the continuum are solutions to the three-body problem satisfying the correct boundary conditions at infinity where the three-body asymptotics is most naturally expressed in terms of the rotationally and permutationally invariant hyperradius ρ defined as the square root of the sum of squares of the inter-particle distances. Since the hyperradius reflects the size of the three-body system, similarly as in the two-body case, the enhancement factor may be obtained as the limiting value $\rho \to 0$ of the three-body wave function. The method of hyperspherical harmonics has been well documented in the literature, but to make this paper self-contained we wish to summarize briefly the theoretical framework necessary to treat the continuum of a Borromean system.

3.1 Coordinate sets and hyperspherical harmonics

For assigned particle positions $(\mathbf{r}_1, \mathbf{r}_2, \mathbf{r}_3)$ and masses (m_1, m_2, m_3), the translationally invariant normalized sets of Jacobi coordinates $\mathbf{x}_i, \mathbf{y}_i$ are defined,

as follows

$$\mathbf{x}_i = \sqrt{\frac{m_j\, m_k}{(m_j + m_k)\, \mu}}\, (\mathbf{r}_j - \mathbf{r}_k), \tag{10a}$$

$$\mathbf{y}_i = \sqrt{\frac{m_i\, (m_j + m_k)}{\mu\, M}}\, \left(\mathbf{r}_i - \frac{m_j\, \mathbf{r}_j + m_k\, \mathbf{r}_k}{m_j + m_k} \right), \tag{10b}$$

$$\mathbf{R} = (m_i \mathbf{r}_i + m_j \mathbf{r}_j + m_k \mathbf{r}_k)/M, \tag{10c}$$

where $\{i, j, k\}$ is a permutation of the particle labels $\{1, 2, 3\}$, $M = m_1 + m_2 + m_3$, and μ denotes an arbitrary mass which just sets the mass scale. Each of the three equivalent pairs $(\mathbf{x}_i, \mathbf{y}_i)$ together with the center of mass coordinate $\mathbf{R}$ describes the system. The transformation between different sets of Jacobi coordinates is referred to as a kinematical rotation and takes the form

$$\begin{pmatrix} \mathbf{x}_j \\ \mathbf{y}_j \end{pmatrix} = \begin{pmatrix} -\cos\omega_{ij} & \sin\omega_{ij} \\ -\sin\omega_{ij} & -\cos\omega_{ij} \end{pmatrix} \begin{pmatrix} \mathbf{x}_i \\ \mathbf{y}_i \end{pmatrix} \tag{11}$$

where the rotation angle, confined by $-\pi/2 \leq \omega_{ij} \leq \pi/2$, is given by

$$\omega_{ij} = \arctan \left[\sigma\{i, j, k\} \sqrt{M\, m_k / m_i\, m_j} \right], \tag{12}$$

with $\sigma\{i, j, k\}$ denoting the sign of the permutation $\{i, j, k\}$.

The Jacobi momenta $\mathbf{k}_i, \mathbf{q}_i$ and $\mathbf{P}$, canonically conjugate to $\mathbf{x}_i, \mathbf{y}_i$ and $\mathbf{R}$, respectively, are defined by the relations,

$$\mathbf{k}_i = \sqrt{\frac{m_j\, m_k\, \mu}{m_j + m_k}}\, \left(\frac{\mathbf{p}_j}{m_j} - \frac{\mathbf{p}_k}{m_k} \right), \tag{13a}$$

$$\mathbf{q}_i = \sqrt{\frac{(m_j + m_k) m_i \mu}{M}}\, \left(\frac{\mathbf{p}_i}{m_i} - \frac{\mathbf{p}_j + \mathbf{p}_k}{m_j + m_k} \right), \tag{13b}$$

$$\mathbf{P} = \mathbf{p}_1 + \mathbf{p}_2 + \mathbf{p}_3, \tag{13c}$$

where $\mathbf{p}_i$ $(i = 1, 2, 3)$ are the laboratory frame momenta.

Instead of the Jacobi coordinates we shall use hyperspherical coordinates comprising of a hyperradius ρ and five angles. The hyperradius ρ determines the size of a three–body system and is invariant with respect to kinematic rotations

$$\rho^2 = x_i^2 + y_i^2, \qquad i = 1, 2, 3. \tag{14}$$

The five angular variables forming a five-dimensional solid angle Ω_ρ include the usual angles (θ_x^i, ϕ_x^i), (θ_y^i, ϕ_y^i) specifying the unit vectors $\hat{\mathbf{x}}_i$, $\hat{\mathbf{y}}_i$ and these are supplemented by the hyperangle α_i defined by the equalities

$$x_i = \rho \sin\alpha_i, \qquad y_i = \rho \cos\alpha_i, \tag{15}$$

where $0 \leq \alpha_i \leq \pi/2$. The five-dimensional volume element $\mathrm{d}\Omega_\rho$ is

$$\mathrm{d}\Omega_\rho = \sin^2\alpha_i \, \cos^2\alpha_i \, \mathrm{d}\alpha_i \, \mathrm{d}\hat{\mathbf{x}}_i \, \mathrm{d}\hat{\mathbf{y}}_i. \tag{16}$$

For the conjugate momenta, we proceed in a similar fashion introducing the hypermomentum κ and the associated hyperangle β_i

$$k_i = \kappa \sin\beta_i, \qquad q_i = \kappa\cos\beta_i, \tag{17}$$

where owing to the energy conservation $Q = \kappa^2/2\mu$.

In the six-dimensional space, the kinetic energy operator $\hat{T}$ takes a separable form

$$\hat{T} = -\frac{1}{2\mu}\left(\frac{\partial^2}{\partial\rho^2} + \frac{5}{\rho}\frac{\partial}{\partial\rho} - \frac{1}{\rho^2}\hat{K}^2\right), \tag{18}$$

where the hypermomentum operator $\hat{K}$ is the generator of rotations in the six-dimensional space. The operator $\hat{K}^2$ takes the form

$$\hat{K}^2 = -\frac{\partial^2}{\partial\alpha_i^2} - 4\cot(2\alpha_i)\frac{\partial}{\partial\alpha_i} + \frac{\hat{\boldsymbol{l}}_i^2}{\sin^2\alpha_i} + \frac{\hat{\boldsymbol{\lambda}}_i^2}{\cos^2\alpha_i}, \tag{19}$$

where the angular momentum operators $\hat{\boldsymbol{l}}_i$ and $\hat{\boldsymbol{\lambda}}_i$ occurring in (19), are defined as

$$\hat{\boldsymbol{l}}_i = -\imath\,\boldsymbol{x}_i \times \frac{\partial}{\partial\,\boldsymbol{x}_i}, \qquad \hat{\boldsymbol{\lambda}}_i = -\imath\,\boldsymbol{y}_i \times \frac{\partial}{\partial\,\boldsymbol{y}_i}, \tag{20}$$

and $\hat{\boldsymbol{l}}_i^2$ and $\hat{\boldsymbol{\lambda}}_i^2$ have eigenvalues $\ell(\ell+1)$ and $\lambda(\lambda+1)$, respectively. The operator (19) has eigenvalues $K(K+4)$ where $K = 2n + \ell + \lambda$ for integer n. The quantum number K has been dubbed hypermomentum, its value is the same in all three Jacobi systems, and the corresponding eigenfunctions are known as hyperspherical harmonics (abbreviated HH hereafter).

From now on we choose set 3 as the basic one and to simplify notation in the following we will suppress the label referring to our particular choice of the Jacobi system. The HH have the explicit form

$$\mathcal{Y}^{\ell\lambda}_{KLM_L}(\Omega_\rho) = \chi^{\ell\lambda}_K(\alpha)\,[Y_\ell(\hat{\mathbf{x}}) \otimes Y_\lambda(\hat{\mathbf{y}})]_{LM_L}\,, \tag{21}$$

where L is the total angular momentum resulting from vector addition $\boldsymbol{L} = \boldsymbol{l} + \boldsymbol{\lambda}$. In (21) the symbol Ω_ρ denotes collectively all five angular variables with Y_{lm} being the usual spherical harmonics. The square bracket in (21) indicates vector coupling of $\mathbf{l}$ and $\boldsymbol{\lambda}$ producing a total angular momentum $\mathbf{L}$ and the appropriate quantum numbers associated with the latter operator are L and M_L. In (21), the hyperangular eigenfunctions are

$$\chi^{\ell\lambda}_K(\alpha) = N^{\ell\lambda}_K \, \sin^\ell\alpha \, \cos^\lambda\alpha \, P_n^{\ell+\frac{1}{2},\lambda+\frac{1}{2}}(\cos 2\alpha),$$

where $P_n^{\alpha,\beta}(x)$ are the Jacobi polynomials (cf. [9]) and $N_K^{\ell\lambda}$ is the normalization constant. The HH in (21) are orthonormalized using the volume element (16) and α stands for any of the α_i.

For clarity reasons, to avoid unnecessary complications, we are going to restrict our considerations to the simplest case when the particles have no internal degrees of freedom. When the particles are moving freely the spacial part of the three-particle wave-function will be described in the c.m. frame by a plane wave, whose HH expansion can be written as

$$\mathrm{e}^{\imath\mathbf{k}\cdot\mathbf{x}+\imath\mathbf{q}\cdot\mathbf{y}} = \frac{(2\pi)^3}{(\kappa\rho)^{5/2}} \sum_{LM_LK\ell\lambda} \mathcal{Y}^{\ell\lambda}_{KLM_L}(\Omega_\rho)\ \imath^K\ \sqrt{\kappa\rho}\, J_{K+2}(\kappa\rho)\ \mathcal{Y}^{\ell\lambda}_{KLM_L}(\Omega_\kappa)^\dagger, \tag{22}$$

where J_{K+2} denotes Bessel function of integer order and solid angle Ω_κ comprises five angular variables that specify the directions of the incident momenta in the six-dimensional space. It is worth noting that since the radial part in (22) depends solely upon K, the plane wave is an invariant under six-dimensional rotations. The two-body interactions break up this invariance and for interacting particles the three-particle wave function in the continuum $\Psi_{\mathbf{k},\mathbf{q}}(\mathbf{x},\mathbf{y})$ will have a more complicated HH expansion. For the simplest case of pair-wise central potentials depending upon the particle separations, we have

$$\Psi_{\mathbf{k},\mathbf{q}}(\mathbf{x},\mathbf{y}) = \frac{(2\pi)^3}{(\kappa\rho)^{5/2}} \sum \mathcal{Y}^{\ell\lambda}_{KLM_L}(\Omega_\rho)\ \psi^L_{K\ell\lambda,\tilde{K}\tilde{\ell}\tilde{\lambda}}(\kappa,\rho)\ \mathcal{Y}^{\tilde{\ell}\tilde{\lambda}}_{\tilde{K}LM_L}(\Omega_\kappa)^\dagger \tag{23}$$

where the summation indices are $L, M_L, K, \ell, \lambda, \tilde{K}, \tilde{\ell}, \tilde{\lambda}$ and the normalization condition reads

$$\int \Psi_{\mathbf{k}',\mathbf{q}'}(\mathbf{x},\mathbf{y})^\dagger\ \Psi_{\mathbf{k},\mathbf{q}}(\mathbf{x},\mathbf{y})\ \mathrm{d}^3x\,\mathrm{d}^3y = \delta(\mathbf{k}'-\mathbf{k})\,\delta(\mathbf{q}'-\mathbf{q}). \tag{24}$$

In the expansion (23), only the total three-particle angular momentum L is a good quantum number and the as yet unspecified hyperradial part $\psi^L_{K\ell\lambda,\tilde{K}\tilde{\ell}\tilde{\lambda}}(\kappa,\rho)$ must be determined from the underlying three-body dynamics. The dependence upon the tilded indices, associated with the incident momenta, enters solely *via* the asymptotic boundary condition at $\rho\to\infty$. The full wave-function $\Psi_{\mathbf{k},\mathbf{q}}(\mathbf{x},\mathbf{y})$ is a solution to the three-body Schrödinger equation

$$(\hat{T}+\hat{V}-Q)\Psi_{\mathbf{k},\mathbf{q}}(\mathbf{x},\mathbf{y}) = 0, \tag{25}$$

with $\hat{V} = \hat{V}_{12}+\hat{V}_{23}+\hat{V}_{31}$ where $\hat{V}_{ij}$ stands for the pair-wise interaction between particles i and j. Inserting (23) in (25) and projecting onto the

hyperangular part of the wave function, results in an infinite set of coupled systems of differential equations enumerated by the conserved total angular momentum L – the only quantum number that does not mix. For an assigned L, we have

$$\left\{\frac{\mathrm{d}^2}{\mathrm{d}\rho^2} - \frac{(K+3/2)(K+5/2)}{\rho^2} + \kappa^2\right\}\ \psi^L_{K\ell\lambda,\tilde{K}\tilde{\ell}\tilde{\lambda}}(\kappa,\rho) = \\ = 2\mu \sum_{K'\ell'\lambda'} \langle K'\ell'\lambda'|\hat{V}|K\ell\lambda\rangle\ \ \psi^L_{K'\ell'\lambda',\tilde{K}\tilde{\ell}\tilde{\lambda}}(\kappa,\rho), \tag{26}$$

and we are left with a multi-channel situation where each channel is specified by three quantum numbers $\{K\ell\lambda\}$. Each system of equations (26) with $L = 0, 1, 2, \ldots$ is infinite because there is no upper limit for K, and, therefore, for practical reasons K must be truncated at some finite value K_{max} so that the orbital momenta ℓ and λ are thereby restricted to vary in finite limits. The value of K_{max} determines the order of the approximation and must be be large enough to ensure the convergence of the method. It should be noted that in (26) the potential term has been sandwiched between the HH functions $\mathcal{Y}^{\ell\lambda}_{KLM_L}(\Omega_\rho)$ and after integration over the five angular variables Ω_ρ, these matrix elements depend solely upon the hyperadius ρ

$$\langle K'\ell'\lambda'|\hat{V}|K\ell\lambda\rangle = \int \mathcal{Y}^{\ell'\lambda'}_{K'LM_L}(\Omega_\rho)^\dagger \sum_{j=1}^{3}\sum_{i\neq j}^{3} V_{ij}(\rho,\Omega_\rho)\ \mathcal{Y}^{\ell\lambda}_{KLM_L}(\Omega_\rho)\ \mathrm{d}\,\Omega_\rho. \tag{27}$$

With the adopted here set 3 of HH, the computation of the potential matrix element $\hat{V}_{12}$ is relatively straightforward because the separation vector between particles 1 and 2 is proportional to $|\mathbf{x}|$ and the calculation of the potential matrix involves a single integration. By contrast, in the two remaining potentials the corresponding separations, r_{23} and r_{31}, respectively, are linear combinations of the two vectors $\mathbf{x}$ and $\mathbf{y}$ which unavoidably leads to five-dimensional integrations in the calculation of the potential matrix. Fortunately, there is a very efficient procedure to overcome this difficulty, based on the observation that all HH with fixed (K, L) values defined with respect to set i (cf. (10)) are linear combinations of HH belonging a set j and this transformation is effected by means of the so called Raynal-Revai (RR) coefficients [12], *viz.*

$$\mathcal{Y}^{\ell_i\lambda_i}_{KLM_L}(\alpha_i,\hat{\mathbf{x}}_i,\hat{\mathbf{y}}_i) = \sum_{\ell_j\,\lambda_j} \langle \ell_j\,\lambda_j|\ell_i\,\lambda_i\rangle_{KL}\ \mathcal{Y}^{\ell_j\lambda_j}_{KLM_L}(\alpha_j,\hat{\mathbf{x}}_j,\hat{\mathbf{y}}_j), \tag{28}$$

where the RR coefficients $\langle \ell_j\,\lambda_j|\ell_i\,\lambda_i\rangle_{KL}$ are functions of the angle specifying the kinematic rotation $i \to j$ given in (12). With the aid of (28), the

potential matrix of $\hat{V}_{23}$ may be computed in basis 1 where this task is simple and subsequently transformed to basis 3.

The radial wave functions must be regular at $\rho = 0$ and the boundary condition imposed on the solutions of (26) is

$$\psi^L_{K\ell\lambda,\tilde{K}\tilde{\ell}\tilde{\lambda}}(\kappa,\rho) \sim \rho^{K+5/2} \qquad \text{for} \qquad \rho \to 0. \tag{29}$$

For $\rho \to \infty$ the potential term in (26) goes to zero so that in this limit the system of equations (26) becomes decoupled. In absence of the potential term, the asymptotic solutions of the radial equations are well known, they are given in terms of the Bessel and Neuman functions [9] $J_{K+2}(\kappa\rho)$ and $Y_{K+2}(\kappa\rho)$, respectively. With the Coulomb interaction present, for large ρ strong interaction potentials become negligible, and we set

$$\lim_{\rho\to\infty} \psi^L_{K\ell\lambda,\tilde{K}\tilde{\ell}\tilde{\lambda}}(\kappa,\rho) = \delta_{K\tilde{K}}\,\delta_{\lambda\tilde{\lambda}}\,\delta_{\ell\tilde{\ell}}\,F_{\mathcal{L}}(\eta,\kappa\rho) + \langle K\ell\lambda|\mathcal{T}^L|\tilde{K}\tilde{\ell}\tilde{\lambda}\rangle\; H^+_{\mathcal{L}}(\eta,\kappa\rho), \tag{30}$$

with

$$H^+_{\mathcal{L}}(\eta,\kappa\rho) = G_{\mathcal{L}}(\eta,\kappa\rho) + \imath\, F_{\mathcal{L}}(\eta,\kappa\rho). \tag{31}$$

where we have extended the standard definition of Coulomb wave functions so that the orbital quantum number ℓ which takes on integer values is replaced by $\mathcal{L} = K + 3/2$ with half-integer $\mathcal{L}$. The T-matrix occurring in (30) $\langle K\ell\lambda|\mathcal{T}^L|\tilde{K}\tilde{\ell}\tilde{\lambda}\rangle$ describes $3 \to 3$ scattering processes and is similar to that encountered in the two-body multichannel problem. In particular, it can be diagonalized which allows to determine the appropriate eigenphases $\delta_{LK\ell\lambda}$ whose rapid variation with energy indicates a resonance.

3.2 Three-body final-state interaction enhancement factor

The formalism developed in the preceding subsection will be now applied to calculate the enhancement factor describing final-state interaction between three particles in a Borromean system. The approximation scheme will be based on the assumption that all interactions are of a short range and therefore the most important effect comes from the distortion of the wave function at very small separations. Bigger separation region is strongly suppressed by the small size of the interaction volume and gives relatively small contribution to the overlap integrals representing reaction transition amplitudes. Thus, similarly as in the two-body case, we shall define the enhancement factor as the limit reached by the square of the absolute value of the ratio – the full three-body wave function divided by the plane wave – when the size of the system represented by ρ goes to zero. It is apparent

from (26) that the role of the centrifugal barrier plays now the quantum number K and the leading term in the wave function in the limit $\rho \to 0$ has $K = 0$ implying that $\ell = \lambda = 0$ and $L = 0$. Therefore, we confine our attention solely to the $L = 0$ set (26) where significant simplifications take place, namely we have $\lambda = \ell$ and K necessarily even: $K = 2(n + \ell)$.

Formally, the three-particle enhancement factor will be defined as the limit

$$F(\boldsymbol{k}, \boldsymbol{q}) = \lim_{\rho \to 0} \left| \frac{\Psi_{\mathbf{k},\mathbf{q}}(\mathbf{x}, \mathbf{y})}{\mathrm{e}^{\imath \mathbf{k}\cdot\mathbf{x} + \imath \mathbf{q}\cdot\mathbf{y}}} \right|^2 , \tag{32}$$

which by making use of (22) and (23), simplifies to the form

$$F(\boldsymbol{k}, \boldsymbol{q}) = \lim_{\rho \to 0} \left| \sum_{\tilde{K},\tilde{\ell}} \frac{\psi^0_{000,\tilde{K}\tilde{\ell}\tilde{\ell}}(\kappa, \rho)}{\sqrt{\kappa\rho}\, J_2(\kappa\rho)} \; \mathcal{Y}^{\tilde{\ell}\tilde{\ell}}_{\tilde{K}00}(\Omega_\kappa)^\dagger \right|^2 , \tag{33}$$

where we have dropped the uninteresting constant factor $|\mathcal{Y}^{00}_{000}(\Omega_\rho)|^2$. To obtain the enhancement factor it is sufficient to calculate the radial wave function $\psi^0_{000,\tilde{K}\tilde{\ell}\tilde{\ell}}(\kappa, \rho)$ for small ρ and take the limit indicated in (33).

The calculation of the radial wave function is carried out similarly as for the two-body case except that scalar quantities now need to be replaced by matrices in channel space. These channels are specified by two quantum numbers $K\ell$ but to simplify the notation it is possible to use a single integer $\nu = \frac{1}{2}\,(\frac{1}{2}K)(\frac{1}{2}K + 1) + \ell + 1$ enumerating all the states under consideration (ν=1,2,3...). Truncating the infinite sequence of K values at some assigned K_{max}, the total number of channels N is

$$N = \tfrac{1}{2}(\tfrac{1}{2}K_{max} + 1)(\tfrac{1}{2}K_{max} + 2), \tag{34}$$

and we have to solve N second order differential equations given in (26). The physical solution of (26) can be envisaged as a column vector in channel space. To obtain the physical solution we must first generate numerically N linearly independent particular solutions vanishing at the origin with an arbitrary slope at $\rho = 0$. These N solutions can be grouped together to form the N columns of a single $N \times N$ square matrix $\mathbf{\Phi}$ (hereafter we denote matrices by boldface symbols). In practice, this matrix may be obtained by solving N times the system of equations (26) imposing for small ρ the boundary condition

$$\Phi_{K\ell,\tilde{K}\tilde{\ell}}(\kappa, \rho) = \delta_{K\tilde{K}}\, \delta_{\ell\tilde{\ell}}\, (\kappa\rho)^{K+5/2}, \tag{35}$$

so that these particular solutions will be enumerated by two quantum numbers $\tilde{K}\tilde{\ell}$. Since the columns of $\mathbf{\Phi}$ are linearly independent, they span the

space of all possible slopes. Therefore, any column vector solution ψ of (26) must be expressible as some linear combination of the N columns of $\mathbf{\Phi}$, and we have

$$\psi(\rho) = \mathbf{\Phi}(\rho) \cdot c, \tag{36}$$

with c denoting a column vector of constant coefficients.

The matrix of physical solutions occurring in (33) differs from $\mathbf{\Phi}$ at most by a constant matrix and the latter will be explicitly determined by making use of the boundary condition for asymptotic ρ. For large ρ the physical solution must be of the form

$$\mathbf{\Psi}(\kappa, \rho) = \boldsymbol{F}(\kappa\rho) + \boldsymbol{H}^{+}(\kappa\rho) \cdot \boldsymbol{T}(\kappa), \tag{37}$$

where $\boldsymbol{T}$ is the true $3 \to 3$ scattering matrix. In formula (37) $\boldsymbol{F}$ denotes a diagonal matrix containing the regular solutions $F_{\mathcal{L}}(\eta, \kappa\rho)$ of (26) in absence of the strong interaction, whereas $\boldsymbol{H}^{+}$ is another diagonal matrix containing outgoing hyperspherical waves $G_{\mathcal{L}}(\eta, \kappa\rho) + \imath\, F_{\mathcal{L}}(\eta, \kappa\rho)$. Since $\mathbf{\Phi}$ is proportional to $\mathbf{\Psi}$, for some large $\rho = \rho_m$, we may set the following matching condition for the wave functions and their derivatives

$$\begin{aligned} \mathbf{\Phi}(\kappa, \rho_m) \cdot \boldsymbol{C}(\kappa) &= \boldsymbol{F}(\kappa\rho_m) + \boldsymbol{H}^{+}(\kappa\rho_m) \cdot \boldsymbol{T}(\kappa), & \text{(38a)} \\ \mathbf{\Phi}(\kappa, \rho_m)' \cdot \boldsymbol{C}(\kappa) &= \boldsymbol{F}(\kappa\rho_m)' + \boldsymbol{H}^{+}(\kappa\rho_m)' \cdot \boldsymbol{T}(\kappa), & \text{(38b)} \end{aligned}$$

where prime denotes derivative with respect to ρ and $\boldsymbol{C}(\kappa)$ is a constant (albeit energy dependent) matrix to be determined. Eliminating $\boldsymbol{T}$ between the two matrix equations (38), we obtain

$$\boldsymbol{C}(\kappa) = \frac{2\kappa}{\pi}[\boldsymbol{H}^{+}(\kappa\rho_m) \cdot \mathbf{\Phi}(\kappa, \rho_m)' - \boldsymbol{H}^{+}(\kappa\rho_m)' \cdot \mathbf{\Phi}(\kappa, \rho_m)]^{-1}, \tag{39}$$

and $\boldsymbol{C}(\kappa)$ is seen to be proportional to the inverse of the Jost matrix. Clearly, formula (39) may be viewed as a three-body extension of (8). Because the matrix $\boldsymbol{C}(\kappa)$ involves the inverse of the Jost determinant it is bound to have the same singularity structure as the T-matrix.

The physical solution can be now expressed entirely in terms of $\mathbf{\Phi}$

$$\mathbf{\Psi}(\kappa, \rho) = \mathbf{\Phi}(\kappa, \rho) \cdot \boldsymbol{C}(\kappa) \tag{40}$$

and the limiting procedure $\rho \to 0$ in (33) may be effected with the aid of (35). Similarly as in the two-body case, the only terms in the summations giving non-vanishing contribution are those with $K = 0$. Leaving out irrelevant numerical factor, the enhancement factor in (33) takes the form

$$F(\boldsymbol{k}, \boldsymbol{q}) = F(-\boldsymbol{k}, -\boldsymbol{q}) = \left| \sum_{K\ell} c_{K\ell}(\kappa)\; \mathcal{Y}^{\ell\ell}_{K00}(\Omega_\kappa) \right|^2, \tag{41}$$

where the expansion coefficients $c_{K\ell}(\kappa)$ are provided as the first row of the matrix $\boldsymbol{C}(\kappa)$ given in (39).

Formula (41) gives the enhancement factor in the form of an expansion in an orthonormal set of momentum dependent HH functions which turns out to be quite useful in effecting phase space integrations. We shall illustrate this point for the case when the transition matrix is assumed to be constant so that the cross section is essentially determined by the enhancement factor. The integration over the five angles $\mathrm{d}\Omega_\kappa$, yields the total cross section

$$\sigma(\kappa) \sim \frac{\kappa^4}{f(\kappa)} \sum_{K\ell} |c_{K\ell}(\kappa)|^2, \tag{42}$$

where κ^4 results from phase space and $f(\kappa)$ denotes the incident flux factor. The summation over K extends over all even numbers from 0 up to K_{max} and in the following we take it to be the value at which the convergence has been attained.

When the incident energy is fixed (i.e, κ is a constant), the quantities of interest are usually the effective mass distributions, or equivalently, the corresponding kinetic energy distributions of the different pairs in their c.m frame. Such distributions are obtained here by integrating only over the directions of $\boldsymbol{k}$ and $\boldsymbol{q}$ retaining the dependence upon the two remaining variables, κ and β. With our choice of 3 as the basic Jacobi set, the distribution of the center of mass energy T_3 of the pair $\{12\}$, takes particularly simple form

$$\frac{\mathrm{d}\sigma}{\mathrm{d}T_3} = \sqrt{T_3(Q-T_3)} \sum_{K'K\ell} c_{K'\ell}(\kappa)^*\, c_{K\ell}(\kappa)\, \chi^{\ell\ell}_{K'}(\beta)\, \chi^{\ell\ell}_{K}(\beta), \tag{43}$$

where $T_3 = Q\,\sin^2\beta$ and the square root factor is a remanet of the phase space. All other factors that depend only upon κ have been dropped as they may be absorbed in the arbitrary normalization constant. The calculation of c.m kinetic energy distributions of the two remaining pairs, i.e $\{23\}$ and $\{31\}$, respectively, may be carried out in exactly the same manner but the HH occurring in (41) need to be first transformed to the appropriate Jacobi system by applying a kinematical rotation. Thus, using the transformation (28) in (41), the distribution of the kinetic energy of the $\{23\}$ pair, T_1, is

$$\begin{aligned}\frac{\mathrm{d}\sigma}{\mathrm{d}T_1} = \sqrt{T_1(Q-T_1)} \sum_{K'K\ell'_3\ell_3\ell_1} & c_{K'\ell'_3}(\kappa)^*\, c_{K\ell_3}(\kappa)\, \chi^{\ell_1\ell_1}_{K'}(\beta_1)\, \chi^{\ell_1\ell_1}_{K}(\beta_1)\times \\ & \times\, \langle \ell_1\ell_1|\ell_3\ell_3\rangle_{K0}\, \langle \ell'_3\ell'_3|\ell_1\ell_1\rangle_{K'0},\end{aligned} \tag{44}$$

where $T_1 = Q \sin^2 \beta_1$ and the corresponding distribution of T_2 follows from (44) in result of P_{12} permutation. It should be perhaps clarified that this permutation in general changes the kinematic rotation angle that enters the RR coefficients and in consequence the T_2 distribution does not have to be the same as that given in (44).

4 Comparison with experiment and conclusions

In the preceding section our considerations have been quite general and now we wish to apply this theory to the investigation of FSI effects in the $pp \to pp\eta$ reaction close to threshold. To simplify matters we assume that the excitation energy is sufficiently low so that the total orbital momentum in the final state is zero and the ${}^3P_0 \to {}^1S_0\, s$ transition amplitude is the sole contributor to the cross section. We label the two protons as 1 and 2, respectively, and the meson as 3 choosing Jacobi set 3 for all computations. With the two protons in a singlet state, Pauli principle requires that in this frame the orbital momenta ℓ_3, λ_3 take only even values. This guarantees that the spatial part wave function will be symmetric with respect to the $\{12\}$ permutation. We have tried several possible forms of the pp potential in the ${}^1S_0$ state: a delta-shell, a Gaussian or a fully realistic Reid potential (for details cf. [6]). The η-p interaction is poorly known, for the real part of the scattering length values between 0.2 and about 1.0 fm have been suggested [13]. Additional difficulty stems from the multi-channel nature of this interaction: already at threshold there are open channels so that ηp scattering length is a complex number. At present there is not enough information to include these additional channels into our formalism, therefore in this work η-p interaction has been simulated by the simplest non-absorptive delta-shell potential operative in the s-wave only whose range has been arbitrarily fixed to be 1 fm. The depth of this potential can be then adjusted as to yield an assigned value of the ηp scattering length $a_{\eta p}$. Since the precise value of the latter is not available [13] we used three values 0.5, 1.0 and 1.5 fm, respectively, which we believe is a representative sample.

All our computations have been carried out for the lowest excitation energy equal Q=15.5 MeV for which two-particle invariant mass spectra are experimentally available. The system of equations (26) was perpetually solved by increasing successively in each step the value of K_{max} until convergence has been attained. For delta-shell and Gaussian pp potentials this occurred at $K_{max} = 24$ but with Reid potential this figure must be doubled. Similarly as in the two-body case [6] the results are completely insensitive to

the shape of the pp potential. The results of our computations are presented in Fig. 2 where they are compared with the data from [4]. Not unexpect-

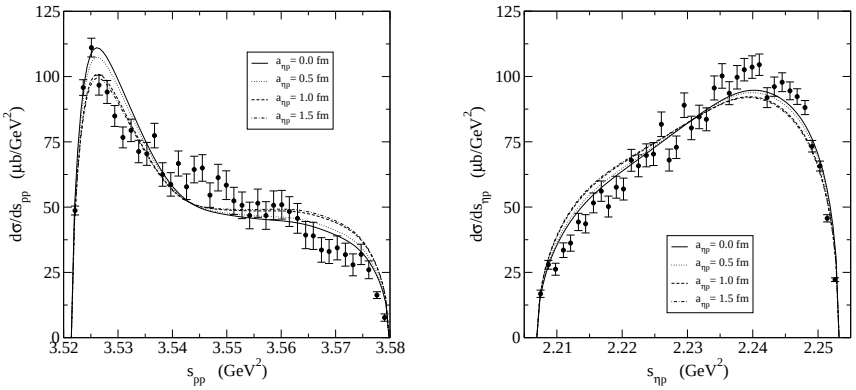

Figure 2: Invariant mass distributions at Q=15.5 MeV obtained from a three-body calculation: left panel pp pair; right panel ηp pair. The data are from [4].

edly, the dominance of the pp interaction is apparent from both plots. Since the values of $a_{\eta p} > 1\, fm$ are probably rather unrealistic [13], we may say that the ηp interaction is of marginal importance as far as invariant mass distributions are concerned.

Comparing the invariant mass spectra obtained in the two-body approach (Fig. 1) with those resulting from the full three-body calculation (Fig. 2) we can see that even when the ηp interaction is completely disregarded, the invariant mass plots are different in these two cases. Although the input in both approaches is the same but the underlying calculational schemes are different. Owing to the proper boundary condition (37) also in absence of η-p interaction the three-body wave function has entangled form, i.e it *cannot* be expressed as a product of the p-p wave function times a plane wave associated with the free propagation of the η. Since in the approximation using the two-body enhancement factor the very existence of the η is unaccounted for, the latter does not depend upon the meson kinematics (in [6] we made an attempt to lift this deficiency by introducing *ad hoc* a linear dependence upon q). By contrast, even in absence of η-p interaction the three-body enhancement factor accounts for the η propagation. In particular, the mass of the η strongly influences the dynamics of the three-body system as can be seen from (10a) and (27).

The three-body calculation is in both spectra closer to experiment. We wish to note here that the curves presented in Fig. 2 and as well as the

dashed curves from Fig. 1 contain no adjustable parameters except for the overall normalization. Our three-body calculation clearly favors smaller $a_{\eta p}$ values $a_{\eta p} \sim 0 \div 0.5\, fm$. For $a_{\eta p} > 0.5\, fm$ the height of the close to threshold peak in s_{pp} plot in Fig. 2 is depressed which is accompanied by a build up of a pronounced shoulder at the high-energy end. At the same time another shoulder appears at the low-energy end in $s_{\eta p}$ distribution in Fig. 2. All these features worsen the agreement with experiment. Unfortunately, it would be difficult to improve the existing estimates of the $a_{\eta p}$ scattering length using the data displayed in Fig. 2, especially that absorptive effects have been ignored.

Summarizing, we have developed a general three-body formalism for calculating FSI effects in a three-particle final state. To the best of our knowledge, this is the first attempt in the literature to derive a three-body final-state interaction enhancement factor. The presented calculational framework employs the hypersherical harmonics method and is applicable for three-body systems in which no binary bound state can exist. The necessary input which must be provided are all three pairwise potentials. Detailed computations carried out for the $pp \to pp\eta$ reaction at Q=15.5 MeV show that in the invariant mass spectra the role of the η-p interaction is marginal and more important is the proper boundary condition imposed on the final-state wave function. The three-body calculations involving no adjustable parameters reproduce quite well the experimental invariant mass spectra.

Partial support under grant KBN 5B 03B04521 is gratefully acknowledged.

References

[1] P. Moskal et al., Prog. Part. Nucl. Phys. **49** (2002) 1.

[2] C. Hanhart, e-Print Archive: hep-ph/0311341.

[3] M. Abdel-Bary et al., Eur. Phys. J. **A 16** (2003) 127.

[4] P. Moskal et al., Phys. Rev. **C 69** (2004) 025203.

[5] K. Nakayama et al., Phys. Rev. **C 68** (2003) 045201.

[6] A. Deloff, Phys. Rev. **C 69** (2004) 035206.

[7] E. Fermi, Nuovo Cim., Suppl. Vol. II, No. 1 (1955) 17
K.M. Watson, *Phys. Rev.* **88** (1952) 1163; *ibid.* **89** (1953) 575;
A.B. Migdal, Zh. Exper. Theor. Fiz. **1** (1955) 17.

[8] M.L. Goldberger and K.M. Watson, *Collision Theory*, Wiley, N.Y., 1964;
M. Froissart and R. Omnes, in *Physique des Hautes Energies*, C. DeWitt and M. Jacob (eds.), Gordon & Breach, New York 1965;
J. Gillespie, *Final state interactions*, Holden-Dey, San Francisco 1964.

[9] M. Abramowitz and I.A. Stegun (eds.) *Handbook of Mathematical Functions*, Dover, New York, 1965.

[10] B.V. Danilin and M.V. Zhukov, Phys. At. Nucl. **56** (1993) 460.

[11] E. Nielsen, D.V. Fedorov, A.S. Jensen and E. Garrido, Phys. Rep. **347** (2001) 373.

[12] J. Raynal and J. Revai, Nuovo Cim. **A 68** (1970) 612.

[13] A.M. Green and S. Wycech, Phys. Rev. **C 55** (1997) 2167; *ibid.* **C 60** (1999) 035208.

Quasi-free production of the η and η' mesons in nucleon-nucleon collisions

J. Stepaniak [a], H. Calén [b]
[a] *Soltan Institute for Nuclear Studies, Warsaw, Poland*
[b] *The Svedberg Laboratory, Uppsala, Sweden*

Abstract: Some aspects of the quasi-free production of mesons in the near threshold region are discussed. A method of data analysis used by WASA/PROMICE Collaboration to extract the excitation function for η production on neutron target is briefly presented. Feasibility of similar study with WASA at COSY is discussed.

1 Introduction

It is rather obvious, that the Fermi motion changes the kinematics of the interaction on the nucleon in nuclei, as compared to that on the target nucleon at rest, but the importance of the effect in the near threshold region is not always sufficiently appreciated, especially for the cross section measurements. The control of the energy available in the quasi free nucleon-nucleon scattering on the event by event basis is of importance. We will discuss here the method of extraction of the cross sections on protons and neutrons from proton-deuteron interaction applied by the WASA Collaboration to the η meson production [1] as well as the possibility of using the same method for the η' production with WASA at COSY.

The energy available in the center of mass of the nucleon-nucleon system is:

$$s = (E_b + E_t)^2 - (\vec{p}_b + \vec{p}_t)^2 = (E_b + E_t)^2 - p_b^2 - p_t^2 - 2p_b p_t cos(\theta) \qquad (1)$$

where $\vec{p}_t$ is the target momentum and $\vec{p}_t = -\vec{p}_{Fermi}$.

The product $p_b p_t$ is not small at high energies of the beam. It is multiplied by the cosine of the angle of the target momentum with respect to the beam. So it is mainly the longitudinal Fermi momentum component, that influence the energy available in the reaction.

The importance of the Fermi momentum effect is quite frequently underestimated, especially for high energy beams. In the near threshold region, where the cross section is a very steep function of energy it can dramatically influence the observed cross section. The most probable value of the Fermi momentum in the deuteron is small, equal to about 50 MeV/c. It seems to be negligible as compared to a few GeV beam energy. In reality e.g. at 1360MeV beam energy the excess energy in the nucleon-nucleon CM system can be changed by 43.5 MeV when 50MeV/c target is moving upstream the beam . At 2500 MeV the change is as large as 58.7 MeV. Such a shift can change the $pp \to pp\eta$ cross section near threshold by an order of magnitude. The distribution of the excess of energy in the CM system for the eta meson production in $pp \to pp\eta$ reaction at 1360 MeV incident energy is shown in figure 1.

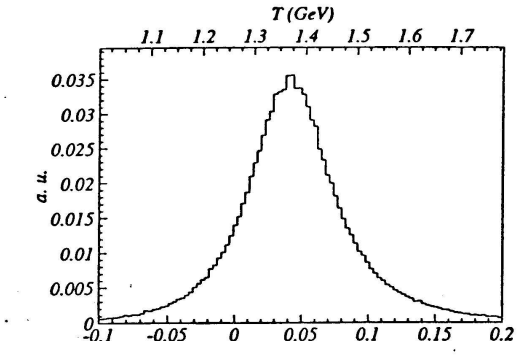

Figure 1: Distribution of the calculated CM excess energy in the nucleon-nucleon system for the 1360 MeV proton beam.

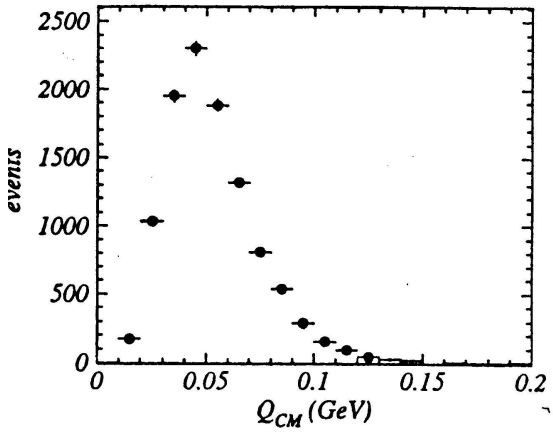

Figure 2: Distribution of the measured Q_{CM} in the nucleon-nucleon system for the 1360 MeV proton beam.

Measured distribution of the Q_{CM} for the $p+n \to d+\eta$ quasi-free reaction is shown in figure 2. The distribution is not symmetric and the average

value of the cross section does not correspond to the nominal beam energy because of the convolution with the energy dependent cross section. One can easily find examples of the papers in which hadron-nucleon cross sections were extracted from the quasi-free interactions on the deuteron without any correction for the effective energy in the nucleon-nucleon system. It leads to an overestimation of the cross section measured in a quasi-free interaction even on the so loosely bound nucleus as a deuteron. Let us take as an example the cross section for the two-pion production in the threshold region (see figure 3). The points from the experiment performed on the deuteron (full squares in the fig. 3 are substantially higher than the points from the experiments performed on free protons. The authors claimed that " The Fermi motion in the deuteron leads to a small enlargement of the beam momentum distribution only" and their measured cross sections were attached to the nominal energies of the beam. In fact the distribution of the energy in nucleon-nucleon CMS in not symmetric, when folded with the cross section and the average corresponding beam energy should be shifted to the right quite substantially.

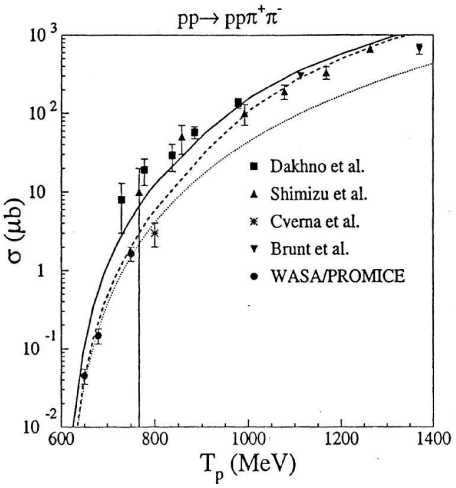

Figure 3: Cross section for the reaction $pp \to pp\pi^+\pi^-$ as a function of beam energy. Solid squares are from an experiment performed on deuteron target. The lines show theoretical predictions.

In the naive understanding of the spectator model the spectator nucleons have to be emitted isotropically with momentum distribution following the squared wave function of nucleons in the deuteron. It is usually wrong near the reaction threshold. The forward-backward asymmetry of spectators can be very pronounced and the tail of high momentum enhanced. It is due to the effective Q value dependence on the direction of the Fermi momentum vector.

2 Cross section extraction method for quasi-free η production

In the study performed by WASA/PROMICE collaboration [1, 2] validity of the impulse approximation was assumed. All the observed events were classified into the following classes of reactions:

1. $p + d \rightarrow d + \eta(p_s)$
2. $p + d \rightarrow p + p + \eta(n_s)$
3. $p + d \rightarrow p + n + \eta(p_s)$
4. $p + d \rightarrow {}^3He + \eta$

where the s subscript denotes a slow spectator nucleon for the dominant quasi-free reaction. It is impossible to judge which nucleon was active in the η production before the ${}^3He$ formation. Therefore we neglected the small fraction of the events with helium nucleus in the final state.

The possible double scattering and screening effects are expected to be on the level of few percent. We neglected it as well. It defines the accuracy of the method.

All the events with the two photons invariant mass consistent with the η mass were divided into two classes according to the event topology: the events with two charged in the forward part of the detector were attributed to the reaction 2, those with one particle were candidates for the reaction 1 or 3. The distinction between reaction 1 and 3 was possible because of the almost two-body kinematics in the first case. The Q_{CM} value was calculated from the measured quantities if only one particle was not observed. In the case of the reaction 3 the transverse component of the target nucleon momentum was neglected to reconstruct the energy excess Q_{CM}. The resolution in Q_{CM} was found to be better than 10 MeV even in this case. It was checked using the Monte Carlo simulation of the process.

In the Monte Carlo generation of the quasi-free pN reactions one should assure the energy conservation. Since spectator is on shell it requires: $E_{target} = m_d - E_s = m_d - \sqrt{m_s^2 + p_s^2}$, where the subscript s stands for "spectator". The reconstructed momentum of target neutron for the reaction $pn \rightarrow d\eta$ was compared with the result of Monte Carlo generation. Monte Carlo events were weighted with the measured cross section. The agreement between MC simulated experimental distributions was observed for several variables. As an example the distributions of the momentum

component of the target neutron is shown in figure 4. It confirmed validity of the assumed model of quasi-free interaction as well as the generation method.

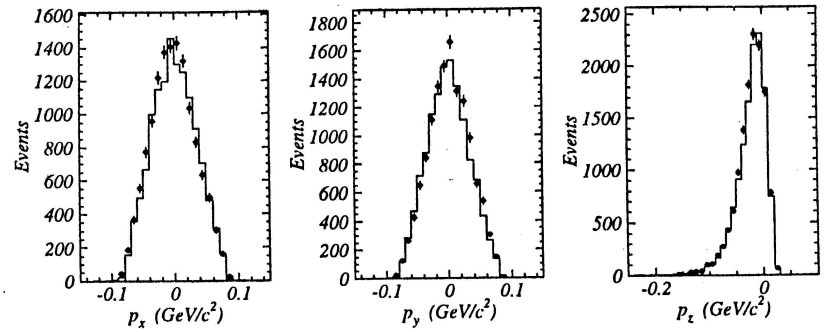

Figure 4: Distributions of the momentum component of the target neutron (opposite to the spectator nucleon) from $pn \to d\eta$ reaction at 1360 MeV; histograms - Monte Carlo, points - the experimental data.

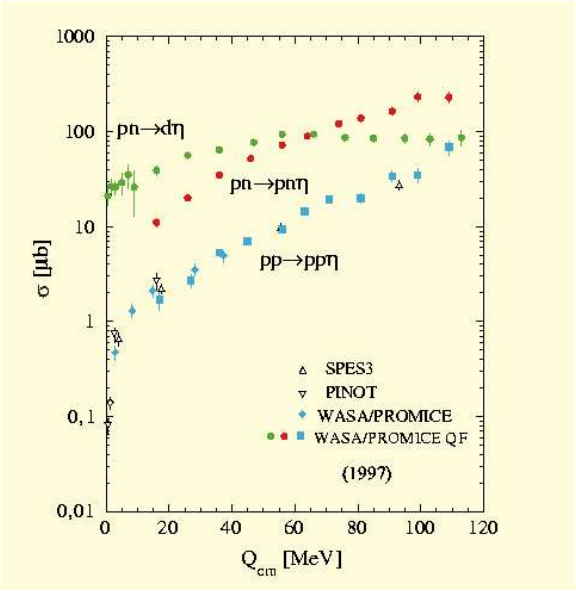

Figure 5: Cross sections for η meson production as a function of the CM excess of energy.

The result of the cross section measurements are presented in figure 5. The points for $pp \to pp\eta$ reaction from the quasi-free interaction are in agreement (within errors) with points from the reaction on free protons It is an additional argument that the impulse approximation can be used to describe the ηmeson production on deuteron at the energy considered and the excitation function can be extracted from the measurement of the quasi-free interactions from the experiment performed at one incident energy.

3 Quasi-free production of η' with WASA at COSY

The feasibility study of the quasi-free creation of the η' meson in the reaction $pn \to pn\eta$ was presented by P. Moskal [3] at COSY-11 Collaboration Meeting 2001. The idea of the experiment was based on the simultaneous measurement of the momenta of spectator proton and the neutron in COSY-11 setup. With WASA at COSY the alternative method : measurement of the η or η' decay products will be possible. The table 1 summarize the acceptances and neutral decay channels branching ratios at the selected beam energies [4].

Table 1: Comparison of BR and acceptances for the η and η' production in the pp interactions at energy excess $Q_{cm} = 40$ MeV.

	η E_{inc} =1360 MeV	η' E_{inc} = 2550 MeV
Total cross section	5μb	0.25 μb
Branching ratio:		
$\gamma\gamma$	0.39	0.02
$\pi^0\pi^0\pi^0$	0.325	0.002
$\pi^0\pi^0\eta$	-	0.21
Acceptance:		
$\gamma\gamma$	66%	52%
$\pi^0\pi^0\pi^0$	12%	6%
$\pi^0\pi^0\eta$	-	4.5

According to our experience at CELSIUS/WASA the neutral decay channels can provide more selective trigger and background condition than the charged ones. The contribution from prompt three π^0 production is much smaller then in the case of channels containing charged pions.

4 Summary

The Collaboration exploited the spread of the energy observed in nucleon nucleon quasi-free interactions at one incident proton energy (1360 MeV) to measure the energy dependence of the cross section for the η meson production. In particular it permitted to study the production in proton-neutron scattering, which was not available before.

To achieve this the Q value was measured on an event by event basis in the nucleon - active nucleon system. It became possible due to the WASA set-up ability to measure the momenta of all the active reaction products including photons from the meson decay.

References

[1] H. Calén et al., Phys. Rev. Lett. **79** (1997) 2642.

[2] S. Haggstrom, PhD Thesis, Uppsala University 1997.

[3] P. Moskal, Schriften des Forschungszentrums Julich, Matter and Materials **11** (2001) 27; e-Print Archive: nucl-ex/0110001.

[4] H. Calén, Letter of Intent for WASA at COSY.

Bremsstrahlung radiation in the deuteron – proton collision

J. Przerwa
Institute of Physics, Jagellonian University, Kraków, Poland

Abstract: The results of the identification of Bremsstrahlung radiation emitted via the $dp \rightarrow dp\gamma$ reaction in data taken with a proton target and a deuteron beam with a momentum of 3.204 GeV/c are presented and discussed.

1 Motivation

Although Bremsstrahlung radiation has been studied since many years, it is still the subject of interest of many theoretical and experimental groups [1, 2, 3, 4]. The idea of using nucleon–nucleon bremsstrahlung as a tool for distinguish among various potential models and estimate of the off-shell amplitudes has attracted attention since calculations of the cross sections of the $NN \rightarrow NN\gamma$ reaction are highly sensitive to the NN potential.

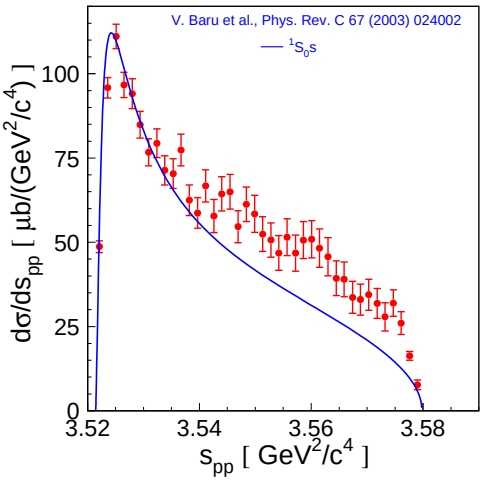

Figure 1: Differential cross section for the $pp \rightarrow pp\eta$ reaction as a function of the invariant mass of the proton–proton system. Data are from reference [5]. The solid line corresponds to the model of reference [6]. The figure is taken from [5].

We would like to investigate bremsstrahlung radiation in view of another process — related to the η–proton interaction. Figure 1 shows a differential cross section for the $pp \rightarrow pp\eta$ reaction as a function of the invariant mass of the proton–proton system. The data have been taken at an excess energy of Q = 15.5 MeV. It has been pointed out that the difference between the data and the theoretical predictions originates from proton–η interaction in the final state. In order to prove that this conclusion does not depend on the applied model it would be desirable to compare this distribution with the one obtained for the ppX system, where X does not interact strongly with protons. Therefore best suited for this purpose would be the $pp\gamma$ system. Let us assume, that the differential cross section for the $pp \rightarrow pp\gamma$ reaction as a function of proton–gamma invariant mass are determined. If the theoretical model, used for the calculations presented by the solid line in figure 1 were in perfect agreement with those data, it would corraborate the assertion that the disagreement between data and theory in the $pp\eta$ case is due to the p–η interaction.

2 Experimental setup

For the first time at the COSY–11 experiments a signal from γ–quanta was observed in the time–of–fligth distribution for the neutral particles measured between the target and the neutral particle detector [7]. This encouraged us to analyse the data in view of the Bremsstrahlung radiation in a free $dp \rightarrow dp\gamma$ and a quasi–free $np \rightarrow np\gamma$ reactions. Data have been taken using a proton target and a deuteron beam with a momentum close to the threshold of the $dp \rightarrow dp\eta$ process. Events corresponding to the $dp \rightarrow dp\gamma$ and $dp \rightarrow ppn\gamma$ reaction have been identified by measuring the outgoing charged as well as neutral ejectiles. COSY–11 detection system [8] — an internal magnetic spectrometer installed at the cooler synchrotron COSY in Jülich [9] — is schematically depicted in the figure 2. The protons and deuterons are detected by dint of drift chambers (D1, D2) and scintillator hodoscopes (S1, S2, S3) while neutrons and photons are registered in a neutral–particle–detector(N) [10]. In order to distinguish neutral particles from charged ones a veto detector (V) is used. The momentum vectors of the charged ejectiles are reconstructed by tracking back the trajectories to the target point [8]. In case of a neutron the time–of–flight between the target and the neutral–particle–detector together with the known position of the hitted detection unit enables to determine its four–momentum vector [10].

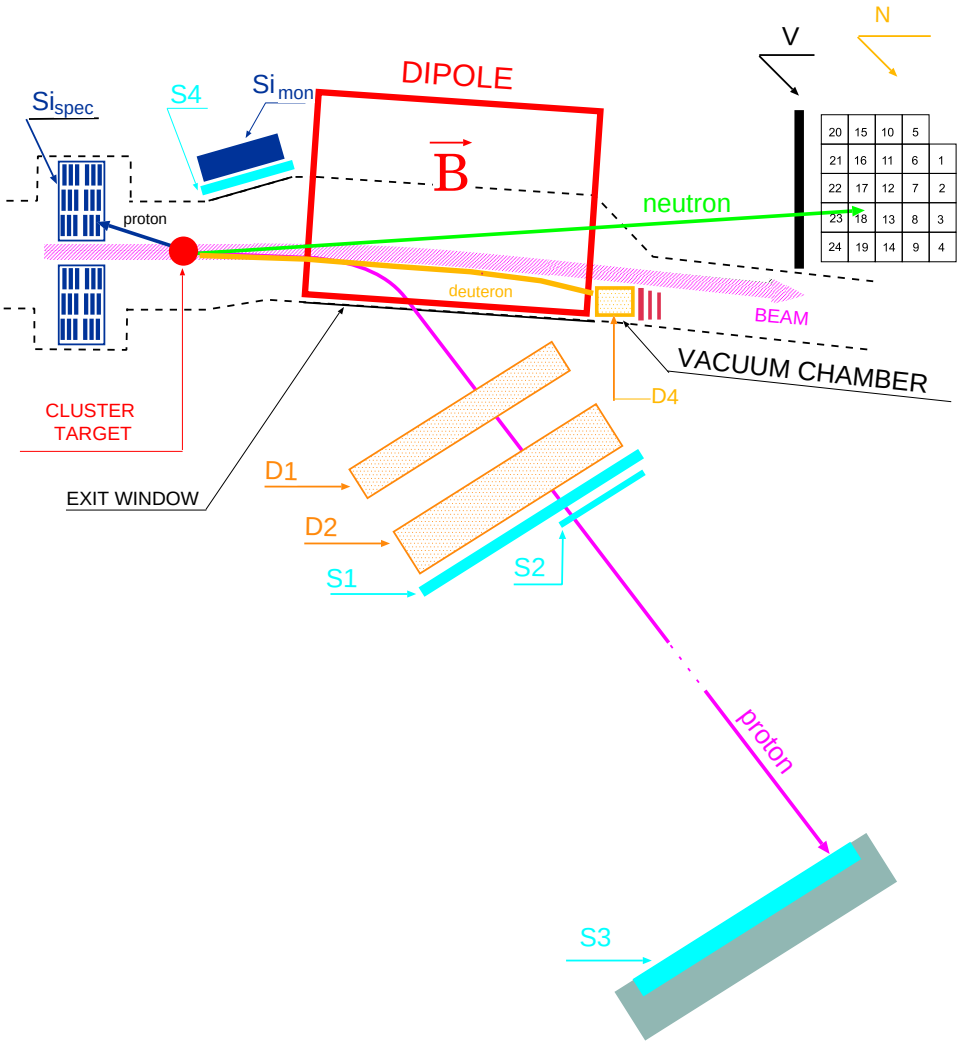

Figure 2: Schematic view of the COSY-11 detection setup [8]. D1, D2, D4 denote the drift chambers; S1, S2, S3, and V the scintillation detectors; N the neutron detector and Si_{mon} and Si_{spec} silicon strip detectors to detect elastically scattered and spectator protons, respectively. For more details concerning detectors D4 and Si_{spec} see contributions [11] and [12]

The time resolution of the neutral–particle–detector and its timing calibration are crucial for the identification of the $dp \to dp\gamma$ reaction. Therefore data analysis was preceded by the time calibration of this detector. The neutron detector is built out of 24 modules [10] and as a first step, the relative

timing between each detection unit was found.

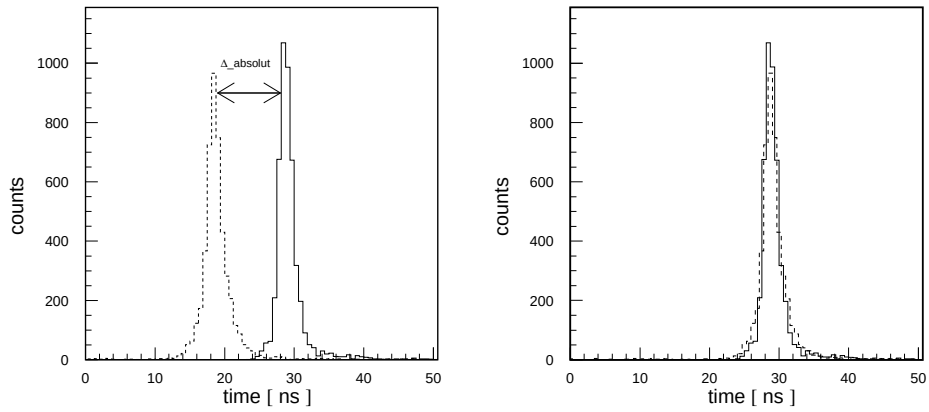

Figure 3: **(left)** Experimental time–of–flight distributions determined between the target and the neutron detector before the general time offset had been determined. The dashed histogram denotes the experimental data whereas the solid one depicts the result of the simulation. **(right)** Experimental time–of–flight distribution (dashed histogram) calculated between the target and the neutron detector with general time offset equal to 13.6 ns compared to the Monte–Carlo simulation (solid histogram).

Then the global time offset in respect to the S1 detector was found by comparing the time–of–flight spectrum derived from experimental data for the $dp \rightarrow ppn_{sp}$ reaction with the corresponding distribution reconstructed from the signals simulated in the detectors (see figure 3).

3 Data analysis

As a first step of the data analysis events with simultaneous signals in any of the drift chambers and the neutron detector were selected. Next, the trajectories of the registered particles were reconstructed and their identification was performed via the invariant mass determination. The mass of the particle is calculated from its momentum — reconstructed from tracking back through magnetic field to the target point — and velocity determined from the time–of–flight measured between S1 and S3 detector. The charged ejectiles can be well identified as shown in figure 4. Three clear peaks evidently visible in this figure correspond to the squared mass of pion, proton, and deuteron.

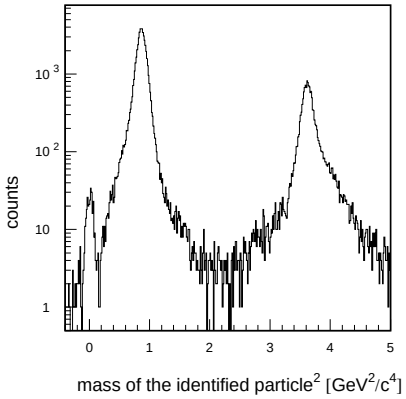

Figure 4: Distribution of the squared mass of charged particles originating from the deuteron–proton reaction measured by means of the COSY-11 detection setup at a beam momentum of 3.204 GeV/c.

Figure 5 presents the time–of–flight distributions between the target and the neutron detector obtained assuming that in coincidence with a neutral particle also a proton (left) or deuteron (right) was identified based on signals from drift chambers and scintillator hodoscopes. The signals from γ–quanta are not visible in the distributions which are predominantly due to quasi–free elastic $dp \rightarrow ppn_{sp}$ and $dp \rightarrow dn\pi^+$ reactions.

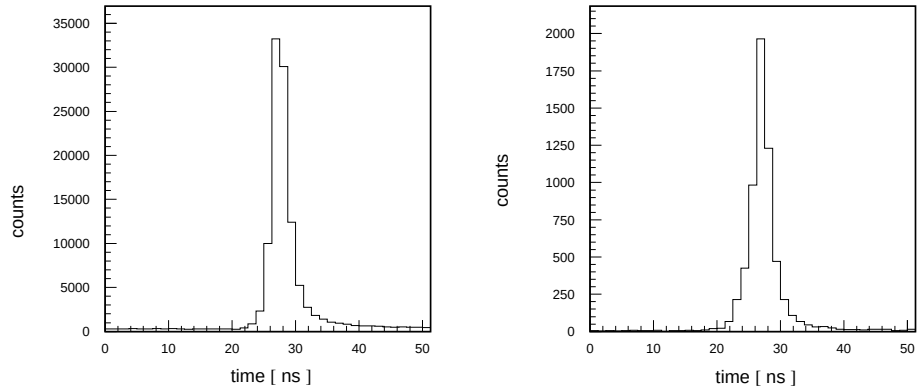

Figure 5: Experimental time–of–flight distributions determined between the target and the neutron detector obtained under the condition that additionally one proton **(left)** or one deuteron **(right)** was registered in drift chambers.

To identify the $dp \rightarrow dp\gamma$ reaction – events with two tracks in drift chambers and a simultaneous signal in a neutron detector have been selected. In figure 6 squared mass of one particle is plotted versus squared mass of the second registered particle. Based on this figure measured reactions can be grouped according to the type of ejectiles. One can clearly select reactions

with two protons, proton and pion, proton and deuteron, and pion and deuteron.

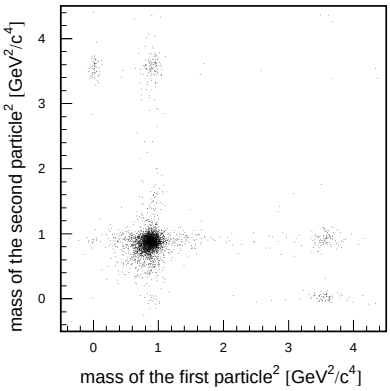

Figure 6: Scatter plot of invariant masses determined for events with two charged particles measured in coincidence.

Next the distribution of the time–of–flight between the target and the neutron detector was determined with requirement that one of the charged particles was identified as a proton and the other as a deuteron. Due to the baryon number conservation, gamma quanta are the only one possible source of a signal in a neutron detector. Indeed a clear peak around the time corresponding to the time–of–light of the light is visible (see figure 7(left)).

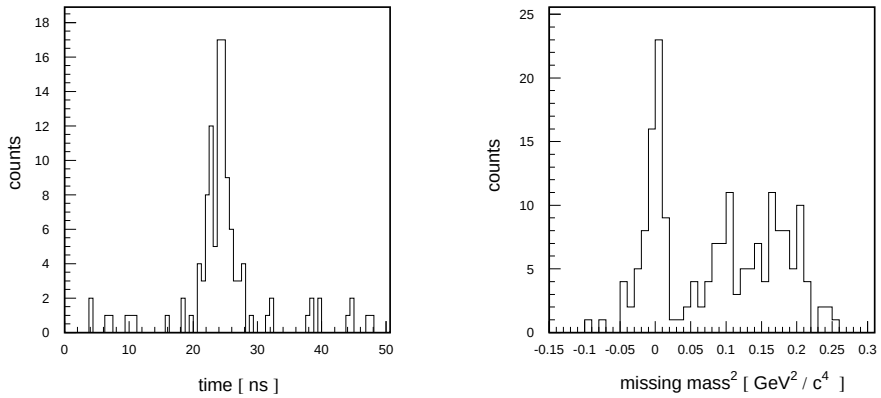

Figure 7: **(left)** Time–of–flight distribution determined between the target and the neutron detector obtained under the assumption that additionally to a signal in the neutron detector, one proton and one deuteron were identified from the signals in the drift chambers. **(right)** Squared missing mass distribution for the $dp \rightarrow dpX$ reaction.

The gamma quanta may originate from the bremsstrahlung reaction ($dp \rightarrow dp\gamma$) or from the decay of mesons produced e.g. via $dp \rightarrow dp\pi^0 \rightarrow dp\gamma\gamma$ or $dp \rightarrow dp\pi^0\pi^0 \rightarrow dp4\gamma$ reactions. It is possible to distiguish between these hypothesis calculating the missing mass produced in the $dp \rightarrow dpX$ reaction.

Figure 7(right) shows the squared missing mass distribution as obtained for the $dp \rightarrow dpX$ reaction. A significant peak around 0 MeV^2/c^4 — the squared mass of the gamma quantum — constitutes an evidence for events associated to the deuteron–proton bremsstrahlung ($dp\gamma$). In addition a broad structure at higher masses originating from two pions emitted from the reaction $dp \rightarrow dp\pi^0\pi^0$ is visible.
The extraction of the total cross section of the $dp \rightarrow dp\gamma$ reaction requires the luminosity and acceptance determination, which will be performed in the near future.

Acknowledgments

The work has been supported by the European Community - Access to Research Infrastructure action of the Improving Human Potential Programme, by the DAAD Exchange Programme (PPP-Polen), and by the Polish State Committe for Scientific Research (grant No. PB1060/P03/2004/26).

References

[1] N. A. Khokholov et al., Phys. Rev. **C 68** (2003) 054002.

[2] M. D. Cozma et al., Phys. Rev. **C 68** (2003) 44003.

[3] R. Bilger et al., Phys. Lett **B 429** (1998) 95–200.

[4] J. Greiff et al., Phys. Rev. **C 65** (2002) 34009.

[5] P. Moskal et al., Phys. Rev. **C 69** (2004) 25203.

[6] V. Baru et al., Phys. Rev. **C 67** (2003) 024002.

[7] P. Moskal et al., e-Print Archive: nucl-ex/0311003.

[8] S. Brauksiepe et al., Nucl. Instr. & Meth. **A 376** (1996) 397.

[9] R. Maier, Nucl. Instr. & Meth. **A 390** (1997) 1–8.

[10] J. Przerwa, e-Print Archive: hep-ex/0408016; diploma thesis, Jagellonian University (2004), Berichte des FZ-Jülich, **Jül 4141** (2004).

[11] C. Piskor-Ignatowicz et al., this proceedings, page 272.

[12] M. Janusz, P. Moskal, this proceedings, page 238.

Measurement of the η meson production via the quasi-free $pn \to pn\eta$ reaction

M. Janusz[a], P. Moskal[a,b]

[a] *Institute of Physics, Jagellonian University, Cracow, Poland*

[b] *Institut für Kernphysik, Forschungszentrum Jülich, Germany*

Abstract: A test of a feasibility to study the quasi-free $pn \to pn\eta$ reaction has been carried out at the COSY-11 facility at the cooler synchrotron COSY in Jülich using a proton beam scattered on a deuteron cluster target. The data are still under evaluation but clearly demonstrate the possibility to reconstruct quasi-free $pn \to pn\eta(\eta')$ reactions at COSY-11.
Preliminary results from the measurement of the $pn \to pnX$ reaction channel will be presented.

1 Introduction

The value of the total cross section for the reaction $pp \to pp\eta$ was found by the WASA/PROMICE collaboration to be about 6.5 times smaller than for the $pn \to pn\eta$ reaction in the excess energy range between 16 MeV and 109 MeV [1]. Here we report on the preliminary results of the measurement carried out by the COSY-11 collaboration of the $pn \to pn\eta$ reaction at the excess energy range between 0 to 20 MeV. As far as the production of mesons in the quasi-free proton-neutron scattering is concerned, a premordial experimental aim of the COSY-11 collaboration is to determine the absolute value and the energy dependence of the total cross section for the $pp \to pp\eta'$ reaction. The measurement of the $pn \to pn\eta$ reaction was conducted as a test of the feasibility to measure the meson production via quasi-free $pn \to pnX$ reactions at the COSY-11 facility equipped with the neutron [2, 3, 4] and the spectator detectors [5, 6]. The $pn \to pn\eta$ reaction was chosen because its total cross section close to the threshold is expected to be by a factor of about fourty larger than the corresponding total cross section for the $pn \to pn\eta'$ reaction. This inference is drawn by analogy to the $pp \to ppX$ reactions [7].

In the test measurement the beam momentum was taken such that the maximum rate of the registered $pn \to pn\eta$ events occurs at the excess energy range between 0 and 20 MeV. Therefore the measurment will allow to

establish the energy dependence of the total cross section of the $pn \to pn\eta$ reaction in the unknown energy region close to the kinematical threshold. The overlap in the excess energy with the data of the WASA/PROMICE collaboration will permit to check the consistency of results obtained at different laboratories.

A schematic view of the COSY-11 facility with the detectors relevant for the measurement of the quasi-free $pn \to pn\eta$ reaction is presented in this proceedings in the preceding contribution [8]. Spectator proton is detected in an array of Si-pad detectors close to the target, the neutron in the neutron detector, and the high momentum protons are measured in the drift chambers and scintillators. Using this setup it is possible to reconstruct momenta of all outgoing nucleons of the $pd \to p_{sp}pn\eta$ reaction and to determine the excess energy for each event.

2 Simulation and data analysis

Details of the experimental technique were already presented on the previous COSY-11 symposium [9], and the results of the first stage of the data analysis were published in the proceedings of the conference HADRON'03 [10].

Here for the completeness we will report the results yet in the significantly abridged form and additionally present first rough estimations of the total cross section at three values of the excess energy.

2.1 Functioning of the detectors

For the measurement discussed in this presentation the spectator and neutron detectors were used for the first time after the installation at the COSY-11 facility. In functioning was fully confirmed during the run. The well agreement between the expectations and the experimental results was already seen by the reviewing of the on-line spectra. Few examples will be discussed below. Figure 1 compares experimental data and Monte-Carlo calculations for the number of hits per module in the neutron detector. There are slight differences in the relative counting rate between various detection units yet the general trend of the observed structure coincides well with the result of the simulations based on the GEANT code. Figure 1 indicates that the applied voltages for each of the 48 photomultipliers have been correctly estimated [4], and we could use the same discrimination level for all detection modules. The appraisals of the gain of the signals in all detection units have been performed prior to the experiment by means of cosmic rays [4].

For more details of the functioning and calibration of the neutron detector the reader is referred to references [2, 8].

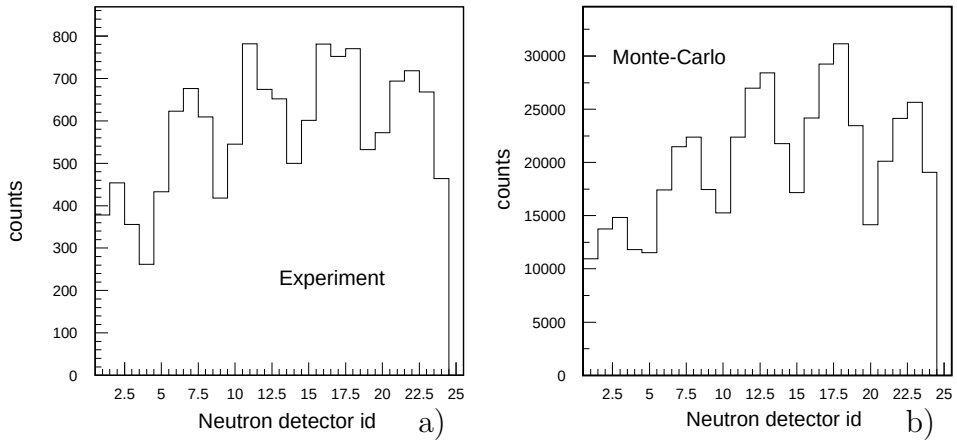

Figure 1: Number of hits per individual module of the neutron detector. Module id's are defined in reference [8].
a) As obtained in the experiment. b) Monte-Carlo simulation.

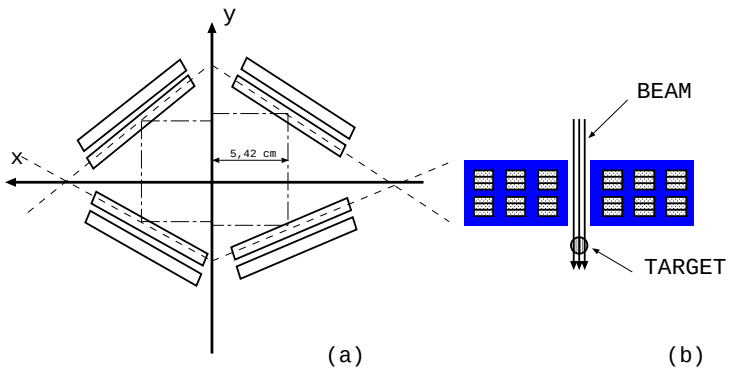

Figure 2: Spectator detector – a schematic view. (a) Seen from aside: z-axis corresponds to the beam line. (b) Seen from above

A schematic view of the spectator detector arrangement is presented in figure 2. This detector previously used by the WASA/PROMICE collaboration [11] consists of four double–layered pads, each one containing eighteen silicon strips in the front layer (which is the plane closer to the beam) and six strips in the back layer. The active area of each single strip in the front

layer amounts to 20 mm $*$ 5 mm, whereas of those in the back layers to 20 mm $*$ 18 mm. The thickness of each of the silicon strips is 300 μ m. Protons, having the kinetic energy smaller than 6 MeV are absorbed in the first layer and for those with larger energy we expect a dependence between energy deposited in the first (dE_1) and second layer (dE_2) as shown in figure 3(left).

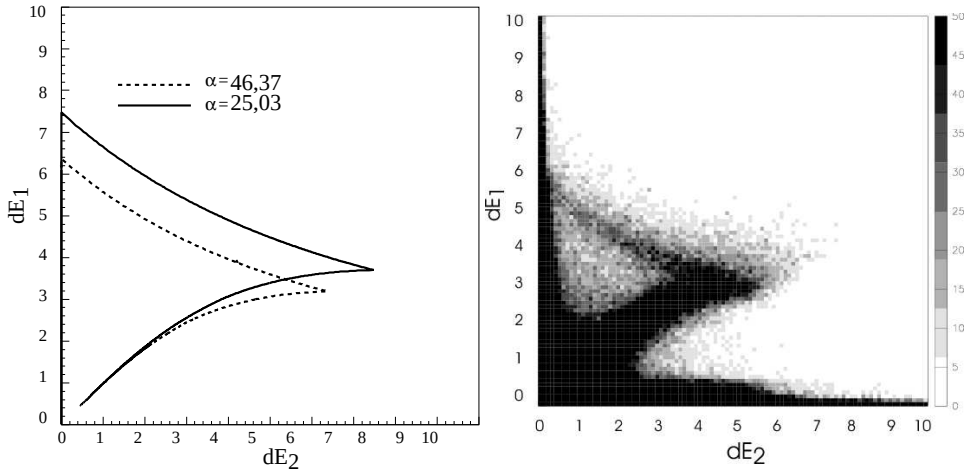

Figure 3: (left) Expectations for the energy losses in the first layer versus second layer derived for two extreme angles accepted by the spectator detector [6]. For the calculations the values of stopping power were taken from tables of reference [21]. (right) On-line spectrum [4] of energy losses in the first layer versus the second layer of the spectator detector. The measurement was conducted with the deuteron target and the proton beam with momentum of 2.075 GeV/c.

The figure shows the result computed for the extreme angles ($46,37^o$ and $26,05^o$) at which the protons may traverse the active area of the spectator detector. The corresponding experimental spectrum obtained on-line is presented in right panel of figure 3. One recognizes that qualitatively the spectrum integrated over all detection units is as expected, however, still the calibration constants need to be determined more precisely to achieve a quantitative agreement. The details of the calibration method can be found in reference [6].

2.2 Appraisals of luminosity

For the determination of the luminosity additionally to the studied reaction a quasi-free $pp \rightarrow pp$ scattering was measured. Events corresponding to the elastically scattered protons can be identified by the correlation between the angles of the scattered particles. In case of the $pp \rightarrow pp$ reaction, according to the two body kinematics, there is a unique relation between these scattering angles. Figure 4a shows the expectation for the relation between the position determined in the S1 detector and the position sensitive silicon detector (Si_{mon}). The configuration of detectors is presented in this proceedings in the previous contribution [8]. The position in these detectors is in a unique relation to the scattering angles. The spread of the points presented in figure 4a is predominantly due to the Fermi motion of the nucleons inside a deuteron target and only to a minor degree due to the experimental resolution. Both these effects were taken into account in the simulations [12]. Figure 4b shows the experimental scatter-plot determined on-line during few hours of data taking. This distribution is not as uniform as the one obtained from Monte-Carlo simulations, since there is a strong dependence of the cross section on the scattering angle, which was not taken into account in the simulations.

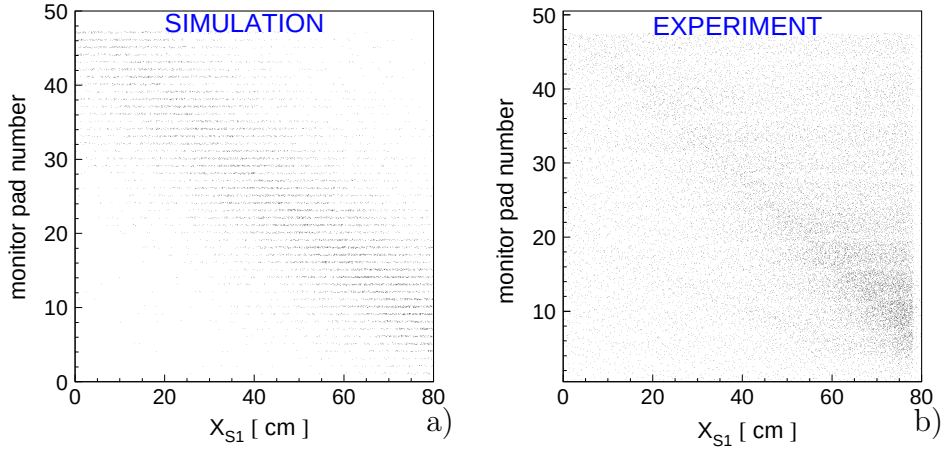

Figure 4: Comparison between the simulation results and experimental data. Figures show the hit position in the Si_{mon} detector as a function of the hit position in the scintillator array S1 (for detector configuration see previous contribution).

During the run we have estimated on-line the absolute value for the luminosity at some measurement periods. This was done by comparing the experimental data and the simulated distributions, and knowing from

the literature [13] the differential cross sections for the elestically scattered protons. For the preliminary estimation of the total integrated luminosity from the whole measurement we used the coincidence rate between S1 and S4 detectors and assumed that the fraction of this trigger rate due to the elastically scattered protons was constant during the entire run. The needed value of the ratio between the luminosity and the $S1 - S4$ trigger rate we determined at measurement periods when the luminosity was calculated. Thus the tentative values of the cross sections quoted in the next sections are burdened by the mentioned assumption and therefore need to be taken with care. The total integrated luminosity was found to be $1.03 \cdot 10^{35}\ cm^{-2}$.

3 Tentative evaluation of the $pn \to pn\eta$ reaction

The data considered were taken by means of the COSY-11 facility [14] using a deuteron cluster target [15] and a proton beam with a momentum of 2.075 GeV/c. In the first step of the analysis events with one reconstructed track in the drift chambers and simultaneous signals in the neutron and spectator detectors have been selected. Next we rejected most of the signals caused by the charged pions by requiring that the particle registered by the spectator detector gave signal in the first layer only, and demanding that the invariant mass of the particle detected by drift chambers and S1 and S3 detectors was by three standard deviation of the mass resolution larger than the mass of the pion. Further, assuming that the slow particle registered in the spectator detector originated from the deuteron we could calculate the total centre-of-mass energy for a quasi-free proton-neutron reaction under the assumption of the impulse approximation. Figure 5 shows spectra of the excess energy in respect to the $pn\eta$ system as obtained in the experiment (5a) and the simulation (5b) for the $pn \to pn\eta$ reaction. The remarkable difference between the distributions comes from the fact that in reality additionally to the $pn \to pn\eta$ reaction also the multi-pion production is registered.

The η and multi-pion production cannot be distinguished from each other on the event-by-event basis by means of the missing mass technique.

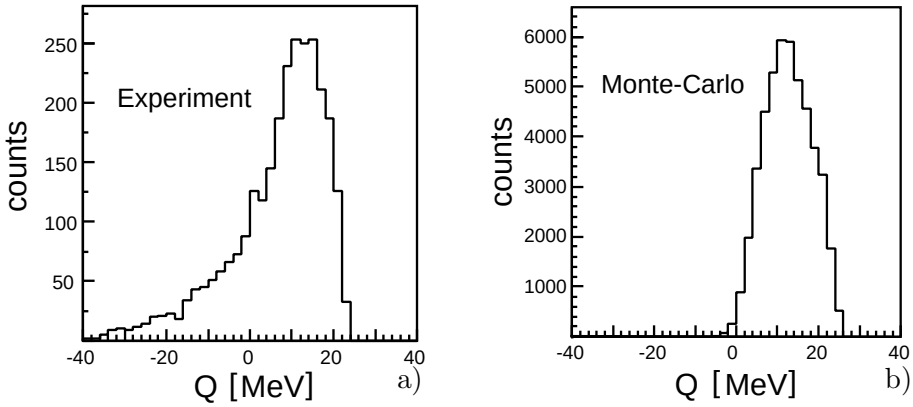

Figure 5: Distributions of the excess energy Q for the quasi-free $pn \to pnX$ reaction, determined with respect to the $pn\eta$ threshold. (a) Experiment. (b) Simulation.

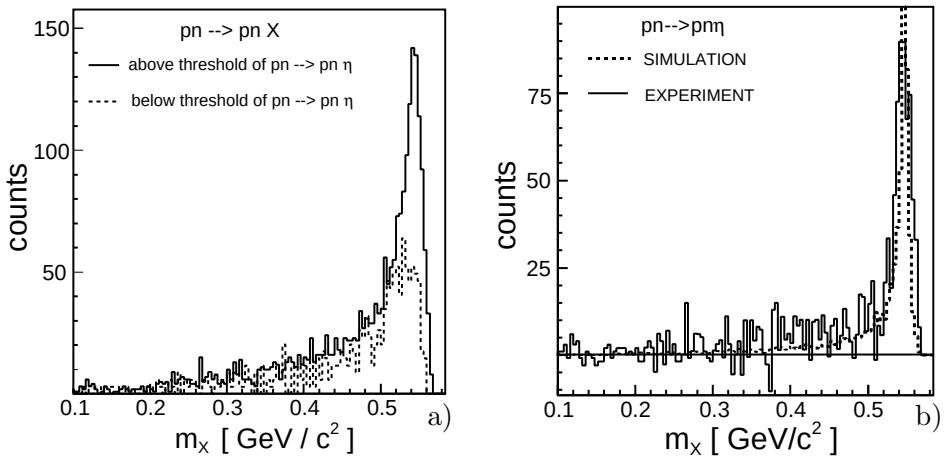

Figure 6: Missing mass spectra as obtained during the June'02 run:
a) Event distribution for $Q < 0$ (dashed line) and for $Q > 0$ (solid line).
b) Solid line represents the difference between number of events above and below threshold for the $pn \to pn\eta$ reaction, and the dashed line corresponds to the Monte-Carlo simulation.

However, we can distinguish the number of the registered $pn \to pn\eta$ reactions from the multi-pion background comparing the missing mass distributions for Q values larger and smaller than zero. Knowing that negative values of Q can only be assigned to the multi-pion events we can derive the shape of the missing mass distribution corresponding to these events. This is shown as the dashed line in figure 6.

A thorough evaluation of the background is in progress, and a suggestion of the method for its subtraction is presented in this proceedings in the subsequent contribution [22]. Here we would like to point out that already a rough comparison of events for positive and negative Q yields a promising result with a clear signal from the $pn \to pn\eta$ reaction, as can be deduced reviewing figures 6a and 6b [10].

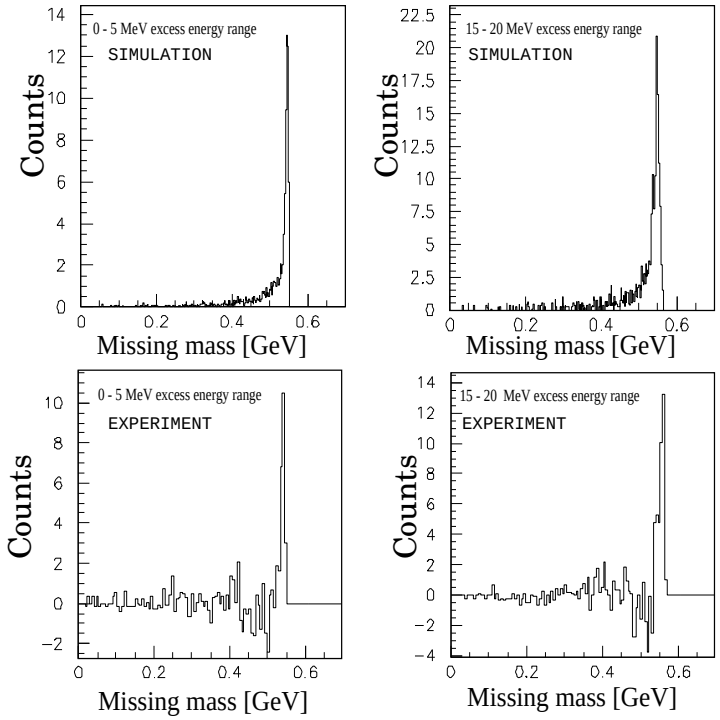

Figure 7: The comparison of the missing mass spectra from simulation and experiment for two energy subranges as indicated inside figures.

Taking into account that the resolution of the excess energy determination amounts approximately to 5 MeV (FWHM) [12] we have divided the whole range of the excess energy into four subranges with widths corresponding to 5 MeV. For each partition the missing mass spectrum was determined. In parallel a missing mass distribution was established also for the negative values of excess energy and after a shift to the kinematical limit and normalization at mass values lower than 0.3 GeV it was subtracted from the histograms for the positive Q values. The normalization was performed separately for each of the considered subranges of Q. Figure 7 shows exem-

plary missing mass spectra from the simulation and the experiment. They are in qualitative agreement, though the modulations below the η peak in the experimental spectra indicates that the background subtraction needs to be improved.

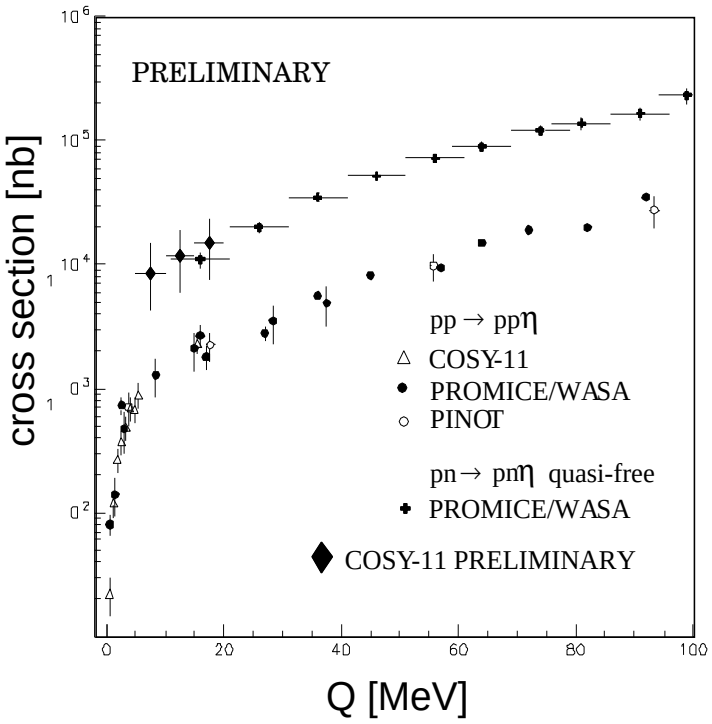

Figure 8: Preliminary results of the total cross section for the η meson production in the quasi-free $p-n$ scattering. Diamonds indicate COSY-11 preliminary results, and the other points show the data from [1, 9, 17, 18, 19, 20].

Figure 8 shows the comparison between the total cross sections for the $pn \to pn\eta$ reaction determined by the WASA/PROMICE collaboration and the preliminary results obtained by the simplified analysis of the COSY-11 data. The error bars for the COSY-11 points have been enlarged arbitrarily by the 40% of the central values to account for possible errors caused by the temporarily too crude approximation of the multi-pion background and luminosity. The aim of the presented analysis was the rough estimation of the cross section in order to gain a motivation for performing a thorough and accurate data analysis requiring an laborious effort.

Acknowledgments

The work has been supported by the European Community - Access to Research Infrastructure action of the Improving Human Potential Programme, by the DAAD Exchange Programme (PPP-Polen), and by the Polish State Committe for Scientific Research (grants No. 2P03B07123
and PB1060/P03/2004/26).

References

[1] H. Calén et al., Phys. Rev. **C 58** (1998) 2667.

[2] J. Przerwa, e-Print Archive: hep-ex/0408016; diploma thesis, Jagellonian University (2004), Berichte des FZ-Jülich, Jül-4141 (2004).

[3] P. Moskal, Ann. Rep. 1996, IKP, FZ–Jülich, Jül-3365 (1997) p.35; and Ann. Rep. 2001, IKP, FZ–Jülich, Jül-3978 (2002) p.19;
T. Rożek, P. Moskal, Ann. Rep. 2002, IKP, FZ–Jülich, Germany (2003).

[4] M. Janusz et al., Ann. Rep. 2002, IKP, FZ–Jülich, Germany (2003).

[5] M. Janusz, P. Moskal, Ann. Rep. 2003, IKP, FZ–Jülich, Germany (2004); E. Białkowski et al., Ann. Rep. 2001, IKP, FZ–Jülich, Jül-3978 (2002) p.22; J. Majewski et al., Ann. Rep. 2001, IKP, FZ–Jülich, Jül-3978 (2002) p.21.

[6] M. Janusz, diploma thesis, Jagellonian University (2004).

[7] P. Moskal, e-Print Archive: hep-ph/0408162.

[8] J. Przerwa, this proceedings, page 231.

[9] P. Moskal, e-print Archieve: nucl-ex/0110001.

[10] P. Moskal et al., AIP. Conf. Proc. No. **717** (2004) 907 [nucl-ex/0311003].

[11] R. Bilger et al., Nucl. Inst. & Meth. **A 457** (2001) 64.

[12] R. Czyżykiewicz, diploma thesis, Jagellonian University (2002), Berichte des FZ-Jülich, Jül-4017 (2002).
available at http://ikpe1101.ikp.kfa-juelich.de/

[13] D. Albers et al., Phys. Rev. Lett. **78** (1997) 1652.

[14] S. Brauksipe et al., Nucl. Instr. & Meth. **A 376** (1996) 397.

[15] H. Dombrowski et al., Nucl. Instr. & Meth. **A 386** (1997) 228.

[16] P. Moskal et al., COSY Proposal No.133.

[17] J. Smyrski et al., Phys. Lett. **B 474** (2000) 182.

[18] F. Hibou et al., Phys. Lett. **B 438** 41 (1998) 41.

[19] F. Calén et al., Phys. Lett. **B 366**(1996) 39.

[20] E. Chivassa et al., Phys. Lett. **B 322** (1994) 270.

[21] Atomic data and Nuclear Data Tables **27** (1982) 147-339.

[22] P. Moskal, this proceedings, page 249

How to disentangle contributions from a single meson and multi-pion production in the missing mass spectra of the quasi-free $pn \to pnX$ reactions

P. Moskal
Institute of Physics, Jagellonian University, Cracow, Poland
Institut für Kernphysik, Forschungszentrum Jülich, Germany

Abstract: An identification of the $pn \to pn\eta$ reaction on the event-by-event basis is impossible if only the four-momentum vectors of nucleons are measured. One can however extract the number of registered $pn \to pn\eta$ events from the missing mass distribution provided that the contribution of the continuous spectrum originating from the multi-pion production can be disentangled from the signal resulting from the production of the η meson. This is a challenging task especially if the resolution of the mass determination is comparable with the excess energy with respect to the $pn \to pn\eta$ reaction, due to the proximity of the measured signal to the kinematical limit. In this report a method allowing to distinguish the contributions of multi-pion and a single meson production in the missing mass spectrum of the quasi-free $pn \to pnX$ reaction is introduced. The technique is based on the plausible assumption whose validity can be clearly corraborated. It permits the evaluation of the data without the necessity of the model-dependent simulations, and does not require an exact knowledge on the dynamics of the background reactions.

1 Introduction

The subject of my talk given at the symposium was "The study of the η-nucleon and η'-nucleon interaction via $pp \to ppMeson$ reactions at COSY-11". Since the achievements I had presented have been reported in the comprehensive form shortly after the meeting in the reference [1], and also in the article [2] the reader interested in the newest information on this subject is referred to these publications. In this report, instead of repeating the already published results, – as an addendum to the previous contribution to this proceedings [3] – I would like to present method to subtract an inevitable multi-pion background from the missing mass spectrum in the case of the η and η' mesons production when investigated via the quasi-free $pn \to pnX$ reactions without the detection of their decay products. Such

a method is highly needed for the correct derivation of the number of the $pn \to pn\eta$ and $pn \to pn\eta'$ events from the missing mass spectra obtained by the COSY-11 collaboration [3, 4].

The measurements of the quasi-free $pn \to pn\eta$ and $pn \to pn\eta'$ reactions are being conducted at the COSY-11 facility by registering all outgoing nucleons from the $pd \to p_{sp}pnX$ reaction and using the missing mass technique for the identification of events with the creation of the meson under investigation. Subscript $_{sp}$ denotes the spectator proton, which does not take part in the reaction. Hereafter I will lead consideration on the example of the η meson production, but all the conclusions are valid for the η' meson as well.

2 Derivation of the background under the supposition of the infinite statistics

The quasi-free $pn \to pnX$ reactions are investigated at the COSY-11 facility [5] equipped with the neutron [6] and spectator [7] detectors. Experiments are conducted using the COSY proton beam [8] scattered on the internal deuteron cluster target [9]. The known momentum of the proton beam and the indirect determination of the four-momentum vector of neutron inside the deuteron at the moment of the collision permit to determine the total energy available for the proton-neutron reaction for each registered event [4, 10]. Therefore, the collected data can be grouped according to the excess energy with respect to the $pn \to pn\eta$ process. The production of the η meson may occur only if the excess energy Q – expressed explicitly as –

$$Q = \sqrt{s} - m_{proton} - m_{neutron} - m_{\eta} \tag{1}$$

acquires positive value. In the case of the negative values of Q only pions may be created.

Figure 1 shows in a schematic manner the mass distributions for the $pn \to pnX$ reaction as expected in the measurement using the COSY-11 detection setup. X denotes the η meson or multi-pion system. The upper panel presents a schematically outlined missing mass spectrum in the case of the negative Q value. The shape of this continuous distribution originates from the convolution of the real invariant mass distribution of the multi-pion system, the efficiency of the COSY-11 detection setup for the simultaneous registration of nucleons from the $pn \to pn$ *pions* reaction, and also from the experimental resolution of the missing mass determination.

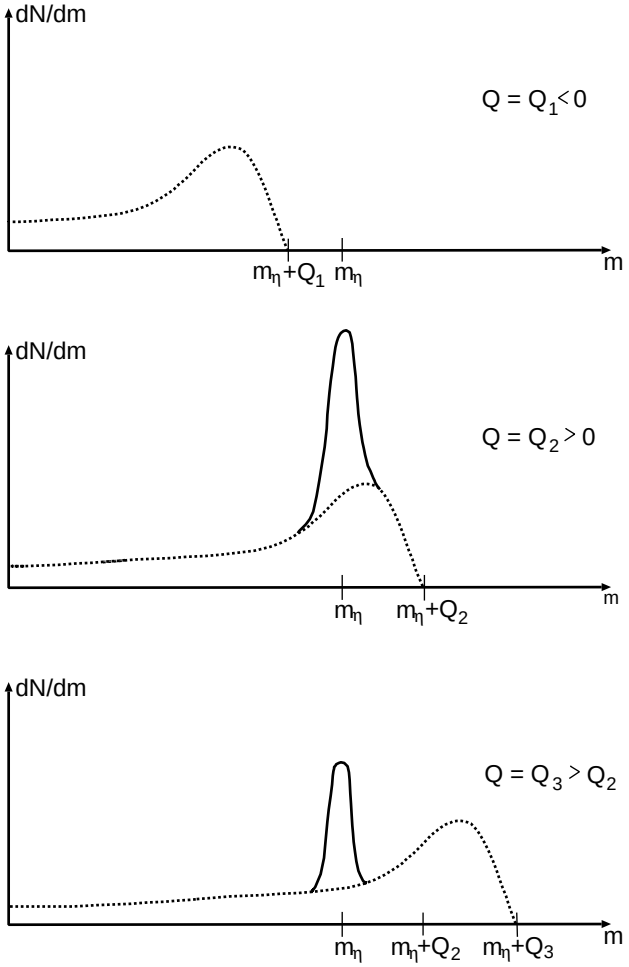

Figure 1: Schematic depiction of the missing mass spectra for the $pn \to pnX$ reaction below ($Q = Q_1$) and above ($Q = Q_2$ and $Q = Q_3$) the threshold for the η meson production. More details concerning the shape of the continuous multi-pion spectrum are presented hereafter in figure 4.

For Q value larger than zero a signal from the η meson is expected on the top of the multi-pion mass distribution at a position corresponding to the η meson mass. An example is shown in the middle panel of figure 1. For the data sample with higher value of Q the peak from η meson will remain at the same position on the mass axis, yet the distribution of multi-pion invariant mass will broaden towards the larger mass values (see the lowest panel of figure 1). However, in practice, as it will be argued later on, the change of the multi-pion background can be approximated as a shift of the

entire spectrum in the direction of the higher masses.

In the case of the $pn \to pn\eta$ reaction, measured by means of the COSY-11 facility, the experimental mass resolution amounts to about 5 MeV(FWHM) [11]. Therefore, for the measurement at only few MeV above the threshold the shape of the pion background must be well known in order to extract the signal from the η meson production as can be deduced by reviewing the middle panel of figure 1. The preliminary analysis of the $pn \to pn\eta$ reaction measured at COSY-11 facility confirms this supposition [3]. The lack of a clear indication of the upper end of the signal resulting from the η meson production constitutes the main problem in disentangling the contributions from the η meson and pions.

The solution of this difficulty could be considered as straightforward if one would assume that the measured shape of the background does not change with the excess energy and that the number of events registered is sufficient for the differential and still statistically significant elaboration of the data. In a subsequent part of this report I will try to give arguments in favour of the former assumption, however, as far as the statistics is concerned, the suggestion will require a further modification which will be proposed later on as well.

Thus, for the simplicity of argumentation, let us first assume that the number of events written on tapes is "infinite" (permitting to neglect any statistical fluctuations) and that the shape of the reconstructed invariant mass of pions is independent of the excess energy Q. In such a case, in order to establish the form of the background it would be sufficient to determine a missing mass spectrum ($\frac{dN^{\pi}}{dm}$) from infinitesimal range of any of the negative values of Q. Assuming that the shape of the background ($\frac{dN^{\pi}}{dm}(m,Q)$) does not depend on Q one can express it in a convenient way as a function of the difference between the kinematical limit $(m_\eta + Q)$ and the given mass m. Furtheron the function describing the form of the background normalized to unity will be denoted by $B(m_\eta + Q - m)$.

The primary purpose of the analysis is to establish the number of events corresponding to the $pn \to pn\eta$ reaction as a function of the excess energy Q. To arrive at this aim it is indispensable to subtract the multi-pion background from the $pn \to pnX$ events for individual values of Q. Being not limited by the statistics one could divide the range of positive values of Q into so narrow subranges that the resultant missing mass spectrum - in each subrange of Q - would be a simple sum of the form B and a signal from the η meson. The discussed situation is depicted schematically in figure 2. Lower panel of this figure shows the method of the construction of the background.

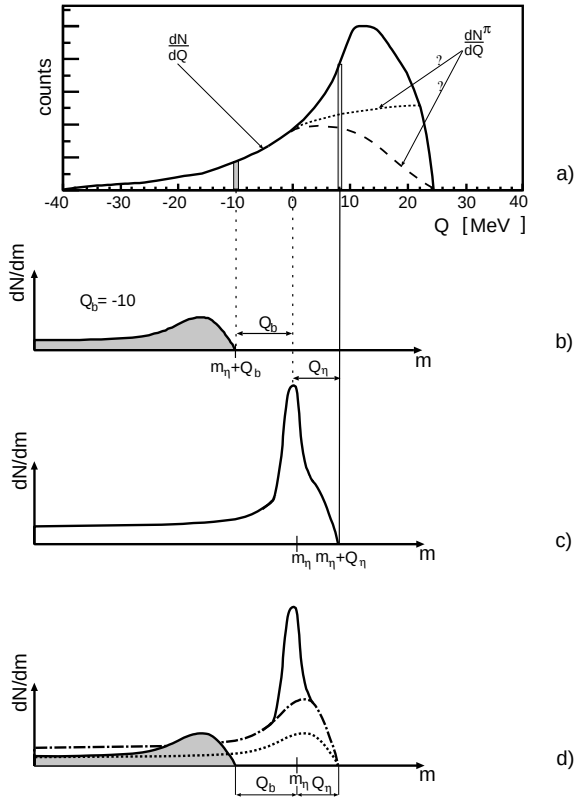

Figure 2: a) Distribution of the excess energy with respect to the $pn \rightarrow pn\eta$ reaction plotted schematically for the beam momentum of $P_b = 2.075\ GeV/c$. The shape results from i) the genuine excitation function for the η meson and multi-pion production in the proton-neutron collisions, ii) the distribution of the Fermi momentum of nucleons in the deuterium target, and iii) the acceptance of the detection system. For the detailed discussion of this issue see e.g. references [4, 10]. The contribution to the spectrum from the pions production $\frac{dN^{\pi}}{dQ}$ cannot be unambiguously derived from the experimental data. Therefore, entirely arbitrary, two different possibilities are pointed out as a dotted and dashed lines.
b), c) Scheme of the missing mass spectra as derived for the negative (Q_b) and positive (Q_η) values of Q. To each value of Q a continuous spectrum of masses can be assigned, originating e.g. from the $pn \rightarrow pn\pi\pi$ reaction. However, there is always a unique relation between the value of Q and the maximum mass which can be created ($m_{max} = m_\eta + Q$). Therefore for a better visualisation, the axis of Q for the $\frac{dN}{dQ}$ distribution and the mass axis of the missing mass spectra $\frac{dN}{dm}$ were arranged such that a maximum mass achievable for a given value of Q lies exactly below the corresponding Q value in the $\frac{dN}{dQ}$ plot.
d) The shape of the background in the mass spectrum for Q larger than zero can be constructed from the shape of the multi-pion mass distribution (shaded histogram) after its shift to the kinematical limit (dotted line) and subsequent normalisation at low masses (dashed-dotted line).

If the two assumptions mentioned above were valid, then in order to derive a signal of the η meson from a missing mass spectrum for positive Q it would be sufficient to subtract a missing mass spectrum determined for negative Q after the shift of the latter to the kinematical limit (dotted line) and normalization at the very low mass values where no events from the η meson production are expected (dashed-dotted line). In such a case the contribution of the $pn \to pn\eta$ reaction could be extracted without the necessity of any assumption of the unknown distribution of the background expressed as a function of the excess energy ($\frac{dN^{\pi}}{dQ}$). Thus, the analysis would not demand an exact knowledge of the dynamics of the background reactions.

3 Estimation of the background under the real experimental conditions

Due to the finite statistics, for the extraction of the missing mass spectrum one needs to take some finite range of the Q values. This does not influence the shape of the distribution from the $pn \to pn\eta$ reaction, yet it alters the form of the multi-pion background. The latter ($\frac{dN^{\pi}}{dm}(m)$), when derived from the finite ΔQ range becomes the convolution of the B function and the number of background events expressed as a function of the excess energy $\frac{dN^{\pi}}{dQ}$. For the range spanned between Q_{min} and Q_{max} the missing mass distribution of the background ($\frac{dN^{\pi}}{dm}$) can be expressed as:

$$\frac{dN^{\pi}}{dm}(m) = \int_{Q_{min}}^{Q_{max}} \frac{dN^{\pi}}{dQ}(Q)\ B(m_{\eta} + Q - m)\ dQ. \qquad (2)$$

In the dN/dQ spectrum we cannot – in the model independent way – extract the function $\frac{dN^{\pi}}{dQ}$ for the positive values of Q (compare dashed and dotted lines in figure 2). Thus, the only way is to take as narrow ranges of ΔQ as it is reasonable when taking into account the experimental resolution of Q, and to assume that within this range the $\frac{dN^{\pi}}{dQ}$ function is constant. It is natural to take the width of the Q subranges equal to the FWHM of the resolution of the Q determination. Such a choice of the width of the ΔQ bin validates partly the assumption that $\frac{dN^{\pi}}{dQ}$ = constant(Q) due to an unavoidable experimental smearing of $\frac{dN^{\pi}}{dQ}$ inside the bin.

By reviewing the experimental distribution $\frac{dN}{dQ}$ shown in the upper panel of figure 3, one recognizes that the obtained statistics is indeed insufficient

for the derivation of the $\frac{dN^{\pi}}{dm}$ spectrum from the bin of Q with the width equal to the experimental resolution (FWHM = 5 MeV).

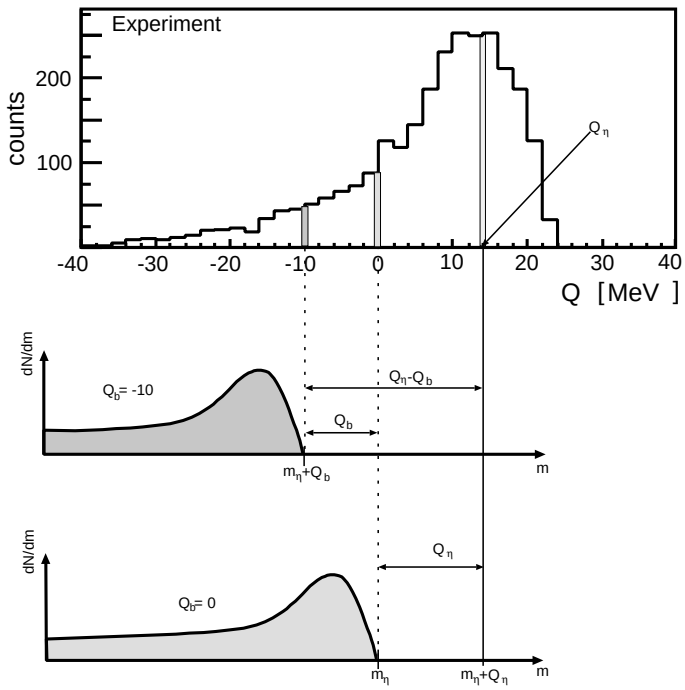

Figure 3: Upper panel: Experimental distribution of the excess energy Q as measured by means of the COSY-11 setup, using a deuteron target and proton beam with a momentum of 2.075 GeV/c [4].
Lower panels: Scheme of the missing mass distribution for two arbitrarily chosen values of Q.

Yet, the statistics can be improved significantly if all events registered with Q less than zero could be taken into account. This can be realized by adding to the missing mass calculated for a given event a value of $(Q_\eta - Q_b)$ which will shift the background events measured at Q_b to the kinematical limit defined by the Q_η. In this manner one constructs the background for the missing mass spectrum obtained for $Q = Q_\eta$. The resultant modified missing mass distribution obtained from the entire data sample of negative Q values can be identified with the function $B(m_\eta + Q_\eta - m)$ needed for the derivation of the background distribution within a finite excess energy bin. In the case of the unlimited statistics this procedure would mean that a smooth background distributions for all Q_b values would be added together. In the case of the small number of events this approach enables to reduce

significantly statistical fluctuations in the background spectrum. In such a way when investigating the missing mass spectrum for the Q_η bin one would obtain directly the background spectrum which after the normalisation could be subtracted form the distribution containing the signal from the η meson. Such background spectrum would be built of all events with Q less than zero. However, again the entire procedure could be justified only if the shape of the background does not alter within the discussed range of the excess energy Q.

4 Why the experimental multi-pion background does not change significantly with the variation of the excess energy

In this section we will present arguments justifying the supposition that the measured shape of the background does not alter if the excess energy changes, at least in the studied energy range. The validity of this assumption was already partly discussed in reference [12], so let us consider here only the most crucial issues. As already mentioned, the shape of background spectrum reflects the real distribution of the invariant mass of the multi-pion systems, the acceptance of the detection setup and the experimental resolution. In practice, from the high statistics measurements of the $pp \to pp\eta$ reaction, we know that the shape of the background can be sufficiently well described assuming that it is due to the two-pions creation only [1, 2]. Adding in the simulations three and four pions events was superfluous, and did not improve the agreement with the experimental distributions significantly.

Solid line in figure 4 demonstrates the invariant mass of the $\pi^0\pi^0$ system produced via $pn \to pn\pi^0\pi^0$ reaction simulated under the assumption that the phase space was homogeneously populated and the dashed line shows the shape of the efficiency of the COSY-11 detection setup. At the upper kinematical limit the efficiency attains its maximum value and then it is rapidly decreasing with the diminishing value of m, whereas, the invariant mass distribution is steeply increasing.

In reality the invariant mass distribution of the $\pi\pi$ system is strongly modified by the primary reaction dynamics and the final state interaction of the outgoing particles. Therefore, the spectra in figure 4 are not the exact predictions but are ment only as a visualisation, which should help to lead qualitative considerations.

With the increase of the Q value the distribution of the multi-pion invari-

ant mass will broaden towards the larger masses. In practice, if the change of the Q value is small in comparison to the excess energy with respect to threshold of $pn \to pn\ pions$ reaction than the shape of the mass distribution at its edge remains approximately unaltered. Interesting for us is the range of about 40 MeV at the higher mass limit. Additionally, although the acceptance of the COSY-11 setup for the given mass depends strongly on the distance from the kinematical limit, its shape remains approximately idependent of the value of Q. The events represented with the solid and dashed lines of the lower panel in figure 4 were simulated with the excess energy of, correspondingly, Q = 0 and Q = 20 MeV with respect to the $pn\eta$ system. By the comparison of the form of both spectra one realised that at the edges there is no noticeable difference between the shape of the curves. Thus this convoluted with the acceptance function independent of the Q value will lead to the form of the background which, as assumed in the conducted considerations, will be a function of the distance from the kinematical limit only, at least in the range of about 50 MeV as can be deduced by inspection of figure 4.

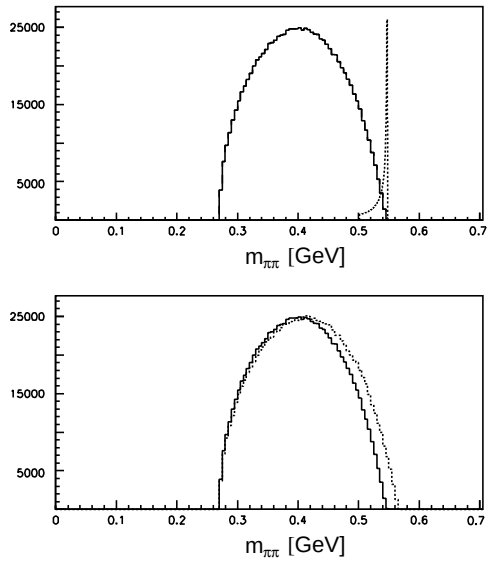

Figure 4: Upper panel: Invariant mass distribution of the $\pi\pi$ system simulated for the excess energy corresponding to the threshold of the $pn\eta$ final state (solid line). Acceptance of the COSY-11 facility shown in arbitrary units (dashed line).
Lower panel: Invariant mass distribution of the $\pi\pi$ system simulated for the excess energy – with respect to the $pn\eta$ final state – of $Q = 0$ MeV (solid line) and $Q = 20$ MeV (dashed line).

It is worth to note, that in the case of the η' meson, due to its twice

larger mass, the relative changes between dashed and solid lines will be much smaller, and hence the advocated assumption will be even better justified.

5 Summary

The technique for disentangling contributions of multi-pion and single meson production to the missing mass spectrum of the quasi-free $pn \to pnX$ reaction have been presented. Introduced method enables to derive a signal of the $pn \to pn\eta$ and $pn \to pn\eta'$ reactions measured close to the threshold, where the mass resolution is comparable with the centre-of-mass excess energy. In this energy range the peak in the missing mass spectrum from the single meson creation is in the close vicinity to the kinematical limit, and therefore the distinction between the signal from the single meson and multi-pion production becomes nontrivial. It was also shown how to combine events of different excess energies in order to win the statistical significance in the determination of the shape of the multi-pion mass distribution. The presented method will certainly be used in the analysis of the data on the quasi-free $pn \to pnX$ reactions taken by the COSY-11 collaboration, but it can also be applied in general for experiments using the missing mass technique for distinguishing between single and multi-meson production.

Acknowledgments

The work has been supported by the European Community - Access to Research Infrastructure action of the Improving Human Potential Programme, by the DAAD Exchange Programme (PPP-Polen), and by the Polish State Committe for Scientific Research (grants No. 2P03B07123 and PB1060/P03/2004/26).

References

[1] P. Moskal, habilitation thesis, [e-Print Archive: hep-ph/0408162].

[2] P. Moskal et al., Phys. Rev. **C 69** (2004) 025203, [e-Print Archive: nucl-ex/0307005].

[3] M. Janusz, P. Moskal, this proceedings, page 238.

[4] P. Moskal et al., AIP Conf. Proc. **717** (2004) 907, [e-Print Archive: nucl-ex/0311003].

[5] S. Brauksiepe et al., Nucl. Instr. & Meth. **A 376** (1996) 397.

[6] J. Przerwa, diploma thesis, Jagellonian University (2004), [e-Print Archive: hep-ex/0408016];
T. Rożek, P. Moskal, Ann. Rep. 2002, IKP, FZ–Jülich, Germany (2003);
P. Moskal, Ann. Rep. 1996, IKP, FZ–Jülich, Jül-3365 (1997) p.35;
and Ann. Rep. 2001, IKP, FZ–Jülich, Jül-3978 (2002) p.19.

[7] R. Bilger et al., Nucl. Inst. & Meth. **A 457** (2001) 64;
M. Janusz, P. Moskal, Ann. Rep. 2003, IKP, FZ–Jülich (2004);
E. Białkowski et al., Ann. Rep. 2001, IKP, FZ–Jülich, Jül-3978 (2002) p.22;
J. Majewski et al., Ann. Rep. 2001, IKP, FZ–Jülich, Jül-3978 (2002) p.21.

[8] R. Maier, Nucl. Instr. and Meth. **A 390** (1997) 1;
D. Prasuhn et al., Instr. and Meth. **A 441** (2000) 167.

[9] H. Dombrowski et al., Nucl. Instr. & Meth. **A 386** (1997) 228.

[10] P. Moskal, Schriften des FZ-Jülich: Matter and Materials **11** (2002) 27, [e-Print Archive: nucl-ex/0110001]

[11] R. Czyżykiewicz, diploma thesis, Jagellonian University (2002), Berichte des FZ-Jülich, **Jül-4017** (2002). [http://ikpe1101.ikp.kfa-juelich.de/]

[12] P. Moskal et al., J. Phys. **G 29** (2003) 2235,
[e-Print Archive: nucl-ex/0307016].

Precise scan of the $dp \to {}^3\mathrm{H}\pi^+/{}^3\mathrm{He}\pi^0$ cross section ratio at the η production threshold

J. Smyrski

Institute of Physics, Jagellonian University, Kraków, Poland

Abstract:
COSY-11 collaboration plans to measure a cusp expected in the beam momentum dependence of the $dp \to {}^3\mathrm{H}\pi^+$ and $dp \to {}^3\mathrm{He}\pi^0$ cross section ratio at the η production threshold. Precise determination of the profile of this cusp will allow to extract the magnitude and sign of the real part of the ${}^3\mathrm{He} - \eta$ scattering length and to draw conclusions about existence of ${}^3\mathrm{He} - \eta$ bound state. The experiment will be performed with the COSY-11 facility detecting the ${}^3\mathrm{He}$ ejectiles and the ${}^3\mathrm{H} - \pi^+$ pairs during a slow ramping of the COSY deuteron beam.

1 Motivation

The η-mesic nuclei postulated by Haider and Liu [1] give a unique possibility for study the ηN interaction in nuclear matter. Unfortunately, up to now there exists no firm experimental evidence for such states. Besides, it is still not clear what can be the lightest nuclei for which η bound state exists. Liu and Heider [2] claimed that bounding of the η and a nucleus should be possible for A>10. Later works indicate that this can happen even in the ${}^3\mathrm{He} - \eta$ system [3, 4, 5]. Existence of the ${}^3\mathrm{He} - \eta$ bound state is especially appealing since it can be described with the well-established Fadeev-Yakubovsky theory [6]. Recent data from MAMI show some indications for photoproduction of η-mesic ${}^3\mathrm{He}$ and its decay to the $\pi^0 pX$ channel [7].

A necessary condition for existence of a bound state is negative value of the real part of the η-nucleus scattering length ($\mathrm{Re}(a) < 0$). Unfortunately, the production cross sections are not sensitive to the sign of $\mathrm{Re}(a)$ but only to its absolute value. Recently Baru and collaborators [8] pointed out that a systematic study of the $pd \to {}^3\mathrm{H}\pi^+/{}^3\mathrm{He}\pi^0$ cross sections ratio in the vicinity of the η production threshold can be used to determine the sign of the real part of the $\eta - {}^3\mathrm{He}$ scattering length and thus for drawing conclusions about

a possible existence of $\eta - {}^3$He bound state. In their calculations they took into account the effect of $\pi^0 - \eta$ mixing and they assumed that the ratio of π^+ and π^0 production cross sections can be expressed according to formula derived in Ref. [9]:

$$R = \frac{d\sigma/d\Omega(dp \to {}^3\mathrm{H}\pi^+)}{d\sigma/d\Omega(dp \to {}^3\mathrm{He}\pi^0)} \simeq \frac{p_{\pi^+}}{p_{\pi^0}} \frac{\mid M_{\pi^+} \mid^2}{\mid M_{\tilde{\pi}^0} + \theta_m M_\eta \mid^2}. \qquad (1)$$

Here M_{π^+} etc. are the corresponding production amplitudes and θ_m is the $\pi^0 - \eta$ mixing angle. At the η production threshold the M_η amplitude changes rapidly due to the strong $\eta - {}^3$He interaction leading to a cusp in the $dp \to {}^3\mathrm{He}\pi^0$ cross section and consequently also in the ratio R. The shape of the cusp depends on the value of the mixing angle θ_m and on the relative phase ϕ between the amplitudes $M_{\tilde{\pi}^0}$ and M_η, however, the authors stress that knowledge of ϕ is not necessary to determine the sign of the real part of $\eta - {}^3$He scattering length a_R since different signs lead to qualitatively different results. For a_R larger than zero one expects a cusp like structure in the ratio R at the η production threshold and for a_R smaller than zero a so-called rounded step is expected. The authors underline that this observation should be still valid if one drops assumption that effect of charge symmetry breaking is caused by the $\pi^0 - \eta$ mixing alone. Their conclusions hold also in case when the additional term appearing in the denominator of Eq.(1) next to the $M_{\tilde{\pi}^0}$ amplitude is proportional to the amplitude for the $\eta - {}^3$He scattering.

The ratio R was measured recently by the GEM collaboration [10] for five beam momenta close to the η threshold. The obtained data indicate the existence of isospin symmetry breaking effect since they are on the average larger than the value of 2 which would be observed in an ideal case of the isospin conservation. However, the data do not show a clear cusp at the η threshold. It might be connected with the fact that the experimental uncertainties are too large and/or the number of data points is too small to cover properly the region of expected cusp. The main goal of the present proposal is to measure the cross section ratio R with much higher precision in the vicinity of the η production threshold in order to determine the shape of the expected cusp and to derive the sign of the real part of the $\eta - {}^3$He scattering length.

We want also to determine the excitation functions separately for the $dp \to {}^3\mathrm{He}\pi^0$ and $dp \to {}^3\mathrm{H}\pi^+$ cross sections. This will allow us to check for existence of a cusp caused by a possible coupling of pion production channels with the ${}^3\mathrm{He} - \eta$ intermediate state. Since one can expect, that this coupling

is of isospin conserving type, then the resulting cusp should cancel in the cross section ratio R.

Measurement of the pion production cross section will also allow us to check a kind of scaling phenomenon related with the observation made at lower energies that the dependence of the invariant matrix element squared $\mid M \mid^2$ on the four momentum transfer squared t follows along of a single curve and is almost independent of the energy [11]. A check of this scaling is very interesting from the point of view of studying the pion production mechanism in the three nucleon system.

2 Experiment

Measurements are planned to be performed with the internal deuteron beam of COSY scattered on a proton target of the cluster jet type and the COSY-11 facility detecting the charged reaction products. The ^{3}He ejectiles will be momentum analyzed in the COSY-11 dipole magnet and their trajectories will be registered with the system of two drift chambers D1 and D2. For particle identification the time of flight (TOF) on a path of 9 m between the start scintillation hodoscope S1 and the stop hodoscopes S3 and S7 will be measured. The π^0 mesons accompanying ^{3}He will be identified using the missing mass method. The detection acceptance for measuring the $dp \rightarrow {}^3\mathrm{He}\pi^0$ reaction covers almost the whole range of the CM pion-proton angles ($\theta^{CM}_{p-\pi^0}$). During the January-2003 COSY-11 beam time devoted to measurements of the $dp \rightarrow pd\eta$ close to threshold [12] we registered the ^{3}He ejectiles in a "parasitic" mode. Resulting missing mass spectra are shown in Fig. 1. In this experiment the range of the $\theta^{CM}_{p-\pi^0}$ angles was restricted to values larger then 100^o ($cos(\theta^{CM}_{p-\pi^0}) < -0.2$) due to limitation of the acceptance caused by omission of the S7 hodoscope in the TOF measurements. In spite of it one can see a clear signal in the missing mass spectra from π^0 production which proves the feasibility of measuring the $dp \rightarrow {}^3\mathrm{He}\pi^0$ reaction.

The $dp \rightarrow {}^3\mathrm{H}\pi^+$ reaction will be registered in parallel to $dp \rightarrow {}^3\mathrm{He}\pi^0$ using the drift chambers D1, D2 and the hodoscopes S1, S3 for detecting the pions π^+ and making use of the scintillators S5 and S8 for a coincident detection of the tritium ions. The scintillator S5 is placed inside the COSY-11 dipole gap and S8 will be installed outside the dipole magnet downstream the beam. The pions will be identified on the basis of TOF between the S1 and S3 and for the tritium identification the missing mass method as well as TOF measurement between the target and the S5 + S8 scintillators will

be used. The detection acceptance for measuring the $dp \rightarrow {}^3\mathrm{H}\pi^+$ reaction is limited to $\theta^{CM}_{p-\pi^+}$ angles larger then 100^o. In this region one expects the largest cusp since it appears on the level of the $d\sigma/d\Omega(dp \rightarrow {}^3He\eta)$ cross section which is much smaller than at the most forward angles.

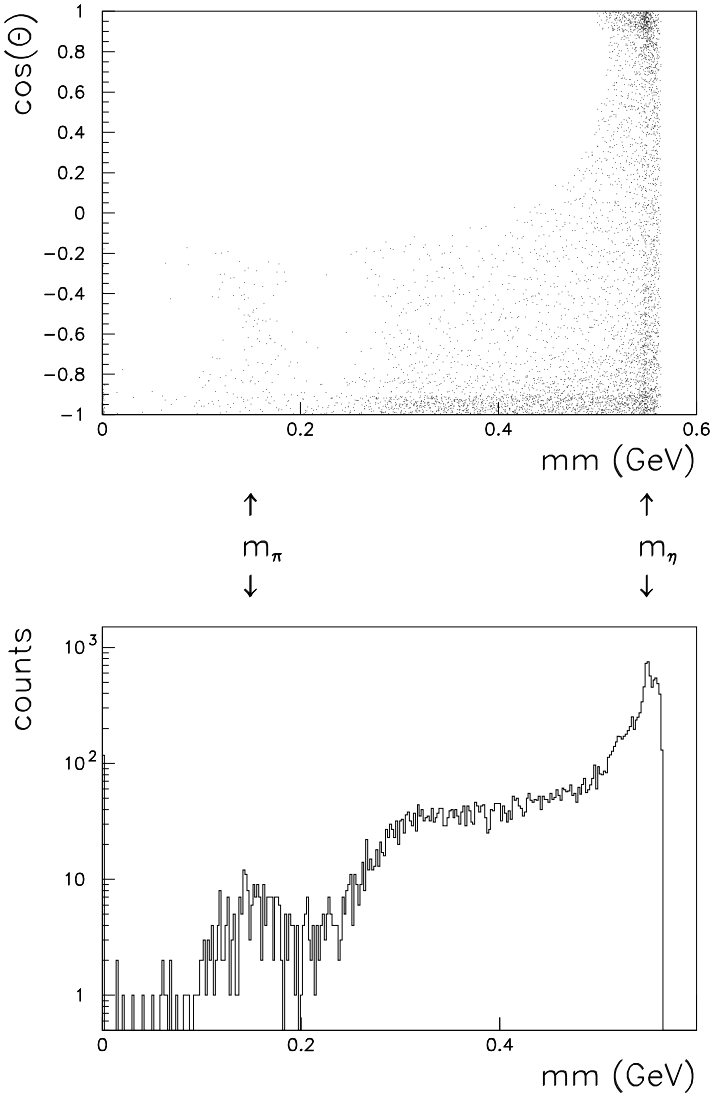

Figure 1: Distributions of the missing mass in $dp \rightarrow {}^3\mathrm{He}X$ measured at COSY-11 with 3.204 GeV deuteron beam in January 2003. The upper figure shows $cos(\theta^{CM}_{p-\pi})$ as a function of the missing mass, and in the lower figure projection of this distribution on the missing mass axis is shown.

During the proposed measurements the deuteron beam will be accelerated to the momentum which is 40 MeV/c below the η production threshold at 3139 MeV/c and then slowly ramped up to the upper momentum of 40 MeV/c above the threshold. The data will be taken during the ramping phase allowing for the reduction of most of the systematic errors associated with relative normalization of points measured at different beam momenta and appearing in the case when the beam is set up for each point separately. As the most serious source of systematic errors we consider displacement of the beam position at the target correlated with the variation of the beam momentum. According to performed simulation displacement of the beam by 1mm in a horizontal plane changes the acceptance for the $dp \to {}^3\mathrm{He}\pi^0$ reaction by 0.7% and the same diplacement but in a vertical direction causes change of 0.3% in the acceptance. For the beam position monitoring in the horizontal plane we will use measurement of the dp elastic and pp quasi-elastic scattering and for the vertical direction we will use reconstruction of the reaction vertices by tracing particle trajectories in the magnetic field of the COSY-11 dipole magnet. In both cases the beam position can be controlled with accuracy better then 1mm and so the resulting systematic errors can be kept below 1% [14]. The precision of the measurement will be thus limited mainly by the statistics only.

The luminosity will be monitored using coincident measurement of the elastic $d-p$ scattering as well as of the $p-p$ and $pp \to d\pi^+$ quasi-free scattering with the forward scattered particles registered in the drift chambers and the recoil particles measured with the silicon strip detectors.

During the COSY-11 run in January 2003, the number of "parasitically" recorded $dp \to {}^3He\pi^0$ events in the angular range $(\Theta_{p-\pi}) > 100^o$) was 460 per day. At present, this number should be by a factor of about 5 higher due to the increase of the number of deuterons stored in the COSY ring from $2\mathrm{x}10^{10}$ in January 2003 to expected $5\mathrm{x}10^{10}$ now and due to the increase of the COSY-11 target density from $2.5\mathrm{x}10^{13}\mathrm{cm}^{-13}$ to $5\mathrm{x}10^{13}\mathrm{cm}^{-2}$. The luminosity should rise from $0.8\mathrm{x}10^{30}\mathrm{cm}^{-2}\mathrm{s}^{-1}$ to $4.0\mathrm{x}10^{30}\mathrm{cm}^{-2}\mathrm{s}^{-1}$. Thus we expect 460x5=2300 $dp \to {}^3\mathrm{He}\pi^0$ events per day for $\Theta_{p-\pi} > 100^o$. Roughly the same counting rate should be measured for the $dp \to {}^3\mathrm{H}\pi^+$ reaction for which the acceptance is about two times smaller but it is compensated by about two times larger cross section. The resulting statistical accuracy of the cross section ratio R in a one day measurement is about 3 %. The proposed measurements will be performed with the COSY deuteron beam ramped slowly in the momentum range from 3.099 GeV/c to 3.179 GeV/c corresponding to the range of excess energies in the $dp \to {}^3\mathrm{He}\eta$ reaction from -10 MeV to 10 MeV. During the offline data analysis this range will

be divided into 20 bins with a width of 4 MeV/c which roughly corresponds to the double momentum spread of the uncooled beam. Since the expected magnitude of the cusp in the cross section ratio R is of about 10 %, then in order to measure it with a 3σ accuracy one needs about one day of beam time for each momentum bin and 20 days for the whole momentum range.

Acknowledgments

The work has been supported by the European Community - Access to Research Infrastructure action of the Improving Human Potential Programme, by the DAAD Exchange Programme (PPP-Polen), and by the Polish State Committe for Scientific Research (grants No. 2P03B07123
and PB1060/P03/2004/26).

References

[1] Q. Haider and L. C. liu, Phys. Lett. **B 172** (1986) 257.

[2] L. C. liu and Q. Haider, Phys. Rev. **C 34** (1986) 1845.

[3] S. Wycech, A. M. Green, J. A. Niskanen, Phys. Rev. **C 52** (1995) 544.

[4] S. A. Rakityansky et al., Phys. Lett. **B 359** (1995) 33.

[5] A. Fix and H. Arenhövel, Phys. Rev. **C 66** (2002) 024002.

[6] O. A. Yakubovsky, Sov. J. Nucl. Phys. **5** (1967) 937.

[7] M. Pfeiffer et al., nucl-ex/0312011.

[8] V. Baru et al., Phys. Rev. **C 68** (2003) 035203.

[9] A. Magiera and H. Machner, Nucl. Phys. **A 674** (2000) 515.

[10] M. Abdel-Bary et al., Phys. Rev. **C 68** (2003) 021603(R).

[11] B. H. Silverman et al., Nucl. Phys. **A 444** (1985) 621.

[12] J. Smyrski et al., "Investigation of near-threshold eta-production in the $dp \to pd\eta$ reaction", COSY Proposal-100 (2002).

[13] J. M. Cameron et al., Phys. Lett. **B 103** (1981) 317.

[14] P. Moskal et al., Nucl. Instr. and Meth. **A 466** (2001) 448.

New results on the pd→^{3}He η production near threshold

H.-H. Adam, A. Khoukaz, N. Lang, T. Lister, R. Santo, S. Steltenkamp
Institut für Kernphysik, Universität Münster, Germany

Abstract: Measurements on the η meson production in proton-deuteron collisions have been performed using the COSY-11 facility at COSY (Jülich). Here we present preliminary results on total and differential cross sections for the pd→^{3}He η reaction at five excess energies between Q = 5.1 and Q = 40.6 MeV. The obtained angular distributions for emitted η mesons in the center of mass system expose a transition from an almost isotropic emission to a highly anisotropic distribution. The extracted total cross sections support a strong η-^{3}He final state interaction and will be compared with model predictions.

1 Introduction

Close to threshold data on the pd →^{3}He η reaction are of great interest to study the strong attractive η-nucleus interaction at low energies, which might be a signal for the existence of quasi-bound η-nucleus states. First observed at the SPES-IV and SPES-II spectrometers at SATURNE [1, 2], the η-production in the reaction channel pd → ^{3}He η reveals remarkable features. Additionally to the unexpected high cross section for this channel, the shape of the excitation function reveals a maximum very close to the production threshold and a large drop of the production amplitude within only a few MeV above threshold, which clearly deviates from pure phase space expectations. In contrast, the angular distributions of the emitted η mesons in the center of mass system appeared to be consistent with pure phase space expectations and exhibit no contributions from higher partial waves.

In order to describe this unexpected near threshold behaviour, a two-step model based on a double-scattering reaction mechanism has been proposed by Kilian and Nann [3]. Calculations by Fäldt and Wilkin [4] exploiting this approach succeeded to reproduce the threshold cross section within a factor of 2.4. However, in order to reproduce the observed rapid drop of the

production amplitude with increasing energy, the two-step approach had to be refined by a strong η-^{3}He final state interaction (FSI) with a large η-^{3}He scattering length.

Further measurements performed at a higher excess energy of $\sim$ 50 MeV by the COSY-GEM-Collaboration [5], resulted in a highly non-isotropic angular distribution and a total cross section that is clearly underestimated by the description of the refined two step model fitted to the SPES data. A different reaction mechanism based on the excitation of the N*(1535) has been suggested [5], however, it fails to reproduce the observed shape of the previously determined excitation function for the near threshold region.

Additional studies have also been carried out by the WASA/PROMICE collaboration at η excess energies between $\sim$22 MeV and $\sim$120 MeV, yielding anisotropic angular distributions for all the measurements in agreement with the GEM results, but with total cross sections that can neither be described by the refined two-step model nor the predicted shape of the resonance model description [6].

Therefore, to clarify the still open question concerning the dominant production process, as well as to investigate the development of the angular distributions with increasing excess energy, additional measurements on the reaction of type pd $\rightarrow$ ^{3}He X have been carried out at η excess energies between Q=5.1 and 40.6 MeV using the COSY-11 installation.

Results of these studies will be presented in the next sections, for information concerning complementary measurements of the $dp \rightarrow dp\eta$ reaction conducted by the COSY-11 collaboration please refer to reference [7].

2 Experiment

The COSY-11 installation [8] is an internal experimental facility located in an arc section of the Cooler Synchrotron COSY at the Forschungszentrum Jülich [9]. A cluster-jet target [10], operated with deuterium gas, was used to provide a low background and high-luminosity deuteron target for the stochastically cooled, high-precision proton beam of COSY.

The COSY-11 facility makes use of one of the accelerators dipoles as a spectrometer magnet to separate the positively charged reaction ejectiles (^{3}He) from the circulating accelerator beam and guiding them towards the forward detection system (figure 1). The forward detection system consists of a set of two drift chambers (D1, D2), used for track reconstruction.

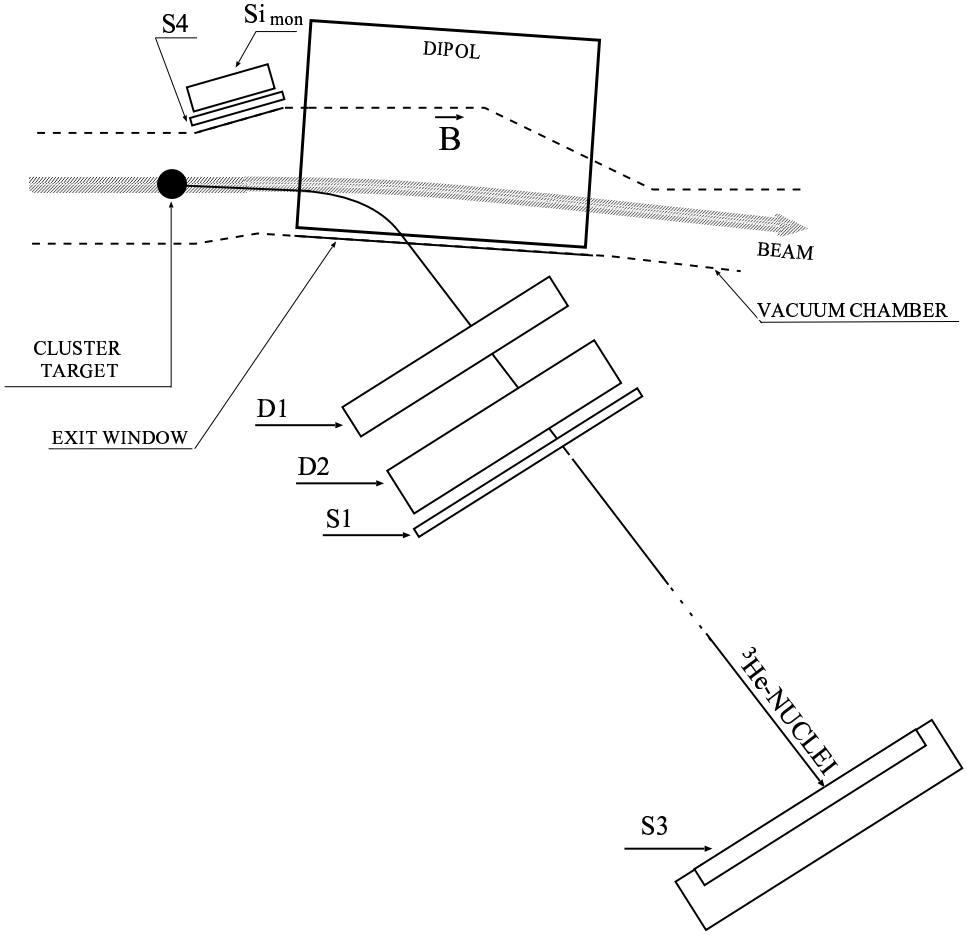

Figure 1: Schematic view of the COSY-11 detection setup [8]. Only detectors needed for the measurements of reactions of type pd $\rightarrow$ ^{3}He X are shown.
D1, D2 denote the drift chambers; S1, S3 and S4 the scintillation detectors; Si $_{mon}$ a silicon strip detector to detect elastically scattered protons and deuterons.

Tracing these tracks back through the well known magnetic field of the spectrometer magnet to the known interaction point leads to a momentum reconstruction. Directly placed behind the second drift chamber, two scintillation detectors (S1, S3) at a distance of $\sim$9 m are used as a start and stop detector combination for a time-of-flight (TOF) measurement. Thus, a particle identification can be performed by reconstructing the mass of the ejectiles using the momentum and velocity information. Additionally, the detected particles can be identified independently by the energy loss

information ΔE of the S1-detector in combination with the reconstructed momentum (ΔE/p plot). Therefore, a full four-momentum vector reconstruction is possible for all detected positively charged particles.

To obtain total cross sections the collected data of the type pd→ ^{3}He X can be normalized using data on the simultaneously measured elastic scattering pd→pd.

3 Data Analysis

The reaction channel pd→ ^{3}He η has been studied at COSY-11 by detection of the emitted ^{3}He nuclei and identification and reconstruction of the produced η mesons using the missing mass technique. To separate events with produced ^{3}He nuclei from background events with detected pions, protons, deuterons and tritium the ΔE/p-plot information has been exploited, leading to a clear signal from produced ^{3}He nuclei due to their comparatively high energy deposition in scintillating material [11]. The only very low remaining contamination of the selected ^{3}He nuclei is evident from the reconstructed mass distribution of accepted events.

The missing mass plot calculated for these selected ^{3}He events exhibits a clearly visible peak at the mass of the η meson on top of a background originating from events from multi-pion-production. This background can be easily reproduced by Monte-Carlo simulation on pd→^{3}He $\pi\pi/\pi\pi\pi/\pi\pi\pi\pi$ events at the corresponding beam energies, resulting in the same shape of $d\sigma/dm$ in the missing mass plot as observed in the experimental data. By subtracting the properly scaled Monte-Carlo generated multi-pion data from the experimental signal, a clean missing mass peak remains with a resolution of better than 6 MeV (FWHM) and in excellent agreement with expectations from Monte-Carlo simulations on the channel pd→ ^{3}He η .

In order to extract differential cross sections the numbers of η events from the missing mass spectra have been extracted separately for each of the angular bins presented in the differential cross section plots.

4 Results

Based on the described missing mass analysis differential cross sections have been extracted for all measured excess energies (Q=5.1, 10.8, 15.2, 20.0 and 40.6 MeV). Over this range of excess energies a transition from a rather flat angular distribution at the two lowest energies to a highly anisotropic

behaviour for the highest measured excess energy of 40.6 MeV is observed (figure 2).

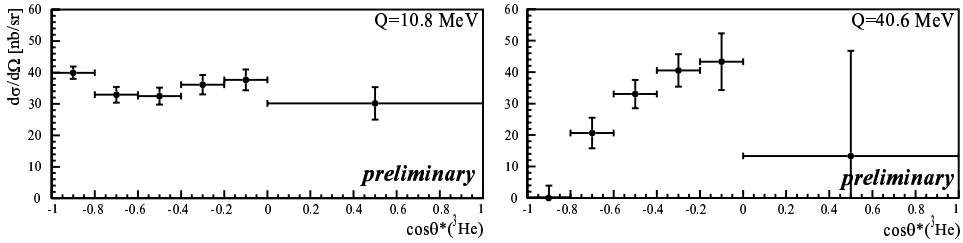

Figure 2: Angular distribtution of the detected ^{3}He-nuclei in the center of mass system. A transition from a rather flat distribution at the two lowest excess energies of 5.1 and 10.8 MeV to a highly anisotropic behaviour for the highest excess energy of 40.6 MeV is observed.

By determining the integrated luminosity via the pd→pd elastic scattering [11, 12] it was also possible to derive total cross sections and production amplitude information for each of the measured excess energies. The obtained production amplitudes close the open gap between the SATURNE data at low energies and the higher energy data from WASA/PROMICE and GEM (figure 3).

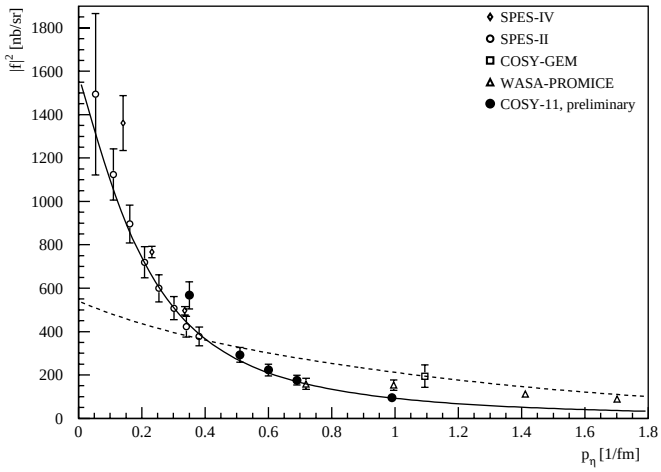

Figure 3: Average production amplitude squared $|f|^2$ as fuction of the cms momentum of the emitted η mesons for the pd→^{3}He η reaction. The solid and dashed lines represent fits to the data based on a strong η-^{3}He FSI and a resonance model description respectively.

The observed shape of the COSY-11 data strongly supports the predictions of the refined two-step model and indicates none or only weak contributions from a production according to the resonance model.

Acknowledgments

This work was supported by the FFE grants (41266606 and 41266654) from the Forschungszentrum Jülich, by the European Community - Access to Research Infrastructure action of the Improving Human Potential Programme and by the DAAD Exchange Programme (PPP-Polen).

References

[1] J. Berger et al., Phys. Rev. Lett. **61** (1988) 919.

[2] B. Mayer et al., Phys. Rev. **C 53** (1996) 2068.

[3] K. Kilian and H. Nann, AIP Conf. Proc. **221** (1990) 185.

[4] G. Fäldt and C. Wilkin, Phys. Lett. **B 221** (1995) 20.

[5] M. Betigeri et al., Phys. Lett. **B 472** (2000) 267.

[6] R. Bilger et al., Phys. Rev. **C 65** (2002) 44608.

[7] C. Piskor Ignatowicz et al., this proceedings, page 272.

[8] S. Brauksiepe et al., Nucl. Instr. & Meth. **A 376** (1996) 373.

[9] R. Maier, Nucl. Instr. & Meth. **A 390** (1997) 1.

[10] H. Dombrowski et al., Nucl. Phys. **A 626** (1997) 427c.

[11] H.-H. Adam, Diploma Thesis, Universität Münster, Germany, 2000.

[12] S. Steltenkamp, Diploma Thesis, Universität Münster, Germany, 2002.

Study of the $d-\eta$ interaction in the $dp \to dp\eta$ reaction

C. Piskor-Ignatowicz[a], P. Moskal[a,b], J. Smyrski[a]
[a] *Institute of Physics, Jagellonian University, Kraków, Poland*
[b] *Institut für Kernphysik, Forschungszentrum Jülich, Germany*

Abstract: Recently the deuteron-η interaction was intensively studied on the theoretical ground. This topic is of the special interest due to the possible existence of the η-nucleus bound or quasi-bound states. In January 2003 the COSY-11 collaboration performed measurements of the near-threshold η meson production in the $dp \to dp\eta$ reaction. The aim of the experiment is the determination of the $d-\eta$ interaction and the study of the η production mechanism in the three nucleon system. Measurements were done for four excess energies in the range from 0.68 MeV to 10.05 MeV. Results of the ongoing analysis of the $dp \to dp\eta$ events as well as of the quasi-free $pp \to pp$ and $pp \to d\pi^+$ processes are presented.

1 Introduction

Study of the $d-\eta$ interaction is of the special interest due to the possible existence of the $d-\eta$ quasi-bound states predicted by Ueda [1]. The η meson production near threshold in the three nucleon system is much less explored as compared to the two nucleon system [2]. The database has improved recently for the $pd \to {}^3He\eta$ reaction [3, 4, 5, 6, 7], however the $pd\eta$ final state remains only poorly explored.

The production mechanism of the η meson is still not well fixed. One of the possible explanations is the two-step model discussed in Refs. [8, 9]. The model assumes that in the first step a virtual pion is produced in the NN collision. In the second step the pion is scattered on the nucleon leading to the creation of the onshell η meson. For the reaction $dp \to dp\eta$ near threshold there exist only data on the total cross section for two excess energies Q = 1.5±0.6 and 3.8±0.6 MeV measured with the spectrometer SPESIII at the SATURNE accelerator [10]. The measured points are shown in Fig. 1. For five higher excess energies 14.5, 33.3, 52.5, 72.3, and 107.1 MeV there exist recently published data from PROMICE/WASA collaboration [11].

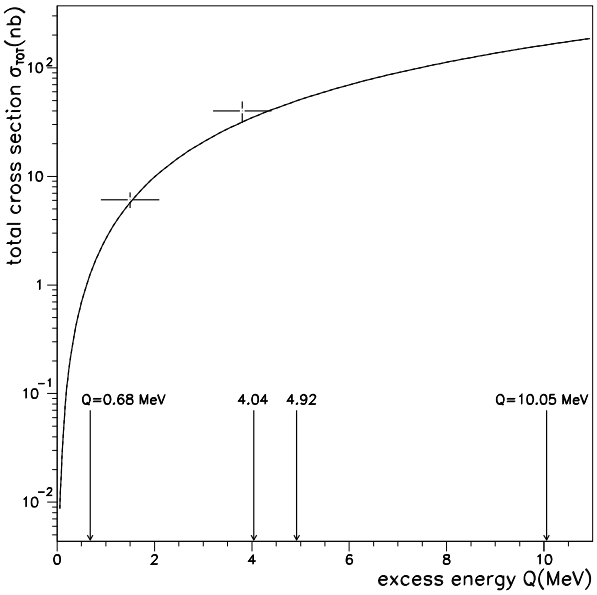

Figure 1: Total cross section of the reaction $dp \rightarrow dp\eta$ as a function of the excess energy Q. Data are taken from Ref. [10]. The solid curve has been calculated with the two-step model as in Ref. [11]. Four arrows indicate values of excess energies for which measurements of the total reaction cross section were performed by the COSY-11 collaboration.

The aim of the experiment performed by the COSY-11 collaboration is the determination of the $d-\eta$ interaction and the study of the η production mechanism in the $dp \rightarrow dp\eta$ reaction. A complementary measurements of the $pd \rightarrow {}^3He\eta$ reaction were also conducted by the COSY-11 collaboration and the results are presented in the previous contribution of this proceedings [6].

Measurements were done at the COoler SYnchrotron (COSY) in Jülich (FZJ). Application of the stochastic cooling to the COSY deuteron beam guarantees precise determination of the beam momentum and much better relative momentum resolution $\Delta p/p \approx 10^{-4}$ than in the case of the SATURNE experiment. Moreover, exact knowledge of the magnetic field in the COSY-11 dipole magnet allows us to determine precisely particle momenta and calculate the excess energy with two times better accuracy than in the SATURNE experiment. Method of the determination of the beam momentum is described in Ref. [12]. Precision knowledge of the excess energy is very important in order to infer about the FSI effect from the energy dependence of the total cross section. The energy dependence is expected to be very sensitive to the $d-\eta$ interaction. Even much weaker $p-\eta$ interaction significantly modifies this shape as observed in the $pp \rightarrow pp\eta$ reaction [13, 14].

2 Experimental setup

The experiment was carried out with the internal deuteron beam of the COSY accelerator scattered on the proton target of the claster jet type. The COSY-11 detection acceptance for such measurement is about ten times larger than in the case of proton beam scattered on deuteron target. In the case of the $dp \rightarrow dp\eta$ reaction at the threshold the outgoing deuterons have about two times larger momentum than the outgoing protons and, consequently, their deflection in the magnetic field of the COSY-11 dipole magnet is two times smaller. They leave the COSY-11 vacuum chamber through 10 cm wide and 5.6 cm high forward window as shown in Fig. 2.

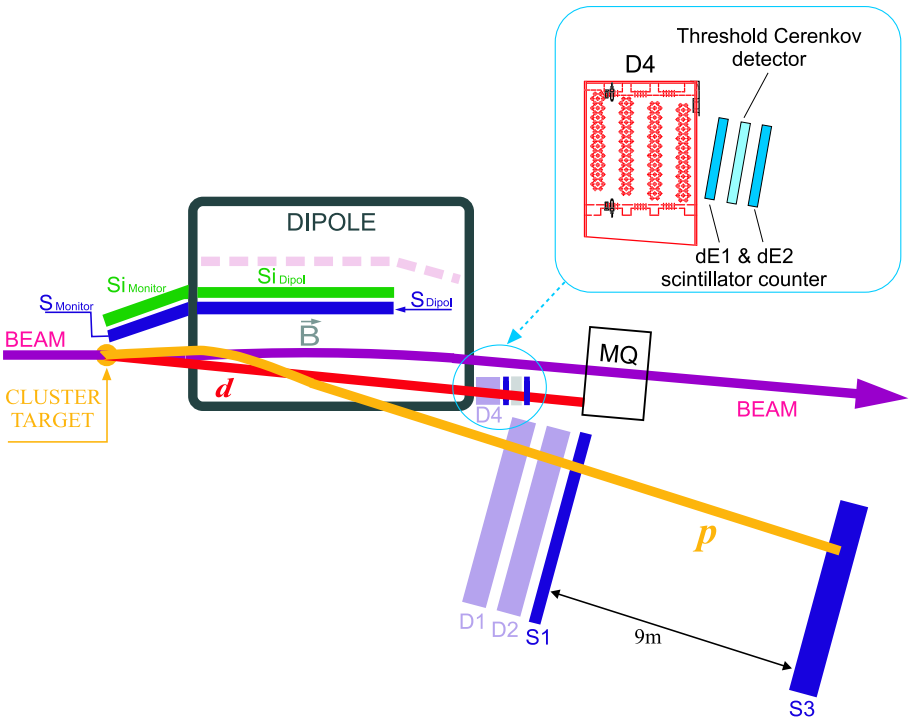

Figure 2: Detection setup of the COSY-11 experiment [15]. Protons are measured in the drift chambers D1, D2, as well as in the scintillator hodoscopes S1, S3. For the deuterons, small drift chamber D4, two scintillators dE1, dE2 and Cerenkov threshold counter were installed.

Protons are registered in the standard COSY-11 drift chambers D1, D2, as well as in the scintillator hodoscopes S1, S3. For the deuterons small drift chamber D4 with two scintillators dE1, dE2 and Cerenkov threshold

counter were installed in the space between the dipole exit window and the quadrupole magnet MQ. The chamber D4 has a box shape with dimensions 13 cm x 18 cm x 18 cm. It consists of seven detection planes: four planes with 10.4 cm vertical wires separated by three planes with 12.70 cm horizontal wires. Each detection plane contains hexagonal cells with the width of 1.1 cm. The distance between adjacent planes is 1.65 cm. As a chamber gas the P10 mixture (90% argon, 10% methane) at atmospheric pressure is used. The sense wire potential is about +1800 V and the field wires are grounded. Two projections of the drift chamber D4 are shown in Fig. 3.

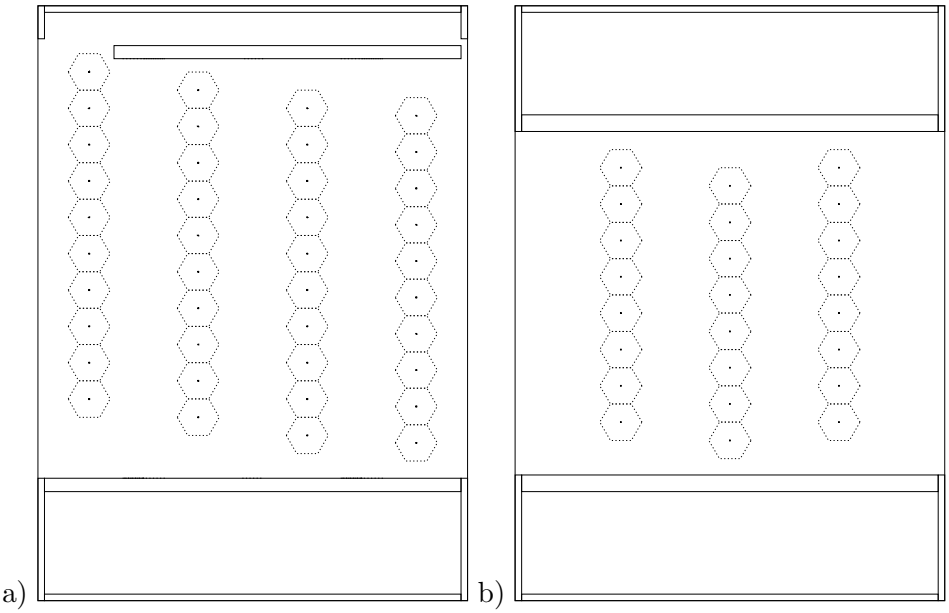

Figure 3: (a) Top view of the D4 drift chamber showing four identical detection planes, containing 10 cells with vertical wires. (b) Side view presenting three planes containing 8 cells of horizontal wires, each.

The chamber allows for the three dimensional particle tracks reconstruction. The particles momenta are determinated by tracing their trajectories in the magnetic field of the dipole magnet back to the target position. Behind the drift chamber D4 two 5 mm thick scintillators dE1 and dE2 are placed. Their signals (if in coincidence) are used as a trigger for the D4 detector readout and as a stop signal for the Time Of Flight (TOF) measurement on the 2 m path from the target. The time of the reaction at the target is derived from measurement of velocity of the associated particle registered in the scintillator hodoscopes S1 and S3 and from the time measured by the

S1 detector. Such a solution enables the particles identification. In order to reduce the proton background a threshold Cerenkov detector consisting of 2 cm plexiglass plate is used. Further improvement of the particle identification is done by taking into account the energy losses in the scintillators.

3 The ongoing data analysis

In the first step of the data analysis the identification of detected particles in S1 and S3 hodoscopes was performed on the basis of the time of flight measurement combined with the momentum determination. Figure 4 presents

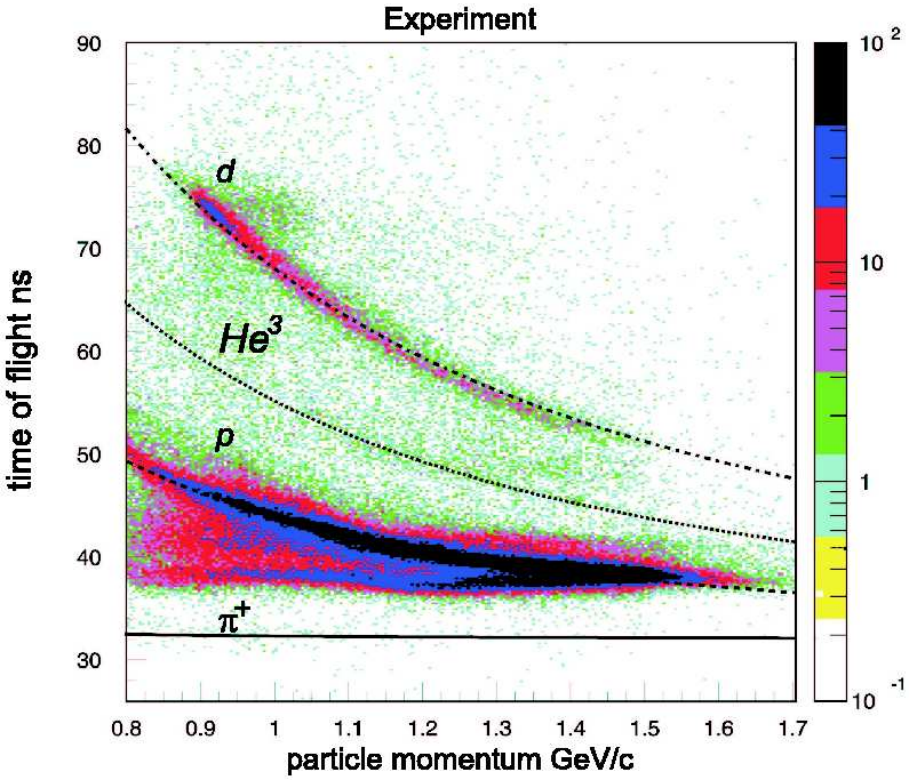

Figure 4: Dependence of time of flight on particle momentum.

TOF vs. momentum distribution for the experimental data with clearly visible bands corresponding to protons, deuterons and ^{3}He. For the luminosity monitoring in the experiment the elastic $d - p$ scattering as well as quasi

free $p - p$ and $pp \rightarrow d\pi^+$ scattering was registered. The scattered particles were detected in coincidence using the drift chambers for the forward scattered particles and the silicon pad detectors for the recoil ones. Figure 5 shows the transversal versus longitudinal momentum distribution for particles measured in the drift chambers D1 and D2.

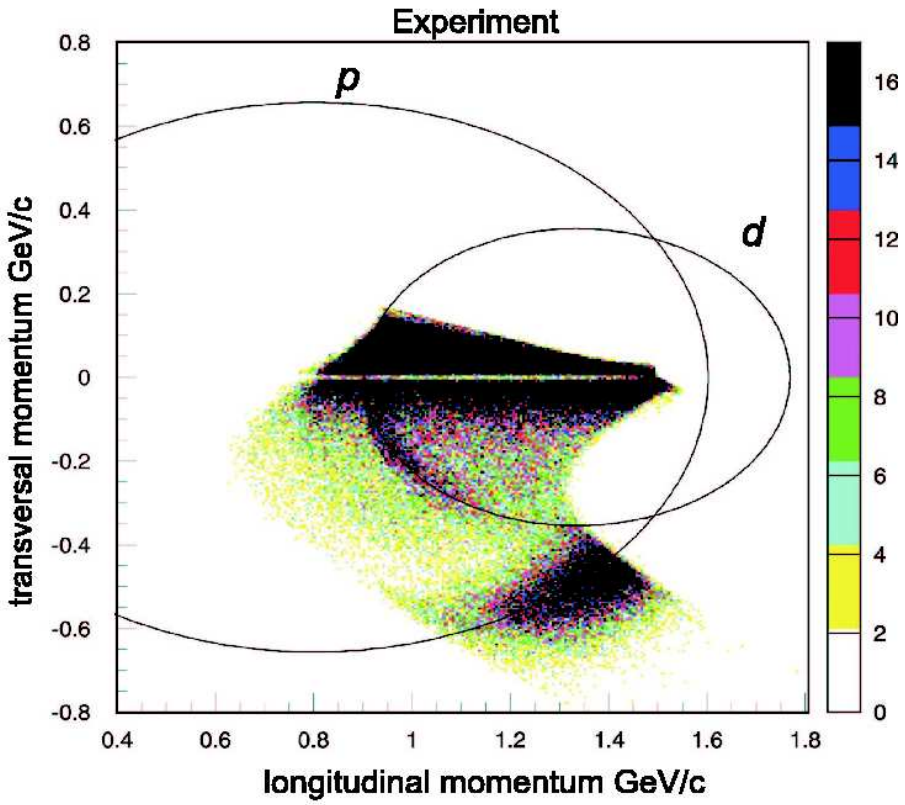

Figure 5: Longitudinal vs. transversal momentum distribution for particles registered in the drift chambers D1 and D2.

Superimposed lines correspond to the kinematical ellipses for protons from the $p-p$ quasi-elastic scattering and deuterons from the $pp \rightarrow d\pi^+$ reactions. The smearing of the data around the expected lines is partly due to the presence of the Fermi motion of protons in deuterons and partly due to the limited experimental resolution. The data cover only a fraction of the kinematically allowed region due to the limited acceptance of the COSY-11 detection system. So far performed analysis indicates that we can clearly

identify quasi free $pp \to pp$ and $pp \to d\pi^+$ reactions. At present we are at the last stage of accomplishing the programme for the analysis of the $dp \to dp\eta$ events. A corresponding computing procedures necessary for the track reconstruction in the drift chamber D4 are being implemented into the complex computer programme anabling the simulation and analysis of the reactions measured by means of the COSY-11 facility.

4 Summary

The COSY-11 collaboration performed measurement of the near-threshold η meson production in the $dp \to dp\eta$ reaction for four excess energies in the range from 0.68 to 10.05 MeV. The identification of detected particles in S1 and S3 hodoscopes was performed. The observed quasi free $p - p$ and $pp \to d\pi^+$ processes as well as the elastic $d - p$ scattering are used for the luminosity monitoring in the experiment. Data analysis is in progress.

Acknowledgments

The work has been supported by the European Community - Access to Research Infrastructure action of the Improving Human Potential Programme, by the DAAD Exchange Programme (PPP-Polen), and by the Polish State Committe for Scientific Research (grants No. 2P03B07123
and PB1060/P03/2004/26).

References

[1] T. Ueda, Phys. Rev. Lett. **66** (1991) 297.

[2] J. Smyrski et al., COSY Proposal No. **99** (2001).

[3] B. Mayer et al., Phys. Rev. **C 53** (1996) 2068.

[4] M. Betigeri et al., Phys. Lett. **B 472** (2000) 267.

[5] R. Bilger et al., Phys. Rev. **C 65** (2002) 44608.

[6] H.-H. Adam et al., this proceedings, page 266.

[7] H.-H. Adam et al., Int. J. of Mod. Phys. **A** (2004) in print.

[8] K. Kilian and H. Nann, AIP Conf. Proc. No. **221** (1990) 185.

[9] G. Fäldt and C. Wilkin, Nucl. Phys. **A 587** (1995) 769.

[10] F. Hibou et al., Eur. Phys. J. **A7** (2000) 537.

[11] R. Bilger et al., Phys. Rev. **C 69** (2004) 014003.

[12] J. Smyrski et al., Phys. Lett. **B474** (2000) 182.

[13] P. Moskal et al., Phys. Rev. **C 69** (2004) 025203.

[14] P. Moskal, e-Print Archive: hep-ph/0408162.

[15] S. Brauksiepe et al., Nucl. Instr. & Meth. **A 376** (1996) 397.

The gluon content of the η and η' mesons

N. G. Stefanis[1a] and S. S. Agaev[b]

[a] *Institut für Theoretische Physik II, Ruhr-Universität Bochum, D-44780 Bochum, Germany*

[b] *High Energy Physics Lab., Baku State University, Z. Khalilov St. 23, 370148 Baku, Azerbaijan*

Abstract: We analyze power-suppressed contributions to singlet pseudoscalar η and η' meson transition form factors. These corrections stem from endpoint singularities and help improve the agreement between QCD theory and the experimental data, in particular, at low-momentum transfers. Using the CLEO data, we extract information on the profile of the η_1 and η_8 distribution amplitudes in the $SU(3)_F$ octet-singlet basis employing both the one-angle and the two-angle mixing schemes. In the former scheme, we find good agreement with the CLEO data, while in the second case, our approach requires non-asymptotic profiles for these mesons.

1 Introduction

Control over power-behaved corrections in QCD processes is crucial for the correct interpretation of high-precision experiments in which intact hadrons appear in the initial and/or final states. Prominent examples are meson-photon transition form factors, as measured by the CLEO collaboration [1] for the pion and the η and η', and the recent JLab high-precision data for the pion's electromagnetic form factor [2].

Because, theoretically, the dynamics of such exclusive processes involves the corresponding meson distribution amplitudes, one can extract crucial information about the nonperturbative partonic structure of pseudoscalar mesons. In contrast to the hard-scattering amplitude, that can be systematically computed within perturbative QCD and is specific for each process, hadron distribution amplitudes are universal quantities that encode the partonic structure of hadrons. Their computation requires the application of nonperturbative methods, like QCD sum rules with nonlocal condensates—introduced in [3, 4, 5] and recently improved in [6]—to derive a realistic pion

[1] Corresponding author: stefanis@tp2.ruhr-uni-bochum.de

distribution amplitude complying with the CLEO data on the pion-photon transition at the 1σ level [7]. In addition, this type of pion distribution amplitude was recently [8] used in conjunction with fixed-order [9, 10] and resummed [11, 12] Analytic Perturbation Theory to calculate the pion's electromagnetic form factor providing very good agreement with the existing data.

Alternatively, one can use the factorization QCD approach in order to extract the shape of the pion (pseudoscalar meson) distribution amplitude directly from the data. The reliability of the latter possibility depends, however, on the way one deals with fixed-order perturbative calculations. To minimize the influence of (disregarded) higher-order contributions, while approaching the kinematic endpoint regions of the process in question (where the nonperturbative dynamics dominate), one may use Borel resummation techniques and, by this way, estimate power-behaved corrections. Indeed, this type of approach [13] was recently used to compute the pion-photon transition form factor and determine the pion distribution amplitude with results for the latter quantity close to the profiles determined with the nonlocal QCD sum rules just mentioned.

In the present exposition, we apply this type of approach (called the RC method) to extract the distribution amplitudes of the η and η' mesons with particular focus being placed on their gluonic content [14]. More details of our approach can be found in [15, 16, 17, 18, 19].

2 η-η' mixing schemes

Physical pseudoscalar mesons η, η' are admixtures of $SU(3)_{\rm F}$ octet (η_8) and singlet (η_1) states:

$$\begin{pmatrix} \eta \\ \eta' \end{pmatrix} = \begin{pmatrix} \cos\theta_p & -\sin\theta_p \\ \sin\theta_p & \cos\theta_p \end{pmatrix} \begin{pmatrix} \eta_8 \\ \eta_1 \end{pmatrix}, \tag{1}$$

where θ_p is the pseudoscalar mixing angle in the octet-singlet scheme (for a review and further references, see [20]).

On the parton level, the states η_8 and η_1 are given by

$$\begin{pmatrix} \eta_8 \\ \eta_1 \end{pmatrix} = \begin{pmatrix} \sin\theta_I & -\cos\theta_I \\ \cos\theta_I & \sin\theta_I \end{pmatrix} \begin{pmatrix} \frac{1}{\sqrt{2}}\left(u\bar{u} + d\bar{d}\right) \\ s\bar{s} \end{pmatrix}, \tag{2}$$

with θ_I being the ideal mixing angle.

Then, in turn, η and η' are admixtures of $q\bar{q}$ pairs (in a quark-flavor basis) expressed via

$$\begin{pmatrix} \eta \\ \eta' \end{pmatrix} = \begin{pmatrix} \cos\alpha_p & -\sin\alpha_p \\ \sin\alpha_p & \cos\alpha_p \end{pmatrix} \begin{pmatrix} \frac{1}{\sqrt{2}}\left(u\bar{u}+d\bar{d}\right) \\ s\bar{s} \end{pmatrix}, \tag{3}$$

where $\alpha_p = \theta_p - \theta_I + \pi/2$ denotes the deviation of the mixing angle from the ideal one due to the $U_A(1)$ anomaly—in contrast to the vector meson $\phi - \omega$ system with $\alpha_v \simeq 0$. Note that the flavor-singlet pseudoscalar state contains also a gluon component: "gluonium". To accommodate the gluonic component, one has to extend the mixing scheme to a 3×3 matrix with three mixing angles; i.e., [21]

$$\begin{pmatrix} \eta \\ \eta' \\ \iota \end{pmatrix} = \begin{pmatrix} \cos\theta_p\cos\gamma + \sin\theta_p\cos\phi\sin\gamma & -\sin\theta_p\cos\gamma + \cos\theta_p\cos\phi\sin\gamma & \sin\phi\sin\gamma \\ \cos\theta_p\sin\gamma + \sin\theta_p\cos\phi & \sin\theta_p\sin\gamma + \cos\theta_p\cos\phi\cos\gamma & \sin\phi\cos\gamma \\ -\sin\theta_p\sin\phi & -\cos\theta_p\sin\phi & \cos\phi \end{pmatrix} \times \begin{pmatrix} \eta_8 \\ \eta_1 \\ G \end{pmatrix}, \tag{4}$$

where ι is a Glueball state and $G = |gg\rangle$ denotes gluonium. Note that $|\eta\rangle \simeq |\eta_8\rangle$ (because $m_\eta \simeq m_8$ due to the Gell-Mann–Okubo mass formula), so that the $|\eta_1\rangle$ admixture is small with practically no room for a $|G\rangle$ contribution. Hence, $\gamma = 0$, and, as a result,

$$\begin{pmatrix} \eta \\ \eta' \\ \iota \end{pmatrix} = \begin{pmatrix} \cos\theta_p & -\sin\theta_p & 0 \\ \sin\theta_p\cos\phi & \cos\theta_p\cos\phi & \sin\phi \\ -\sin\theta_p\sin\phi & -\cos\theta_p\sin\phi & \cos\phi \end{pmatrix} \begin{pmatrix} \eta_8 \\ \eta_1 \\ G \end{pmatrix}. \tag{5}$$

A physical state is then a superposition of the sort

$$|\psi\rangle = x|Q\rangle + y|S\rangle + z|G\rangle\,, \qquad x^2+y^2+z^2 = 1 \tag{6}$$

with components (in the quark-flavor basis) given by

$$\begin{aligned} |Q\rangle &= \frac{1}{\sqrt{2}}\left(u\bar{u}+d\bar{d}\right) \\ |S\rangle &= |s\bar{s}\rangle \\ |G\rangle &= |gg\rangle\,. \end{aligned} \tag{7}$$

The physical states η and η' are

$$|\eta\rangle = x_\eta|Q\rangle + y_\eta|S\rangle\,, \qquad |\eta'\rangle = x_{\eta'}|Q\rangle + y_{\eta'}|S\rangle + z_{\eta'}|G\rangle \tag{8}$$

with mixing coefficients

$$x_\eta^2 + y_\eta^2 = 1\,, \qquad x_{\eta'}^2 + y_{\eta'}^2 + z_{\eta'}^2 = 1 \tag{9}$$

related to the mixing angles

$$x_\eta = \cos\alpha_p\,, \qquad y_\eta = -\sin\alpha_p \tag{10}$$

and

$$x_{\eta'} = \cos\phi\sin\alpha_p\,, \quad y_{\eta'} = \cos\phi\cos\alpha_p\,, \quad z_{\eta'} = \sin\phi\,. \tag{11}$$

The $SU(3)_{\rm F}$ octet-singlet basis is provided by

$$\begin{aligned} |\eta_1\rangle &= \frac{1}{\sqrt{3}}\,|u\bar{u} + d\bar{d} + s\bar{s}\rangle \\ |\eta_8\rangle &= \frac{1}{\sqrt{6}}\,|u\bar{u} + d\bar{d} - 2s\bar{s}\rangle\,. \end{aligned} \tag{12}$$

One notes that the octet-singlet and the quark-flavor basis are equivalent, but that the parameterizations of the decay constants are different.

Let us now have a closer look to the decay constants of $M = \eta, \eta'$ mesons. Their parameterization is defined via

$$\langle 0|J^i_{\mu 5}|M\rangle = i f_P^i p_\mu\,, \tag{13}$$

where $J^i_{\mu 5}$ is the axial-vector current ($i = Q, S$ or $i = 1, 8$). In the quark-flavor basis, the decay constants follow the pattern of state mixing, i.e.,

$$\begin{aligned} f_\eta^Q &= f_Q\cos\alpha_p \qquad f_\eta^S = -f_S\sin\alpha_p \\ f_{\eta'}^Q &= f_Q\sin\alpha_p \qquad f_{\eta'}^S = f_S\cos\alpha_p\,. \end{aligned} \tag{14}$$

In the octet-singlet basis the situation is different:

$$\begin{aligned} f_\eta^8 &= f_8\cos\theta_8 \qquad f_\eta^1 = -f_1\sin\theta_1 \\ f_{\eta'}^8 &= f_8\sin\theta_8 \qquad f_{\eta'}^1 = f_1\cos\theta_1\,. \end{aligned} \tag{15}$$

Note that in general, $\theta_8 \neq \theta_1 \neq \theta_p$. In the present analysis, we use the octet-singlet basis with the one-angle (standard) parameterization with

$$\begin{aligned} f_\pi = 0.131\text{GeV} \qquad f_1 = 1.17 f_\pi \\ f_8 = 1.26 f_\pi \qquad \theta_p = -15.4^\circ, \end{aligned} \tag{16}$$

and the two-angle mixing scheme with the parameters

$$\theta_p = -15.4^\circ,\ \theta_1 = -9.2^\circ,\ \theta_8 = -21.2^\circ. \tag{17}$$

3 Electromagnetic $\eta\gamma$, $\eta'\gamma$ transition form factor

In the Standard Hard-scattering Approach (HSA), the transverse momenta are neglected (collinear approximation) and the meson (π, η, $\eta'\ldots$) consists in leading twist ($t = 2$) only of valence $|q\bar{q}\rangle$ and $|gg\rangle$ Fock states. Let us summarize some important issues:

- The $\eta - \eta'$ system shows flavor mixing due to the $SU(3)_{\rm F}$ symmetry breaking and the $U(1)_{\rm A}$ axial anomaly.
- The quark-singlet $|\eta_1\rangle$ and the gluonium state $|gg\rangle$ mix under evolution; both carry flavor-singlet quantum numbers.
- The gluon content of the η' can reach the level of 26% [21].
- The meson-photon transition form factor contains a singlet and an octet part: $F_{\rm M\gamma}(Q^2) = F^1_{\rm M\gamma}(Q^2) + F^8_{\rm M\gamma}(Q^2)$.
- The singlet part, $F^1_{\rm M\gamma}(Q^2)$, has a quark and a gluonic component ([22]—using the standard HSA; [14]—using the endpoint-sensitive RC method). This means

$$F^{1g}_{\rm M\gamma}(Q^2) = \left(T^1_{\rm H}(x,Q^2,\mu_{\rm F}^2) \quad T^g_{\rm H}(x,Q^2,\mu_{\rm F}^2)\right) \otimes \begin{pmatrix} \phi_1(x,\mu_{\rm F}^2) \\ \phi_g(x,\mu_{\rm F}^2) \end{pmatrix}, \quad (18)$$

  where $\otimes$ denotes integration over longitudinal momentum fractions x from 0 to 1 and $\mu_{\rm F}$ is the factorization scale.

The transition form factor in the HSA can be expressed in terms of the convolution

$$F_{\rm M\gamma}(Q^2) = \int_0^1 dx \phi_{\rm M}(x,\mu_{\rm F}^2) T_{\rm H}(x,Q^2;\mu_{\rm F}^2,\mu_{\rm R}^2) \quad (19)$$

with $Q^2 = -q^2 > 0$ and q is the four-momentum of the virtual photon. Figure 1 shows an example of the Feynman diagrams contributing to $F_{\rm M\gamma}$ at NLO.

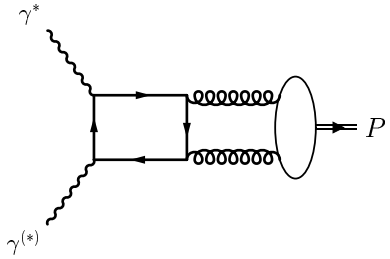

Figure 1: A sample of a Feynman diagram contributing to the (pseudoscalar) meson-photon transition form factor at NLO.

In Fig. 1, the partonic subprocess $\gamma * + \gamma \to q + \bar{q}$ is described by the hard-scattering amplitude $T_{\rm H}(x, Q^2; \mu_{\rm F}^2, \mu_{\rm R}^2)$ ($\mu_{\rm R}$ being the renormalization scale), whereas the nonperturbative dynamics is contained in the universal meson distribution amplitude $\phi_{\rm M}(x, \mu_{\rm F}^2)$. Note that ϕ_8 satisfies a scalar evolution equation, analog to the π case, while ϕ_1 and ϕ_g evolve together via a (2×2)-matrix evolution equation. Thus, we have [23]

$$\frac{d\phi_8(x,\mu_{\rm F}^2)}{d\ln\mu_{\rm F}^2} = V(x,u,\alpha_S(\mu_{\rm F}^2)) \otimes \phi_8(u,\mu_{\rm F}^2) \tag{20}$$

with a LO solution given in terms of Gegenbauer polynomials ($\bar{x} \equiv 1-x$):

$$\phi_8(x,\mu_{\rm F}^2) = 6x(1-x)\left[1 + \sum_{n=2,4,\ldots} B_n^8(\mu_{\rm F}^2)\, C_n^{3/2}(2x-1)\right] \tag{21}$$

and

$$\phi_8(x,\mu_{\rm F}^2) = \phi_8(\bar{x},\mu_{\rm F}^2)\,.$$

In Eq. (21), the projection coefficients B_n^8 encode the nonperturbative information that is not amenable to QCD perturbation theory, as we have already mentioned. On the other hand, the singlet ϕ_1 and gluonium ϕ_g distribution amplitudes fulfill the matrix evolution equation

$$\frac{d}{d\ln\mu_{\rm F}^2}\begin{pmatrix}\phi_1(x,\mu_{\rm F}^2)\\ \phi_g(x,\mu_{\rm F}^2)\end{pmatrix} = \begin{pmatrix}V_{qq} & V_{qg}\\ V_{gq} & V_{gg}\end{pmatrix}(x,u,\alpha_S(\mu_{\rm F}^2)) \otimes \begin{pmatrix}\phi_1(u,\mu_{\rm F}^2)\\ \phi_g(u,\mu_{\rm F}^2)\end{pmatrix} \tag{22}$$

with LO solutions provided by

$$\phi_1(x,\mu_{\rm F}^2) \;=\; 6x(1-x)\left[1 + \sum_{n=2,4,\ldots} B_n^1(\mu_{\rm F}^2)\, C_n^{3/2}(2x-1)\right]$$

$$\phi_g(x,\mu_{\rm F}^2) \;=\; x(1-x)\sum_{n=2,4,\ldots} B_n^g(\mu_{\rm F}^2)\, C_{n-1}^{5/2}(2x-1)\,. \tag{23}$$

The normalization conditions are

$$\int_0^1 dx \phi_{1,8}(x,\mu_{\rm F}^2) = 1 \qquad \int_0^1 dx \phi_g(x,\mu_{\rm F}^2) = 0\,. \tag{24}$$

The quark component of the singlet state reads

$$\phi_1(x,\mu_{\rm F}^2) = 6x\overline{x}\left(1 + \sum_{n=2,4..}^{\infty}\left\{B_n^q\left[\frac{\alpha_{\rm s}(\mu_0^2)}{\alpha_{\rm s}(\mu_{\rm F}^2)}\right]^{\frac{\gamma_+^n}{\beta_0}} + \rho_n^g B_n^g\left[\frac{\alpha_{\rm s}(\mu_0^2)}{\alpha_{\rm s}(\mu_{\rm F}^2)}\right]^{\frac{\gamma_-^n}{\beta_0}}\right\} C_n^{3/2}(x-\overline{x})\right) \tag{25}$$

with the symmetry condition $\phi_1(x,\mu_{\rm F}^2) = \phi_1(\bar{x},\mu_{\rm F}^2)$, whereas the gluon component is

$$\phi_g(x,\mu_{\rm F}^2) = x\overline{x}\sum_{n=2,4..}^{\infty}\left\{\rho_n^q B_n^q\left[\frac{\alpha_{\rm s}(\mu_0^2)}{\alpha_{\rm s}(\mu_{\rm F}^2)}\right]^{\frac{\gamma_+^n}{\beta_0}} + B_n^g\left[\frac{\alpha_{\rm s}(\mu_0^2)}{\alpha_{\rm s}(\mu_{\rm F}^2)}\right]^{\frac{\gamma_-^n}{\beta_0}}\right\} C_{n-1}^{5/2}(x-\overline{x}) \qquad (26)$$

with the symmetry condition $\phi_g(x,\mu_{\rm F}^2) = -\phi_g(\bar{x},\mu_{\rm F}^2)$. The associated anomalous dimensions [17] are

$$\gamma_\pm^n = \frac{1}{2}\left[\gamma_{qq}^n + \gamma_{gg}^n \pm \sqrt{(\gamma_{qq}^n - \gamma_{gg}^n)^2 + 4\gamma_{qg}^n\gamma_{gq}^n}\right], \qquad (27)$$

$$\rho_n^q = 6\frac{\gamma_+^n - \gamma_{qq}^n}{\gamma_{gq}^n} \qquad \rho_n^g = \frac{1}{6}\frac{\gamma_{gq}^n}{\gamma_-^n - \gamma_{qq}^n} \qquad (28)$$

with

$$\gamma_{qq}^n = C_F\left[3 + \frac{2}{(n+1)(n+2)} - 4\sum_{j=1}^{n+1}\frac{1}{j}\right],$$

$$\gamma_{gg}^n = N_c\left[\frac{\beta_0}{N_c} + \frac{8}{(n+1)(n+2)} - 4\sum_{j=1}^{n+1}\frac{1}{j}\right], \qquad (29)$$

$$\gamma_{qg}^n = \frac{12n_f}{(n+1)(n+2)}, \quad \gamma_{gq}^n = C_F\frac{n(n+3)}{3(n+1)(n+2)}. \qquad (30)$$

The numerical values of these parameters ($n_f = 3$) are

$$\begin{aligned}\gamma_{qq}^2 &= -\frac{50}{9}, \quad \gamma_{gg}^2 = -11, \quad \gamma_{gq}^2 = \frac{10}{27}, \quad \gamma_{qg}^2 = 3\\ \gamma_+^2 &\simeq -\frac{48}{9}, \ \gamma_-^2 \simeq -\frac{101}{9}, \ \rho_2^q \simeq \frac{16}{5}, \quad \rho_2^g \simeq -\frac{1}{90}.\end{aligned} \qquad (31)$$

The required Gegenbauer polynomials are

$$\begin{aligned}C_2^{3/2}(x-\overline{x}) &= \frac{3}{2}\left[5(x-\overline{x})^2 - 1\right] = 6\left(1 - 5x\overline{x}\right)\\ C_1^{5/2}(x-\overline{x}) &= 5(x-\overline{x}).\end{aligned} \qquad (32)$$

4 Hard-scattering amplitudes for the $\eta\gamma$ and $\eta'\gamma$ transition

The form factor for the $\eta\gamma$ and $\eta'\gamma$ transition, given by $F_{\mathrm{M}\gamma}(Q^2) = F^1_{\mathrm{M}\gamma}(Q^2) + F^8_{\mathrm{M}\gamma}(Q^2)$, contains a singlet part comprising quark and gluon components:

$$Q^2 F^1_{\mathrm{M}\gamma}(Q^2) = \int_0^1 dx f^1_{\mathrm{M}} N_1 \Big\{ T^q_{\mathrm{H,LO}}(x)\phi_1(x,\mu_{\mathrm{F}}^2) + \int_0^1 dx \frac{\alpha_{\mathrm{s}}(\mu_{\mathrm{R}}^2)}{4\pi} C_{\mathrm{F}} \Big[T^q_{\mathrm{H,NLO}}(x,Q^2,\mu_{\mathrm{F}}^2)\phi_1(x,\mu_{\mathrm{F}}^2) + T^g_{\mathrm{H,NLO}}(x,Q^2,\mu_{\mathrm{F}}^2)\phi_g(x,\mu_{\mathrm{F}}^2) \Big] \Big\} . \quad (33)$$

The octet part contains only a quark component; it reads

$$Q^2 F^8_{\mathrm{M}\gamma}(Q^2) = \int_0^1 dx f^8_{\mathrm{M}} N_8 \left[T^q_{\mathrm{H,LO}}(x)\phi_8(x,\mu_{\mathrm{F}}^2) + \frac{\alpha_{\mathrm{s}}(\mu_{\mathrm{R}}^2)}{4\pi} C_{\mathrm{F}} T^q_{\mathrm{H,NLO}}(x,Q^2,\mu_{\mathrm{F}}^2)\phi_8(x,\mu_{\mathrm{F}}^2) \right] . \quad (34)$$

The expressions for the involved hard-scattering amplitudes are

$$T^q_{\mathrm{H,LO}}(x) = x^{-1} + \bar{x}^{-1} ; \quad (35)$$

$$T^q_{\mathrm{H,NLO}}(x,Q^2,\mu_{\mathrm{F}}^2) = \frac{1}{x}\left[\ln^2 x - \frac{x \ln x}{\overline{x}} - 9 \right] + \frac{1}{x}(3 + 2\ln x) \ln \frac{Q^2}{\mu_{\mathrm{F}}^2} + (x \leftrightarrow \overline{x}) \quad (36)$$

$$T^g_{\mathrm{H,NLO}}(x,Q^2,\mu_{\mathrm{F}}^2) = \frac{x \ln^2 x}{\overline{x}} + \left(6 - \frac{4}{\overline{x}} \right) \ln x + 2 \frac{x \ln x}{\overline{x}} \ln \frac{Q^2}{\mu_{\mathrm{F}}^2} - (x \leftrightarrow \overline{x}) \quad (37)$$

and the charge factors read

$$N_1 = \frac{1}{\sqrt{3}} \left(e_u^2 + e_d^2 + e_s^2 \right) , \qquad N_8 = \frac{1}{\sqrt{6}} \left(e_u^2 + e_d^2 - 2e_s^2 \right) . \quad (38)$$

5 $\eta\gamma$, $\eta'\gamma$ transition form factor in the RC approach

Let us outline here the essentials of the endpoint-sensitive RC method.

- Solve the renormalization group equation for $\alpha_s(\lambda Q^2)$ in terms of $\alpha_s(Q^2)$ [24] to $\alpha_s^2(Q^2)$ accuracy.
- Expand the hard-scattering amplitude $T(Q^2)$ of the process as a power series in $\alpha_s(Q^2)$ with factorially growing coefficients $C_n \sim (n-1)!$.

- Use the Borel integral technique to resum them by
  - determining first the Borel transform $\mathcal{B}[T]$ of this series
  - inverting then $\mathcal{B}[T]$ to get

$$[T]^{\rm resum}(Q^2) \sim \text{P.V.} \int_0^\infty du \exp\left[\frac{-4\pi u}{\beta_0 \alpha_s(Q^2)}\right] \mathcal{B}[T](u).$$

  At this point a couple of important remarks are in order. (i) The Borel transforms contain poles on the positive u axis that are exactly *IR renormalon poles*; hence a principal value (P.V.) prescription has to be used. (ii) A direct way to obtain the Borel resummed expressions is via the *Inverse Laplace Transformation.*

  Then, one finds

$$\alpha_s(xQ^2) = \frac{4\pi}{\beta_0} \int_0^\infty du e^{-ut} R(u,t) x^{-u} \tag{39}$$

  with

$$R(u,t) = 1 - \frac{2\beta_1}{\beta_0^2} u(1 - \gamma_{\rm E} - \ln t - \ln u)\,. \tag{40}$$

- Endpoint singularities $x \to 1$ $\bar{x} \to 1$ transform into IR renormalon (multi-)pole divergences at $u_0 = n$ (in our case $n = 1, 2, 3, 4$) in the Borel u plane.

- Removing these poles via the P.V. prescription, we obtain *resummed* expressions for

$$[Q^2 F^1_{{\rm M}\gamma}(Q^2)]^{\rm resum}\,, \qquad [Q^2 F^8_{{\rm M}\gamma}(Q^2)]^{\rm resum}\,.$$

- The pole at $u_0 = n$ of the Borel plane corresponds to power-suppressed corrections $\sim (1/Q^2)^n$ contained in the scaled form factors.

Let us close this section, by commenting upon the importance of power corrections from the theoretical point of view and in comparison with the standard HSA. The latter prefers to set $\mu_{\rm R}^2 = Q^2$. Then, large NLO logarithms are present. The RC method sets instead $\mu_{\rm R}^2 = xQ^2$. As a result, the term $\ln(\mu_{\rm R}^2/xQ^2)$ in the NLO contribution is eliminated, but the integration over x gives rise to *power-suppressed contributions* in the endpoint regions $x \to 0, 1$. Note in this context that because asymptotically both approaches

have to yield the same results, one has to verify that the induced power corrections do not affect this regime, leaving the asymptotic behavior of perturbative QCD unchanged. Hence, in technical terms, one has to ensure that

$$\int_0^\infty du \mathrm{e}^{-ut} R(u,t) \overset{Q^2\to\infty}{\to} \int_0^\infty du \mathrm{e}^{-ut}\,.$$

In view of the above remarks, the best (perturbative) procedure is the one that minimizes the NLO contribution while keeping power corrections under control.

The present analysis employs the following scales:

- $\mu_{\mathrm{R}}^2 = xQ^2$ (renormalization scale)
- $\Lambda^{(n_f=4)} = 0.25$ GeV
- $\mu_0^2 = 1$ GeV^2 (normalization scale)
- $\mu_{\mathrm{F}}^2 = Q^2$ (factorization scale)

The estimated influence of higher-twist uncertainties is of the order of $(10-15)\%$.

6 Borel Resummed $\eta\gamma$ and $\eta'\gamma$ transition form factors

The NLO expression for the transition form factor, calculated with the RC method [14], comprises a quark component

$$\begin{aligned} Q^2 F^1_{\mathrm{M}\gamma}(Q^2)_1^{\mathrm{quark}} &\sim \alpha_{\mathrm{s}}(Q^2 x) t(x,\mu_{\mathrm{F}}^2) \otimes \phi_1(x,\mu_{\mathrm{F}}^2) \\ &+ \alpha_{\mathrm{s}}(Q^2 \overline{x}) t(\overline{x},\mu_{\mathrm{F}}^2) \otimes \phi_1(x,\mu_{\mathrm{F}}^2) \\ &= 2\alpha_{\mathrm{s}}(Q^2 x) t(x,\mu_{\mathrm{F}}^2) \otimes \phi_1(x,\mu_{\mathrm{F}}^2) \end{aligned} \tag{41}$$

with

$$t(x,\mu_{\mathrm{F}}^2) = \frac{1}{x}\left[\ln^2 x - \frac{x\ln x}{\bar{x}} - 9\right] + \frac{1}{x}(3+2\ln x)\ln\frac{Q^2}{\mu_{\mathrm{F}}^2} \tag{42}$$

and a gluon component

$$Q^2 F^1_{\mathrm{M}\gamma}(Q^2)_1^{\mathrm{gluon}} \sim 2\alpha_{\mathrm{s}}(Q^2 x) g(x,\mu_{\mathrm{F}}^2) \otimes \phi_g(x,\mu_{\mathrm{F}}^2) \tag{43}$$

with

$$g(x,\mu_{\mathrm{F}}^2) = \frac{x\ln^2 x}{\overline{x}} + \left(6 - \frac{4}{\overline{x}}\right)\ln x + 2\ln\left(\frac{Q^2}{\mu_{\mathrm{F}}^2}\right)\frac{x\ln x}{\overline{x}}\,. \tag{44}$$

Summing up, we can write–in the context of the RC method–the transition form factors $Q^2 F^1_{\mathrm{M}\gamma}(Q^2)$ and $Q^2 F^8_{\mathrm{M}\gamma}(Q^2)$ as follows

$$Q^2 F^1_{\mathrm{M}\gamma}(Q^2) \;=\; f^1_{\mathrm{M}} N_1 \left\{ T^q_{\mathrm{H},0}(x) \otimes \phi_1(x,\mu_{\mathrm{F}}^2) + \frac{C_{\mathrm{F}}}{2\pi} \left[\alpha_{\mathrm{s}}(Q^2 x) t(x,\mu_{\mathrm{F}}^2) \right.\right.$$

$$\left.\left. \otimes\, \phi_1(x,\mu_{\mathrm{F}}^2) + \alpha_{\mathrm{s}}(Q^2 x) g(x,\mu_{\mathrm{F}}^2) \otimes \phi_g(x,\mu_F^2) \right] \right\} \tag{45}$$

and

$$Q^2 F^8_{\mathrm{M}\gamma}(Q^2) \;=\; f^8_{\mathrm{M}} N_8 \left[T^q_{\mathrm{H},0}(x) \otimes \phi_8(x,\mu_{\mathrm{F}}^2) + \frac{C_{\mathrm{F}}}{2\pi}\, \alpha_{\mathrm{s}}(Q^2 x) t(x,\mu_{\mathrm{F}}^2) \right.$$

$$\left. \otimes\, \phi_8(x,\mu_{\mathrm{F}}^2) \right] . \tag{46}$$

Now recall that the running coupling $\alpha_s(xQ^2)$ in terms of $\alpha_s(Q^2)$ [24] reads

$$\alpha_{\mathrm{s}}(Q^2 x) \simeq \frac{\alpha_{\mathrm{s}}(Q^2)}{1+\ln x/t} \left[1 - \frac{\alpha_{\mathrm{s}}(Q^2)\beta_1}{2\pi\beta_0} \frac{\ln[1+\ln x/t]}{1+\ln x/t} \right]$$

where we have used

$$t = \frac{4\pi}{\beta_0 \alpha_{\mathrm{s}}(Q^2)} = \ln \frac{Q^2}{\Lambda^2}\,, \quad \beta_0 = 11 - \frac{2}{3} n_f\,, \quad \beta_1 = 51 - \frac{1}{9} 3 n_f\,.$$

In this way, we finally arrive at the following expressions for the resummed singlet and octet transition form factors within the RC method:

$$Q^2 F^1_{\mathrm{M}\gamma}(Q^2) \;=\; f^1_{\mathrm{M}} N_1 \left\{ 6 + A(\mu_{\mathrm{F}}^2) + \frac{12 C_{\mathrm{F}}}{\beta_0} \left[\left(1 + A(\mu_{\mathrm{F}}^2)\right) \right.\right.$$

$$\times \int_0^\infty du \mathrm{e}^{-ut} R(u,t) Q_1(u) - 5A(\mu_{\mathrm{F}}^2) \left.\left. \int_0^\infty du \mathrm{e}^{-ut} R(u,t) Q_2(u) \right] \right.$$

$$\left. + \frac{2C_{\mathrm{F}}}{\beta_0} B(\mu_{\mathrm{F}}^2) \int_0^\infty du \mathrm{e}^{-ut} R(u,t) G(u) \right\}\,, \tag{47}$$

$$Q^2 F^8_{\mathrm{M}\gamma}(Q^2) \;=\; f^8_{\mathrm{M}} N_8 \left\{ 6 + C(\mu_{\mathrm{F}}^2) + \frac{12 C_{\mathrm{F}}}{\beta_0} \left[\left(1 + C(\mu_{\mathrm{F}}^2)\right) \int_0^\infty du \mathrm{e}^{-ut} \right.\right.$$

$$\left.\left. \times\; R(u,t) Q_1(u) - \; 5C(\mu_{\mathrm{F}}^2) \int_0^\infty du \mathrm{e}^{-ut} R(u,t) Q_2(u) \right] \right\}\,. \tag{48}$$

In the above expressions, the following abbreviations have been used [14]:

$$R(u,t) = 1 - \frac{2\beta_1}{\beta_0^2} u(1 - \gamma_E - \ln t - \ln u)\,, \tag{49}$$

$$Q_1(u) = \frac{2}{(1-u)^3} - \frac{2}{(2-u)^3} - \frac{2a}{(1-u)^2} + \frac{1+2a}{(2-u)^2} + 3\frac{a-3}{(1-u)(2-u)}\,,$$

$$\begin{aligned} Q_2(u) &= \frac{2}{(2-u)^3} - \frac{4}{(3-u)^3} + \frac{2}{(4-u)^3} - \frac{2a}{(2-u)^2} \\ &+ \frac{1+4a}{(3-u)^2} - \frac{1+2a}{(4-u)^2} + 6\frac{a-3}{(2-u)(3-u)(4-u)}\,, \end{aligned} \tag{50}$$

$$G(u) = \frac{4}{(4-u)^3} - \frac{2}{(3-u)^3} + \frac{2}{(2-u)^2} - 2\frac{5-a}{(3-u)^2} + 4\frac{3-a}{(4-u)^2}\,, \tag{51}$$

with $a \equiv \ln(Q^2/\mu_{\rm F}^2)$ and the Gegenbauer coefficients being given by

$$\begin{aligned} A(\mu_{\rm F}^2) &= 6B_2^q \left[\frac{\alpha_{\rm s}(\mu_{\rm F}^2)}{\alpha_{\rm s}(\mu_0^2)}\right]^{\frac{48}{81}} - \frac{B_2^g}{15}\left[\frac{\alpha_{\rm s}(\mu_{\rm F}^2)}{\alpha_{\rm s}(\mu_0^2)}\right]^{\frac{101}{81}} \\ B(\mu_{\rm F}^2) &= 16B_2^q \left[\frac{\alpha_{\rm s}(\mu_{\rm F}^2)}{\alpha_{\rm s}(\mu_0^2)}\right]^{\frac{48}{81}} + 5B_2^g\left[\frac{\alpha_{\rm s}(\mu_{\rm F}^2)}{\alpha_{\rm s}(\mu_0^2)}\right]^{\frac{101}{81}} \\ C(\mu_{\rm F}^2) &= 6B_2^q \left[\frac{\alpha_{\rm s}(\mu_{\rm F}^2)}{\alpha_{\rm s}(\mu_0^2)}\right]^{\frac{50}{81}}\,. \end{aligned} \tag{52}$$

7 Phenomenological Analysis

In this section we perform numerical computations of the Borel resummed and rescaled by Q^2 $\eta\gamma$ and $\eta'\gamma$ transition form factors in order to extract the η and η' meson distribution amplitudes from the CLEO data. We shall also compare our theoretical predictions with those obtained with the standard HSA [22, 25], the aim being to reveal the role of power corrections at low-momentum transfer in the exclusive process under consideration.

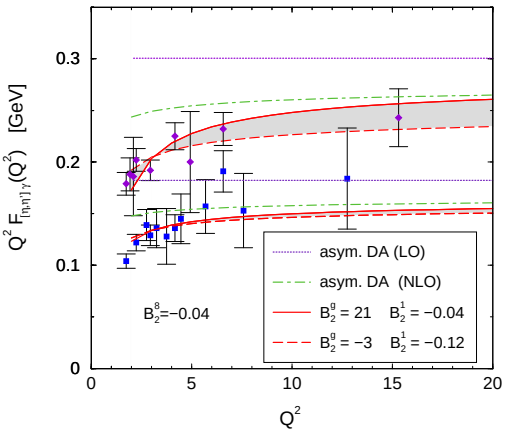

Figure 2: η (lower curves) and η' (upper curves) transition form factors obtained with the standard HSA in [22]. The shaded area corresponds to the range of values $B_2^8(\mu_0^2) = -0.04 \pm 0.04$ $B_2^1(\mu_0^2) = -0.08 \pm 0.04$ $B_2^g(\mu_0^2) = 9 \pm 12$ (see [22, 26] for further details).

Let us start our discussion by quoting the results obtained in [22] (see also [26]) using the standard HSA. Their main predictions are shown in Fig. 2 in comparison with the CLEO data [1].

As one sees from this figure, the agreement between the theoretical predictions and the low-momentum data is rather poor—especially when using asymptotic profiles for the η, η' meson distribution amplitudes. To decrease the magnitude of the form factors at low Q^2, and achieve this way a better agreement with the data, the standard HSA would call for the two-angles mixing scheme and for distribution amplitudes mainly with $B_2^q(\eta_1)$, $B_2^q(\eta_8) < 0$. The inclusion of power-law corrections changes the low-momentum behavior of the form-factor predictions significantly, as one observes from Fig. 3. Indeed, using the standard octet-singlet mixing scheme, one can reproduce the trend of the CLEO data rather well in the whole momentum range explored—especially with a non negligible gluon contribution (the Gegenbauer coefficients are given in Fig. 3)—because the effect of power corrections is to enhance the absolute value of the NLO correction to the form factors by more than a factor of $2.5 - 3$. Since the contribution of the NLO term to the form factors is negative, the power corrections reduce the leading-order prediction for the form factors considerably, while at the highest Q^2 values measured by the CLEO collaboration this influence becomes more moderate.

The 1σ regions in the form of shaded areas for the scaled form factors for the $\eta\gamma$ and $\eta'\gamma$ transition in the RC method and using the octet-singlet scheme are displayed in Fig. 4. The central line corresponds to the coefficients values $B_2^q(\eta_1) = B_2^q(\eta_8) = 0.05$; $B_2^g(\eta_1) = 17$. A full-fledged discussion of these issues is given in [14], together with error estimates arising from varying the values of the theoretical parameters used in the analysis.

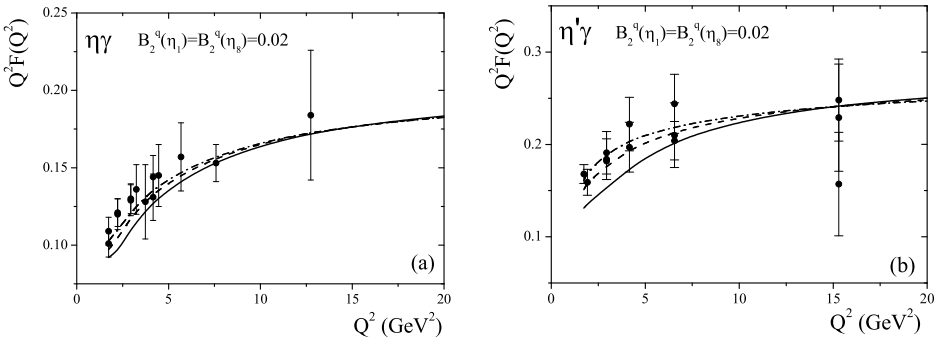

Figure 3: Predictions for the scaled form factors as functions of Q^2 of the $\eta\gamma$ (left panel) and $\eta'\gamma$ (right panel) electromagnetic transition. For the solid curves the designation is $B_2^g(\eta_1) = 0$. The dashed lines correspond to $B_2^g(\eta_1) = 10$; for the dash-dotted curves we use $B_2^g(\eta_1) = 15$. The data are taken from Ref. [1].

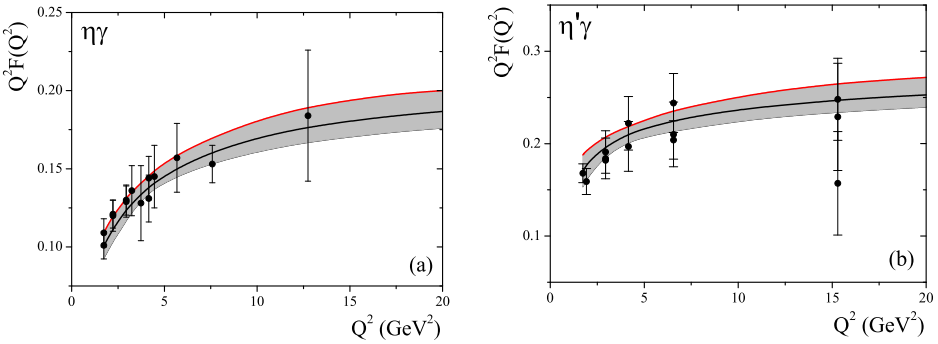

Figure 4: The $\eta\gamma$ (left) and $\eta'\gamma$ (right) scaled transition form factors as functions of Q^2. The central solid curves are found using the values $B_2^q(\eta_1) = B_2^q(\eta_8) = 0.05$ and $B_2^g(\eta_1) = 17$. The shaded areas demonstrate the 1σ regions for the transition form factors.

It is important to emphasize that our calculations do not exclude the usage of the two-angles mixing scheme in conjunction with the RC method. But in such a case, a considerably larger contribution of the non-asymptotic terms to the distribution amplitudes of the η_1 and η_8 states would be required. Carrying out such a computation [14], we obtained the results shown in Fig. 5. Inspection of the left panel of this figure reveals that the $\eta\gamma$ transition FF found within this scheme lies significantly lower than the data. Therefore, to improve the agreement with the experimental data, a relatively large contribution of the first Gegenbauer polynomial to the distribu-

tion amplitudes of the η_1 and η_8 states seems necessary. The Gegenbauer coefficients corresponding to the predictions shown in Fig. 5 are $B_2^q(\eta_1) = 0.15$, $B_2^q(\eta_8) = 0.15$ and $B_2^g(\eta_1) = 18$. We consider the values $B_2^q(\eta_1) = B_2^q(\eta_8) = 0.15$ as actually determining the *lower* bound for the admissible set of distribution amplitudes in the context of the two-angles mixing parameterization scheme. Hence, in that scheme, we obtain

$$B_2^q(\eta_1) = B_2^q(\eta_8) = 0.15,\ B_2^g(\eta_1) \in [16,\, 20]\,. \tag{53}$$

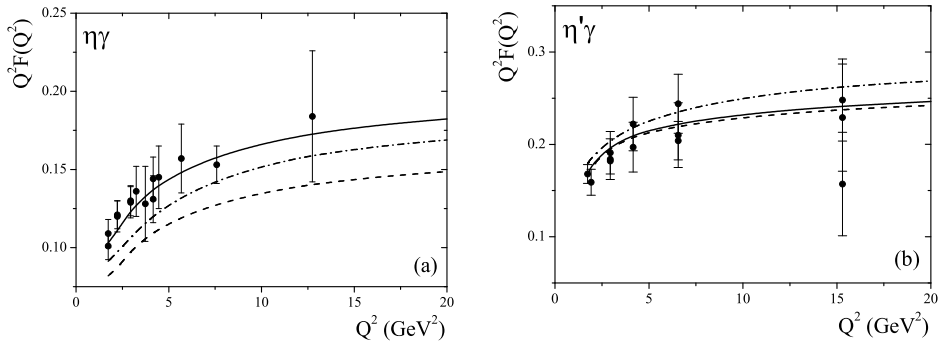

Figure 5: The $\eta\gamma$ (a) and $\eta'\gamma$ (b) electromagnetic transition form factors vs. Q^2. The solid lines correspond to the ordinary octet-singlet mixing scheme with parameters $B_2^q(\eta_1) = B_2^q(\eta_8) = 0.02$ and $B_2^g(\eta_1) = 18$. The broken lines are obtained within the two-angles mixing scheme. The dashed lines describe the situation with the same parameters as the solid curves. The parameters for the dash-dotted curves are $B_2^q(\eta_1) = B_2^q(\eta_8) = 0.15$, $B_2^g(\eta_1) = 18$.

Let us close this section by summarizing the main differences between the standard HSA and the RC method: (i) Form factors in the HSA overshoot the CLEO data—especially in the low Q^2 region—even with the NLO corrections included. (ii) Values of the Gegenbauer coefficients $B_2^q(\eta_1)$, $B_2^q(\eta_8) > 0$ increase the disagreement, while $B_2^g(\eta_1) > 0$ reduces the disagreement. Hence, a better agreement with the CLEO data would call for the two-angles mixing scheme and $B_2^q(\eta_1)\,, B_2^q(\eta_8) < 0$. (iii) The inclusion of power corrections enhances the (negative) NLO correction to the form factors at low Q^2 by factors $2.5 - 3$. In order to quantify these statements, we show in Fig. 6, the numerical results for the ratio

$$R_{\mathrm{M}\gamma}(Q^2) = \frac{[Q^2 F_{\mathrm{M}\gamma}(Q^2)]^{\mathrm{res}}_{\mathrm{NLO}}}{[Q^2 F_{\mathrm{M}\gamma}(Q^2)]^{\mathrm{HSA}}_{\mathrm{NLO}}} \tag{54}$$

for some selected values of the expansion coefficients. As a result, the RC method, employing the one-angle mixing scheme, is in good agreement with the CLEO data. (iv) Using instead the two-angles mixing scheme, the RC method favors non-asymptotic profiles for the distribution amplitudes of η_1 and η_8, e.g., $B_2^q(\eta_1),\ B_2^q(\eta_8) \geq 0.15$ and $B_2^g(\eta_1) \in [16,\ 20]$, while the region $B_2^q(Q^2 \simeq 2\ \mathrm{GeV}^2) < 0$ seems to be incompatible with the CLEO data.

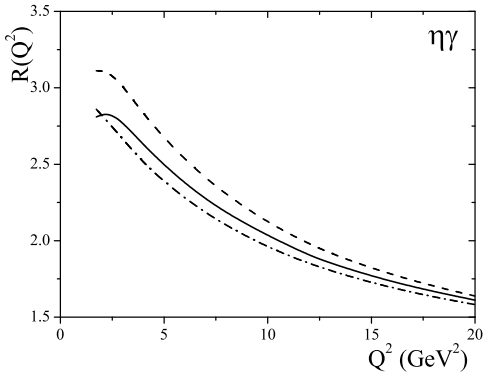

Figure 6: The ratio $R(Q^2)$ for the $\eta\gamma$ form factor. The solid line corresponds to the input parameters $B_2^q(\eta_1) = B_2^q(\eta_8) = B_2^g(\eta_1) = 0$. The dash-dotted curve describes the same ratio, but for $B_2^q(\eta_1) = B_2^q(\eta_8) = 0$, $B_2^g(\eta_1) = 14$, while the dashed one corresponds to $B_2^q(\eta_1) = B_2^q(\eta_8) = 0.05$, $B_2^g(\eta_1) = 10$.

8 Conclusions

The renormalon-inspired RC method enables the inclusion of power corrections originating from the kinematic endpoint region ($x \to 0, 1$), where non-perturbative QCD dominates and fixed-order perturbative computations of such corrections yields divergent results. We found that power-suppressed ambiguities to form factors vary between 3% at high and 11% at low Q^2 values. On the other hand, we have verified that the asymptotic limit of $[Q^2 F_{\mathrm{M}\gamma}(Q^2)]^{\mathrm{resum}}$ coincides, as it should, with the standard HSA result, leaving the asymptotic properties of QCD perturbation theory unchanged. The effect of power corrections at $Q^2 \leq 5\ \mathrm{GeV}^2$ enhances the (negative) NLO correction by $2.5 - 3$ times, providing this way agreement with the trend of the CLEO data. In the standard octet-singlet scheme we found $B_2^q(\eta_1) = B_2^q(\eta_8) \geq 0.055 \pm 0.065, \quad B_2^g(\eta_1) = 18 \pm 4.5$, whereas in the two-angles mixing scheme, we found $B_2^q(\eta_1) = B_2^q(\eta_8) \geq 0.15, \quad B_2^g(\eta_1) \in [16,\ 20]$. The distribution amplitude of the η and η' mesons, obtained in this work, can be useful in the investigation of other exclusive processes that involve η and η' mesons, especially at lower momentum-transfer values, where the standard HSA is most unreliable.

Acknowledgments

One of us (N.G.S.) would like to thank the organizers of the workshop for the hospitality and the exciting atmosphere during the meeting.

References

[1] J. Gronberg et al. (CLEO), Phys. Rev. **D 57** (1998) 33.

[2] J. Volmer et al. (The Jefferson Lab F(pi)), Phys. Rev. Lett. **86** (2001) 1713.

[3] S. V. Mikhailov and A. V. Radyushkin, JETP Lett. **43** (1986) 712; Sov. J. Nucl. Phys. **49** (1989) 494; Phys. Rev. **D 45** (1992) 1754.

[4] A. P. Bakulev and A. V. Radyushkin, Phys. Lett. **B 271** (1991) 223.

[5] S. V. Mikhailov, Phys. Atom. Nucl. **56** (1993) 650.

[6] A. P. Bakulev, S. V. Mikhailov and N. G. Stefanis, Phys. Lett. **B 508** (2001) 279; ibid. **B 590** (2004) 309(E).

[7] A. P. Bakulev, S. V. Mikhailov and N. G. Stefanis, Phys. Rev. **D 67** (2003) 074012; Phys. Lett. **B 578** (2004) 91.

[8] A. P. Bakulev, K. Passek-Kumericki, W. Schroers and N. G. Stefanis, Phys. Rev. **D 70** (2004) 033014.

[9] D. V. Shirkov and I. L. Solovtsov, Phys. Rev. Lett. **79** (1997) 1209.

[10] D. V. Shirkov, Theor. Math. Phys. **127** (2001) 409; Eur. Phys. J. **C 22** (2001) 331; D. V. Shirkov and I. L. Solovtsov, Phys. Part. Nucl. **32S1** (2001) 48.

[11] N.G. Stefanis, W. Schroers and H.C. Kim, Phys. Lett. **B 449** (1999) 299; Eur. Phys. J. **C 18** (2000) 137.

[12] A. I. Karanikas and N. G. Stefanis, Phys. Lett. **B 504** (2001) 225 (2001); N. G. Stefanis, Lect. Notes Phys. **616** (2003) 153.

[13] S. S. Agaev, Phys. Rev. **D 69** (2004) 094010.

[14] S. S. Agaev and N. G. Stefanis, Phys. Rev. **D** (in press) [hep-ph/0307087].

[15] S. S. Agaev, Phys. Rev. **D 64** (2001) 014007.

[16] S. S. Agaev and A. I. Mukhtarov, Int. J. Mod. Phys. **A 16** (2001) 3179.

[17] S. S. Agaev and N. G. Stefanis, Eur. Phys. J. **C 32** (2004) 507.

[18] S. S. Agaev, Phys. Lett. **B 360** (1995) 117 ibid. **B 369** (1996) 379(E); [hep-ph/9611215].

[19] S. S. Agaev, Mod. Phys. Lett. **A 10** (1995) 2009; ibid. **A 11** (1996) 957; ibid. **A 13** (1998) 2637.

[20] Th. Feldmann, Int. J. Mod. Phys. A 15, 159 (2000).

[21] E. Kou, Phys. Rev. **D 63** (2001) 054027.

[22] P. Kroll and K. Passek-Kumerički, Phys. Rev. D **67** (2003) 054017.

[23] G. P. Lepage and S. J. Brodsky, Phys. Rev. D **22** (1980) 2157; A. V. Efremov and A. V. Radyushkin, Phys. Lett. B **94** (1980) 245; Theor. Math. Phys. **42** (1980) 97 [Teor. Mat. Fiz. **42**(1980) 147]; A. Duncan and A. H. Mueller, Phys. Rev. D **21** (1980) 1636.

[24] H. Contopanagos, G. Sterman, Nucl. Phys. B **419** (1994) 77.

[25] A. Ali and A. Ya. Parkhomenko, Eur. Phys. J. C **30** (2003) 183.

[26] K. Passek-Kumerički, hep-ph/0311039.

Tests of Chiral Perturbation Theory in η decays

A. Kupść

The Svedberg Laboratory, Uppsala Universitet, Uppsala, Sweden
for CELSIUS/WASA

Abstract:
The eta meson with its variety of possible decays is well suited as a low energy Quantum Chromodynamics (QCD) laboratory. There are several theoretical predictions for processes such as $\eta \to 3\pi$, $\eta \to \pi^\circ\gamma\gamma$ etc. and therefore there is a need for new precise data.
A low background measurement of kinematical distributions of decay products of eta decays with branching ratios $>10^{-6}$ can be done in reaction $pd \to {}^3\mathrm{He}\eta$ close to threshold. Eta events are tagged by measuring the outgoing ^{3}He ions at 0° without bias on a decay channel. The reaction provides a source of eta mesons with very low background.
The decays which are specially well suited to be studied in these conditions are $\eta \to \pi^+\pi^-\pi^\circ$, $\eta \to \pi^+\pi^-\gamma$, $\eta \to \pi^+\pi^-e^+e^-$ and decays involving muons.

1 Physics motivation

The eta meson is well suited as a low energy Quantum Chromodynamics (QCD) laboratory. The systematical way of dealing with this regime of QCD is provided by the so called Chiral Perturbation Theory (CHPT) which uses the underlying chiral symmetry of massless quark QCD and SU(3)-octet of pseudoscalar mesons pions, kaons and eta as degrees of freedom. Systematical expansion is performed in powers of momenta of the meson and quark masses. At each level of calculation one has to introduce new counterterms in order to restore renormalizability of the theory. CHPT provides an accurate description of the strong and electroweak interactions of the pseudoscalar mesons at low energies [1]. Eta meson with similar mass as kaons and variety of possible decays should be equally important for tests of CHPT. There were so far however no such clean source of etas as in the case of kaons. In addition the wave function of the η physical state has some admixture of SU(3) singlet state which is a complication for

the calculations. Recently the interest in eta decays increased as they were considered as possible source of Standard Model contributions to rare kaon decays and to the anomalous magnetic moment of the muon. It was also pointed out that $\eta \to 3\pi$ is a valuable source of information on light quark masses.

Higher order predictions of CHPT contain arbitrary counter-terms. These should be taken from other experiments or from phenomenological models such as Vector Meson Dominance Model. Therefore predictions from CHPT should be compared with precise measurements of kinematical distributions of the decay products which allow to constrain the phenomenological assumptions. Experiments with high yield, clean source of eta mesons and with detectors with nearly full phase space coverage are best suited for precise measurement of kinematical distributions.

Decay	BR [2]	Observable
$\eta \to \pi^+\pi^-\pi^\circ$	$(23.6\pm0.4)\%$	Dalitz plot
$\eta \to \pi^+\pi^-\gamma$	$(4.68\pm0.11)\%$	distributions
$\eta \to \pi^+\pi^-e^+e^-$	$(4^{+14}_{-2.4})\times10^{-4}$	BR/distributions
$\eta \to \pi^\circ\gamma\gamma$	$(7.2\pm1.4)\times10^{-4}$	BR/distribution s
$\eta \to \pi^\circ e^+e^-$	10^{-9}(**)	BR
$\eta \to \mu^+\mu^-\gamma$	$(3.1\pm0.4)\times10^{-4}$	formfactor
$\eta \to \mu^+\mu^-$	$(5.8\pm0.8)\times10^{-6}$	BR
$\eta \to e^+e^-\gamma$	$(4.9\pm1.1)\times10^{-3}$	formfactor
$\eta \to e^+e^-e^+e^-$	2×10^{-5}(**)	formfactor
$\eta \to e^+e^-$	10^{-9}(**)	BR

(**) – not measured: theory prediction.

Table 1: List of eta decays studied by CELSIUS/WASA.

Some of the eta decays proposed to be investigated by CELSIUS/WASA collaboration are listed in table 1. As indicated in the table many of the decays are sensitive to the 2π prompt background which is inherent to any eta production mechanism. Below there are some examples of not-so-rare eta decays of interest for tests of CHPT.

The decay $\eta \to 3\pi$ was pointed as one of the key ingredients in the determination of ratios of light quark masses [3]. This hadronic decay is heavily suppressed and occurs due to u and d quark mass difference. The decay width is very sensitive to the mass difference of the quarks: $\Gamma_{\eta\to\pi^+\pi^-\pi^0} \propto \Gamma_0(m_d - m_u)^2$.

Ref	a	b	c
Layter [4]	-1.08±0.014	0.034±0.027	0.046±0.031
Gomley [5]	-1.17±0.02	0.21±0.03	0.06±0.04
Crystal Barrel [6]	-0.94±0.15	0.11±0.27	–
Crystal Barrel [7]	-1.22±0.07	0.22±0.11	0.06 fixed
tree	-1.00	0.25	0.00
one-loop	-1.33	0.42	0.08
dispersive	-1.16	0.26	0.1
tree dispersive	-1.10	0.31	0.001
absolute dispersive	-1.21	0.33	0.04

Table 2: Theoretical predictions [8] and experimental data on Dalitz plot slopes for the decay $\eta \to \pi^+\pi^-\pi^\circ$.

The decay width is obtained in ChPT when leading term of the expansion in quark masses is used and precise calculations of Γ_0 in the chiral limit. For estimating the error on the u and d quark mass ratio, except for uncertainty of experimental decay width, it is important to know the systematical error of the calculations.

The error of the experimental decay width is mainly determined by the uncertainty of the full decay width of the eta, which is obtained from the partial decay width of eta into two photons. That quantity has to be obtained in eta production experiments in e^+e^- colliders or in eta electroproduction in the electromagnetic field of the nucleus. To check systematical error of the calculations of the Γ_0 one should compare other predictions for the $\eta \to \pi^+\pi^-\pi^\circ$ and $\eta \to 3\pi^\circ$ decays. In particular, the decay distribution parameters of $\pi^+\pi^-\pi^\circ$ are strongly correlated with Γ_0.

The decay distribution of $\eta \to \pi^+\pi^-\pi^\circ$ is presented as a Dalitz plot using following normalized variables:

$$x = \sqrt{3}\frac{T_{\pi^-} - T_{\pi^+}}{Q}; y = 3\frac{T_{\pi^\circ}}{Q} - 1$$

where T_π $\pi = (\pi^+, \pi^-, \pi^\circ)$ – pion kinetic energy in the η rest frame and $Q = m_\eta - 2m_{\pi^+} - m_{\pi^\circ}$. The Dalitz plot density (normalized to the center) is usually parametrized as: $1 + ax + by + cxy$.

Table 2 summarizes theoretical predictions and present experimental results for the Dalitz plot parameters. Old high statistics data [4] and [5] are inconsistent with each other and more recent data from Crystal Barrel suffer from large errors.

Another check of Γ_0 is the ratio r =BR($\eta \to \pi^+\pi^-\pi^\circ$)/BR($\eta \to 3\pi^\circ$) which should be around 1.5. Tree level calculations give $r = 1.51$ while one-loop $r = 1.43$ [1]. Experimentally $r = 1.40 \pm 0.03$ [2] but recent result from CMD2 experiment shows higher value: $1.52 \pm 0.04 \pm 0.08$ [9]. The most precise value of the ratio could be obtained in experiment where the two decays are measured simultaneously with the same trigger.

The decay $\eta \to \pi^+\pi^-\gamma$ is an example of decay into odd intrinsic parity channel and therefore it is governed by anomalous component of the effective chiral Lagrangian. The most precise data come from an old experiment with 18k collected events [4]. Precise energy distribution of the photon will allow to check calculation for that sector of CHPT [10].

In CHPT all low level contributions to the $\eta \to \pi^\circ\gamma\gamma$ decay are suppressed so it provides a window for higher order effects. High order CHPT calculations has lead to decay width which is two times less than experimental value [11]. Recent result from Crystal Ball [12] seems to resolve this discrepancy by setting the experimental value in agreement with CHPT predictions. However measurement of $\eta \to \pi^\circ\gamma\gamma$ is a very difficult experiment and suffer form high background of prompt two π° production and from the decay $\eta \to 3\pi^\circ$. There is no clean data sample which would allow for extracting kinematical distributions of the decay products.

The decay $\eta \to \pi^+\pi^-e^+e^-$ is a conversion decay related to $\eta \to \pi^+\pi^-\gamma$. It is the most probable eta decay with four charged particles in the final state. Recently it was pointed out as a mean to search for CP violation in flavor conserving processes which are not constrained by limits on neutron electric dipole moment. The observable would be an asymmetry in distribution of angle between $\pi^+\pi^-$ and e^+e^- production planes at level of 10^{-3}-10^{-2} [13].

2 Sources of eta mesons

For ion storage rings such as CELSIUS or COSY two reactions as sources of eta mesons production are considered: $pd \to {}^3\mathrm{He}\eta$ at threshold and $pp \to pp\eta$ a few hundred MeV above threshold.

Some conditions for a source of etas for precise tests of CHPT:

1. Eta yield which allow studies of decays with BR 10^{-6}.

2. Effective trigger which does not introduce bias on the decay system.

3. Precise determination of the eta momentum to be used as stringent kinematical constraint in decay identification and event reconstruction.

4. Since most of the decays contain pion pair in the final state it is desirable that prompt two pion production is suppressed as much as possible.

The reaction $pd \rightarrow {}^3\mathrm{He}\eta$ close to threshold as a source of ηs was first employed for eta decay experiments at Saturne II synchrotron at Saclay [14]. The production of η is tagged in a very clean way by measuring ^{3}He in a spectrometer at 0°. The η production cross section in the reaction raises very quickly from threshold to a plateau value of 0.4 μb at 2 MeV excess energy, while background from prompt $pd \rightarrow {}^3\mathrm{He}\pi^+\pi^-$ reaction remains at the percent level [15]. This tagging method enables to collect simultaneously very clean data sample of all eta decays. The main problem with the reaction is rather low cross section.

A way to reach decays with lower BR is to use $pp \rightarrow pp\eta$ reaction at beam kinetic energies of 1350-1500 MeV. The reaction cross section is 5-20 μb. The η is tagged by measuring two outgoing protons in forward direction up to 18°. The trigger can not be based on the tagging system exclusively since the rate is too high for the data acquisition system. Therefore specific conditions for different decays have to be used. There is also large background from two pion prompt production.

3 Experiments at CELSIUS

Experiments at CELSIUS/WASA with $pp \rightarrow pp\eta$ reaction were done at beam kinetic energies 1360 and 1450 MeV. Selectivity of the trigger for neutral decay modes is above one per cent. The selectivity for the decay channels with charged particles is ten times lower (see table 3).

For studies of η decays using $pd \rightarrow {}^3\mathrm{He}\eta$ reaction close threshold detection of outgoing ^{3}He ions which should give a signal for the trigger and a measurement of the ^{3}He energy for precise determination of the η momentum. The solution for CELSIUS/WASA uses accelerator dipoles as a filter to deflect ^{3}He recoils and kinetic energy measurement in telescopes. Internal D_2 pellet target is available on regular basis since February 2004. Initial tests of eta tagging with $pd \rightarrow {}^3\mathrm{He}\eta$ reaction have been done with 3 different setups of the tagging telescope setups. Latter it was decided to use an internal semiconductor HpGe detector placed in the beam pipe vacuum. It has energy resolution better than 1 MeV for ^{3}He kinetic energies less than 420 MeV and acceptance at 1 MeV above threshold is 50%. The tagging detector provides trigger and very clean signal of ^{3}He ions with kinetic energy

reaction	$pp \to pp\eta$		$pd \to {}^3\mathrm{He}\eta$
T_{beam} [MeV]	1360		893
decays	*charged*	*neutral*	*All*
Luminosity	$5{\times}10^{30}$	$5{\times}10^{30}$	$5{\times}10^{30}$
triggers	2FC2CC	2FC CN	^{3}He
Rate	1.2 kHz	400 Hz	1 Hz
DAQ Rates			
$\eta \to \pi^\circ\pi^+\pi^-$	0.7 Hz	0	0.2 Hz
$\eta \to N\gamma$	0	3 Hz	0.7 Hz
final samples:			
$\eta \to \pi^\circ\pi^+\pi^-$	5%	–	$> 20\%$
$\eta \to N\gamma$	–	50%	$> 80\%$

Table 3: Performance of eta tagging in CELSIUS/WASA.

consistent with kinematics of $pd \to {}^3\mathrm{He}\eta$ reaction. With the initial performance of the deuterium pellet target and the tagging system 1η event per second is collected with luminosity $5{\times}10^{30}\mathrm{cm}^{-2}\mathrm{s}^{-1}$ by the data acquisition while the trigger rate is few Hz.

The quality of the tagging in $pd \to {}^3\mathrm{He}\eta$ reaction can be tested by decay $\eta \to \gamma\gamma$. The process has very simple kinematics since the η is nearly at rest in the center of mass system. Therefore momenta of the photons are in plane with the beam and the velocity of the eta can be reconstructed from the photons directions alone. The β is given by a simple formula:

$$\beta = \frac{\sin(\theta_1 + \theta_2)}{\sin\theta_1 + \sin\theta_2} = 0.42.$$

Figure 1 shows experimental correlations plots for planarity vs invariant mass and velocity vs energy sum of two photons with highest energy in the events selected by the ^{3}He trigger. The information provides very clean signature of the $pd \to {}^3\mathrm{He}\eta(\to \gamma\gamma)$ events. The corresponding plots from Monte Carlo simulation of $pd \to {}^3\mathrm{He}\eta(\to All)$ are shown in figure 2. From the comparison one sees that majority of events in the plots comes from $pd \to {}^3\mathrm{He}\eta$ reaction. The main background is due to beam-rest gas interactions – events with correct energy but wrong β (from scattering angle information). Tagging by measurement ^{3}He at 0° tends to enhance this contribution since it is not sensitive to position of the interaction point. The background can be removed by a constrain on the vertex position for the decays with charged particles. After applying cuts on β and the planarity

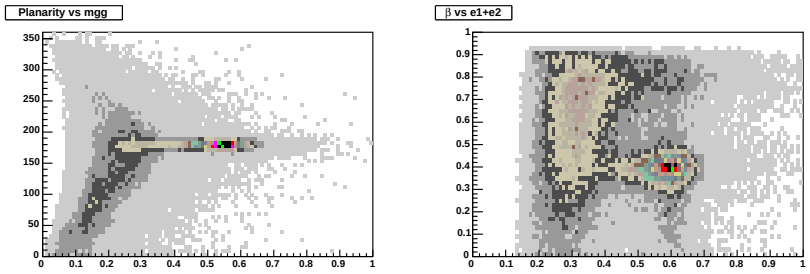

Figure 1: Experiment: Planarity vs invariant mass of two photons and β vs energy sum of the two photons.

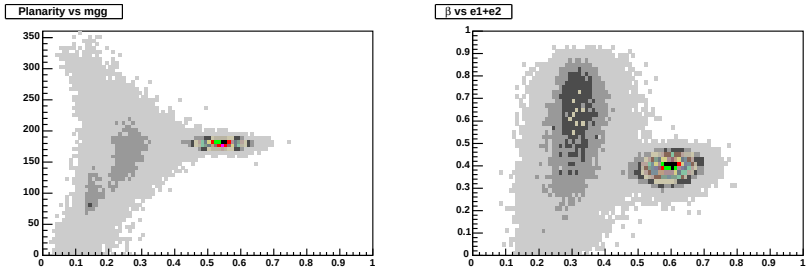

Figure 2: Planarity vs invariant mass of two photons and β vs energy sum of the two photons. Monte Carlo with all η decays.

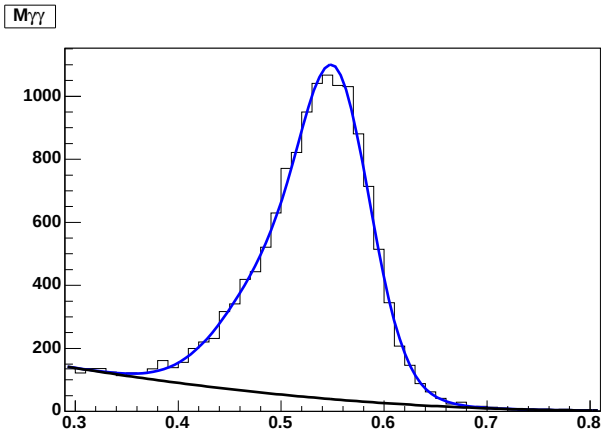

Figure 3: Invariant mass of two photons after cuts on planarity and β (Experiment).

one obtains very clean peak in the invariant mass of the two photons – figure 3. Since the trigger is not biased by a particular eta decay channel one estimates that in total 130k of eta decays events were collected in the spring runs. Analysis of particular decay modes is under way.

4 Outlook

Studies of η decays using $pd \rightarrow {}^3\mathrm{He}\eta$ reaction will continue during fall 2004 and spring 2005 before CELSIUS shutdown when WASA detector will be moved to COSY.

Programme of η decays for WASA@COSY will focus on rare decays with BR$<10^{-5}$. One expects improvements in eta tagging in $pp \rightarrow pp\eta$ at energies about 1500 MeV. There are indications that accelerator background conditions will be improved at COSY. Development of the trigger system is aimed at reduction of decay channel dependence and increased selectivity. The goal is to achieve sensitivity up to 10^{-9} for decays involving photons and electrons to be able to observe $\eta \rightarrow e^+e^-$ and $\eta \rightarrow \pi^\circ e^+e^-$ decay channels.

References

[1] J. Gasser and H. Leutwyler, Nucl. Phys. **B 250** (1985) 539.

[2] K. Hagiwara et al., Phys. Rev. **D 66** 010001 (2002).

[3] H. Leutwyler, Phys. Lett. **B 378** (1996) 313.

[4] J. G. Layter et al., Phys. Rev. **D 7** (1973) 2565.

[5] M. Gomley et al., Phys. Rev. **D 2** (1970) 501.

[6] C. Amsler et al., Phys. Lett.**B 346** (1995) 203.

[7] C. Abele et al., Phys. Lett. **B 417** (1998) 197.

[8] J. Bijnenes and J. Gasser, Physica Scripta **T 99** (2002) 34.

[9] R. R. Akhmetshin et al., Phys. Lett. **B 509** (2001) 217.

[10] B. Holstein, Physica Scripta **T 99** (2002) 55.

[11] D. M. Alde et al., Z. Phys. **C 25** (1984) 225.

[12] B.M.K. Nefkens and J.W. Price, Physica Scripta **T 99** (2002) 114.

[13] C.Q. Geng, J.N. Ng, T.H. Wu, Mod.Phys.Lett. **A 17** (2002) 1489; Dao-Neng Gao, Mod.Phys.Lett. **A 17** (2002) 1583.

[14] J. Berger et al., Phys. Rev. Lett. **61** (1988) 919.

[15] B. Mayer et al., Phys. Rev. **C 53** (1996) 2068.

[16] M. Jacewicz, PhD dissertation, Uppsala University 2004.

Hadronic decays of η and η'

N. Beisert, B. Borasoy

Physik Department -T39, TU München, 85747 Garching, Germany

Abstract: The hadronic decays $\eta \to \pi\pi\pi$, $\eta' \to \pi\pi\pi$ and $\eta' \to \eta\pi\pi$ are investigated within a $U(3)$ chiral unitary approach. Final state interactions are included by deriving the effective s wave potentials for meson meson scattering from the chiral effective Lagrangian and iterating them in a Bethe-Salpeter equation. With only a small set of parameters we are able to explain both rates and spectral shapes of these decays.

1 Introduction

The hadronic decays $\eta \to \pi\pi\pi$ and $\eta' \to \pi\pi\pi$ are of great interest since they violate isospin symmetry. At such low energies the calculations of the decay amplitudes are based on effective chiral Lagrangians which have the same symmetries and symmetry breaking patterns as the underlying QCD Lagrangian. They are written in terms of effective degrees of freedom, usually the octet of pseudoscalar mesons – pions, kaons and the eta – [1], however, they can easily be extended to include the η' also [2].

The inclusion of the η', however, spoils the conventional chiral counting scheme, since its mass $m_{\eta'}$ does not vanish in the chiral limit so that higher loops will still contribute to lower chiral orders. This can be prevented by imposing large N_c counting rules within the effective theory in addition to the chiral counting scheme. In the large N_c limit the axial anomaly vanishes and the η' converts into a Goldstone boson. The properties of the theory may then be analyzed in a triple expansion in powers of small momenta, quark masses and $1/N_c$, see e.g. [2, 3, 4, 5]. In particular, $m_{\eta'}$ is treated as a small quantity. Phenomenologically, this is not the case since $m_{\eta'} = 958$ MeV, and it is therefore preferable to treat the η' as a massive state.

Furthermore, final state interactions have already been shown to be substantial in $\eta \to \pi\pi\pi$ both in a complete one-loop calculation in $SU(3)$

ChPT [6] and under the inclusion of final state interactions using extended Khuri-Treiman equations [7]. The last calculation comes closest to the experimental decay rate but still remains below it, if the usual quark mass ratios are employed. On the other hand, the experimental rate of the decay can be reproduced by increasing the quark mass ratio $1/Q^2 = [(m_d - m_u)/(m_s - \hat{m})] \cdot [(m_d + m_u)/(m_s + \hat{m})]$ with $\hat{m} = (m_u + m_d)/2$ from $1/(24.1)^2$ to $1/(22.4 \pm 0.9)^2$ which is considered to be the most accurate determination of this quark mass ratio.

It is thus obligatory to include final state interactions also in the decay $\eta' \to \pi\pi\pi$. We have applied the following approach: after deriving effective potentials for meson meson scattering from the chiral effective Lagrangian, we iterate them utilizing a Bethe-Salpeter equation (BSE). This method has been proven to be useful both in the purely mesonic sector and under the inclusion of baryons [8, 9]. The BSE generates dynamically bound states of the mesons and baryons and accounts for the exchange of resonances without including them explicitly. The usefulness of this approach lies in the fact that from a small set of parameters a large variety of data can be explained [10].

This method allows us to account for final state interactions and to study the importance of resonances in different isospin channels, a topic of interest, e.g., in the dominant hadronic decay mode of the η', $\eta' \to \eta\pi\pi$. It has been claimed that this decay can be described in a tree-level model via the exchange of the scalar mesons $\sigma(560)$, $f_0(980)$ and $a_0(980)$ which are combined together with $\kappa(900)$ into a nonet [11] (see also [12, 13, 14, 15, 16]). The authors find that the exchange of the scalar resonance $a_0(980)$ dominates. By iterating the effective chiral potentials to infinte order in a Bethe-Salpeter equation, we can investigate the importance of these resonances explicitly.

2 Sketch of the approach

In our approach, the effective Lagrangian of second and fourth chiral order is employed to derive the interaction kernel A for meson meson scattering. The underlying idea is that the initial particle, i.e. the η or η', decays via chirally constrained vertices derived from the effective Lagrangian into three mesons and that two out of these three mesons rescatter an arbitrary number of times, see Fig. 1 for illustration. There are three possible ways in combining two of the mesons to a pair while leaving the third one unaffected which corresponds to the s-, t- and u-channel, respectively. Interactions of the third meson with the pair of rescattering mesons are neglected. Such an infinite meson meson rescattering can be generated by application of the

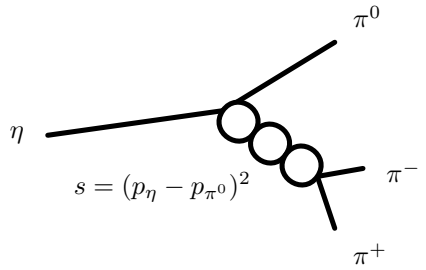

Figure 1: Shown is a possible contribution to final state interactions in the decay $\eta \to \pi^0\pi^+\pi^-$. Here, it takes place in the s-channel between $\pi^+\pi^-$ and the bubble chain represents part of the solution to the BSE at energy $\sqrt{s}$.

Bethe-Salpeter equation. To this end, the s wave potentials for meson meson scattering are derived from the chiral effective Lagrangian and iterated in a Bethe-Salpeter equation. The BSE then generates the propagator for two interacting particles in a covariant fashion.

The Bethe-Salpeter equation for the two-particle propagator T from a local interaction A is given by [17, 18]

$$T(p, q_i, q_f) = A(p, q_i, q_f) + \int \frac{i\, d^d k}{(2\pi)^d} \frac{T(p, q_i, k) A(p, k, q_f)}{(k^2 - m^2)((k-p)^2 - \bar{m}^2)}. \quad (1)$$

The solution for T amounts to an infinite resummation of the interaction kernel A and two free meson propagators G with masses $m, \bar{m}$, and can be diagrammaticaly depicted as an infinite interaction chain, Fig. 2. In short notation, both the equation and its solution can be written as

$$T = A + TGA, \qquad T = (1 - GA)^{-1} A = A + AGA + AGAGA + \ldots \quad (2)$$

For the decays considered here we would like to use these final-state interactions in such a way as to reproduce to a large extent the one-loop result from conventional ChPT. The second term in the expansion of T, AGA, equals the unitary corrections in one-loop ChPT (i.e. without tadpoles). Tadpoles which are not included in our approach have been shown to yield numerically small effects in scattering processes in the physical region and can furthermore be partially absorbed by redefining chiral parameters [8].

In the evaluation of the BSE we will restrict ourselves to s waves, since they are expected to dominate most of the decays discussed here, and indeed this simplification gives results already in agreement with experiment. An improvement of the results – particularly for the spectral shape of the Dalitz distributions – may be expected by including the p waves, but this is beyond

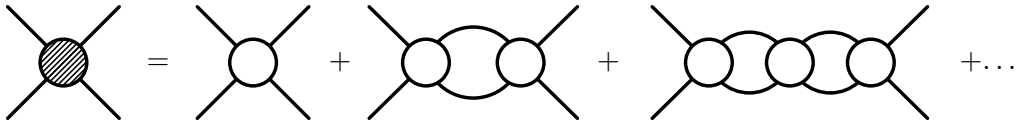

Figure 2: Solution to the Bethe-Salpeter equation $T = A + AGA + AGAGA + \ldots$

the scope of the present investigation. We can further simplify the integral in the BSE (1), since we are only interested in the physically relevant piece of the solution T with all momenta put on the mass shell. The amplitude A contains in general off-shell parts which deliver via the integral a contribution even to the on-shell part of the solution T. However, these off-shell parts yield exclusively chiral logarithms which – besides being numerically small – can be absorbed by redefining the regularization scale of the loop integral. Furthermore the off-shell parts are not uniquely defined in ChPT. We will therefore set all the momenta in the amplitudes in (1) on-shell, which has also been done in previous work, see e.g. [8]. Finally, we need to consider all two-meson channels. In particular, those which have the same set of quantum numbers can couple amongst each other. Consequently, the objects A, T, G are promoted to matrices in channel space and are functions of the two particle invariant mass squared p^2. With these simplifications the BSE equation reduces to (2) as a matrix equation for every p^2 and the solution is obtained by matrix inversion. The matrix G is a diagonal matrix with elements given by the integral

$$G_{m\bar{m}}(p^2) = \int \frac{d^d k}{(2\pi)^d} \frac{i}{(k^2 - m^2)((k-p)^2 - \bar{m}^2)} \tag{3}$$

where m and $\bar{m}$ are the masses of the two mesons in the corresponding channel. In dimensional regularization the renormalized integral is evaluated as

$$\begin{aligned} G_{m\bar{m}}(p^2) = \frac{1}{16\pi^2}\Bigg[&- 1 + \ln\frac{m\bar{m}}{\mu^2} + \frac{m^2 - \bar{m}^2}{p^2}\ln\frac{m}{\bar{m}} \\ &- \frac{2\sqrt{\lambda_{m\bar{m}}(p^2)}}{p^2}\operatorname{artanh}\frac{\sqrt{\lambda_{m\bar{m}}(p^2)}}{(m+\bar{m})^2 - p^2}\Bigg] \\ \lambda_{m\bar{m}}(p^2) = &\big((m-\bar{m})^2 - p^2\big)\big((m+\bar{m})^2 - p^2\big), \end{aligned} \tag{4}$$

where μ is the regularization scale which can be chosen independently for every channel.

3 Summary of the results

In this section, we summarize our results. A detailed presentation of the results can be found in [10]. Neglecting small corrections from electromagnetic interactions the amplitude for the decay $\eta \to \pi\pi\pi$ is proportional to $m_u - m_d$ and provides a sensitive probe on $SU(2)$ symmetry breaking. Our results are in reasonable agreement with experiment after employing Dashen's theorem. Conversely, this decay may be used to constrain the double quark mass ratio Q and we obtain $Q = 23.4 \pm 0.8$, a value which is in agreement with the requirement by Dashen's theorem and indicates that higher order corrections to this low-energy theorem may be small, in contradistinction to what has been discussed in [19, 20, 21].

For the decay $\eta' \to \pi\pi\pi$ which also violates isospin we obtain agreement with the available data. Our result for the neutral mode, $\Gamma(\eta' \to \pi^0\pi^0\pi^0) = 291$ eV, is within the experimental error ranges $\Gamma(\eta' \to \pi^0\pi^0\pi^0) = (311 \pm 77)$ eV, while our result for the charged decay mode, $\Gamma(\eta' \to \pi^0\pi^+\pi^-) = 294$ eV, for which only an upper experimental limit of 1005 eV exists, is expected to receive substantial contributions from p waves.

The third and final decay we investigated is $\eta' \to \eta\pi\pi$. Again, reasonable agreement with data is achieved and we can furthermore confirm within our approach the importance of the $a_0(980)$ resonance for this decay as has been claimed in the literature.

Our results are in overall good agreement with the decay rates, although the approach includes only a few parameters. In the case of the slope parameters we are also in the right ballpark, but the experimental situation is less settled here and one needs new experiments with higher statistics in order to reduce the error bars. Since we included only s waves in our approach, we cannot expect, of course, to reproduce the spectral shapes of the decays very precisely. The p waves, although small in magnitude for most decays discussed here, will alter our results for the Dalitz parameters and must be included in order to make more accurate statements.

The method described here has also successfully been applied to the anomalous decays $\eta/\eta' \to \gamma\gamma$ and $\eta/\eta' \to \pi^+\pi^-\gamma$ [22] and is furthermore applicable to a variety of decays such as η' decay modes into $n\pi$ with $n \geq 4$ and the CP-violating decays $\eta, \eta' \to \pi\pi$.

Acknowledgments

Financial support of the Deutsche Forschungsgemeinschaft is gratefully acknowledged.

References

[1] J. Gasser and H. Leutwyler, Nucl. Phys. **B 250** (1985) 465.

[2] R. Kaiser and H. Leutwyler, Eur. Phys. J. **C 17** (2000) 623.

[3] H. Leutwyler, Phys. Lett. **B 374** (1996) 163.

[4] P. Herrera-Siklody, J. I. Latorre, P. Pascual and J. Taron, Nucl. Phys. **B 497** (1997) 345.

[5] R. Kaiser and H. Leutwyler, *"Pseudoscalar decay constants at large $N(c)$"*, in *Proceedings of the Workshop Nonperturbative Methods in Quantum Field Theory,* eds. A. W. Schreiber, A. G. Williams and A. W. Thomas (World Scientific, Singapore, 1998).

[6] J. Gasser and H. Leutwyler, Nucl. Phys. **B 250** (1985) 539.

[7] J. Kambor, C. Wiesendanger and D. Wyler, Nucl. Phys. **B 465** (1996) 215.

[8] J. A. Oller and E. Oset, Nucl. Phys. **A 620** (1997) 438.

[9] N. Kaiser, P. B. Siegel and W. Weise, Nucl. Phys. **A 594** (1995) 325.

[10] N. Beisert and B. Borasoy, Nucl. Phys. **A 716** (2003) 186

[11] A. H. Fariborz and J. Schechter, Phys. Rev. **D 60** (1999) 034002.

[12] J. Schechter and Y. Ueda, Phys. Rev. **D 3** (1971) 2874.

[13] C. A. Singh and J. Pasupathy, Phys. Rev. Lett. **35** (1975) 1193, Erratum-ibid. **35** (1975) 1748.

[14] N. G. Deshpande and T. N. Truong, Phys. Rev. Lett. **41** (1978) 1579.

[15] A. Bramon and E. Masso, Phys. Lett. **B 93** (1980) 65, Erratum-ibid. **B 107** (1980) 455.

[16] P. Castoldi and J. M. Frère, Z. Phys. **C 40** (1988) 283.

[17] N. Beisert and B. Borasoy, Phys. Rev. **D 67** (2003) 074007.

[18] J. Nieves and E. Ruiz Arriola, Nucl. Phys. **A 679** (2000) 57.

[19] J. F. Donoghue, B. R. Holstein and D. Wyler, Phys. Rev. Lett. **69** (1992) 3444.

[20] J. F. Donoghue, B. R. Holstein and D. Wyler, Phys. Rev. **D 47** (1993) 2089.

[21] J. Bijnens, Phys. Lett. **B 306** (1993) 343.

[22] B. Borasoy and R. Nißler, Eur. Phys. J. **A 19** (2004) 367;
B. Borasoy and R. Nißler, Nucl. Phys. **A** (in print), hep-ph/0405039.

.

Measurements of η' Decays using WASA@COSY

M. Wolke
Department of Radiation Sciences, Uppsala University, Sweden
Institut für Kernphysik, Forschungszentrum Jülich, Germany

Abstract: Studies of hadronic, radiative, and (semi–)leptonic decays of the η' allow to shed light on a broad field of fundamental physics questions. Isospin symmetry breaking decays provide a well-suited tool to extract the light quark mass difference. Differential distributions in hadronic decays both test predictions obtained within ChPT approaches, and enclose information on the scalar meson sector. Precision measurements on radiative decay widths will constrain our knowledge on pseudoscalar mixing, the manifestation of QCD anomalies, and the structure of the η'. The latter is also subject of investigation in semileptonic decays probing the η' transition form factor. The presently available experimental information is reviewed, and prospects for η' decay physics with WASA at COSY are presented.

1 Introduction

The axial U(1) anomaly prevents the pseudoscalar singlet η_0 from being a Goldstone boson. The dominant contribution to the mass of the singlet state arises from the divergence of the singlet axial–vector current, that acquires an additional term related to the gluonic field strength tensor and, consequently, does not vanish in the chiral limit. The primordial interest of studying the physical η' arises from the fact, that its wavefunction is predominated by the singlet state of the pseudoscalar meson nonet. However, since η and η' are mixtures of the octet and singlet fields, η_8 and η_0, respectively, the η' can not be disentangled from the η, and a proper study of η' physics requires to account for the η as well.

A variety of aspects of low–energy hadron dynamics become accessible from precision data on η and η' decays. Experimental results can be compared with model–independent calculations within the framework of Chiral

Perturbation Theory (ChPT) with a clear connection to Quantum Chromodynamics.

This report focuses on some key experiments that will become feasible combining the high quality and precision of the Cooler Synchrotron COSY with the 4π spectrometer WASA. The experimental programme extends the physics results already obtained on the dynamics of close–to–threshold η and η' production in hadronic collisions [1, 2].

2 Some Words on Current and Constituent Quark Masses

Since we are not able to measure the (current) mass of an isolated quark, i.e. the fundamental quantity entering the QCD Lagrangian, we are *confined* to extract quark masses from hadronic objects, where quarks are assigned a constituent quark mass. The relationship is delicate, and it is necessary to understand the origin of both current and constituent quark masses, since the difference of the first causes charge symmetry breaking (CSB), while the latter is being observed in hadronic objects (this part of the text *borrows heavily* from [3]; according to [3], the authors *borrow heavily* from [4]):

Flavour–dependent quark masses are generated by flavour–dependent couplings of quarks to vacuum expectation values of Higgs fields. However, it should be noted that there is no general fundamental understanding of masses in the standard model [3]. Physical observables are related by renormalization to the strong coupling constant g and the current quark masses m_f^{curr}, which are bare parameters of the QCD Lagrangian: Observables are computed by expansions in powers of g, giving rise to divergences that are regularized by means of a cutoff parameter λ. With a sufficient number of observables the bare parameters can be expressed in terms of the physical observables at a given cutoff. In the next step, further observables can be computed from the previously used physical results, independently of λ in case of a renormalizable theory. Unlike quantum electrodynamics, where bare charge and mass of the electron can be expressed in terms of the physically observed quantities, confinement restricts us to use indirect methods like hadronic masses in QCD. A kinematical reference point has to be chosen to define quark masses, and their actual value becomes dependent on the reference point, however, the results of calculations are invariant (renormalization group [5]). Since from a given value of the *running* mass, dependent on the reference point, one can calculate the mass for a different reference point in perturbative QCD, the current masses in the QCD Lagrangian can

be well defined stating the actual renormalization point. Requiring that observables are independent of the cutoff λ leads to a renormalization group invariant mass, i.e. independent of the kinematical reference point, but dependent on the QCD invariant scale parameter Λ. For example values given in [4] are $m_u = 6.3 \pm 1.9\,\mathrm{MeV}$ and $m_d = 11.0 \pm 3.2\,\mathrm{MeV}$ for $\Lambda = 200\,\mathrm{MeV}$.

Due to the strong interaction colour forces the energy of the vacuum can be lowered when condensates are formed, i.e. when expectation values $< \bar{\Psi}(0)\Psi(0) >$, where Ψ denotes the quark field operator, acquire non–zero values. Consequently, the colour force leads to a quark self–energy term or "mass" (*dynamical symmetry breaking (DSB)*), that can be shown numerically to be consistent with the constituent quark masses m_f^{const}. These are identical for up and down quarks in the chiral limit, and small current quark mass differences are retained as differences of the constituent masses [6, 7, 8, 9, 10, 11]. Since any Hamiltonian with a confining potential — that can always be shifted by a constant — contains another unknown in addition to mass terms, the actual mass becomes model dependent. For example, in the extreme case of the MIT bag model [12] with massless quarks, the quark kinetic energy acts as a constituent mass [13, 14]. Both confining potentials and quark energy terms are flavour independent. Any difference between up– and down–quark constituent masses arises from the difference in the current mass. Consequently, charge symmetry breaking effects observed at the hadronic level of constituent masses, are expected to relate directly to the current mass difference, i.e. to the flavour dependence of the quark mass spectrum. Effects are expected in observables, that depend on the constituent quark mass difference rather than the ratio, since the latter yields $m_u^{const}/m_d^{const} \approx 1$ despite a large current mass difference.

3 Charge Symmetry Breaking and Hadronic Decays

In quantum chromodynamics the interactions of light up and down quarks are identical (*charge symmetry*), as long as the mass difference $\Delta m = m_d - m_u$ is neglected. The charge symmetry operation P_{cs} is defined as a 180° isospin rotation around the y–axis, with the z–axis being related to charge, i.e.

$$P_{cs}|\,d> = |\,u>, \quad P_{cs}|\,u> = -|\,d> \ . \tag{1}$$

Charge symmetry breaking (CSB) arises from the difference between up and down quarks, i.e. both electromagnetic energy differences related to electric charges and magnetic moments as well as the light quark mass difference (for

a review see [3]). Complementarily to estimates of Δm from pseudoscalar meson masses, where CSB via the electromagnetic interaction cannot be neglected, and to meson production processes, where the information from recent results might be distorted by the hadronic environment [15], isospin symmetry breaking decays $\eta' \to 3\pi$ provide a clean approach; CSB effects can be directly related to Δm, since electromagnetic effects are expected to be small [16, 17].

Mixing between the isospin eigenstates $|\tilde{\pi}^0>$ and $|\tilde{\eta}>$ given by

$$\begin{aligned} |\,\tilde{\pi}^0> &= \frac{1}{\sqrt{2}}|\,u\bar{u} - d\bar{d}> \\ |\,\tilde{\eta}> &= \cos\Theta_{ps}|\,\eta_8> - \sin\Theta_{ps}|\,\eta_0>\,, \end{aligned} \tag{2}$$

where $|\eta_8>$ and $|\eta_0>$ are the SU(3) octet and singlet representations

$$\begin{aligned} |\,\eta_8> &= \frac{1}{\sqrt{6}}\left(u\bar{u} + d\bar{d} - 2s\bar{s}\right) \\ |\,\eta_0> &= \frac{1}{\sqrt{3}}\left(u\bar{u} + d\bar{d} + s\bar{s}\right)\,, \end{aligned} \tag{3}$$

occurs due to a non–vanishing matrix element of the quark mass contribution to the QCD Hamiltonian density $\mathcal{H}_m$

$$\begin{aligned} &< \tilde{\pi}^0\,|\,\mathcal{H}_m\,|\,\tilde{\eta}> \\ &= \left\langle \frac{1}{\sqrt{2}}\left(u\bar{u} - d\bar{d}\right)\,|\,\mathrm{m}_u u\bar{u} + \mathrm{m}_d d\bar{d} + \mathrm{m}_s s\bar{s}\,|\,\frac{1}{\sqrt{3}}\left(u\bar{u} + d\bar{d} - s\bar{s}\right)\right\rangle = \\ &= \frac{1}{\sqrt{6}}\left(\mathrm{m}_u - \mathrm{m}_d\right)\,. \end{aligned} \tag{4}$$

where a pseudoscalar singlet–octet mixing angle $\Theta_{ps} = -19.5^\circ$ was used (see also [18]). With the physical states

$$\begin{aligned} |\,\pi^0> &= \cos\Theta_{\pi\eta}|\,\tilde{\pi}^0> + \sin\Theta_{\pi\eta}|\,\tilde{\eta}> \\ |\,\eta> &= -\sin\Theta_{\pi\eta}|\,\tilde{\pi}^0> + \cos\Theta_{\pi\eta}|\,\tilde{\eta}> \end{aligned} \tag{5}$$

the mixing angle $\Theta_{\pi\eta}$ is related to the light quark mass difference by [19, 20, 21]

$$\sin\Theta_{\pi\eta} = \frac{\sqrt{3}\left(\mathrm{m}_d - \mathrm{m}_u\right)}{4\left(\mathrm{m}_s - \hat{\mathrm{m}}\right)} \tag{6}$$

with the average light quark mass $\hat{\mathrm{m}} = (\mathrm{m}_u + \mathrm{m}_d)/2$. Measuring the ratios of partial decay widths of isospin symmetry forbidden and allowed decays,

$\eta' \to 3\pi$ and $\eta' \to \eta 2\pi$, respectively, i.e. an observable, that vanishes in the limit $\Delta \mathrm{m} = 0$,

$$\begin{aligned} \mathcal{R}_1 &= \frac{\Gamma\left(\eta' \to \pi^0\pi^0\pi^0\right)}{\Gamma\left(\eta' \to \eta\pi^0\pi^0\right)} \\ \mathcal{R}_2 &= \frac{\Gamma\left(\eta' \to \pi^0\pi^+\pi^-\right)}{\Gamma\left(\eta' \to \eta\pi^+\pi^-\right)} \end{aligned} \tag{7}$$

the $\pi - \eta$ mixing angle can be derived in η' decays from

$$\mathcal{R}_i = \mathrm{P}_i \sin^2 \Theta_{\pi\eta}\,, \tag{8}$$

with P_i denoting phase space factors (see also [22]).

While the $\eta\pi^+\pi^-$ final state is the strongest decay channel of the η', only an upper limit is reported for $\Gamma(\eta' \to \pi^0\pi^+\pi^-)/\Gamma_{tot} \leq 5\,\%$ [23]. For the neutral decay modes in equation 7 the ratio $\mathcal{R}_1 = 7.4 \pm 1.2 \times 10^{-3}$ has been measured at GAMS–2000 with a total statistics of ≈ 130 events, leading to $\sin\Theta_{\pi\eta} = 0.023 \pm 0.002$ [24, 25]. However, there is considerable uncertainty in the literature about the value of $\sin\Theta_{\pi\eta}$, with values ranging from 0.010, as extracted from meson masses using PCAC relations in [19] in agreement with the estimate given in [26], $0.0013 - 0.0014$ [27, 28, 29] up to 0.034 ± 0.013 [30].

With the WASA $4\,\pi$ electromagnetic calorimeter at COSY, in the tagging reaction $pp \to pp\eta'$ a statistical accuracy for $\sin\Theta_{\pi\eta}$ of $1\,\%$ could be achieved for the lowest estimate of [19] within a running time of 10 to 12 weeks at a luminosity of $10^{32}\,\mathrm{cm}^{-2}\,\mathrm{s}^{-1}$, improving the precision of the existing experimental value by an order of magnitude (see table 1).

The energy dependence of hadronic decays $\eta' \to \eta\,2\pi$ and $\eta' \to 3\pi$, that is contained in the Dalitz plot distribution of the decay products, is discussed in the framework of Chiral Perturbation Theory in [31, 32, 33]. Presently, the data on the modes with highest statistics, $\eta' \to \eta\,2\pi$ mode are inconclusive, whether the 2π mass distributions deviate from phase space. For the $\eta' \to 3\pi$ decays, no experimental data on the Dalitz plot parameters are presently available.

Hadronic decay modes also constrain the interpretation of the scalar nonet: In [34] the decays $\eta' \to \eta\,2\pi$ are found to be dominated by isovector $a_0(980)$ exchange and the experimental data are used to fix unknown scalar–pseudoscalar–pseudoscalar couplings. In a recent study of the $\eta \to 3\pi$ decays scalar exchange contributions are concluded to contribute as much as $30\,\%$ to the total decay amplitude [35], and it is pointed out that for $\eta' \to 3\pi$ a stronger influence of diagrams involving $f_0(980)$ and $a_0(980)$ is expected, since the exchange particles are much closer to the mass shell.

4 Some Words on Symmetries and Anomalies

...which *borrow heavily* from [36] and [37]. By definition, the term *quantum anomaly* characterizes the event, that a certain invariance of an action at the classical level cannot be preserved at the quantum level. Each global symmetry of the Lagrangian is — according to Noether's theorem in classical field theory — associated with a conserved current. Gauge bosons interact with a current that is associated with gauge invariance, and if the gauge invariance of a classical action is no longer conserved when quantum corrections, i.e. loops, are taken into account, the related current is no longer conserved (*internal* anomaly). The result is usually a *disaster* [37], since the underlying theory cannot be quantized consistently and becomes self–contradictory, i.e. the structure of gauge theories is restricted by the requirement of an absence — or cancellation by a special choice of fields — of internal anomalies [1].

The situation differs for an *external* anomaly, which is actually addressed by the radiative decays of the pseudoscalars: In this case the non–conserved current is not linked to the gauge bosons, and is associated with an *external* global symmetry of the Lagrangian.

In the limit of vanishing quark masses $\mathrm{m}_i = 0\,(i = 1..3)$ the QCD action S_{QCD} and the Lagrangian [2] are given by

$$\begin{aligned} \mathrm{S}_{QCD} &= \int d^4\mathrm{x}\mathcal{L}_{QCD}\,(\mathrm{x}) \\ \mathcal{L}_{QCD} &= -\frac{1}{2}\,\mathrm{tr}\,(G_{\mu\nu}G^{\mu\nu}) + \sum_{i=1}^{N_f=3} \bar{q}_i\,(i\gamma^\mu D_\mu - \mathrm{m}_i)\,q_i\ , \end{aligned} \tag{9}$$

with the gluonic field strength tensor $G_{\mu\nu} = \delta_\mu A_\mu - \delta_\nu A_\nu - i\mathrm{g}\,[A_\mu, A_\nu]$, the "gluon" gauge fields A_μ, i.e. *unobservable internal excitations that bind quarks and antiquarks [36]*, covariant derivatives $D_\mu = \delta_\mu - i\mathrm{g}A_\mu$, the strong coupling constant g, and quark fields q_i. The action has a global SU(3) × SU(3) chiral symmetry, i.e. S_{QCD} in equation 9 is invariant under global flavour transformations

$$\begin{aligned} \text{SU(3) vector} \quad q_i &\rightarrow (\exp i\alpha_a\lambda_a)_{ij}\,q_j \\ \text{SU(3) axial} \quad q_i &\rightarrow (\exp i\beta_a\lambda_a\gamma_5)_{ij}\,q_j\ , \end{aligned} \tag{10}$$

[1] *Borrow* of the example from [37]: The internal triangle anomaly in the Glashow–Weinberg–Salam model cancels only if quarks and leptons bear their definite values of hypercharge.

[2] The number of quark flavours $\mathrm{N}_f = 3$ is used with respect to the COSY energy range.

with the Gell–Mann λ matrices and $i, j = 1..\mathrm{N}_f = 3$. The global flavour symmetry (eq. 10) is explicitly broken by the quark mass term in the QCD Lagrangian (eq. 9). Implementing additionally U(1) phase transformations

$$\begin{aligned} \text{SU(3) vector} \quad q_i &\rightarrow (\exp i\alpha)\, q_i \\ \text{SU(3) axial} \quad q_i &\rightarrow (\exp i\beta\gamma_5)\, q_i \end{aligned} \tag{11}$$

extends the chiral $\mathrm{SU}(3) \times \mathrm{SU}(3)$ to the global $\mathrm{U}(3) \times \mathrm{U}(3)$ symmetry. Scale transformations, i.e. a scaling of coordinates and rescaling of quark and gluon fields

$$\begin{aligned} A_\mu(\mathrm{x}) &\rightarrow \tau A_\mu(\tau \mathrm{x}) \\ q(\mathrm{x}) &\rightarrow \tau^{3/2} q(\tau \mathrm{x})\ , \end{aligned} \tag{12}$$

also leave the classical action invariant.

At the quantum level, both currents associated with $\mathrm{SU}(3) \times \mathrm{SU}(3)$ symmetry (eq. 10) and the vector U(1) transformation (eq. 11 [3]) are conserved and, consequently, are anomaly–free. On the other hand, the currents related to axial U(1) symmetry (eq. 11) and the dilatation current (eq. 12) are not conserved, and are associated with anomalies. To focus on physics issues related to this introductory text, only the axial U(1) anomaly will be discussed below [4]. In the chiral limit, the current generating the axial U(1) transformation is given by

$$\mathrm{j}^\mu_A = \sum_{q=u,d,s} \bar{q}\gamma_\mu\gamma_5 q\,, \tag{13}$$

and the naive differentiation yields current conservation. However, to calculate physical observables, the theory requires a gauge invariant ultraviolet regularization, and the current in equation 13 ceases to be conserved:

$$\delta_\mu \mathrm{j}^\mu_A = \frac{\sqrt{3}\,\alpha_s}{4\,\pi} \mathrm{G}^A_{\mu\nu} \tilde{\mathrm{G}}^{A\mu\nu}\ , \tag{14}$$

where $\mathrm{G}^A_{\mu\nu}$ denotes the gluonic field strength tensor.

[3] Vector U(1) invariance is the symmetry that ensures a constant number of quarks in any QCD process.

[4] See [37] for details on the scale anomaly.

The textbook example: $\pi^0 \to \gamma\gamma$

Additional anomalies arise if interactions of quarks with external fields, e.g. photons, are included. For example, the divergence of the flavour–octet axial current (see eq. 13)

$$\mathrm{j}_3^\mu = \bar{u}\gamma_\mu\gamma_5 u - \bar{d}\gamma_\mu\gamma_5 d \tag{15}$$

is $\delta_\mu \mathrm{j}_3^\mu = 0$ in pure QCD, but becomes non–vanishing when the interaction with photons is switched on (fig. 2a):

$$\delta_\mu \mathrm{j}_3^\mu = \frac{3\,\alpha_{em}}{2\,\pi}\left(\mathrm{Q}_u^2 - \mathrm{Q}_d^2\right)\mathrm{F}_{\mu\nu}\tilde{\mathrm{F}}_{\mu\nu}\,. \tag{16}$$

Q_u^2 and Q_d^2 are the quark electric charges, and $\mathrm{F}_{\mu\nu}$ is the electromagnetic field strength tensor. The transition amplitude of the axial current of equation 15 into two real photons with momenta $\mathrm{k}^{(i)}$ and polarization vectors $\epsilon^{(i)}$ $(i = 1, 2)$ is given by [37]

$$< 0|\mathrm{j}_3^\mu|\gamma\gamma >= -3\frac{i\mathrm{q}_\mu}{\mathrm{q}^2}\frac{4\,\alpha_{em}}{\pi}\left(\mathrm{Q}_u^2 - \mathrm{Q}_d^2\right)\epsilon^{\mu\nu\alpha\beta}\mathrm{k}_\mu^{(1)}\epsilon_\nu^{(1)}\mathrm{k}_\alpha^{(2)}\epsilon_\beta^{(2)} + \ldots\,, \tag{17}$$

where $\mathrm{q} = \mathrm{k}^{(1)} + \mathrm{k}^{(2)}$ is the momentum transfer at the axial vertex. Physically, the singularity for low momentum transfer $\mathrm{q}^2 \to 0$ in the axial current, which is a consequence of the propagating massless quarks in the triangle graph (fig. 2a), can only be understood if massless colourless particles exist coupling both to photons and the axial current [5]. In the case of the axial current in equation 15, the current j_3^μ has the quantum numbers of the π^0, and thus the π^0 is identified with the massless particle coupling to the axial vector current required by the singularity in the two–photon transition of equation 17, which actually leads to the spontaneous breaking of axial SU(3) flavour symmetry. The relation required between the $\pi^0 \to \mathrm{j}_3^\mu$ amplitude and the $\pi^0 \to \gamma\gamma$ coupling is [6]

$$< 0|\mathrm{j}_3^\mu|\pi^0 >= \sqrt{2}i\mathrm{f}_\pi\mathrm{q}_\mu \tag{18}$$

with the pion $\pi^0 \to \mu\nu$ leptonic decay constant f_π and pion momentum q_μ.

For η and η' — coupling to the flavour singlet η_0 — the situation is complicated by the gluonic component in the axial anomaly (eq. 14).

[5] The matching of the singularity in the axial current at the quark level actually proves the existence of massless hadrons [38].

[6] The relation is exactly the PCAC result for the $\pi^0 \to \gamma\gamma$ amplitude in terms of f_π.

5 Radiative Decays

Two–photon decays $\eta\ (\eta') \to \gamma\gamma$ provide insight into the $U_A(1)$ anomaly of QCD, since they are determined by the pseudoscalar singlet and octet couplings to the divergences of the relevant axial–vector currents and the singlet–octet mixing angle Θ_{ps} [39]:

The physical states $|\,\eta>$ and $|\,\eta'>$ are considered to be mixtures of the SU(3) octet and singlet representations $|\,\eta_8>$ and $|\,\eta_0>$:

$$\begin{pmatrix} \eta \\ \eta' \end{pmatrix} = \begin{pmatrix} \cos\Theta_{ps} & -\sin\Theta_{ps} \\ \sin\Theta_{ps} & \cos\Theta_{ps} \end{pmatrix} \begin{pmatrix} \eta_8 \\ \eta_0 \end{pmatrix} \tag{19}$$

With commonly accepted values of the pseudoscalar mixing angle Θ_{ps} the η' is dominated by the singlet state η_0. In the quark–flavour basis, using equation 3, η and η' are given by

$$\begin{pmatrix} \eta \\ \eta' \end{pmatrix} = \begin{pmatrix} \cos\alpha_{ps} & -\sin\alpha_{ps} \\ \sin\alpha_{ps} & \cos\alpha_{ps} \end{pmatrix} \begin{pmatrix} \frac{u\bar{u}+d\bar{d}}{\sqrt{2}} \\ s\bar{s} \end{pmatrix}, \tag{20}$$

where $\alpha_{ps} = \Theta_{ps} - \Theta_i + \pi/2$ denotes the deviation between the pseudoscalar and ideal mixing, Θ_{ps} and $\Theta_i = \arctan 1/\sqrt{2}$, respectively.

Octet and singlet decay constants f_8 and f_0 are defined analogously to the pion decay constant as couplings of the SU(3) states $|\,\eta_8>$ and $|\,\eta_0>$ to the divergence of the relevant axial–vector currents, which transforms for the physical states $|\eta>$ and $|\eta'>$ to

$$\begin{aligned} <0|\delta_\mu j_8^\mu|\eta> &= m_\eta^2 f_8 \cos\Theta_{ps} & <0|\delta_\mu j_0^\mu|\eta> &= -m_\eta^2 f_0 \sin\Theta_{ps} \\ <0|\delta_\mu j_8^\mu|\eta'> &= m_{\eta'}^2 f_8 \sin\Theta_{ps} & <0|\delta_\mu j_0^\mu|\eta'> &= m_{\eta'}^2 f_0 \cos\Theta_{ps} \end{aligned} \tag{21}$$

The divergences of the axial–vector currents are given by (see eq. 14)

$$\begin{aligned} \delta_\mu j_8^\mu &= \frac{2}{\sqrt{6}} \left(m_u \bar{u} i\gamma_5 u + m_d \bar{d} i\gamma_5 d - 2 m_s \bar{s} i\gamma_5 s \right) \\ \delta_\mu j_0^\mu &= \frac{2}{\sqrt{3}} \left(m_u \bar{u} i\gamma_5 u + m_d \bar{d} i\gamma_5 d + m_s \bar{s} i\gamma_5 s \right) + \frac{\sqrt{3}\,\alpha_s}{4\,\pi} G^A_{\mu\nu} \tilde{G}^{A\mu\nu} . \end{aligned} \tag{22}$$

The origin of the term proportional to $G\tilde{G}$ — the *topological charge density* — in the divergence of the singlet axial–vector current [7] that does not vanish in the chiral limit is the AVV (axialvector–vector–vector) triangle anomaly of

[7] The term does not contribute to e.g. vector currents.

QCD [40, 41]. Consequently, the pseudoscalar singlet state couples to gluons, and the η' with a dominant singlet component may contain a gluonium fraction.

Using equation 22 and neglecting m_u and m_d the matrix element of the strong anomaly over the vacuum is given by

$$\begin{aligned} <0|\frac{3\,\alpha_s}{4\pi}G\tilde{G}|\eta> &= \sqrt{\frac{3}{2}}m_\eta^2\left(f_8\cos\Theta_{ps}-\sqrt{2}f_0\sin\Theta_{ps}\right) \\ <0|\frac{3\,\alpha_s}{4\,\pi}G\tilde{G}|\eta'> &= \sqrt{\frac{3}{2}}m_{\eta'}^2\left(f_8\sin\Theta_{ps}+\sqrt{2}f_0\cos\Theta_{ps}\right), \end{aligned} \qquad (23)$$

and depends on the singlet and octet decay constants f_0 and f_8 and the pseudoscalar mixing angle Θ_{ps}. Two parameters can be fixed from the radiative decay widths

$$\begin{aligned} \Gamma\left(\eta\to\gamma\gamma\right) &= \frac{2}{3}\left(\frac{m_\eta}{4\,\pi}\right)^3\alpha_{em}^2\left(\frac{\cos\Theta_{ps}}{f_8}-\frac{2\sqrt{2}\sin\Theta_{ps}}{f_0}\right)^2 \\ \Gamma\left(\eta'\to\gamma\gamma\right) &= \frac{2}{3}\left(\frac{m_{\eta'}}{4\,\pi}\right)^3\alpha_{em}^2\left(\frac{\sin\Theta_{ps}}{f_8}+\frac{2\sqrt{2}\cos\Theta_{ps}}{f_0}\right)^2, \end{aligned} \qquad (24)$$

i.e. the pseudoscalar decay constants can be expressed in terms of the mixing angle Θ_{ps}. The latter can be constrained from radiative decays of vector ($V=\rho,\omega,\phi$) and pseudoscalar ($P=\eta,\eta'$) mesons in $V\,(P)\to P\,(V)\gamma$ processes [39]: For example, in

$$\Gamma\left(P\to V\gamma\right)=\frac{\alpha_{em}}{8}g_{VP\gamma}^2\left(\frac{m_P^2-m_V^2}{m_P^2}\right)^3 \qquad (25)$$

the vertex coupling $g_{VP\gamma}$ corresponds to the on–shell vector–pseudoscalar electromagnetic form factor and is given by

$$g_{\omega\eta'\gamma}=\frac{\cos\Theta_{ps}}{2\sqrt{2}f_0}\sin\Theta_v+\frac{\sin\Theta_{ps}}{4f_8}\left(\sqrt{2}\cos\Theta_v-\sin\Theta_v\right) \qquad (26)$$

for the decay $\eta'\to\omega\gamma$ [39]. Θ_v denotes the vector mixing angle. Due to the different dependences of the $g_{VP\gamma}$ couplings on the pseudoscalar mixing angle, in the range between $\Theta_{ps}=-10^\circ$ and $\Theta_{ps}=-23^\circ$ derived from the quadratic and linear Gell–Mann-Okubo mass formula, respectively, the strongest constraints on the value of Θ_{ps} are expected from the decays $\phi\to\eta\,(\eta')\,\gamma$ [39].

Precision values on the pseudoscalar nonet parameters will also provide information on the underlying structure of the physical states. As discussed above, the η' might be expected to have a gluonium component, related to the gluonic coupling of the pseudoscalar singlet state. The η–η' system (eqs. 19 and 20) can be reconstructed to include a gluonic component equivalently to the quark content [42]:

$$\begin{aligned} |\eta\rangle &= \mathrm{X}_\eta \left| \frac{u\bar{u} + d\bar{d}}{\sqrt{2}} \right\rangle + \mathrm{Y}_\eta \, |s\bar{s}\rangle \\ |\eta\rangle &= \mathrm{X}_{\eta'} \left| \frac{u\bar{u} + d\bar{d}}{\sqrt{2}} \right\rangle + \mathrm{Y}_{\eta'} \, |s\bar{s}\rangle + \mathrm{Z}_{\eta'} \, |gluonium\rangle \end{aligned} \tag{27}$$

In the Vector meson Dominance Model (VDM) the radiative decay rates of $P(V) \to V(P)\gamma$ and $P \to \gamma\gamma$ processes can be expressed in terms of the light and strange quark and gluonium fractions in the η and η' wavefunctions denoted by $\mathrm{X}_{\eta(\eta')}$, $\mathrm{Y}_{\eta(\eta')}$, and $\mathrm{Z}_{\eta'}$, respectively (fig. 1 and [43]).

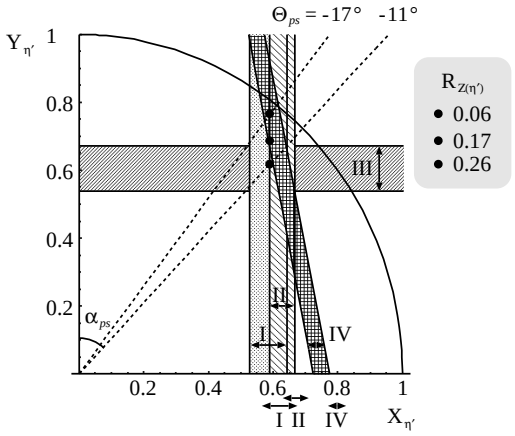

Figure 1: Experimental constraints on the quark content of the η' wavefunction from the radiative decays $\eta' \to \omega\gamma$ (I), $\eta' \to \rho\gamma$ (II), $\phi \to \eta'\gamma$ (III), and $\eta' \to \gamma\gamma$ (IV). Full dots denote the gluonium fraction $\mathrm{R}_{\mathrm{Z}(\eta')}$ (eq. 28) for different pseudoscalar mixing angles Θ_{ps}. The figure is taken from [43], experimental results were updated according to [44].

In the analysis of [43] the maximum η' gluonic admixture

$$\mathrm{R}_{\mathrm{Z}(\eta')} = \frac{\mathrm{Z}_{\eta'}}{\mathrm{X}_{\eta'} + \mathrm{Y}_{\eta'} + \mathrm{Z}_{\eta'}} \tag{28}$$

was extracted to range between 6 % ($\Theta_{ps} = -17°$) and 26 % ($\Theta_{ps} = -11°$). Later, recent measurements [45, 46, 47, 48] of the $\phi \to \eta'\gamma$ branching ratio included in the PDG value [44] in figure 1 seem to favour both lower values of the pseudoscalar mixing angle $|\Theta_{ps}|$ and a larger gluonic fraction $\mathrm{R}_{\mathrm{Z}(\eta')}$ in the η' wavefunction. However, with a pseudoscalar mixing angle $\Theta_{ps} =$

$12.9^{+1.9}_{-1.6}{}^{\circ}$, in [47] $Y_{\eta'}$ determined from the decay $\phi \to \eta'\gamma$ is roughly 20 % larger compared to the value given in figure 1. The gluonic component $Z^2_{\eta'}$ is concluded to be consistent with values between zero and 15 % within one standard deviation. Obviously, a more conclusive interpretation lacks precision of the experimental data, with present errors on the radiative decay branching ratios of 3.3 % ($\eta' \to \rho\gamma$), 6.6 % ($\eta' \to \gamma\gamma$), and 10.2 % ($\eta' \to \omega\gamma$), respectively [44]. A statistical accuracy at the 1 % level could be achieved with the WASA facility at COSY within few weeks (table 1). To minimize systematical uncertainties, a direct measurement of the branching ratios — as reported in [49] for the decay $\eta \to \gamma\gamma$ — is mandatory: In this case, the branching ratio for the decays $\eta' \to V\gamma$, with $V = \rho, \omega, \gamma$, is given by the ratio of the number of observed decays $N(\eta' \to V\gamma)$ and the total number of measured η' events $N(pp \to pp\eta')$, which is determined from the missing mass with respect to the pp tagging system

$$B(\eta' \to V\gamma) = \frac{N(\eta' \to V\gamma)}{N(pp \to pp\eta')} \times \left(A_{\eta' \to V\gamma} \epsilon^{analysis}_{\eta' \to V\gamma} \epsilon^{electronics}_{\eta' \to V\gamma} \right)^{-1} , \qquad (29)$$

considering the detector acceptance $A_{\eta' \to V\gamma}$ and both efficiencies for reconstruction $\epsilon^{analysis}_{\eta' \to V\gamma}$ and readout electronics for $\eta' \to V\gamma$ decays. Thus, the direct measurement avoids additional uncertainties from the identification of any other η' decay channel for normalization. With counting the number of $\eta' \to V\gamma$ decays from the number of identified $pp \to pp\eta'$ events, systematic errors due to target and beam conditions and the efficiency for the $pp \to pp\eta'$ tagging reaction do not contribute to the branching ratio. For $\Gamma(\eta \to \gamma\gamma)/\Gamma_{tot}(\eta)$ the systematical error was determined to be 0.75 % in [49]. The experiment requires a trigger based solely on the detection of two protons in the WASA Forward Detector (FD), with an estimated rate of about 50 kHz. In view of an anticipated rate capability of the future WASA data acquisition system in the order of 10 kHz the experiment seems feasible with an improved trigger condition on the pp system, e.g. by means of a *missing mass* trigger, exploiting the supplementary FD energy loss information in addition to multiplicity counting [50].

5.1 Chanowitz Equations

The AVV triangle anomaly (fig. 2a) is responsible for the two–photon decay of the η', as it is in the case of both η and π^0. Theoretically, the triangle anomaly is accounted for by the Wess–Zumino–Witten (WZW) term of the effective Lagrangian [51, 52], that reproduces the anomalous behaviour of

the effective action under chiral transformations [8].

The WZW Lagrangian also predicts another anomaly of higher order in processes with three pseudoscalar particles, i.e. values for the couplings $(\pi^0\pi^+\pi^-\gamma)$, $(\eta\pi^+\pi^-\gamma)$, and $(\eta'\pi^+\pi^-\gamma)$ in the chiral limit. The amplitude of the non–resonant $\eta' \to \pi^+\pi^-\gamma$ decay is determined by parameters of both the AVV triangle (fig. 2a) and the AAAV (axialvector–axialvector–axialvector–vector) box anomaly (fig. 2b). However, the $\pi^+\pi^-\gamma$ decay mode of the η' is dominated by $\eta' \to \rho\gamma$, obscuring a direct signal from processes involving the box anomaly.

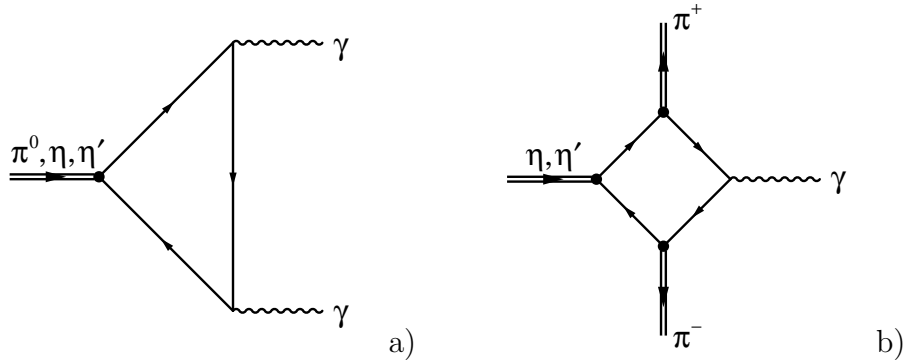

Figure 2: Anomalies in radiative decays of pseudoscalar mesons: (a) (AVV) Triangle anomaly, and (b) (AAAV) box anomaly.

In terms of the triangle anomaly constant $\mathrm{B}_{\eta,\,\eta'}\,(0)$ the radiative decays $\eta,\,\eta' \to \gamma\gamma$ (eq. 24) are described by

$$\Gamma\left(\eta,\,\eta' \to \gamma\gamma\right) = \frac{\mathrm{m}^3_{\eta,\,\eta'}}{32\,\pi}\left|\mathrm{B}_{\eta,\,\eta'}\,(0)\right|^2 . \tag{30}$$

The box anomaly constants $\mathrm{E}_{\eta,\,\eta'}\,(0)$ modify the $\pi^+\pi^-$ mass spectrum in the decays $\eta,\,\eta' \to \pi^+\pi^-\gamma$ according to [53, 54]

$$\frac{d\,\Gamma_{\eta,\,\eta'}}{d\,\mathrm{m}_{\pi\pi}} = \frac{1}{24\,\pi^3}\left|\frac{2\mathrm{G}_\rho\,(\mathrm{m}_{\pi\pi})\;\mathrm{g}_{\eta^{(\prime)}\rho\gamma}}{\mathrm{D}_\rho\,(\mathrm{m}_{\pi\pi})} + \mathrm{E}_{\eta,\,\eta'}\,(0)\right|\,\mathrm{k}^3_\gamma\,\mathrm{q}^3_\pi\,, \tag{31}$$

where k_γ and q_π are the four–momenta of the outgoing γ and $\pi^\pm$, $\mathrm{g}_{\eta^{(\prime)}\rho\gamma}$ denotes the coupling constant for the ρ contribution to the $\pi^+\pi^-\gamma$ decay mode of η and η', and $\mathrm{D}_\rho\,(\mathrm{m}_{\pi\pi}) = (\mathrm{m}^2_\rho - \mathrm{m}^2_{\pi\pi}) - i\,\mathrm{m}_\rho\,\Gamma_\rho(\mathrm{m}_{\pi\pi})$ and

[8] The term *anomalous* refers to matrix elements of wrong parity.

$G_\rho\,(m_{\pi\pi}) = \sqrt{6\,\pi\,\frac{m_\rho m_{\pi\pi}}{q_\pi^3}\,\Gamma_\rho(m_{\pi\pi})}$ are the ρ propagator and its coupling to the $\pi^+\pi^-$ channel, respectively, which can be obtained from fitting the available $e^+e^- \to \pi^+\pi^-$ data. The mass dependent width of the ρ is described by a standard relativistic Breit–Wigner amplitude

$$\Gamma_\rho(m_{\pi\pi}) = \Gamma_\rho(m_\rho)\,\left[\frac{q_\pi(m_{\pi\pi})}{q_\pi(m_\rho)}\right]^3\,\left[\frac{m_\rho}{m_{\pi\pi}}\right]^\lambda \tag{32}$$

with the q^3 dependence accounting for the p–wave matrix element and phase space, and a damping–power λ ($\lambda = 1$ for elementary pointlike couplings).

Triangle and box anomaly constants $B_{\eta,\,\eta'}\,(0)$ and $E_{\eta,\,\eta'}\,(0)$ are approximations of functions $B_{\eta,\,\eta'}\,(k_{\gamma 1}k_{\gamma 2})$ and $E_{\eta,\,\eta'}\,(q_{\pi^+}k_\gamma, q_{\pi^-}k_\gamma)$ at their chiral point with vanishing four–momenta, which relates them to the pseudoscalar nonet parameters [9], i.e. singlet and octet coupling constants f_0 and f_8 and the pseudoscalar mixing angle Θ_{ps} via the four Chanowitz equations [55, 56]

$$\begin{aligned} B_\eta\,(0) &= -\frac{\alpha_{em}}{\pi\,\sqrt{3}}\left[\frac{\cos\Theta_{ps}}{f_8} - 2\,\sqrt{2}\,\xi\,\frac{\sin\Theta_{ps}}{f_0}\right] \\ B_{\eta'}\,(0) &= -\frac{\alpha_{em}}{\pi\,\sqrt{3}}\left[\frac{\sin\Theta_{ps}}{f_8} + 2\,\sqrt{2}\,\xi\,\frac{\cos\Theta_{ps}}{f_0}\right] \end{aligned} \tag{33}$$

$$\begin{aligned} E_\eta\,(0) &= -\frac{\sqrt{4\,\pi\,\alpha_{em}}}{4\,\pi^2\,\sqrt{3}}\,\frac{1}{f_\pi^2}\left[\frac{\cos\Theta_{ps}}{f_8} - \sqrt{2}\,\frac{\sin\Theta_{ps}}{f_0}\right] \\ E_{\eta'}\,(0) &= -\frac{\sqrt{4\,\pi\,\alpha_{em}}}{4\,\pi^2\,\sqrt{3}}\,,\frac{1}{f_\pi^2}\left[\frac{\sin\Theta_{ps}}{f_8} + \sqrt{2}\,\frac{\cos\Theta_{ps}}{f_0}\right] \end{aligned} \tag{34}$$

where f_π is the pion decay constant with the relation analogous to equation 33

$$B_\pi\,(0) = \frac{\alpha_{em}}{\pi\,\sqrt{3}}\,\frac{\sqrt{3}}{f_\pi}$$

The four Chanowitz equations allow to determine the four unknowns: f_0, f_8, Θ_{ps}, and the discrete parameter ξ in the triangle anomaly constants which is related to the quark charges in the underlying theory of strong interactions. The value $\xi = 1$ is a prerequisite for fractional quark charges, i.e. QCD, while most integral quark charge models result in $\xi = 2$. Since we

[9] The couplings $B_{\eta,\,\eta'}\,(k_{\gamma 1}k_{\gamma 2})$ and $E_{\eta,\,\eta'}\,(q_{\pi^+}k_\gamma, q_{\pi^-}k_\gamma)$ are believed to depend only very weakly on the energy.

strongly believe in QCD being the theory of strong interactions, ξ is usually set to one in the analysis of radiative decays. However, it should be kept in mind, that experimental data on all four radiative decays $\eta(\eta') \to \gamma\gamma$ and $\eta(\eta') \to \pi^+\pi^-\gamma$ allow a test of QCD.

On the one hand, the extraction of the box anomaly contribution is strongly dependent on the model employed in the description of the ρ. On the other hand, from the two–photon widths of η and η' (eq. 33) using additional information from radiative $J/\Psi \to \eta(\eta')\gamma$ decays and the AFN relation [57, 58])

$$\frac{\Gamma\left(J/\psi \to \eta'\gamma\right)}{\Gamma\left(J/\psi \to \eta\gamma\right)} = \left[\frac{\mathrm{m}^2_{J/\psi} - \mathrm{m}^2_{\eta'}}{\mathrm{m}^2_{J/\psi} - \mathrm{m}^2_{\eta}}\right]^3 \left[\frac{\mathrm{m}_{\eta'}}{\mathrm{m}_{\eta}}\right]^4 \times \left[\frac{\sqrt{2}\,\mathrm{f}_0\,\sin\Theta_{ps} + \mathrm{f}_8\,\cos\Theta_{ps}}{\mathrm{f}_8\,\sin\Theta_{ps} - \sqrt{2}\,\mathrm{f}_8\,\sin\Theta_{ps}}\right]^2 \tag{35}$$

the parameters of the pseudoscalar nonet are completely determined without any assumption about the ρ, and can be used to predict the box anomaly constant $E_{\eta'}$. Consequently, the ρ shape and the box anomaly parameters are closely related to each other — the approach might allow an alternative to extract the ρ line shape in a clean way.

So far, experimentally no uniform picture has been derived: A box anomaly contribution has been extracted by the Crystal Barrel collaboration in the $p\bar{p}$ annihilation channels $p\bar{p} \to \pi^0\pi^0\eta'$, $p\bar{p} \to \pi^+\pi^-\eta'$ and $p\bar{p} \to \omega\eta'$ with a total number of 7392 η' decays [59].

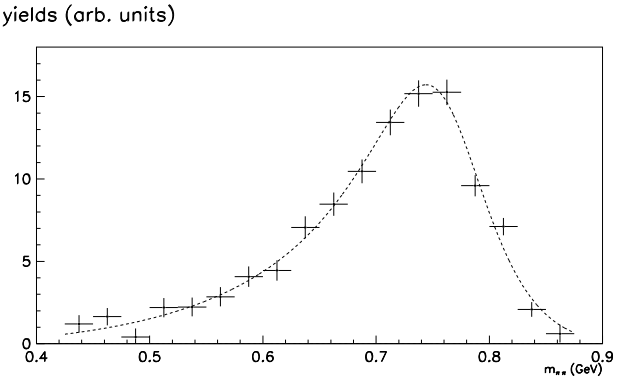

Figure 3: Distribution of the $\pi^+\pi^-$ invariant mass for $\eta' \to \pi^+\pi^-\gamma$ decays [59]. Crosses denote experimental data, the dashed line is the result of the fit used to extract box anomaly parameters with a statistical significance of $4\,\sigma$.

It should be noted, that the $\mathrm{m}_{\pi^+\pi^-}$ invariant mass distribution shown in figure 3 is free of background, since the spectrum was obtained by determining the number of $\eta' \to \pi^+\pi^-\gamma$ events in each bin of the $\pi^+\pi^-$ invariant mass seperately. From the Crystal Barrel data, depending on the ρ model applied, evidence for a nonresonant box anomaly component in $\eta' \to \pi^+\pi^-\gamma$ decays is found with a statistical significance of at least $4\,\sigma$. Both ρ models tested

result in a box anomaly constant $E_{\eta'}$ consistent with the prediction from the $\eta(\eta') \to \gamma\gamma$ decays (eqs. 30 and 33) and J/ψ decays (eq. 35). However, either model clearly favours one of the two possible values $\xi = 1$ or $\xi = 2$, and the ambiguity could not be resolved due to the lack of statistics [59].

The box anomaly contribution extracted from the Crystal Barrel data is rather disfavoured (confidence level 3 %) by the L3 result (fig. 4 and [60]), which is consistent with a pure ρ line shape (C.L. 37 %). On the other

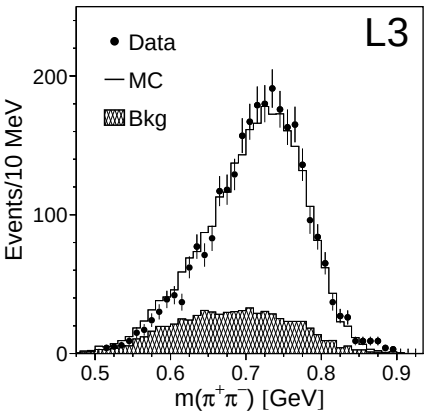

Figure 4: $\pi^+\pi^-$ effective mass distribution in the decay $\eta' \to \pi^+\pi^-\gamma$ from L3 [60]. Points denote experimental data, the solid line is the best fit result with $m_\rho = 766\,\mathrm{MeV}$ and $\Gamma_\rho = 150\,\mathrm{MeV}$. The estimated background (shaded area) is mainly attributed to decays of the $a_2(1320)$.

hand, the Crystal Barrel data would require a mass $m_\rho = 790\,\mathrm{MeV}$ when neglecting the anomaly related non–resonant contribution, i.e. 20 MeV above the presently accepted value [44]. In this respect, these two results with the up to now highest statistics are inconsistent.

6 Leptonic Decays

Electromagnetic processes involving photons and mesons reflect the coupling of photons to the electric charges of the quark fields, i.e. these processes contain information about the charge distribution in mesonic matter. The complete characterization of the electromagnetic meson structure is contained in the form factor, which is, in the non–relativistic case, related to the charge density distribution by a Fourier transformation. For charged particles, electron scattering experiments (fig. 5a) and e^+e^- annihilation processes (fig. 5b) allow to study the meson form factor in the whole physically accessible range of momentum transfer (for an introduction see [61]) complementarily.

In electron scattering on a charged meson (e.g. $e^-\pi^- \to e^-\pi^-$ in fig. 5a) , the momentum transferred by the virtual exchange photon is given by the

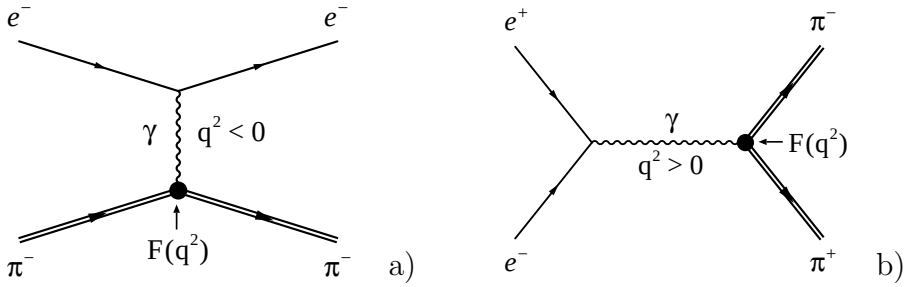

Figure 5: One–photon exchange processes and $\pi^{\pm}$ form factor $F(q^2)$: (a) Space–like exchange in $e^-\pi^- \to e^-\pi^-$ scattering, and (b) time–like process in $e^+e^- \to \pi^+\pi^-$ annihilation.

difference between the squares of the changes in energy and momentum of the electron. The *space–like* process is characterized by

$$q^2 = (\Delta E_e)^2 - (\Delta p_e)^2 < 0\,, \tag{36}$$

since in elastic collisions the electron energy remains unchanged, and only the direction of the momentum changes. The differential scattering cross section is given by

$$\frac{d\,\sigma}{d\,q^2} = \left[\frac{d\,\sigma}{d\,q^2}\right]_{pointlike} \left[F\left(q^2\right)\right]^2 . \tag{37}$$

Thus, the form factor $F\left(q^2\right)$ characterizing the spatial charge distribution can be determined comparing experimental results on the differential cross section with the exact calculation for a pointlike particle.

In annihilation processes (e.g. $e^+e^- \to \pi^+\pi^-$ in fig. 5b) a virtual photon is emitted which then creates the meson system, with a momentum transfer

$$q^2 = (2E)^2 - (\vec{p} - \vec{p})^2 = (2E)^2 = s > 0 \tag{38}$$

for the (*time–like*) annihilation of an electron and a positron with momenta $\vec{p}$ and $-\vec{p}$ and energies $E = \sqrt{p^2 + m_e^2}$. The differential cross section can be expressed analoguously to equation 37, and the process $e^+e^- \to \pi^+\pi^-$ can be calculated exactly for pointlike mesons in QED.

For neutral mesons, the scattering process with single photon exchange of figure 5a is forbidden due to C–parity, which is conserved in strong and electromagnetic interactions. Consequently, the electromagnetic form factors of neutral mesons are always zero, and, the internal structure of neutral

mesons can only manifest itself in radiative decays into a photon and meson of opposite C–parity, i.e. for decays of pseudoscalar mesons P in decays $P \to V\gamma$. The photon can be either real or virtual, in the latter case (fig. 6a) with a subsequent decay into a lepton pair l^+l^- (*internal conversion*)

$$\begin{aligned} P &\to V\gamma \\ P &\to V\gamma^* \to Vl^+l^- \,, \end{aligned} \tag{39}$$

where the invariant mass $\mathrm{m}_{l^+l^-}$ of the lepton pair ($l = e, \mu$) is equal to the four–momentum of the virtual photon.

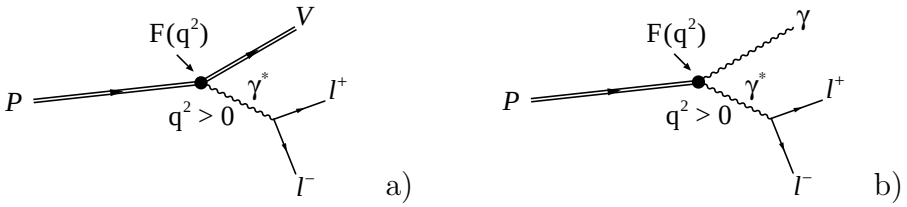

Figure 6: Conversion decays of a pseudoscalar meson P to (a) a vector meson (V) or (b) a photon and an intermediate γ^* converting to a lepton pair l^+l^-.

The lepton invariant mass distribution depends on the electromagnetic structure at the $P \to V$ transition vertex, which is due to a cloud of virtual states, i.e. the corresponding *transition form factor* describes transition dynamics rather than static properties as in the case of the electromagnetic form factor. Replacing the vector meson V in the conversion decay by a photon (*Dalitz decay* $P \to \gamma\gamma^* \to \gamma l^+l^-$, fig. 6b) the structure of the $P \to \gamma$ vertex is probed, defining the electromagnetic properties of the decaying meson. The lepton pair mass spectrum is given by

$$\frac{d\,\Gamma}{d\,\mathrm{q}^2} = \left[\frac{d\,\Gamma}{d\,\mathrm{q}^2}\right]_{pointlike} \left|\mathrm{F}_{PV(\gamma)}\left(\mathrm{q}^2\right)\right|^2 \,. \tag{40}$$

The transition form factor in equation 40 for a pointlike meson can be calculated reliably from QED, and — normalized to the two photon decay width — the lepton pair mass spectrum is obtained:

$$\frac{d\,\Gamma\left(l^+l^-\gamma\right)}{d\,\mathrm{q}^2\,\Gamma\left(\gamma\gamma\right)} = \frac{2\,\alpha_{em}}{3\,\pi}\sqrt{1-\frac{4\mathrm{m}_l^2}{\mathrm{q}^2}}\left[1+\frac{2\mathrm{m}_l^2}{\mathrm{q}^2}\right]\frac{1}{\mathrm{q}^2}\left[1-\frac{\mathrm{q}^2}{\mathrm{m}_P^2}\right]^3\left|\mathrm{F}_{P\gamma}\left(\mathrm{q}^2\right)\right|^2 \tag{41}$$

Calculations of transition form factors are available from purely phenomenological models based on vector meson dominance (see [61]), and dynamical quark triangle loop models [62, 61], and experimental results can be compared with ChPT predictions (for the η transition form factor see e.g. [63]) [10].

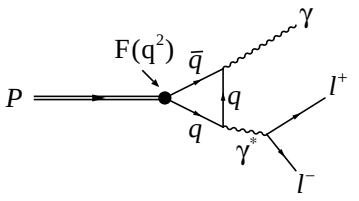

Figure 7: Dalitz decay $P \to \gamma\gamma^* \to \gamma l^+ l^-$ in the quark triangle loop model.

In the dynamic approach of quark triangle loop models, which assume the process to be dominated by quark triangle anomalies (fig. 7), the transition form factor is related to the quark model meson constituents [62]

$$\mathrm{F}_{P\gamma}\left(\mathrm{q}^2\right) = \left(\frac{1}{1-\mathrm{q}^2/\mathrm{m}_P^2}\right) \left\{ \frac{\sum_q \frac{\mathrm{g}_{Pq\bar{q}}}{\mathrm{m}_q}\mathrm{Q}_q^2 \left[1 - \frac{\arcsin^2\left(\sqrt{\mathrm{q}^2}/2\mathrm{m}_q\right)}{\arcsin^2\left(\mathrm{m}_P/2\mathrm{m}_q\right)}\right]}{\sum_q \frac{\mathrm{g}_{Pq\bar{q}}}{\mathrm{m}_q}\mathrm{Q}_q^2} \right\}, \quad (42)$$

with constituent quark masses m_q and quark charges Q_q. The phenomenological couplings $\mathrm{g}_{Pq\bar{q}}$ of the pseudoscalar meson to the constituent quark–antiquark pairs can be interpreted — model–dependently — as information on the meson structure.

Presently, the available data for $\eta' \to l^+ l^- \gamma$ consist of 33 ± 7 $\mu^+\mu^-\gamma$ events [65, 61]. Thus, a detailed analysis of the leptonic mass spectrum is presently not possible due to the lack of statistics. Significant progress could be made using the WASA facility at COSY.

7 Conclusion

The move of the WASA facility to COSY offers the unique possibility to extend both the present η decay programme of WASA at CELSIUS and the investigations of η' production dynamics in nucleon–nucleon scattering at COSY to precision studies of η' decays. The combination of operating COSY at high intensity in combination with an internal pellet target will provide luminosities of $10^{32}\,\mathrm{cm}^{-2}\,\mathrm{s}^{-1}$.

[10] A detailed discussion in the case of η decays is given in [64].

Table 1: Counting rate estimates for reconstructed η' decays for WASA at COSY based on an expected luminosity of $10^{32}\,\mathrm{cm}^{-2}\,\mathrm{s}^{-1}$, branching ratios given in [66], including detector efficiencies from [67]. A total cross section of 300 nb is assumed at an excess energy of 45 MeV (beam momentum 3.350 GeV/c) with respect to the η' threshold [68].

Decay mode	Branching fraction Γ_i/Γ_f	Existing data [events]	Counting rate [events/day]
hadronic			
$\pi^+\pi^-\eta$	44.3 ± 1.5 %	8200	18000
$\pi^0\pi^0\eta$	20.9 ± 1.2 %	5400	14500
$3\,\pi^0$	$1.56 \pm 0.26 \cdot 10^{-3}$	130	145
$\pi^+\pi^-\pi^0$	$< 5.$ %	-	85 [11]
radiative			
$\rho^0\gamma$	29.5 ± 1.0 %	9550	44000 [12]
$\omega\gamma$	3.03 ± 0.31 %	160	1200
$\gamma\gamma$	2.12 ± 0.14 %	2767	17100
semi–leptonic			
$\mu^+\mu^-\gamma$	$1.04 \pm 0.26 \cdot 10^{-4}$	33	15
$e^+e^-\gamma$	$< 9. \cdot 10^{-4}$	-	45 [13]

Expected η' production rates of $2.5 \cdot 10^6$ events/day in proton–proton scattering as tagging reaction (table 1) will substantially improve statistics and precision of the world data set of established hadronic, radiative, and (semi–)leptonic decays of the η', a unique proving ground for fundamental physics issues.

Acknowledgements

Inspiring discussions with Bugra Borasoy are gratefully acknowledged. Most of all, thanks to the organizers for the unprecedented hospitality and great atmosphere in Kraków.

[11] assuming $\Gamma(\eta' \to \pi^+\pi^-\pi^0) \approx \Gamma(\eta' \to 3\,\pi^0)$ [33]
[12] including non–resonant decays $\eta' \to \pi^+\pi^-\gamma$
[13] assuming $\Gamma(\eta' \to e^+e^-\gamma)/\Gamma_{tot} \approx 3 \cdot 10^{-4}$ [69]

References

[1] P. Moskal, M. Wolke, A. Khoukaz, and W. Oelert,
Prog. Part. Nucl. Phys. **49** (2002) 1–90; hep–ph/0208002.

[2] P. Moskal, e–Print Archive: hep–ph/0408162.

[3] G. A. Miller, B. M. K. Nefkens, and I. Slaus,
Phys. Rept. **194** (1990) 1–116.

[4] J. Gasser and H. Leutwyler, Phys. Rept. **87** (1982) 77–169.

[5] A. Peterman, Phys. Rept. **53** (1979) 157–248.

[6] Y. Nambu and G. Jona-Lasinio, Phys. Rev. **122** (1961) 345–358.

[7] Y. Nambu and G. Jona-Lasinio, Phys. Rev. **124** (1961) 246–254.

[8] M. D. Scadron, Ann. Phys. **148** (1983) 257–281.

[9] A. Barducci, R. Casalbuoni, S. De Curtis, D. Dominici, and R. Gatto,
Phys. Rev. **D 38** (1988) 238–278.

[10] G. Krein, P. Tang, and A. G. Williams,
Phys. Lett. **B 215** (1988) 145–150.

[11] E. M. Henley and G. Krein, Phys. Rev. Lett. **62** (1989) 2586–2588.

[12] A. Chodos, R. L. Jaffe, K. Johnson, C. B. Thorn, V. F. Weisskopf,
Phys. Rev. **D 9** (1974) 3471–3495.

[13] T. DeGrand, R. L. Jaffe, K. Johnson, J. Kiskis,
Phys. Rev. **D 12** (1975) 2060–2076.

[14] N. G. Deshpande, D. A. Dicus, K. Johnson, and V. L. Teplitz,
Phys. Rev. **D 15** (1977) 1885–1894.

[15] V. Baru, J. Haidenbauer, C. Hanhart, and J. A. Niskanen,
Phys. Rev. **C 68** (2003) 035203.

[16] D. G. Sutherland, Phys. Lett. **23** (1966) 384–385.

[17] R. Baur, J. Kambor, and D. Wyler,
Nucl. Phys. **B 460** (1996) 127–142,

[18] B. M. K. Nefkens and J. W. Price, Phys. Scripta **T 99** (2002) 114–122,

[19] D. J. Gross, S. B. Treiman, and F. Wilczek,
Phys. Rev. **D 19** (1979) 2188–2196.

[20] T. Feldmann, P. Kroll, and B. Stech, Phys. Rev. **D 58** (1998) 114006,

[21] R. Kaiser and H. Leutwyler, Eur. Phys. J. **C 17** (2000) 623–649.

[22] H. Machner and A. Magiera, "Search for mixing between light mesons." Letter of Intent to the FEMC04 workshop, jan, 2004.

[23] A. Rittenberg. LRL Report No. UCRL–18863 (unpublished), 1969.

[24] F. Binon et al., Phys. Lett. **B 140** (1984) 264–268.

[25] D. Alde et al., Z. Phys. **C 36** (1987) 603.

[26] J. Gasser and H. Leutwyler, Nucl. Phys. **B 250** (1985) 465–516.

[27] K. Maltman and T. Goldman, Nucl. Phys. **A 572** (1994) 682–692,

[28] J. Piekarewicz, Phys. Rev. **C 48** (1993) 1555–1561,

[29] C.-T. Chan, E. M. Henley, T. Meissner, Phys. Lett. **B 343** (1995) 7–12.

[30] B. Bagchi, A. Lahiri, S. Niyogi, Phys. Rev. **D 41** (1990) 2871–2876.

[31] N. Beisert and B. Borasoy, Nucl. Phys. **A 705** (2002) 433–454.

[32] N. Beisert and B. Borasoy, Nucl. Phys. **A 716** (2003) 186–208.

[33] N. Beisert, B. Borasoy, this proceedings, page 307.

[34] A. H. Fariborz and J. Schechter, Phys. Rev. **D 60** (1999) 034002.

[35] A. M. Abdel-Rehim, D. Black, A. H. Fariborz, and J. Schechter, Phys. Rev. **D 67** (2003) 054001.

[36] G. A. Christos, Phys. Rept. **116** (1984) 251–336.

[37] M. A. Shifman, Phys. Rept. **209** (1991) 341–378.

[38] G. 't Hooft,breaking," *Recent Developments in Gauge Theories. Proceedings, NATO Advanced Study Institute, Cargese, France, August 26 – September 8, 1979*, G. 't Hooft, C. Itzykson, A. Jaffe, H. Lehmann, P. Mitter, I. Singer, and R. Stora, eds., vol. 59 of *Nato Advanced Study Institute Series B, Physics*, p. 241. Plenum Press, New York, 1980.

[39] P. Ball, J. M. Frère, and M. Tytgat,
Phys. Lett. **B 365** (1996) 367–376.

[40] S. L. Adler, Phys. Rev. **177** (1969) 2426–2438.

[41] J. S. Bell and R. Jackiw, Nuovo Cim. **A 60** (1969) 47–61.

[42] J. L. Rosner, Phys. Rev. **D 27** (1983) 1101–1108.

[43] E. Kou, Phys. Rev. **D 63** (2001) 054027.

[44] S. Eidelman et al., Phys. Lett. **B 592** (2004) 1–1109.

[45] R. R. Akhmetshin et al., Phys. Lett. **B 473** (2000) 337–342.

[46] R. R. Akhmetshin et al., Phys. Lett. **B 494** (2000) 26–32.

[47] A. Aloisio et al., Phys. Lett. **B 541** (2002) 45–51.

[48] V. M. Aulchenko et al., J. Exp. Theor. Phys. **97** (2003) 24–33.

[49] R. Abegg et al., Phys. Rev. **D 53** (1996) 11–19.

[50] J. Zlomanczuk, WASA Note 030325JZ, 2003.
http://www5.tsl.uu.se/wasa/group/CWNotes/030325JZ

[51] J. Wess and B. Zumino, Phys. Lett. **B 37** (1971) 95–97.

[52] E. Witten, Nucl. Phys. **B 223** (1983) 422–432.

[53] M. Benayoun et al., Z. Phys. **C 58** (1993) 31–54.

[54] M. Benayoun, P. Leruste, L. Montanet, and J. L. Narjoux,
Z. Phys. **C 65** (1995) 399–420.

[55] M. S. Chanowitz, Phys. Rev. Lett. **35** (1975) 977–980.

[56] M. S. Chanowitz, Phys. Rev. Lett. **44** (1980) 59–63.

[57] V. A. Novikov, M. A. Shifman, A. Vainshtein, and V. I. Zakharov,
Nucl. Phys. **B 165** (1980) 55–66.

[58] R. Akhoury and J. M. Frère, Phys. Lett. **B 220** (1989) 258–264.

[59] A. Abele et al., Phys. Lett. **B 402** (1997) 195–206.

[60] M. Acciarri et al., Phys. Lett. **B 418** (1998) 399–410.

[61] L. G. Landsberg, Phys. Rept. **128** (1985) 301–376.

[62] L. Ametller, L. Bergström, A. Bramon, and E. Masso, Nucl. Phys. **B 228** (1983) 301–315.

[63] L. Ametller, Phys. Scripta **T 99** (2002) 45–54.

[64] J. Stepaniak et al., Phys. Scripta **T99** (2002) 133–139.

[65] R. I. Dzhelyadin et al., Sov. J. Nucl. Phys. **32** (1980) 520.

[66] K. Hagiwara et al., Phys. Rev. **D 66** (2002) 010001.

[67] H. Calén, Letter of Intent to the FEMC04 workshop, jan, 2004. http://www.fz-juelich.de/ikp/wasa/data/LoI_Calen.pdf

[68] A. Khoukaz et al., Eur. Phys. J. **A 20** (2004) 345–350.

[69] R. A. Briere et al., Phys. Rev. Lett. **84** (2000) 26–30.